The Geodesy and Geology of Earthquakes and Aseismic Slip

John Dale B. Dianala

Thesis submitted to the University of Oxford

for the degree of Doctor of Philosophy

in

Earth Sciences



Department of Earth Sciences

University of Oxford

Hilary, 2021

Primary supervisor: Professor Richard Thomas Walker

Co-supervisor: Professor Barry Parsons

Declaration

The contents of this thesis are all my own work, except where otherwise stated. The views and opinions expressed herein are mine and not necessarily those of any other person or body unless so attributed.

Para sa bayan

Abstract

The Geodesy and Geology of Earthquakes and Aseismic Slip

John Dale B. Dianala
St Cross College, Oxford

Hilary, 2021

In this thesis, I explore the geodetic and geologic evidence of earthquake ruptures and aseismic fault deformation in different settings in order to understand: 1) the distribution of seismic or aseismic slip, and 2) the physical factors that influence the mechanics of faulting. In a case study of the Tien Shan (Central Asia), mapping and paleoseismology of faults along a supposed 400-km signal of fault creep paints a more nuanced picture than existing regional studies. With data from the field and high-resolution digital elevation models, the 3-5 mm/yr N–S shortening gradient in GPS data appears to be distributed variably across different basins in the mountain belt. From an apparently creeping rangefront fault in Karkara, more structures to the west accommodate active deformation. Distributed folding and thrust faults in the middle of the neighboring wide basin of Issyk-Kul takes up the majority of internal basin shortening. In the narrow basins further southwest (Karakudzhur and eastern Naryn), fresh-looking fault scarps indicate Holocene activity, with along-strike morphology and extents that could be from rupture that have generated M $\sim$ 7 earthquakes. Moving to the Philippines, analyzing the deformation field from satellite radar interferometry (InSAR) data and inverting for the source parameters of a series of four M_w 6.4–6.8 earthquakes in late 2019 reveals a previously unrecognized seismogenic conjugate fault system on the island of Mindanao. The distribution of blind and surface fault ruptures correlates with the heterogenous geology in the shallow crust. Finally, detailed InSAR time-series analysis and modeling of the mode of slip on the creeping segment of the Philippine Fault shows that while $\sim$100 km of the fault creeps on Leyte island throughout the seismogenic zone, a 20-km long seismogenic asperity exists in the middle. This asperity ruptured in a M_w 6.5 earthquake in July 2017. Fluids on the faults and rate-strengthening lithologies can promote interseismic aseismic slip (and impede seismic slip), while seismogenic potential shows up in structurally complex sections of the seismogenic crust in these different cases.

Extended Abstract

The Geodesy and Geology of Earthquakes and Aseismic Slip

John Dale B. Dianala

St Cross College, Oxford

Hilary Term, 2021

Knowing where active faults are and whether they are aseismic or capable of producing earthquakes requires detailed examination of the landscape and tectonic deformation at different parts of the earthquake cycle. Further, our understanding of fault-related hazards and mechanics are tied to the structure of the faults and mode of slip in the seismogenic zone. However, natural examples of variably behaving faults are limited. Hence, in this thesis, I parse geodetic and geologic observations of earthquakes and aseismic slip (creep) on several faults in different tectonic settings. I specifically characterize the behavior of faults in the Tien Shan and the Philippines using high-resolution data, with the goals of 1) constraining the slip mode of faults (seismic and/or aseismic) to help evaulate their potential for being sources of seismic hazard, and 2) understanding the physical (primarily geologic) factors that influence the mechanics of faulting.

Chapter 2 presents the results of reconnaisance mapping and paleoseismology of faults across several basins in the central Tien Shan. Regional GPS studies have determined that as a consequence of the India-Eurasia collision, 20 mm/yr of short-

ening is distributed across this 200-km wide ENE-WSW trending mountain belt north of the stable Tarim Basin and south of the Kazakh platform. However, despite the presence of known E–W Quaternary faults along several rangefronts within the middle of the belt, the existing catalog of earthquakes show that large seismic events cluster in the northern and southern parts of the central Tien Shan. With field investigation and high-resolution imagery and digital elevation models (DEMs) from satellite and drone photogrammetry, I find that a previously described apparent signal of fault creep along a 400-km NE–SW transect in the middle of the region is a 3-5 mm/yr N–S shortening gradient that manifests in wide basins as distributed thrust faulting. At the eastern end of the transect, while the Karkara Rangefront Fault may be creeping in the current interseismic period, secondary faulting less than 10 km to its north appears to have ruptured the surface post-3,000 years ago. Westward, in eastern Issyk-Kul, the shortening gets distributed on young folds, likely underlain by shallow thrust faults, in the middle of the thick sedimentary basin and distal from rangefronts. To the south of Issyk-Kul Basin, the narrower Karakudzhur and eastern Naryn basins each have E–W Holocene fault scarps with variable vertical separation and well preserved morphology along-strike. The lengths of these scarps could be associated with prehistoric ruptures that generated M $\sim$ 7 earthquakes, and dating constrains a surface rupturing event postdating $\sim$4,200 years ago on the Naryn Fault.

Deformation in the Philippines, while found along the rapid oblique-convergent boundary between Eurasia and the Philippine Sea Plate, is also much more distributed and variable than previously assumed. In **Chapter 3**, I study a sequence of four significant earthquakes on Mindanao island that occurred in October and December 2019, primarily in M_w 6.4 (October 16th; 10/16), M_w 6.6 (10/29), M_w 6.5 (10/31), and M_w 6.7 (December 15th; 12/15) events that were 30 kilometers of each other. As the most significant onshore earthquakes on the island in almost a cen-

tury, I infer their source parameters using satellite radar interferometry (or InSAR), with ALOS-2 and Sentinel-1 data, and corroborate the geodetic data with seismological analysis and field observations. InSAR displacement maps show a combination of blind and shallow ruptures on NW-striking left-lateral faults and conjugate NE-striking right-lateral faults. Wrapped interferograms provide evidence of a six- to ten-kilometer long NE-trending ground rupture, likely associated with the 10/31 event, which has the shallowest centroid depth int he sequence (at seven kilometers). To the south, the source of the 12/15 event is a NW-striking left-lateral fault with the top of the fault at 3 km depth, with a centroid at 12 kilometers depth. The 10/16 and 10/29 earthquakes have deeper centroids (17 km and 18 km, respectively) but possibly on faults contiguous along-strike with the shallower events. The three 'blind' ruptures may be related to the buried suture zone faults, overlain by more than three kilometers of sedimentary sequences. The surrounding volcanic rheology also could have played a role in limiting the extent of seismic slip. Their location also coincides with the inferred suture zone between Eurasian margin and island arc basements, providing the first geodetic constraints on this poorly-understood terrane boundary.

In **Chapter 4**, I present the first distributed slip model of the rate of interseismic creep along the Leyte island section of the Philippine Fault. Of the total 1,200-km length of the Philippine Fault, which accommodates the horizontal component of oblique plate convergence in the Philippines, the Leyte island section has been thought to be aseismic because of the rapid creep rates of up to 35 mm/yr (estimated from campaign GPS surveys). However, a M_w 6.5 earthquake happened right in the middle of the fault in July 2017. I use InSAR observations to derive both the interseismic and coseismic slip distributions from kinematic inversions using a probabilistic (Bayesian) framework. Velocity maps from stacking and time-series analysis of ALOS interferograms spanning four years (2007–2011) show a step-change

in ground deformation right on the fault. Inverting for slip at depth reveals along-strike variations of aseismic slip rate over ∼100 km. Aseismic slip on the surface reaches rates of more than 30 mm/yr, equivalent to the long-term slip rate (33 ± 2 mm/yr). Over the same period, a 20-km segment along the releasing bend of the fault in Tongonan appears to be locked. This segment ruptured in M_w 6.5 and M_w 5.8 earthquakes on 6 and 10 July 2017, respectively, as constrained by Sentinel-1 and ALOS-2 InSAR data. Seismic slip is largely restricted within the Tongonan segment, with up to 1.5 ± 0.2 meters of left-lateral displacement. The slip budget and complementarity between the extents of interseismic and coseismic slip suggest that a seismogenic asperity exists in Tongonan. The presence of active hydrothermal systems and rate-strengthening materials provide physical conditions that can promote aseismic slip.

These different case studies in the Tien Shan and the Philippine highlight previously unknown sources of seismic hazard, and adds further constraints on those that have limited data, with evaluations on the possible magnitude of earthquakes that could be generated by the different faults. Juxtaposing these two regions goes along with the continuing, broader acknowldgement of how distributed faulting that comes with structural complexity and geological heterogeneity, regardless of tectonic setting (i.e., within continental interiors or along a plate boundary), may lead to apparent aseismicity within the known record, but in no way precludes the potential for earthquakes.

Acknowledgements

First and foremost, it is difficult to fully express gratitude to my supervisor, Richard Walker, for the opportunity to work on research with him at Oxford (and in the field!) for my academic development. I am grateful to his openness and for the latitude he has given me to develop my work throughout the past four years. I am also thankful to Barry Parsons, who has dedicated his own time to provide input and mentorship that shaped aspects of my work in dimensions unfamiliar to my previous training.

I've had the benefit of collaborating with numerous people across continents. I thank Marion Thomas and Romain Jolivet who helped start me up early in my DPhil and guiding me throughout in the critical analysis of fault mechanics. I would like to acknowledge the contribution of Yo Fukushima, as well as the local government officials in the Province of Leyte and its different municipalities in aid of the Philippine Fault work. I thank Yu Morishita, Alex Copley, and James Jackson for the work in response to the 2019 earthquakes in Mindanao. The COMET consortium has been vital to ensuring that we have data for the Philippine earthquakes that have happened since the start of my DPhil, with Tim Wright as Director. This thesis would also not be possible without the support of my colleagues and mentors at the University of the Philippines-National Institute of Geological Sciences: Mario Aurelio, Mahar Lagmay, and Richard Ybañez. Discussions with peers at the Energy Development Corporation and PHIVOLCS have also been helpful.

The work on the Tien Shan would not be possible without the tireless support of Kanatbek Abdrakhmatov and the rest of the team in the Kyrgyz Institute of Seismology, Aidyn Mukambayev (Kazakhstan National Data Center), and Christoph Grützner (University of Jena) over the years. Magda Patyniak, Alana Williams, and Erkin Rahimdinov also provided valuable help.

For the completion of this thesis, I would like to thank Emma Hill and Conall Mac Niocaill for their time to review and comment on the manuscript.

The more mundane aspects of the DPhil journey have been greatly rewarding thanks to the many individuals I've worked with and befriended in and out of the academic sphere. I thank my *kababayans* at the Oxford Philippines Society– it has been a great, memorable Oxford experience with a tight-knit community of Filipino friends. I'd be remiss to not thank Baptiste, Simon, Austin, Eleanor, David, and Yu during our time overlapping in the department. Special thanks are due to my fellow DPhil compatriots at 50.03, Roberta, Wendy, Neill, and Ben; to Qi for her boundless enthusiasm for most anything; and of course, Nick, the consummate 'partner in crime' day in and day out, making daily life abroad more worthwhile than I thought it would be.

While not physically around in the UK, I thank Jeremy for being there through thick and thin since the start of our journeys as wide-eyed earthquake geologists in the Philippines. And I owe much of what I have achieved today to the love and support of my parents, brother, and every imaginable extended family member.

Finally, this DPhil has been made possible through the Newton Agham PhD scholarship, funded by the UK Department of Business, Energy, and Industrial Strategy and the Commission on Higher Education of the Philippines, and delivered by the British Council. Thanks to St Cross College, the Gilchrist Educational Trust, and the Burdett-Coutts Fund for providing travel and study grants; and the University of the Philippines for providing me the leeway to develop my academic career.

Contents

Declaration iii

Abstract v

Extended Abstract vii

Acknowledgements xi

Contents **xiii**

Contents xviii

List of Figures **xix**

List of Figures xxiii

List of Tables **xxv**

List of Tables xxvi

1 Introduction **1**

1.1 Fast and slow fault slip 1

1.2 Observing the earthquake cycle 4

1.3 Overview of the thesis 6

1.4 Publications arising from this thesis 7

2 Holocene surface ruptures in the central Tien Shan: implications for the seismogenic potential of active faults in mountain basins **9**

2.1 Introduction 9

2.2 Regional tectonic background 12
2.3 The GPS deformation signal: detailed velocity profiles and fault locations 13
2.4 Evidence of active Holocene faulting 20
2.4.1 Methods 20
2.4.2 Karkara: Faulting north of the rangefront 23
2.4.3 Eastern Issyk-Kul: Shallow thrust-folds in a contracting basin 31
2.4.4 Karakudzhur: satellite- and drone-derived DEMs of a centuries old scarp 39
2.4.5 Naryn: fresh scarps and paleoseismic evidence 46
2.5 Discussion 55
2.5.1 Seismogenic faults in the central Tien Shan and potential seismic hazard 55
2.5.2 Distributed shortening across intermontane basins 57
2.6 Summary and conclusions 58

3 Conjugate blind and surface fault ruptures of the October–December 2019 southern Mindanao seismic sequence due to shallow crustal heterogeneity 61

3.1 Introduction 61
3.2 Regional tectonic setting 63
3.3 Body-wave seismology 66
3.4 InSAR observations of rupture geometry 69
3.5 Inversion for fault geometry from InSAR data 73
3.6 Field evidence of surface rupturing 77
3.7 Discussion 79
3.7.1 Locating surface and buried ruptures 79
3.7.2 Geological controls of seismic slip 80

3.7.3 Implications for tectonics: regional stress field and active deformation of a complex suture zone 82
3.8 Conclusion 84

4 The relationship between seismic and aseismic slip on the creeping segment of the Philippine Fault 87
4.1 Introduction 87
4.2 Tectonic setting 92
4.2.1 The Philippine Fault: geodynamic and seismic context 92
4.2.2 Seismotectonics of Leyte Island 93
4.3 Interseismic (2007-2011) velocity field and aseismic fault slip 97
4.3.1 InSAR data processing 97
4.3.2 Manifestation of surface aseismic slip 104
4.3.3 Subsidence in Tongonan 108
4.3.4 Modeling deformation sources 108
4.3.5 Results: Variable aseismic slip rate and apparent locked section 117
4.4 Coseismic: 6 July 2017 M_w 6.5 Mainshock and M_w 5.8 Aftershock . . 123
4.4.1 Data and Methods 125
4.4.2 Results: Surface deformation and slip on the fault 128
4.5 Discussion 133
4.5.1 Complementary distribution of seismic and aseismic slip . . . 133
4.5.2 The role of geometry and structural complexity on seismic and aseismic slip distribution 134
4.5.3 Physical factors that can lead to aseismic slip 137
4.5.4 Seismic and aseismic slip budget: probabilistic return period of significant earthquakes on the Tongonan Segment 139
4.5.5 Limitations of assuming elastic homogeneity 143
4.6 Summary and Conclusions 145

5 Summary and concluding remarks **147**

5.1 The relationship between shallow crustal heterogeneity and seismic ruptures 148

5.2 Using geodesy with geology to characterize fault behavior, apparent aseismicity, and seismic hazard 149

5.3 The way forward 150

Bibliography **153**

Bibliography **153**

Appendices **179**

A Radiocarbon dating reports **179**

B IRSL dating results **195**

C Best-fit focal mechanism solutions of the October–December 2019 earthquake sequence **199**

D Sentinel-1 ascending track interferograms of the 2019 southern Mindanao earthquake sequence **205**

E Details of the inversion for the 2019 Mindanao fault geometry parameters **209**

E.1 Velocity structure of the Green's function 210

E.2 Results of modeling for the 2019/10/16 southern Mindanao earthquake 211

E.3 Forced NE-striking fault model for the 2019/10/16 southern Mindanao earthquake 216

E.4 Results of modeling for the 2019/12/15 southern Mindanao earthquake 219

F Simulated interferograms of blind fault ruptures: possible geometry for the 2019/10/29 southern Mindanao earthquake **225**

G Drone photomosaic of fissuring associated with the 2019 southern Mindanao earthquake sequence **227**

H Estimating step-change on profiles **229**

I Resolution analysis **231**

J Supporting Information for "The relationship between seismic and aseismic slip on the creeping segment of the Philippine Fault" **233**

J.1 Introduction . . . 233

J.2 Interseismic data (2007-2011) interferogram network . . . 234

J.3 Uncertainties in interseismic velocity estimates from N-SBAS time-series analysis and stacking . . . 236

J.4 Manifestation of shallow aseismic slip on cultural features in Leyte . . 238

J.5 Geothermal wells in Tongonan in relation to the subsidence source . . 240

J.6 Empirical statistics (covariance functions) of noise in interseismic InSAR velocity maps . . . 242

J.7 Fit of interseismic mean model prediction in the ALOS descending line-of-sight (LOS) . . . 243

J.8 Correlation analysis between aseismic slip rate and subsidence parameters . . . 244

J.9 Empirical statistics (covariance functions) of noise in coseismic InSAR displacement maps . . . 245

J.10 Mean and mode of posterior distribution of coseismic slip . . . 246

J.11 Downsampled Sentinel-1 coseismic LOS displacement data and model predictions for the July 2017 earthquakes . . . 247

J.12 Downsampled ALOS-2 coseismic LOS displacement data and model predictions for the July 2017 earthquakes 248
J.13 Results of test where we include a Central Fault Line in the modeling of interseismic aseismic slip 249

List of Figures

1.1 The earthquake cycle and different slip modes 3

2.1 Seismotectonics of the Tien Shan 11

2.2 Sites investigated in eastern Issyk Kul (Kyrgyzstan) and Karkara (Kazakhstan) 16

2.3 Profiles of GPS velocities and SRTM elevation of Karkara and eastern Issyk-Kul and the schematic configuration of faults 17

2.4 Shaded elevation map of the southern central Tien Shan (Karakudzhur and Naryn) and GPS velocities 18

2.5 Profiles of GPS velocities and SRTM elevation of Karakudzhur and Naryn 19

2.6 Location of paleoseismic trench, Karkara (Kazakhstan) 25

2.7 Fault outcrop in Karkara (Kazakhstan) 28

2.8 Paleoseismic trench in Karkara 29

2.9 Topographic profiles of eastern Issyk-Kul 34

2.10 Eastern Issyk-Kul folds in the field. 35

2.11 Sackungen in Sary Tologoy, far eastern Issyk-Kul (Kyrgyzstan) 36

2.12 Geomorphology of the Cholpon fold 37

2.13 Mikhailovka scarp: young scarp in the plains of eastern Issyk-Kul . . 38

2.14 Morphology and scarp profiles of the possible paleoearthquake rupture in Karakudzhur. 42

2.15 Single-event scarp in Karakudzhur. 43
2.16 Comparison of the cumulative and possible single-event scarps in the eastern section of the Karakudzhur Fault. 44
2.17 Field photos of the Karakudzhur Fault. 45
2.18 Active faulting in eastern Naryn Basin. 50
2.19 Paleoseismic section of a north-dipping surface-rupturing thrust fault in Tash-Bashat (eastern Naryn) 51
2.20 The Dobulu scarp in eastern Naryn. 52
2.21 Basalt outcrop on the Naryn Fault. 53
2.22 Bashnura section of the Naryn fault. 54
2.23 Potential seismogenic faults in the central Tien Shan 56

3.1 Tectonics of Mindanao (Philippines). 65
3.2 Seismotectoncis of the Cotabato Basin. 68
3.3 Sentinel-1 descending and ALOS-2 ascending track interferograms covering the October-December 2019 earthquake sequence 72
3.4 Data, model prediction, and residuals of the 'best-fit' uniform slip models. 76
3.5 Evidence of fault surface ruptures in the field 78
3.6 Schematic cross-section of the tectonic terranes in southern Mindanao and the Cotabato Basin 84

4.1 Active tectonics of the island of Leyte in the Philippines. 91
4.2 Seismotectonics of Leyte island 96
4.3 Interseismic surface deformation in Leyte 101
4.4 ALOS LOS velocity profiles across the Philippine Fault 103
4.5 Estimated fault-parallel and vertical velocity in northern Leyte 107

4.6 Subsidence data, model prediction, and residuals from modeling using leveling data . . . 113

4.7 Posterior distribution and joint probabilities of subsidence source parameters from inversion with leveling data . . . 114

4.8 Rate and extent of aseismic slip on the Philippine Fault in Leyte and model fit . . . 118

4.9 Mode, skewness, kurtosis, and resolution of the interseismic slip model of the Philippine Fault in Leyte . . . 121

4.10 Downsampled InSAR LOS velocity data, model prediction, and residuals in the Tongonan area . . . 122

4.11 Summary of the July 2017 earthquakes in Leyte . . . 124

4.12 Sentinel-1 wrapped and unwrapped coseismic interferograms of the 2017 Leyte earthquake . . . 129

4.13 ALOS-2 wrapped and unwrapped coseismic interferograms of the 2017 Leyte earthquake . . . 130

4.14 Coseismic slip model of the July 2017 Leyte earthquake . . . 132

4.15 Rate and extent of aseismic and seismic slip on the Philippine Fault in Leyte . . . 135

4.16 Probability distribution of seismic and aseismic slip budget, and return period . . . 144

C.1 Minimum misfit solution for the 2019/10/16 southern Mindanao earthquake . . . 200

C.2 Same as Figure C.1, but for the 2019/10/29 event. . . . 201

C.3 Same as Figure C.1, but for the 2019/10/31 event. . . . 202

C.4 Same as Figure C.1, but for the 2019/12/15 event. . . . 203

D.1 Sentinel-1 ascending track interferograms covering the October 2019 southern Mindanao earthquakes . . . 206
D.2 Sentinel-1 ascending track interferogram of the 2019/12/15 southern Mindanao earthquake . . . 207

E.1 Joint distributions of 10/16 event fault geometry parameters . . . 212
E.2 Continued from E.1. . . . 213
E.3 Continued from E.2. . . . 214
E.4 Sequence plots of the Grond bootstrap sampling for the 10/16 event parameters . . . 215
E.5 Same as Figure E.4, but with the strike bounds constrained to NE-trending strikes. . . . 217
E.6 Downsampled InSAR data, model predictions, and residual of the best fitting forced NE-strike fault model of the 10/16 earthquake . . . 218
E.7 Joint distributions of 12/15 event fault geometry parameters . . . 220
E.8 Continued from E.7. . . . 221
E.9 Continued from E.2. . . . 222
E.10 Sequence plots of the Grond bootstrap sampling for the 10/16 event parameters . . . 223
E.11 Downsampled InSAR data, model predictions, and residual of the best fitting fault parameters of 12/15 earthquake in Sentinel-1 ascending track 163 line-of-sight . . . 224

F.1 Forward models of surface deformation based on uniform elastic dislocation models (*Okada*, 1985) of geometries based on the focal mechanism nodal planes of the 10/29 southern Mindanao earthquake . . . 226

G.1 Interpreted photomosaic of fissuring assocaited with shallow surface rupture of the 2019/10/31 Mindanao earthquake . . . 228

J.1 ALOS ascending track acquisition perpendicular and temporal baseline 234
J.2 Similar to J.1, but for ALOS descending track 76 acquisition perpendicular and temporal baseline. 235
J.3 Similar to J.1, but for ALOS descending track 77 acquisition perpendicular and temporal baseline. 235
J.4 Uncertainty in interseismic surface deformation maps of Leyte island 237
J.5 Displaced cultural features on the creeping segment of the Philippine Fault 239
J.6 Schematic location of the subsidence source model with respect to the geothermal wells in Tongonan, Leyte (Philippines) 241
J.7 Covariograms of ALOS interseismic InSAR data 242
J.8 Downsampled ALOS descending track data, prediction, and residuals of the mean model of intersesimic slip on the Philippine Fault in Leyte 243
J.9 Joint marginals of aseismic slip rate (i.e., of patches adjacent to subsidence signal) with sill deflation rate on the Philippine Fault in Leyte 244
J.10 Covariograms of coseismic InSAR data on the Philippine Fault in Leyte 245
J.11 Comparison of mean and mode of the posterior PDF of coseismic slip of the 2017 Leyte (Philippines) earthquake 246
J.12 Sentinel-1 data, model predictions, and residuals of the coseismic slip model of the 2017 July earthquake on Leyte 247
J.13 ALOS-2 data, model predictions, and residuals of the coseismic slip model of the 2017 July earthquake on Leyte 248
J.14 ALOS data, model predictions, and residuals of an interseismic slip model including the Central Fault in Leyte, compared to a model without the Central fault 250
J.15 Modeled shallow aseismic slip rate on the Philippine Fault in Leyte including the Central Fault branch 251

List of Tables

2.1 Summary of radiocarbon dating results 30

2.2 Summary of IRSL dating results from samples from different depths at the given locations. 41

3.1 Source parameters of the October–December 2019 southern Mindanao earthquakes. 67

3.2 Epochs of interferograms covering the October–December 2019 earthquakes in southern Mindanao. 71

3.3 Boundary and best-fitting parameters for the 10/16 and 12/15 earthquakes. 74

4.1 Summary of ALOS SAR data per track used for interseismic time-series analysis and stacking. 98

4.2 *A priori* bounds and inversion results for a horizontal rectangular source for the observed subsidence (from leveling surveys) 112

4.3 Summary of coseismic interferograms of the 2019 southern Mindanao earthquakes 125

4.4 Seismic moment (M_o) and moment magnitude (M_w) estimates of the July 2017 earthquakes 141

E.1 velocity structure of Green's function from Pyrocko 210

E.2 Best, mean, standard deviation (SD) and percentile bounds of parameters from the fault geometry inversion for the 10/16 earthquake . . . 211
E.3 Best, mean, standard deviation (SD) and percentile bounds of parameters from the fault geometry inversion for the 10/16 earthquake forced to a NE-SW strike 216
E.4 Best, mean, standard deviation (SD) and percentile bounds of parameters from the fault geometry inversion for the 12/15 earthquake . . . 219

Chapter 1

Introduction

1.1 Fast and slow fault slip

Earthquakes represent the unpredictable end-member of a spectrum of fault behavior. In the concept of 'stick-slip' (*Brace and Byerlee*, 1966), coseismic fault slip happens in a matter of a few seconds to several minutes (at rates of up to one m/s) when the shear stress on the fault plane overcomes the frictional forces holding it together and releasing the elastic strain in the surrounding crust (Figure 1.1a). For the largest events near populated areas, the slow build-up of tectonic forces–resulting to long periods of quiesence spanning multiple human generations–have led to many catastrophic disasters in society. Hence, there is broad cross-disciplinary interest in the study of earthquakes.

On the other side of the behavior spectrum, faults can also slip slowly and aseismically in time (rates of sub to a few cm/yr of slip), which *Louderback* (1942) introduced as creep, effectively preventing the build up of elastic strain. As shown in Figure 1.1b, continental faults are believed to creep at depth, which is due to the depth-dependence of fault rheology (i.e., ductility in the lower crust *Sibson*, 1977; *Blanpied et al.*, 1998). This is why, with the exception of intermediate-depth and deep-focus earthquakes, seismic slip is largely restricted to the upper brittle sec-

tion of the Earth's crust (the seismogenic zone), and seismic and aseismic slip to be largely complementary (*Scholz*, 1998). There also is a class of faults that appear to creep throughout the seismogenic zone, at or near the secular rate. These so called 'creeping faults' pose a different type of hazard due to the continuous rupture on the ground, but are less likely to be sources of great earthquakes (see *Harris*, 2017, for a review of known creeping continental faults).

Throughout the latter half of the 20th century, the nomenclature of fault behavior has expanded to include a catalog of 'slow earthquake' phenomena, like non-volcanic tremor, low frequency events, and slow slip events, recognizing the continuum of the different ways faults can slip (e.g., *Ide et al.*, 2007; *Peng and Gomberg*, 2010) (Figure 1.1c). Numerical models also demonstrate how seismic slip could propagate across creeping fault sections (e.g., *Noda and Lapusta*, 2013). How faults behave in different periods of the earthquake cycle, the variability of slip behavior at different parts of a fault, and the physical factors that lead to these, continue to be a rich ground for scientific inquiry in fault and earthquake mechanics (see *Avouac*, 2015; *Bürgmann*, 2018; *Collettini et al.*, 2019, and references therein).

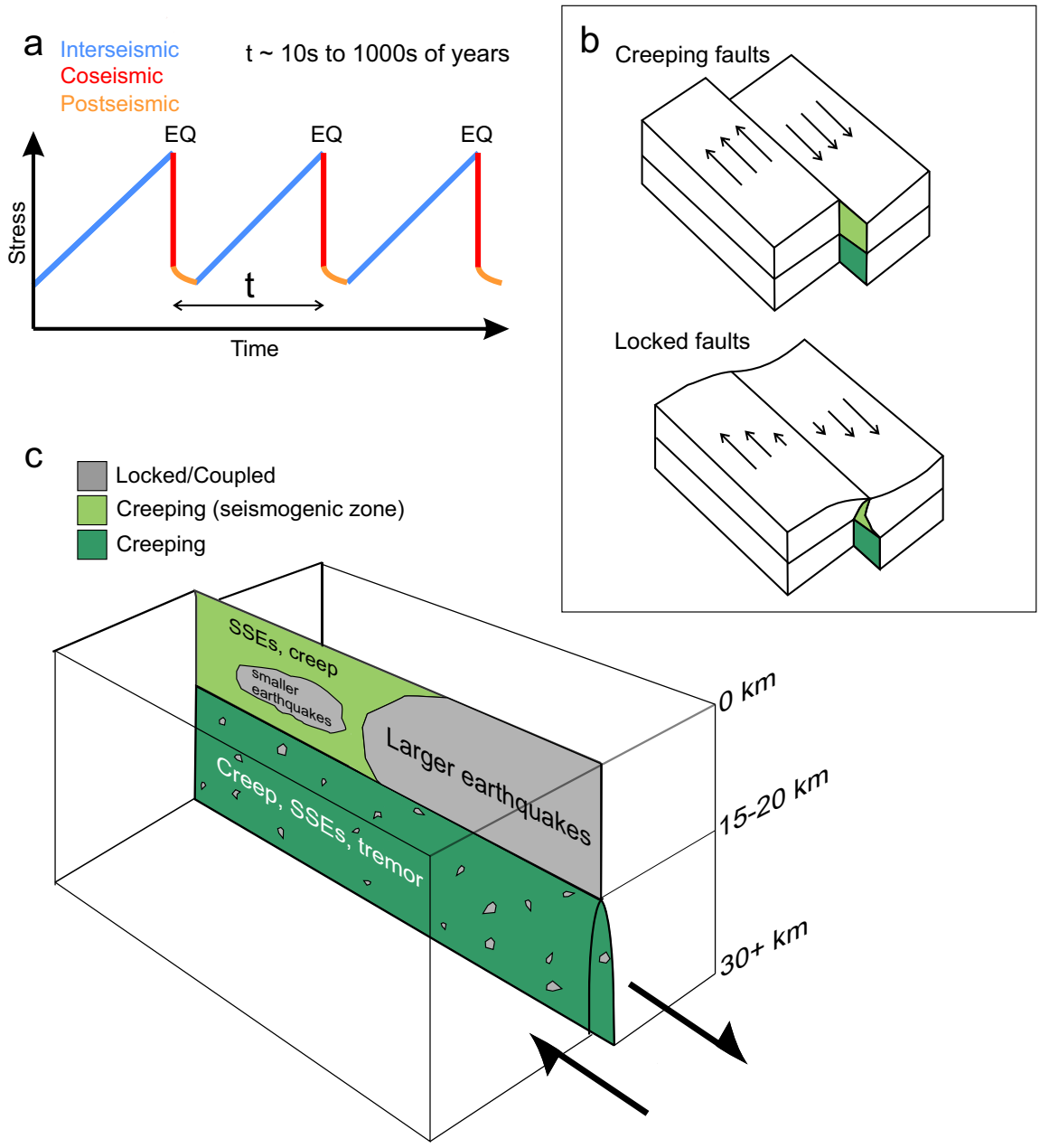


Figure 1.1: a) Idealized earthquake cycle model, where every earthquake (EQ) involves a period of slow build up of stress (interseismic), rapid slip resulting to stress decrease (coseismic), and a gradual deceleration of slip (postseismic). b) Block models of a fully creeping fault and fault locked at the surface. See text for discussion. c) Schematic model of where different slip phenomena have been observed on a partially coupled fault, like the San Andreas Fault in Parkfield (modified from *Bürgmann*, 2018). SSEs: slow slip events.

1.2 Observing the earthquake cycle

Satellite geodesy has revolutionized our capability to analyze fault behavior in a natural setting and in quick disaster response to earthquakes (*Elliott et al.*, 2016). From the work of *Reid* (1910) on the Elastic Rebound theory, laying out the basis of the earthquake cycle, to the first measurements of surface fault creep (*Tocher*, 1960; *Steinbrugge and Zacher*, 1960), careful analysis of the displacements due to faulting play a key role in understanding earthquakes. For example, most continental creeping faults that have been studied in detail are in California (USA) (*Harris*, 2017). With modern Global Positioning System (GPS) and interferometric synthetic aperture radar (InSAR), recording slow interseismic fault movement and locating earthquake ruptures (whether observed at the surface or not) has started to become systematic around the world (e.g., *Prescott et al.*, 1981; *Massonnet et al.*, 1993; *Wright et al.*, 2001; *Cavalié et al.*, 2008; *Fattahi and Amelung*, 2016). Episodic creep and variable coupling is also now widely seen to be more ubiquitous with the growing number of observations from continental faults and subduction zones (*Bürgmann*, 2018; *Jolivet and Frank*, 2020) (Figure 1.2).

High-resolution satellite optical imagery and photogrammetry also provide increasingly improving resolution of data useful for mapping offsets from individual earthquakes and preserved fault scarps, with techniques like pixel tracking and the generation of digital elevation models for wide areas (e.g., *Barnhart et al.*, 2011; *Zhou et al.*, 2015). The characteristics and complexity of earthquake ruptures in recent events and even older earthquake scarps can be documented with remote sensing, providing important details in the understanding of regional tectonics and seismic hazard (e.g., *Zinke et al.*, 2014; *Walker et al.*, 2015; *Arrowsmith et al.*, 2016).

One limitation of reliance on modern-age geodetic observations is that they only capture, at best, the last half-century of fault displacements (e.g., the creep records on the Hayward fault; *Lienkaemper et al.*, 2012). The interseismic period can be

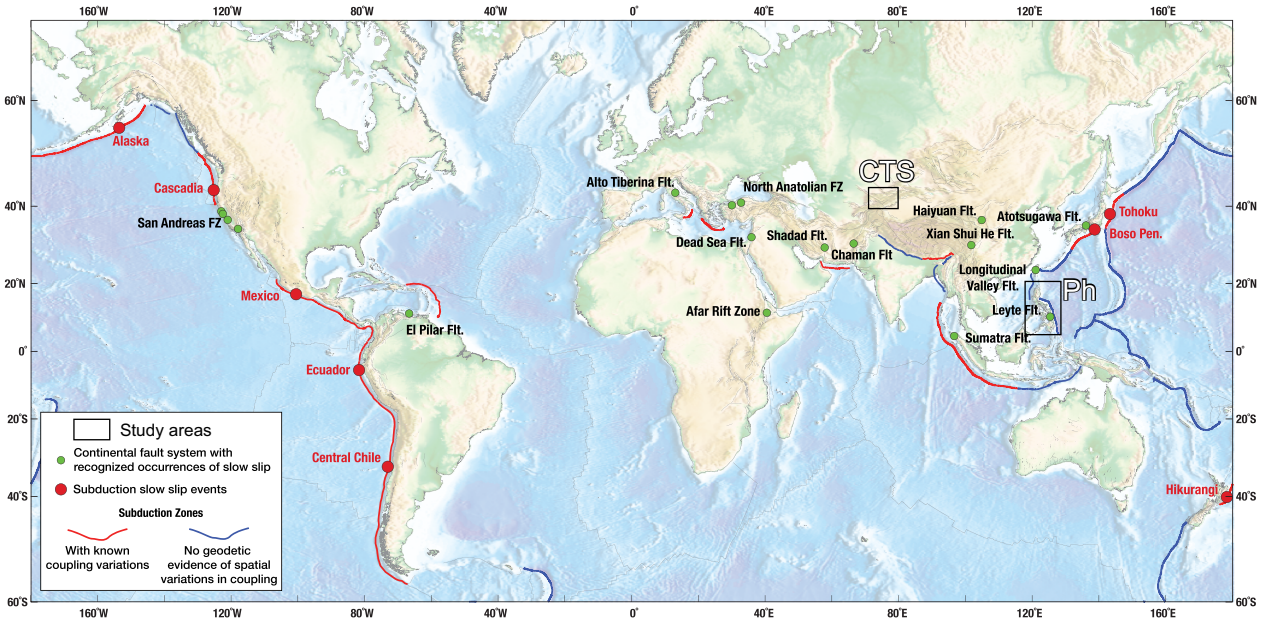


Figure 1.2: Map of faults that are known to creep from *Jolivet and Frank* (2020), with location of case studies in this thesis enclosed in black boxes. CTS: Central Tien Shan. Ph: the Philippines.

much longer, so the record of earthquakes and faulting can only be appreciated in full by putting present-day observations in the context of the rupture history and tectonic setting. Measuring and dating of offsets from paleoseismic investigation reveal that earthquake recurrence can be in the order of a hundred to several thousand years for the largest events (e.g., *Sieh et al.*, 1989; *Landgraf et al.*, 2016), and even exhibit clustering in time and space (e.g., *Sieh et al.*, 2008; *Goldfinger et al.*, 2013; *Dolan et al.*, 2016). Earthquakes can also occur on geologically older structures that have been reactivated (e.g., *Okamura et al.*, 2007). Hence, areas that have been relatively seismically quiet in our current record, especially in places that undergo lower strain rates, often have underestimated seismic risk (*England and Jackson*, 2011). The occurrence of earthquakes in low-strain rate regions away from plate boundaries have a lot more spatio-temporal complexity that warrants close investigation (*Molnar*, 1988; *Stein et al.*, 2009; *Landgraf et al.*, 2017).

1.3 Overview of the thesis

In this thesis, I investigate the behavior of faults that have purported evidence of seismic and aseismic slip in both relatively low and fast strain-rate settings as this allows us to appreciate the common and contrasting characteristics of faults in different regions. Throughout this work, I focus on geodetic and geologic observations to characterize the seismogenic potential of individual structures amidst zones of distributed deformation. Further, I focus on faults in regions where the published literature is limited to help provide a baseline set of parameters useful for: 1) the understanding of seismic hazard (e.g., potential size and timing of earthquakes), and 2) shedding light to the mechanics of faulting (e.g., the mode of slip, and the geologic factors control the extent of seismic and/or aseismic slip).

Chapter 2 is on the active faults and the evidence of earthquakes in basins of the central Tien Shan, which is far from any plate boundary. I present the surface expression of faulting shortening in several basins that cross a 400-km long transect of apparent creep (described by *England and Molnar*, 2015), and I also characterize their seismogenic potential by analyzing the GPS velocity field, mapping fresh fault scarps, and dating of offsets in paleoseismic investigation.

In **Chapter 3**, I study a series of four $M_w = 6.4$–6.8 earthquakes that happened in a span of two months (October–December 2019), less than 30 km of each other, on the island of Mindanao (the Philippines). I constrain the source parameters primarily with InSAR and compare this with seismological analysis and field observations of surface rupturing, in the context of the region's geology and tectonics.

Chapter 4 takes a detailed look at the creeping segment of the Philippine Fault on Leyte Island. I present the first probabilistic interseismic and coseismic slip models on ∼100-km of the Philippine Fault, a 1,200-km long left-lateral strike slip fault. I use interseismic InSAR, leveling, and coseismic interferograms of the July 2017 Ormoc (Leyte) earthquake, to separate fault and geothermal subsidence deformation sources.

I discuss the mechanics of seismic and aseismic slip along with previous studies on the structure and geology of the fault zone.

Finally, **Chapter 5** summarizes the important aspects and findings of the different case studies in this thesis.

1.4 Publications arising from this thesis

Chapter 3 is being prepared for submission as:

Dianala, J. D. B., Morishita, Y., Parsons, B., Walker, R., Copley, A., Aurelio, M.A., Ybañez, R., Lagmay, A.M.F.A. Complex conjugate blind and surface ruptures in the October–December 2019 Mindanao (Philippines) earthquake sequence due to crustal heterogeneity

Chapter 4 has been published in the Journal of Geohysical Research: Solid Earth:

Dianala, J. D. B., Jolivet, R., Thomas, M. Y., Fukushima, Y., Parsons, B., & Walker, R. (2020). The relationship between seismic and aseismic slip on the Philippine Fault on Leyte Island: Bayesian modeling of fault slip and geothermal subsidence. *Journal of Geophysical Research: Solid Earth*, 125. https://doi.org/10.1029/2020JB020052

Chapter 2

Holocene surface ruptures in the central Tien Shan: implications for the seismogenic potential of active faults in mountain basins

2.1 Introduction

Interseismic deformation in continental interiors happens more slowly than at plate boundary settings; hence, the seismic hazard in these regions is considered to be relatively low. However, the earthquake cycle tends to be protracted with low strain rates, affecting our ability to constrain and infer the temporal occurrence of intracontinental seismic events (e.g., *Stein et al.*, 2009; *Grützner et al.*, 2017). Investigating the presumption of hazard by mapping earthquake sources would therefore have important implications to society, given that hundreds of thousands of lives have been lost to intraplate earhtquakes in the past century alone (*England and Jackson*, 2011). Further, knowledge of earthquake occurrences within the continents allows

us to better understand the dynamics of complex systems of interacting faults in the continents (*Landgraf et al.*, 2017).

The known seismic record in continental Asia shows a clustering of earthquakes with magnitudes greater than 7.0 on the northern and southern edges of the central Tien Shan, as shown in Figure 2.1 (see also *Havenith et al.*, 2015). Despite being host to some of the largest intracontinental seismic events in the instrumental record (*Kulikova and Krüger*, 2015) and mapped late Quaternary fault scarps (*Thompson et al.*, 2002), the reason for the absence of large earthquakes in the interior of the mountain belt is unclear. Paleoseismology indicates that earthquakes have long recurrence intervals in the region (in the order of thousands of years; e.g., *Landgraf et al.*, 2016; *Patyniak et al.*, 2017; *Campbell et al.*, 2019). This suggests that the historical record may just be within a long interseismic period, or incomplete if the latest events were not long before humans started noting earthquakes, especially for the remote areas. At the same time, *England and Molnar* (2015) suggest that a steep gradient in GPS surface velocity may be due to a creeping or shallowly locked fault (yellow line in Figure 2.1), so fault-related deformation may be aseismic. Few studies have attempted to reconcile the geodetic and geologic evidence to infer the seismic behavior of individual faults (e.g., *Goode et al.*, 2011; *Mackenzie et al.*, 2018; *Rust et al.*, 2018), hence, tectonic deformation in under-explored areas needs to be examined carefully.

In this chapter, we investigate the faults that fall along the apparent GPS velocity step (as mapped by *England and Molnar*, 2015, from hereon referred to as the 'EM line'). Creeping faults are known to leave evidence of surface displacement on cultural features (e.g., *Lienkaemper et al.*, 1991; *Mu et al.*, 2011) and also in the landscape (e.g., *Blanton et al.*, 2020). In the Tien Shan, previous studies have shown that surface rupture scarps from earthquakes that happened over a century ago are still well-preserved (*Arrowsmith et al.*, 2016; *Abdrakhmatov et al.*, 2016) thanks to the

remote location and semi-arid environment. Even older surface ruptures can still be distinguished (*Campbell et al.*, 2019). This chapter highlights the value in exploiting remote sensing data that can resolve subtle features related to faulting, improving our inferences of tectonic shortening from the geodetic data. Most importantly, the findings add to the current paucity in observations, helping to elucidate the complex temporal and spatial mechanics of earthquake occurrence within continental interiors.

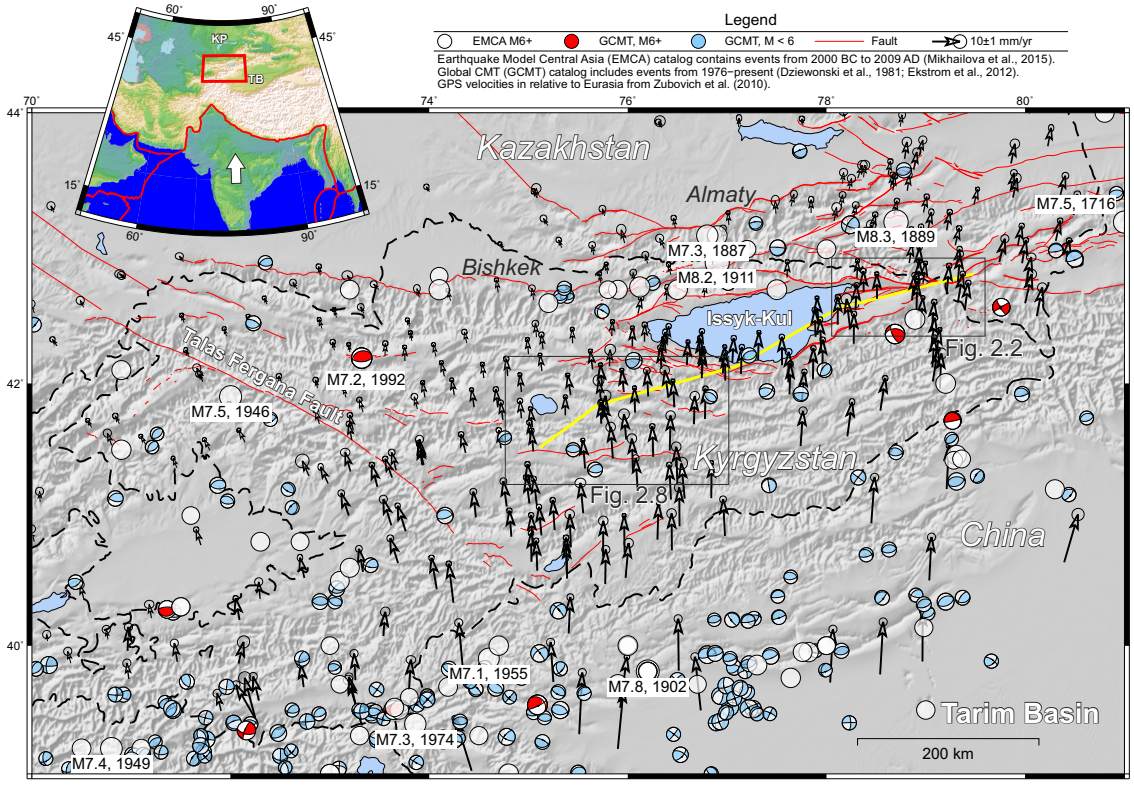


Figure 2.1: Seismotectonics of the Kyrgyz central Tien Shan, in between the Tarim and Kazakh platforms, with a shaded SRTM (*NASA*, 2013) terrain map overlain with earthquake epicenters from the Earthquake Model Central Asia (EMCA; *Mikhailova et al.*, 2015) and Global Centroid Moment Tensor (*Dziewonski et al.*, 1981; *Ekström et al.*, 2012) catalogs. Earthquakes with magnitudes ≥ 7.0 are labeled with their magnitude and year of occurrence. Vectors are GPS velocity data with their error ellipses (*Zubovich et al.*, 2010). Inset: location of the Tien Shan with respect to the major tectonic features. TB: Tarim Basin, KP: Kazakh Platform. White arrow indicates northward movement of India relative to Eurasia.

2.2 Regional tectonic background

More than a thousand kilometers north of the Himalayan collision zone, the Tien Shan is a 200–300 km wide mountain belt that extends more than 2,000 km E–W along the northern edge of the Tarim Basin. In response to the India–Eurasia collision (*Tapponnier and Molnar*, 1979), the convergence between the relatively stable Tarim and Kazakh platforms has resulted to an amalgamation of intermontane basins bounded by Pre-Cambrian and Paleozoic-cored mountain ranges and suture zones (e.g., *Buslov et al.*, 2007). Exhumation of the ranges began in the Oligocene (e.g., *Sobel et al.*, 2006; *Macaulay et al.*, 2014) with apparently rapid shortening and crustal thickening in the past ∼10 Ma, at around 20 mm/yr of horizontal contraction across the whole belt (*Abdrakhmatov et al.*, 1996).

In the Kyrgyz side of the central Tien Shan, late Quaternary faulting manifests along basin-bounding E–W thrust faults, with sub-millimeter to 3 mm/yr slip rates on faults (*Thompson et al.*, 2002), and the NW–SE right-lateral Talas Fergana Fault (*Burtman et al.*, 1996), which marks the western bound of the ranges and thrust faults in the central Tien Shan (e.g., *Bande et al.*, 2017; *Rizza et al.*, 2019). As shown in Figure 2.1, focal mechanism solutions of modern earthquakes from the Global Centroid Moment Tensor Catalog (GCMT) and the surface velocity field from GPS (*Zubovich et al.*, 2010) indicate a dominant N–S shortening direction at present.

Human settlement that arose along with Silk Road trade has also contributed to documenting historical seismic activity (*Kalmetieva et al.*, 2009). The known epicentral and rupture locations appear to cluster in the northern part of the range, primarily with the 1889 M_w ∼8 Chilik (*Abdrakhmatov et al.*, 2016), 1911 M_w ∼8 Chon-Kemin (*Bogdanovich et al.*, 1914; *Arrowsmith et al.*, 2016), and 1992 M_w 7.2 Suusamyr earthquakes (*Ghose et al.*, 1997; *Ainscoe et al.*, 2019). Paleoseismic work has extended the record of repeated earthquakes in the northern Tien Shan, mostly

around the capital city of Bishkek and the western half of Issyk-Kul Basin (e.g., *Landgraf et al.*, 2016; *Patyniak et al.*, 2017; *Deev et al.*, 2018).

2.3 The GPS deformation signal: detailed velocity profiles and fault locations

England and Molnar (2015) reviewed the latest available regional surface velocity data from *Zubovich et al.* (2010) and suggest the existence of a creeping or a shallowly locked fault along a 400-km ENE–WSW trend ('EM line), the dashed yellow line in Figure 2.1. The GPS velocity profiles by *England and Molnar* (2015) include station data within 200-km wide swaths and do not focus on individual faults. In this section, we inspect the signal in more detail in association with active faults. We extract data along five profiles that only include stations 25 km on either side of the profile lines, focusing on faults that have been identified from remote sensing and in the field (Section 2.4).Two profiles cover the faults east of Lake Issyk-Kul (Figure 2.2), and three profiles cover the Karakudzhur and Naryn basins (Figure 2.4), southwest of Issyk-Kul. Regionally, the GPS data show little variation in the E–W velocities except at a few locations (labeled as possible strike-slip shear in Profiles Q–Q' and O–O' in Figures 2.3 and 2.5, respectively). These local deviations may correspond to geologic evidence of Cenozoic strike-slip faulting and earthquake ruptures across the orogen (e.g., *Buslov et al.*, 2007; *Abdrakhmatov et al.*, 2016). The following discussion focuses on the gradient in the northward surface velocities, corresponding to the deformation on E–W trending thrust faults in different basins.

The sharpest gradient in surface velocities can be found between Kegen and Karkara (Profile R–R', Figure 2.3) with 3 mm/yr of shortening over 10 km between stations MNJ4 and SHL4, where the Karkara Rangefront Fault is said to be creeping to the surface or has a shallow (< 5 km) locking depth (*Mackenzie et al.*, 2018).

However, this does not discount the possible existence of other active faults between the two stations (discussed in Section 2.4.2).

The other profiles do not show a similar velocity step in other locations of the 'EM line', i.e., eastern Issyk-Kul, Karakudzhur, and Naryn. Instead, the wide basins have broader velocity gradients. To the west of Karkara, between 3.5 to 5.0 mm/yr of N–S contraction is distributed across 50 km in eastern Issyk-Kul, where we have mapped shallow thrust faults (discussed in Section 2.4.3) in the middle of basin between the Kungey and Terskey Ranges (Profiles Q–Q' , Figure 2.3). In western Naryn, southwest of Issyk-Kul, there is 3 to 4 mm/yr of horizontal shortening over 35 km that is distributed across several active faults, including the Kadjerty Fault (which has a slip rate of $1.5^{+0.4}_{-0.3}$ mm/yr; *Thompson et al.*, 2002) (Profile N–N', Figure 2.5). *Goode et al.* (2011) suggest that part of the apparent uplift of folds in the interior of western Naryn basin, seen from InSAR LOS velocity data, is driven by creeping blind thrusts (south dipping fault in Profile N–N', Figure 2.5). A similar ∼3 mm/yr velocity difference across 15 km can be observed in Profile O–O' across the Naryn and Kadjerty Faults in central Naryn. Remarkably, the N–S velocity field to the north and south of western Naryn is flat, highlighting the localization of shortening across the basin.

The northward shortening does not appear to exhibit a clear step-change or gradient across the Karakudzhur Fault. In the eastern side of the basin (Km 50 in Profile P–P', Figure 2.5), no velocity data exists on the hanging wall side except for those on the opposite side of the Terskey Range in southwestern Issyk-Kul (Km 70). The eastern section of the Naryn fault (origin of Profile P–P') also does not have many stations on the hanging wall. This makes it difficult to infer geodetically whether the fault actually creeps in the shallow crust or if the fault is locked (e.g., *Savage and Burford*, 1973). The findings by *Campbell et al.* (2019) related to repeated prehistoric seismic activity in $M_w \approx 7$ events suggest that the latter may be the case

for the Karakudzhur fault. In Profile O–O', where the GPS observations across the Karakudzhur fault are more closely spaced, there is no velocity step across it. The evidence of surface ruptures in Karakudzhur and Naryn are discussed in Sections 2.4.4 and 2.4.5, respectively.

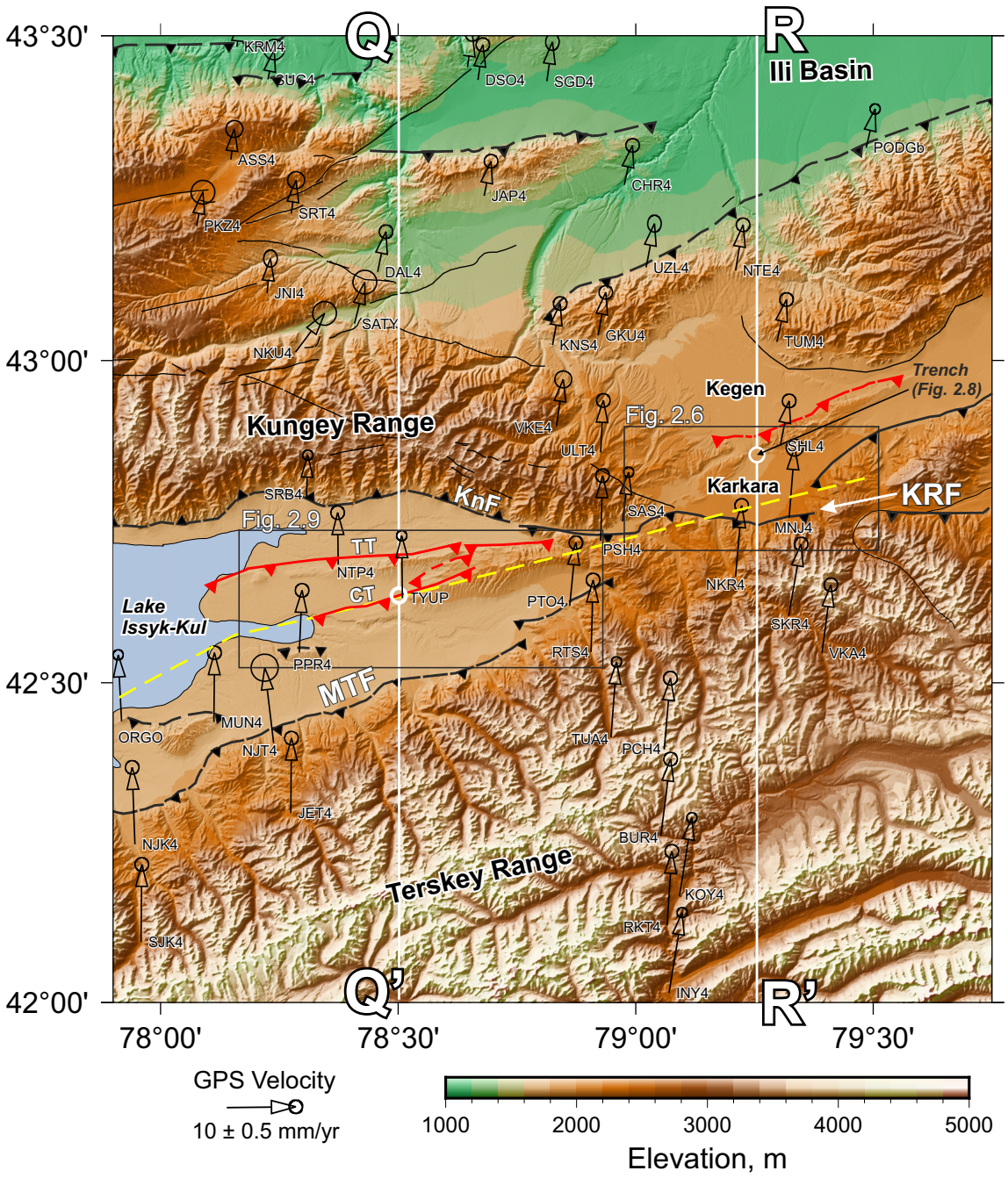


Figure 2.2: Shaded elevation map of eastern Issyk Kul and Karkara and GPS velocities. Black boxes include the fault systems we discuss in the text. GPS vectors and their uncertainty ellipses from *Zubovich et al.* (2010). Dashed yellow line indicates the location of creep (as mapped in *England and Molnar*, 2015, referred to as the 'EM line' in the text). GPS velocity and elevation profiles Q–Q' and R–R' are in Figure 2.3. KRF: Karkara Rangefront Fault, MTF: Main Terskey Fault, KnF: Kungey Fault, TT: Tyup Thrust, CT: Cholpon Thrust.

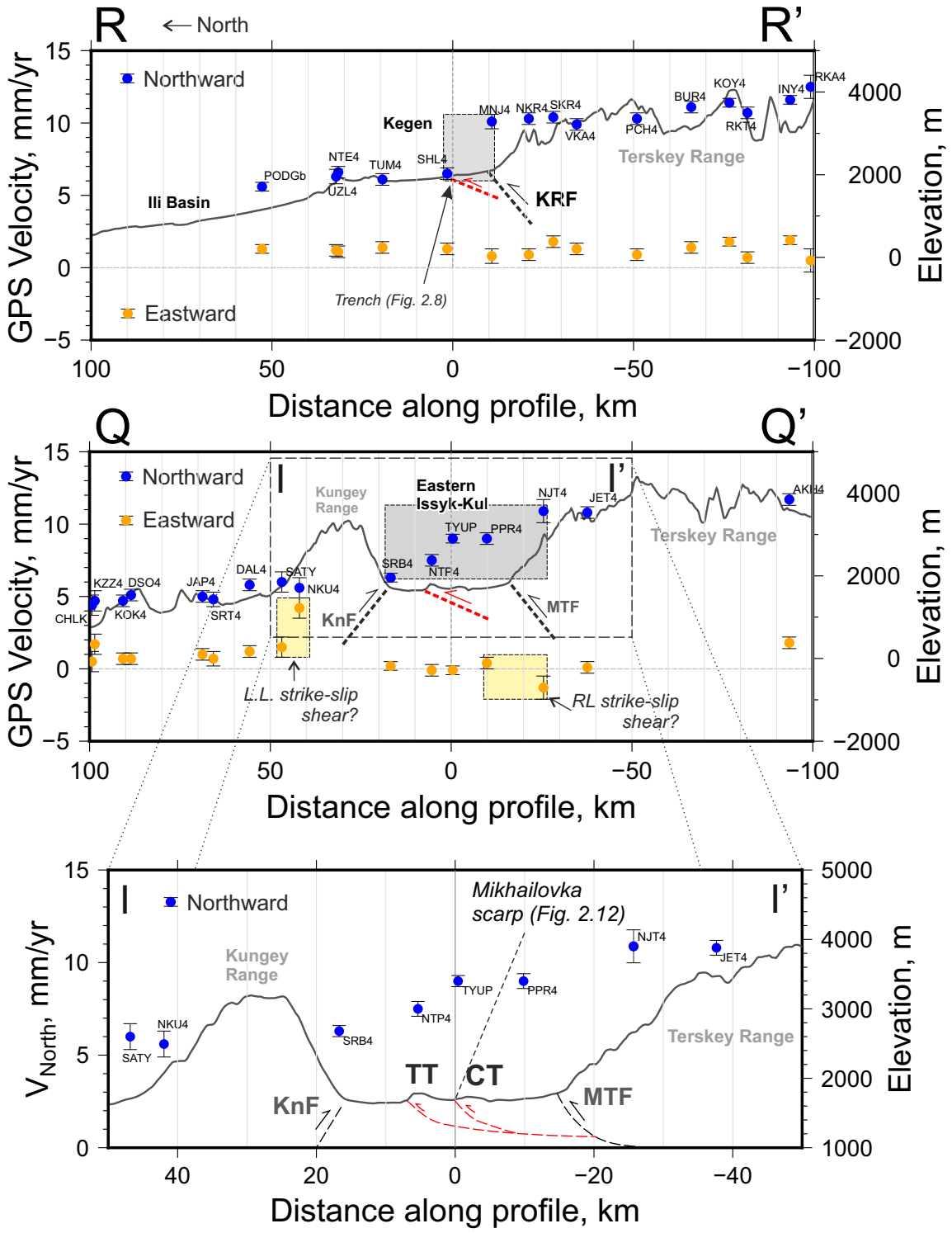


Figure 2.3: Profiles of GPS velocities (**?**, from[]Zubovich2010 and SRTM elevation of Karkara (Profile R–R') and eastern Issyk-Kul (Profile Q–Q'), as located in Figure 2.2, and the schematic configuration of faults. Highlighted in red are the faults we have mapped from remote sensing and in the field. Profile I–I' shows a closer look at the shortening within the Issyk-Kul basin (TT: Tyup Thrust, CT: Cholpon Thrust, MTF: Main Terskey Fault, KnF: Kungey Fault). Blue circles: northward velocity. Orange: eastward velocity. Yellow boxes highlight deviations in the E–W velocity field. Gray box highlights the N–S velocity gradient across Issyk-Kul Basin. Yellow boxes highlight deviations in the E–W velocity field.

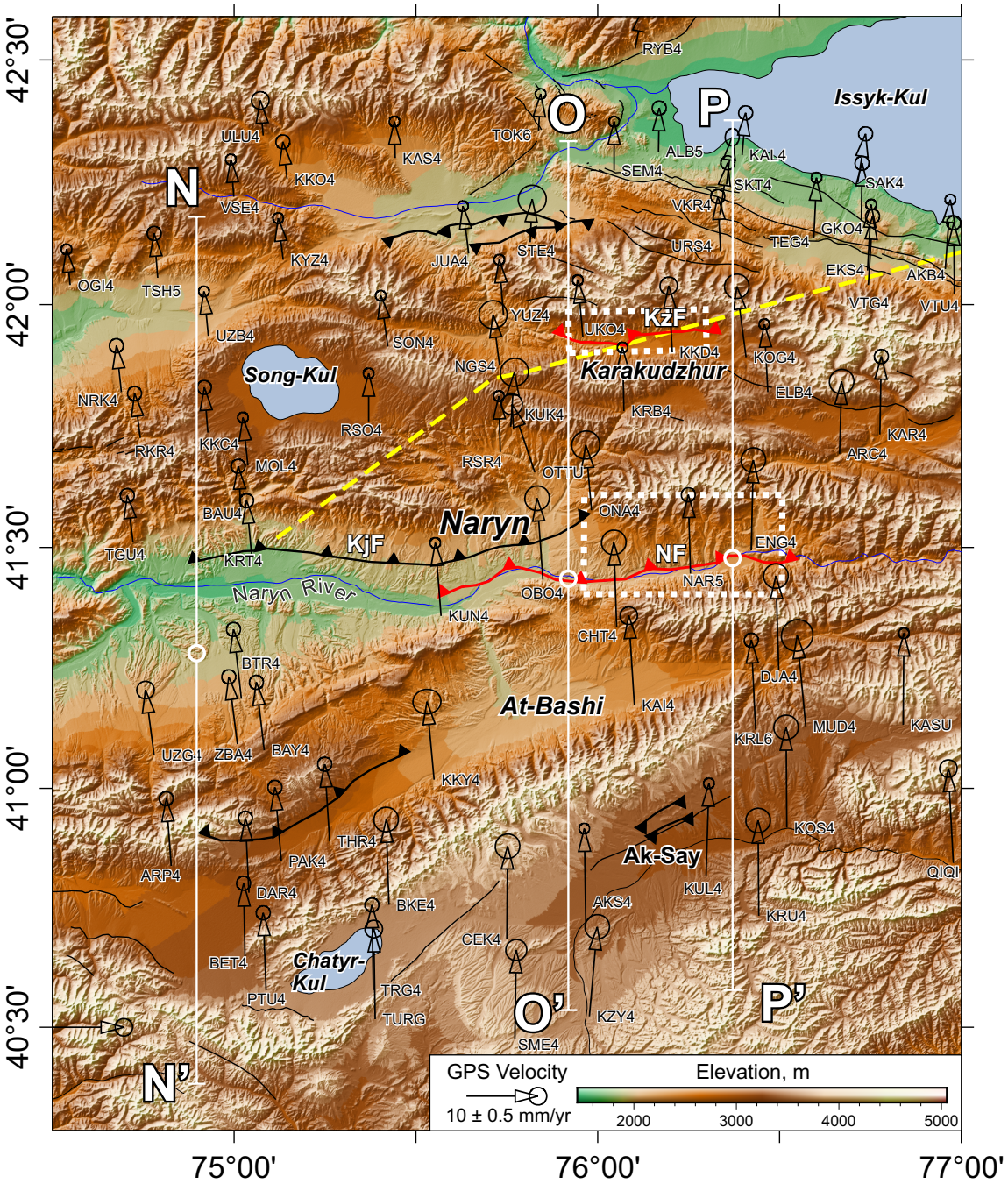


Figure 2.4: Shaded elevation map of the southern central Tien Shan and GPS velocities. White boxes show the localities–Karakudzhur and Upper Naryn basins–we detail in this study. GPS vectors and their uncertainty ellipses from *Zubovich et al.* (2010), and the 'EM line' (from *England and Molnar*, 2015) in yellow dashes. GPS and elevation profiles along P–P', O–O', and N–N' are shown in Figure 2.5.

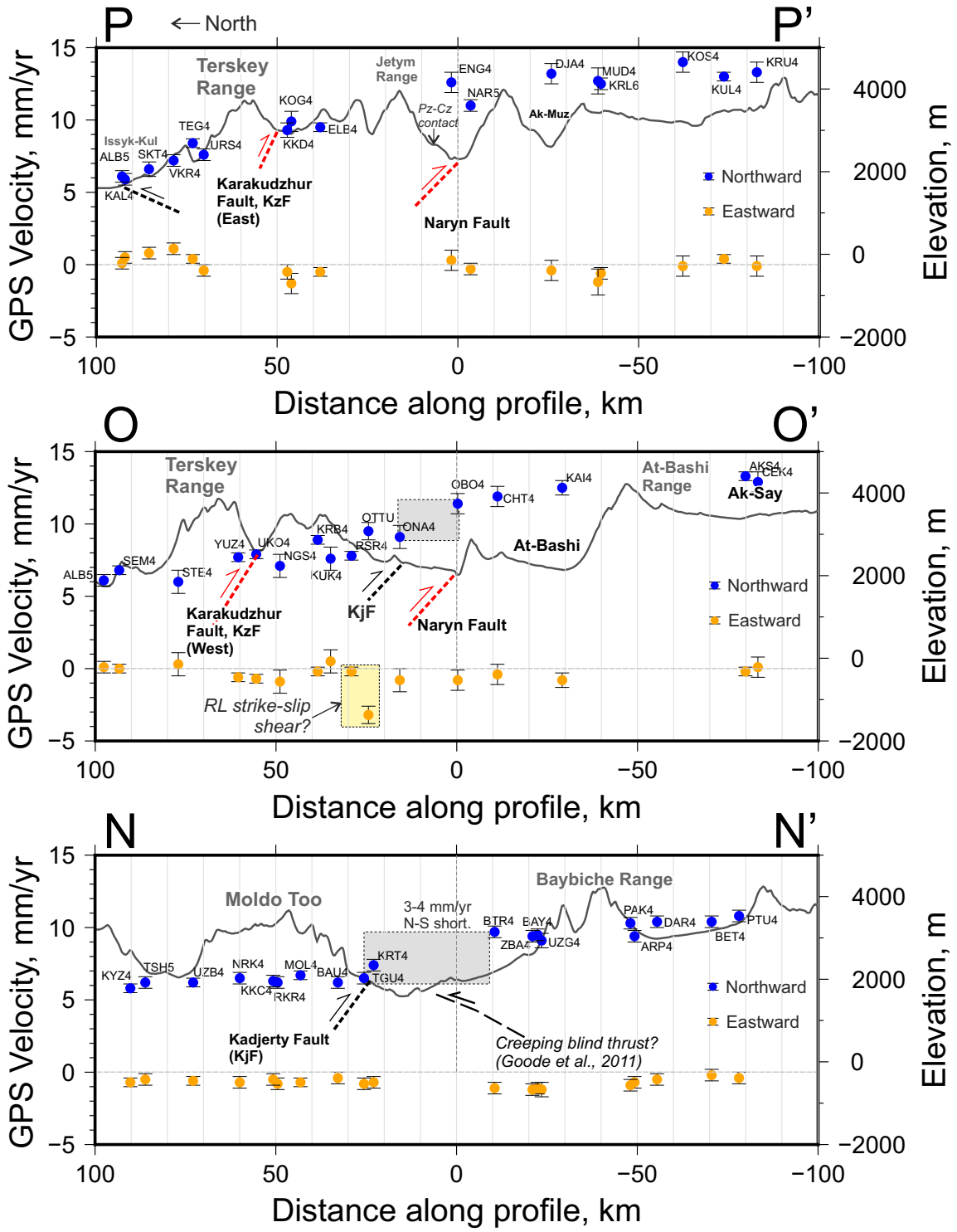


Figure 2.5: Profiles of GPS velocities (*Zubovich et al.*, 2010) and SRTM elevation of Karakudzhur and Naryn. Profile N–N' is centered on western Naryn basin, Profile O–O' in central Naryn, and Profile P–P' in eastern Naryn. Highlighted in red are the faults we have mapped from remote sensing and in the field. Blue circles: northward velocity. Orange: eastward velocity. Gray box highlights the magnitude of shortening across Naryn. Yellow boxes highlight deviations in the E–W velocity field.

2.4 Evidence of active Holocene faulting

As it is unclear from the GPS signal alone whether faults along the 'EM line' are creeping or not, we make use of a wide array of methods to identify fault scarps and evidence of the mode of slip.

2.4.1 Methods

Satellite remote sensing

We explored freely-available optical imagery (Google Earth, and Bing Aerial and Google Satellite imagery on QGIS) and the 8-m resolution High Mountain Asia digital elevation models (HMA DEM; *Shean*, 2017) to map the freshest looking scarps in the landscape, on top of the 30-m resolution SRTM data (*NASA*, 2013). For the Karakudzhur and Naryn Basins, which is not covered by the HMA DEM, we obtained stereographic Pleiades multispectral imagery and processed them using known photogrammetry workflows in ERDAS Imagine to produce a model of the landscape (e.g., *Middleton et al.*, 2015; *Mackenzie et al.*, 2018; *Ainscoe et al.*, 2019). We used 0.5-cm resolution panchromatic images obtained from two different viewing angles to generate a point cloud, imported the point clouds to ASCII text files with libLAS, and used the Generic Mapping Tools (GMT) *surface* program to produce gridded elevation models with an output pixel size of 1 x 1 m (in Universal Transverse Mercator Zone 43 North projection and WGS84 datum). The output pixel size does not necessarily reflect the ground resolution of the stereo-DEM; in any case, our qualitative checks show good agreement between offset estimates

Field methods

Across two field campaigns, we traversed specific sites to document the scarps and geologic features on the faults. We also did drone Structure-from-Motion (SfM)

surveys (*Westoby et al.*, 2012) to help resolve smaller scarps in Karakudzhur and Naryn with very high resolution DEMs. We used DJI Phantom 2 and DJI Phantom 4 Pro drones with onboard GPS, with manual piloting of the former; the latter was automatically set to follow a pre-determined flight path of the scarp area in the free version of *Pix4D Capture* application on a Lenovo Tab 7 tablet. Image overlap was maintained between 40–80%, with off-nadir viewing angles to mitigate for doming errors (*James and Robson*, 2014). Photogrammetric processing was done in AgiSoft PhotoScan to obtain the elevation point clouds with millimeter precision, following well-established workflows (e.g., *James and Robson*, 2012; *Westoby et al.*, 2012). Gridded elevation data was then derived using GMT as described above. While drone surveys are limited by the battery capacity (e.g., 20 minutes of flying time), the DEMs from drone SfM provide better resolution of smaller scarps compared to the DEMs derived from satellite photogrammety.

We used a pair of Ashtech Promark 100 receivers, each attached to an L1 GPS/GLONASS antenna, to obtain differential GPS (dGPS) location data of ground control points of the drone SfM DEMs, with one receiver as the base station and the other as a rover. Only selected DEMs (primarily those in Naryn) have ground-control-points for georectification due to instrument failure in the field (i.e., the touch controls of the rover receiver was highly erratic).

Scarp profiling

To document the remnants of likely ground offsets from past fault ruptures, we analyze scarps along different parts of the fault traces. For the cumulative scarp profile on the Naryn fault (Figure 2.22e), we used the continuous dGPS survey data obtained from traversing across the scarp on foot with the rover antenna on a handheld pole. Other elevation profiles were extracted from the gridded elevation data from satellite stereo- and drone SfM DEMs using the Profile Tool in QGIS.

We measure the vertical separation across the scarps by either fitting equal and unequal slopes on opposite sides of the fault (e.g., *Ainscoe et al.*, 2019). There is a noticeable vertical offset between the satellite stereo-DEMs and the drone SfM DEMs covering the same locations likely due to differences in the vertical datum. However, the agreement between the elevation profiles from satellite stereo- and the drone SfM DEMs indicates that the positional accuracy and vertical measurements are nonetheless reliable for the purposes of identifying and measuring scarp offsets (see Figure 2.16b for a comparison).

Absolute dating

We also collected samples from trenches, pits, and natural exposures that would be appropriate for dating using standard procedures (e.g., *Middleton et al.*, 2017). Radiocarbon samples (mainly freshwater shells) were manually picked out from the loose deposits, stored in zip bags, and sent to Beta Analytic for processing and Accelerator Mass Spectrometry (AMS) dating. Detailed reports of the dating are found in Appendix A. For deposits that had no material suitable for radiocarbon dating, we rely on ages from K-feldspar infrared stimulated luminescence (IRSL) dating to constrain burial ages. We collected fine sediment samples using steel tubes that were hammered horizontally into the exposed stratigraphy. The samples were sent for processing and analysis at the University of Sheffield – Department of Geography. The details of the samples and their ages are summarized in Table 2.2, with graphs of the ages of individual grains in Appendix B.[1] Self-consistent ages of at least ten grains (aliquots) at a minimum value are considered reliable estimates (Rhodes, *pers. comm*).

[1] Analyzed by Professor Edward Rhodes

2.4.2 Karkara: Faulting north of the rangefront

In this section, we summarize our findings on the style of faulting and present results from paleoseismic trenching in the Karkara Valley, which is in the southern part of the Kegen Basin (Figure 2.2). *Mackenzie et al.* (2018) suggest the GPS velocity gradient across Karkara Valley is from creeping or shallow locking of the Karkara Rangefront Fault (KRF). The findings we detail below shows how the deformation signal could be distributed across more structures (e.g., inlcuding the fault in a paleoseismic trench, Figure 2.6a) found between the two closest GPS stations that constrain the inferred creep.

Karkara Valley is bounded to the south by the Karkara Rangefront Fault (KRF), which runs E–W on the northern edge of the Terskey Range foothills, and the Kegen Basin Fold (KBF), a NE–SW trending antiform to the north. The exact structural relationship of the KBF with the mountain front is unknown. The regional topography and elevation profile from SRTM data (Profile R–R', Figure 2.3) shows the transition from the up to ∼4,000-m high plateau in the south (Terskey Range) to the relatively flat, north sloping Kegen Basin, to below 1,000 m in the Ili Basin. The KBF may have formed through north-verging detachment faulting related to the KRF (*Mackenzie et al.*, 2018).

Near the confluence of the Karkara and Zhel'Karkara rivers (Figure 2.6), at the Kazakh side of the northeast Kyrgyzstan–Kazakhstan border, there is a ∼ 12-m high exposure of steeply dipping beds that is unconformably overlain by a 2- to 8-meter-thick sequence of predominantly gravelly deposits (Figure 2.7). While close inspection of the outcrop was not possible, the beds dip to the north, similar to the Cenozoic rocks observed by *Mackenzie et al.* (2018) in the area. The variable thickness of the overlying gravelly section is correlated to the oppositely-dipping faults at the southern and northern sides of the same natural cross-section, which also has noticeable warping of the surficial deposits on the hanging walls (Figure

2.7b). On the northern side of the outcrop, a north-dipping reverse fault, parallel to the bedding planes, appears to have displaced the unconformity by around two meters. On the southern side, a shallow south-dipping thrust fault can be traced from the displacement of strata across the shallower deposits. We estimate up to one meter of slip based on the displacement of a light gray gravelly layer around five meters from the surface. The deeper structure of the shallow thrust fault is obscured by talus; however, it appears that the Cenozoic base is highly sheared, marking the down-dip extension of the fault zone.

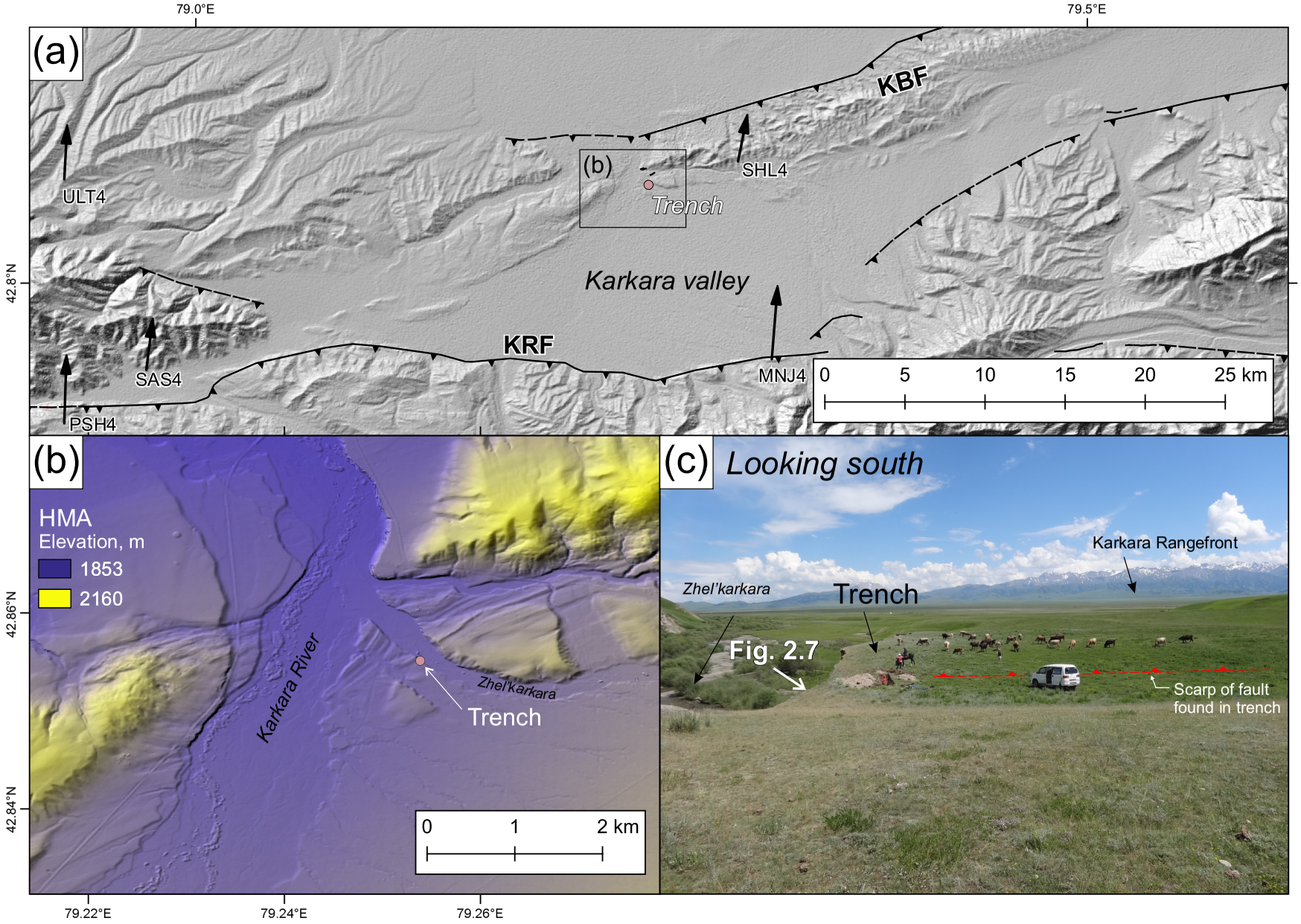


Figure 2.6: a) Location of paleoseismic trench (pink dot) in the Karkara valley, with a shaded SRTM DEM KRF: Karkara Rangefront Fault. KBF: Kegen Basin Fold. b) Shaded elevation map using the 8-meter resolution High Mountains Asia data (*Shean*, 2017). c) Field photo, looking south, of the fault scarp and trench location. White arrow points to the location of the outcrop of the deeper stratigraphy of the site, shown in Figure 2.7.

Paleoseismic trench

We dug a trench along the scarp of the south-dipping thrust fault in Karkara Valley to help constrain the fault kinematics and age of slip. Due to security constraints, only a relatively small trench was possible. As displayed in Figure 2.8, the trench stratigraphy includes a pebbly clast-supported unit on the southern side (Unit 1), a 0.5-m thick fine-sand loess unit (Unit 2), a slightly coarser sand caliche unit that thins out towards the south (Unit 3), and 30-cm of very fine sand that grades to the surface topsoil (Unit 4). We found five freshwater shells at different depths from the loess, caliche, and the bottom of the top soil unit, and one bulk organic sediment sample at the sandy base of the top soil unit. No radiocarbon material was recovered from the gravel unit. Table 2.1 summarizes the results of radiocarbon dating.

Correlating the ages of the samples with the trench interpretation, the ages generally show a consistent younging of the deposits according to relative stratigraphic position and depth. The calibrated radiocarbon ages suggest that the loess unit was deposited between 12.7 ka and 10.3 ka cal BP, the caliche unit at around 8.5 ka to 8.4 ka cal BP, and that the whole exposed sequence was capped by the topmost layer at the earliest by 3.7 ka cal BP to 1.3 ka cal BP. The much older age of the bulk sediment sample (bulk1) compared to age of the freshwater shells in the same layer may indicate the presence of old carbon in the bulk sample.

We interpret that the gravels observed in the trench are in thrust contact with the loess, similar to the shallow thrusting exposed by the riverside. It is less clear if the gravels also thrust over the caliche or not, and there is no apparent displacement across the top soil unit. As we find two distinct gravel wedges at different depths, it is possible that we may be observing two separate thrusting events (Unit 1a and Unit 1b). As shown in Figure 2.8, Unit 1a only cuts through Unit 2, so displacement related to it is probably older than ∼8.5 ka cal BP. Pinning the age of the thrusting of Unit 1b is less straightforward as there are no clear stratigraphic markers of offset

to suggest that the fault cuts through Unit 3 or not. In any case, the event has to be older than ∼1.4 ka cal BP, given the youngest sampled age for the bottom of the topsoil and the lack of evidence of any surface slip that cuts through Unit 4. These two events have around one meter of cumulative slip, which is the amount of offset observed lower in the gravel sequence in the outcrop (see Figure 2.7). Alternatively, if the thrusting of Unit 1a and Unit 1b were due to distributed slip on the surface, all the evidence suggests is that we have no significant fault slip after 2–1.4 ka cal BP.

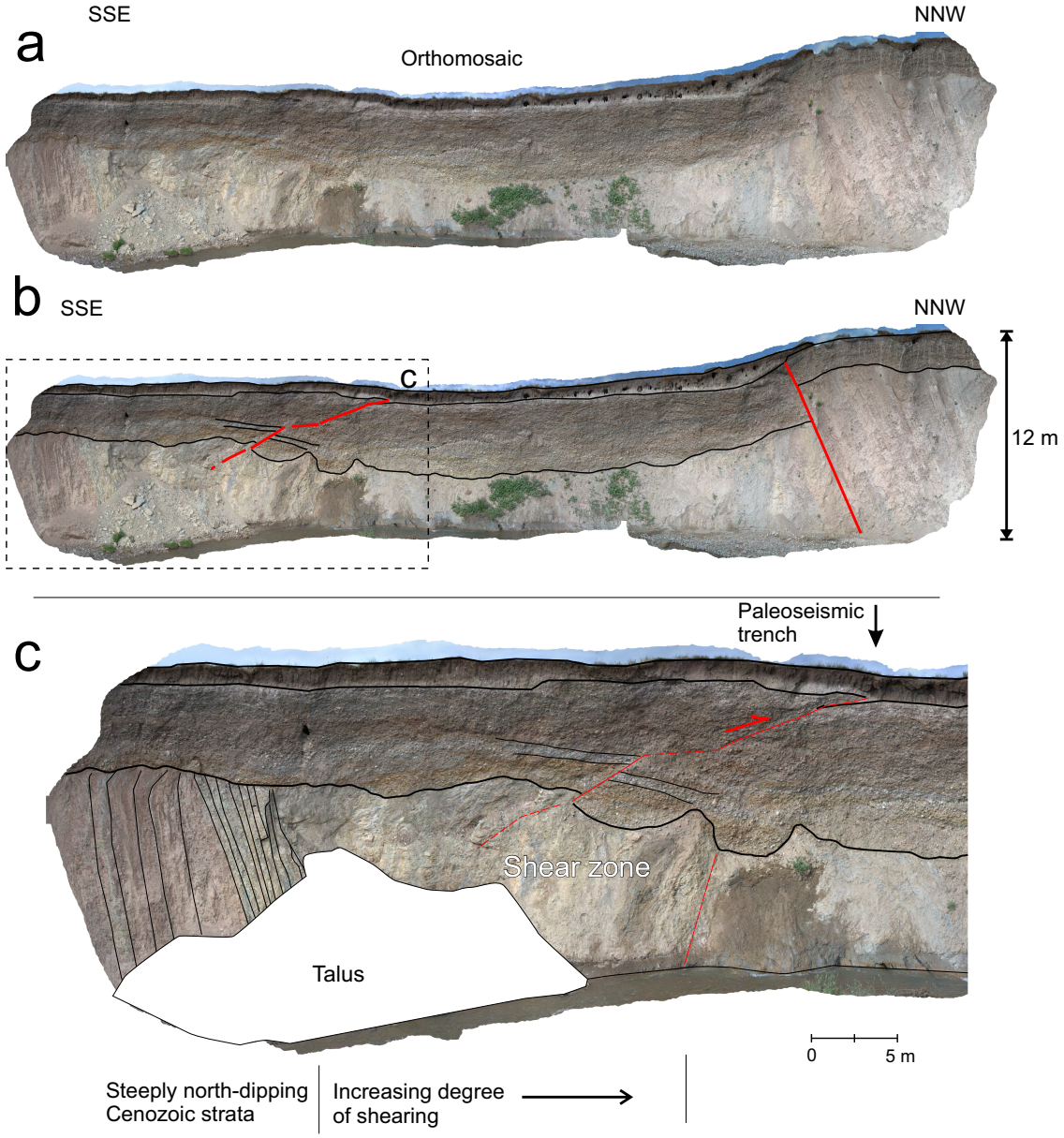


Figure 2.7: Natural exposure of a fault zone in Karkara Valley, southwest of the Kegen Basin Fold. a) Photo orthomosaic showing Quaternary sedimentary fill unconformably overlying steeply-dipping Cenozoic beds. b) The same, but with the oppositely dipping faults that bound either side of the whole sequence highlighted in red. c) Closer view of the southern fault highlighting the north-verging thrust in the gravely deposits and the location of the paleoseismic trench in the background.

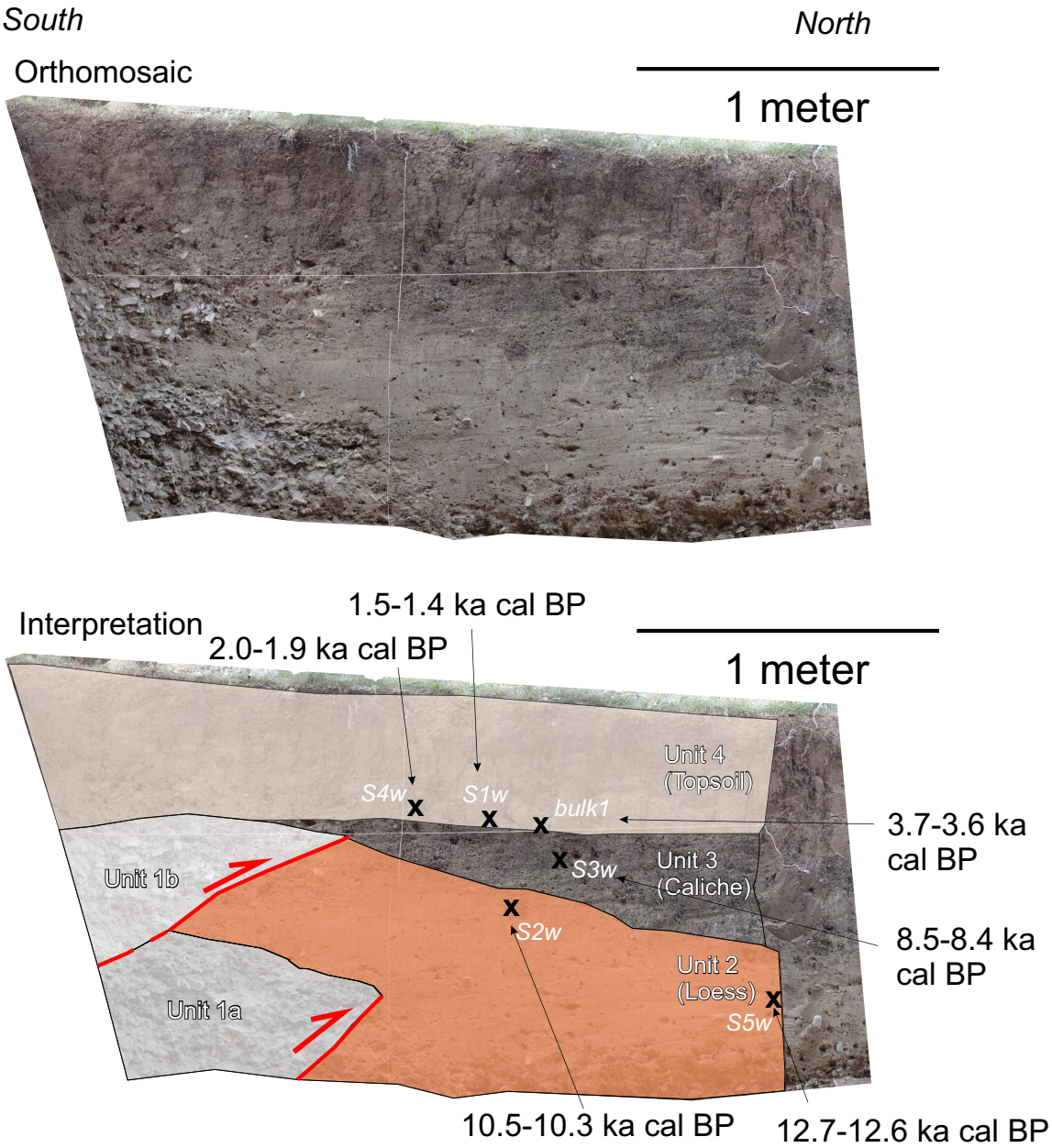


Figure 2.8: Paleoseismic trench wall in Karkara, as located in Figure 2.7. Ages indicate calibrated radiocarbon dating results (Table 2.1). See text for discussion.

Table 2.1: Radiocarbon dating results of samples from Karkara (Kazakhstan) and Naryn (Kyrgyzstan). Reports from Beta Analytic are found in Appendix A.

Sample	Lab code[a]	Material	Conv. age[b], B.P.	Cal. age (95%)[c]	Age, cal years B.P.
S1w	Beta-499692	Freshwater Shell	1,530 ± 30	428 to 598 AD	1,522 - 1,352
S2w	Beta-499693	Freshwater Shell	9,240 ± 30	8,561 to 8,331 BC	10,510 - 10,280
S3w	Beta-499694	Freshwater Shell	7,630 ± 30	6,512 to 6,429 BC	8,461 - 8,378
S4w	Beta-499695	Freshwater Shell	2,010 ± 30	61 BC to 65 AD	2,010 - 1,885
S5w	Beta-499696	Freshwater Shell	10,660 ± 30	10,751 to 10,621 BC	12,700 - 12570
bulk1	Beta-499699	Organic sediment	3,420 ± 30	1,776 to 1,636 BC	3,725 - 3,585
K17-NA1	Beta-472013	Freshwater shell	8,800 ± 30	7,976 to 8,126 BC	9,925 - 10,075
K17-NA2	Beta-472014	Freshwater shell (fragment)	13,120 ± 40	14,017 to 13,615 BC	15,966 - 15,564
K17-NA4	Beta-472016	Freshwater shell	310 ± 30	1,485 to 1,650 AD	465 - 300

[a]Beta Analytic-assigned code.
[b]Conventional age: uncalibrated age calculated using a half-life of 5,568 years and have been rounded to the nearest 10 years.
[c]Calibrated age: 95% probability using conventional age calibrated with the INTCAL13 calibration curve (*Reimer et al.*, 2013).

2.4.3 Eastern Issyk-Kul: Shallow thrust-folds in a contracting basin

The 'EM line' continues to the southwest of Karkara in Issyk-Kul basin, a trapezoid-shaped basin that is elongated E–W. The most prominent feature of this basin is Lake Issyk-Kul, an endorheic lake with a shore line at 1,607 m altitude, and a central basin 700 m deep with evidence of active sub-lacustrine anticline growth (*Gebhardt et al.*, 2017). Late Cenozoic activity is also apparent in the sub-aerial margins of the basin. While we were unable to document outcrops showing faulting, the eastern side of the basin has an undulating topography that appears to be the product of shallow fault-related folding, which has uplifted the Neogene section (*Burgette*, 2017). Profile R–R' in Figure 2.9 shows that sub-parallel ENE–WSW trending ridges, with the Tyup Fold to the north and the Cholpon Fold to the south, both have north-facing slopes that are steeper than their southern slopes. We interpret this geomorphology to be a product of imbricate thrust faults in a foreland-like configuration with the Terskey Range (Figure 2.9). The Tyup and Cholpon folds appear to be merged towards the east, where the Terskey Range and Kungey Range are perhaps in near collision given their proximity with each other (Figure 2.10a). The young deposits in the gulleys of the Cholpon fold appears to dip very gently towards the north (Figure 2.10b).

We identified fault scarps that follow the trend of the folding. At higher elevations to the east, on the northern slopes of the foothills of the Terskey Range, the High Mountain Asia (HMA) DEM reveals scarps that may indicate the western extension of the Karkara Rangefront Fault (around 30 km west of Karkara, as shown in Figure 2.2). On the opposite side of the ridge, east of Sary Tologoy, we find uphill-facing scarps (sackungen), above 2,000 m elevation, that are continuous with scarps in the lower areas to the east (Figure 2.11). Imagery from Google Earth and Bing maps, and our field investigation show ponding on the uphill side, suggesting relative uplift

of the southern side. Ponding may also be due to lateral displacement, however, we cannot identify significant horizontal offsets to suggest such. A small trench that we dug across the scarp did not reveal good indicators of displacement. Several mechanisms are proposed for the genesis of sackungen (Guttiérez-Santolalla et al., 2005; see also McCalpin, 1999). The sackungen in Sary Tologoy may be due to distributed shallow tensional fracturing in a topographically-rugged locality or gravity-related secondary dip-slip (normal) faulting.

At the plains near the shoreline of Lake Issyk-kul, the high-resolution DEMs reveal a previously unrecognized ENE-trending 20-km long scarp (Figure 2.12). The regional geomorphology suggests the west-southwestward propagation of the Cholpon fold, with the formation of a prominent water gap, and the possible deflection of the Dzhergalan River (Figure 2.12a). The scarp is around 6-7 meters high in Mikhailovka, on the western end, and we can trace it up to Cholpon in the east. We were not able to identify suitable sites for dating offsets as most of the land is modified (either by farming or human settlement), although the scarp can be recognized at different points (e.g., Figure 2.13a). We also did not find any clear evidence of displacement on cultural features (roads, fences, houses) along the scarp as most concrete structures did not appear stable enough for the discrimination between deformation due to tectonic or material wear (e.g., the pavement in Figure 2.13b is made of a thin layer of concrete). There is also no obvious scarp on lower river terraces to the west by the lake shore (Figure 2.13d).

We interpret this scarp to be of tectonic origin, primarily related to the propagating thrust front of the Cholpon fold. The active uplift of the fold could be responsible for the water gaps and the westward deflection of the Dzhergalan River. We did not find evidence of lacustrine stratigraphy exposed on the canyon walls, which would otherwise strongly suggest a lacustrine origin for the scarp. Offlapping stratigraphy, indicative of regression or relative uplift of the lakeshore, and varves are found in

other parts of the region (Figure 2.13c). Instead, we find very thick horizontal beds of fine sand underlying either side of the scarp, with the cliff face on the scarp being more prone to slope failure (Figure 2.12). The elevation profiles suggest that there could have been some channel development near the scarp; however, the abandoned stream is only limited to the western most section and is at lower elevation than the scarp (Profile 3 in Figure 2.9). We also do not find a terrace symmetrical to the scarp to the north, which would otherwise be strong evidence of a fluvial origin for its whole length. Further, the growing antinclines on the lake bed (*Gebhardt et al.*, 2017), to the west, supports the wider extent of shortening within Issyk-Kul basin.

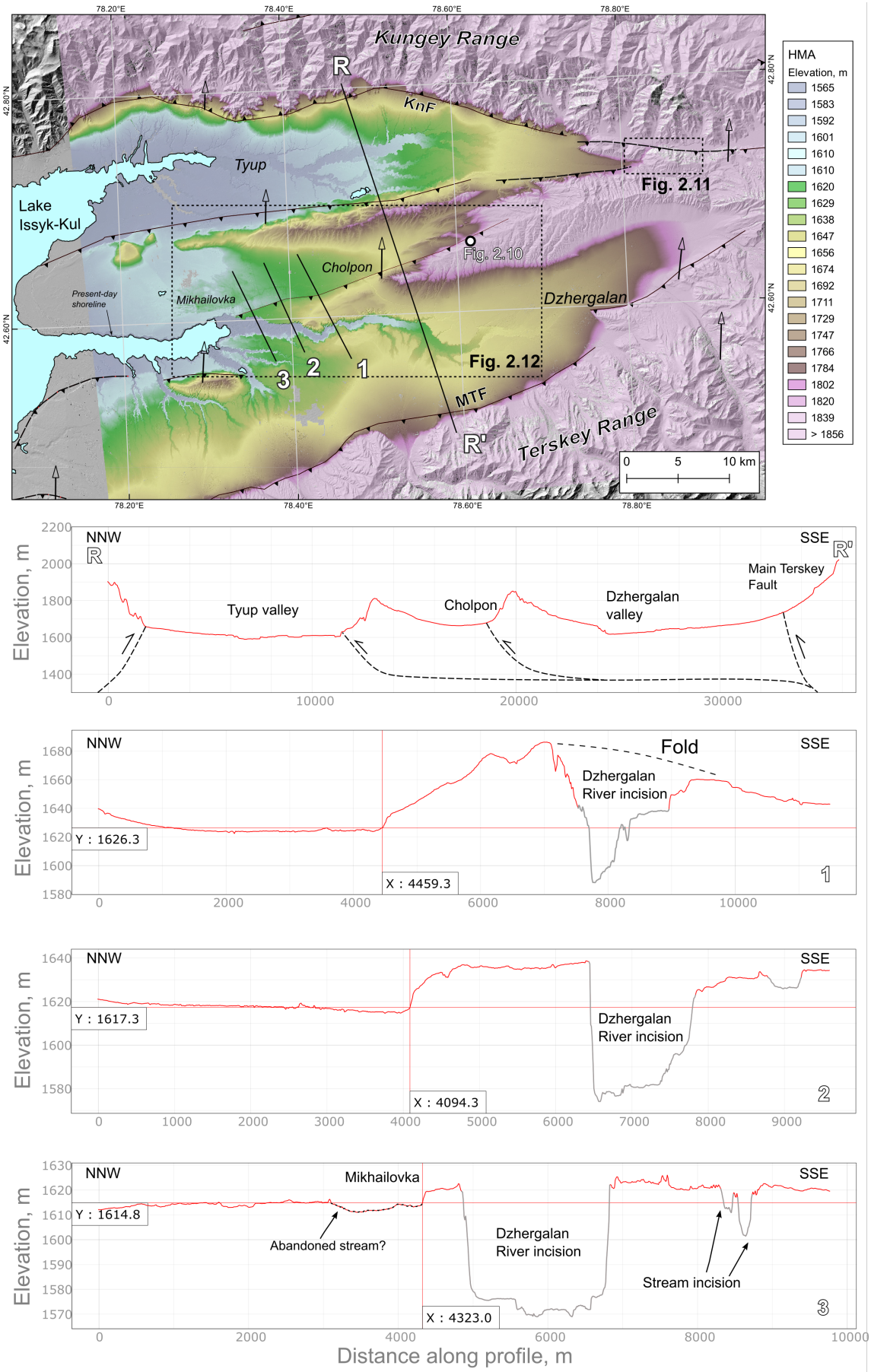


Figure 2.9: Shaded elevation map (top) and topographic profiles of eastern Issyk-Kul from 8-m resolution HMA elevation data. On the map. present-day extent of Lake Issyk-Kul is masked by the light blue polygon. The vertical exaggeration differs between profiles to highlight specific features.

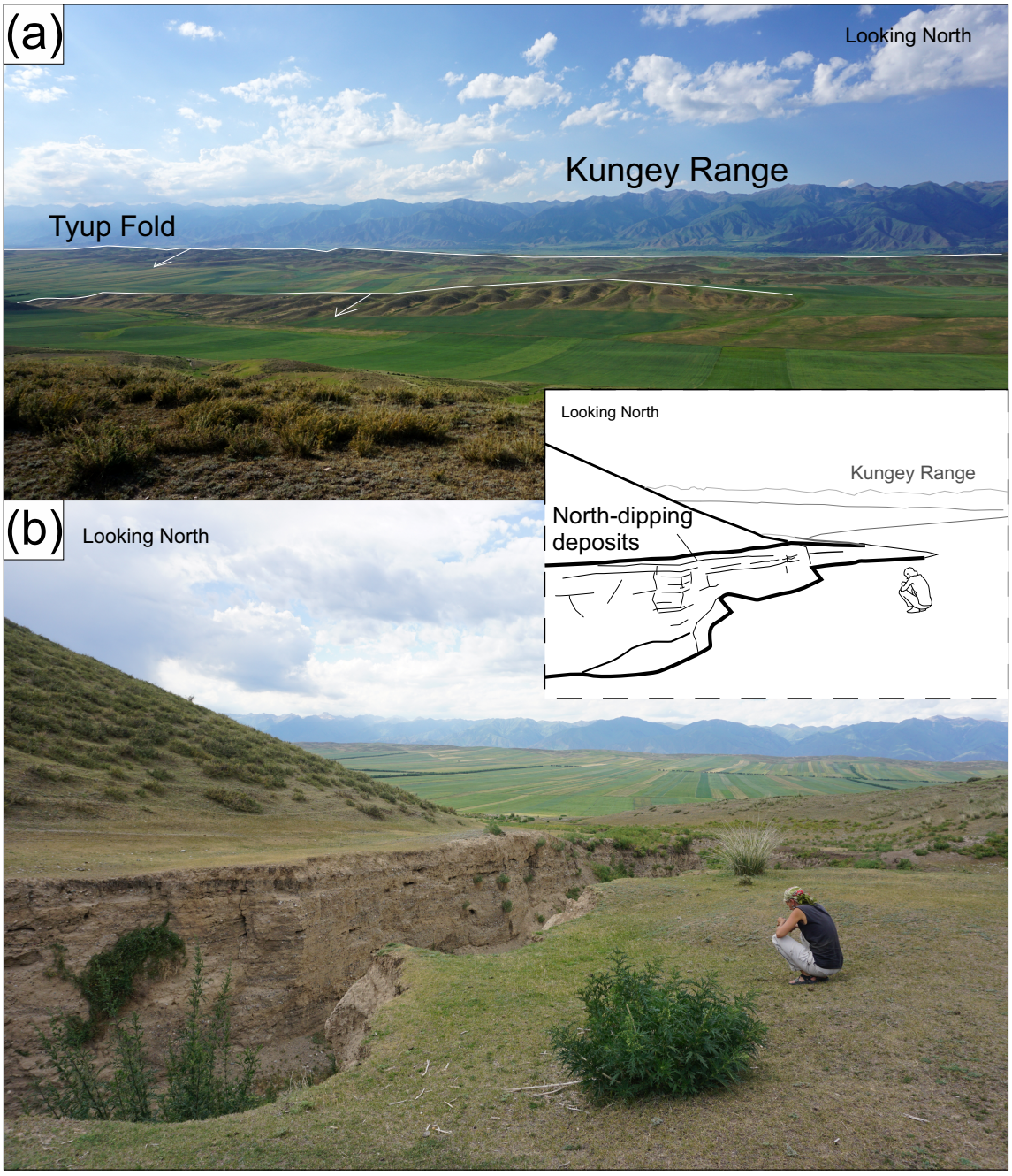


Figure 2.10: Photos of the young folds in eastern Issyk-Kul basin. a) View from the crest of the Cholpon fold, looking northward towards the Kungey Range, with the backlimb of the anticlines highlighted by the white arrows. b) Very shallowly northward-dipping deposits on the Cholpon Fold. Inset shows simplified sketch.

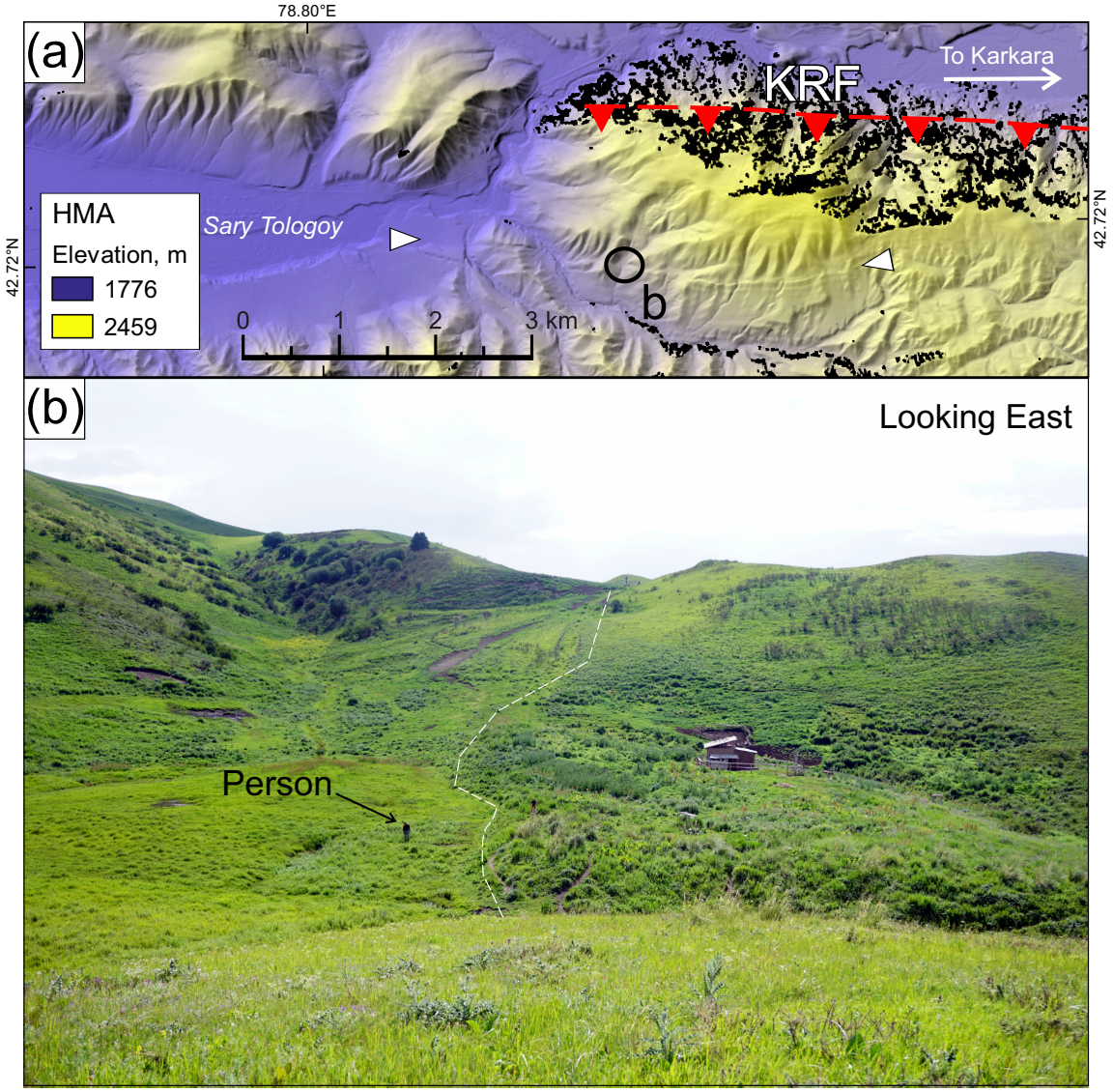


Figure 2.11: Likely secondary deformation in the form of sackungen in Sary Tologoy, far eastern Issyk-Kul (Kyrgyzstan). a) Shaded HMA elevation map, with the scarp highlighted by the white triangles. KRF: Karkara Rangefront Fault. b) Ponding observed on the northern, upstream side of a gulley, upslope of the scarp (white dashed line) in the field, as located in (a). Downslope direction is to the south (right side of the photo).

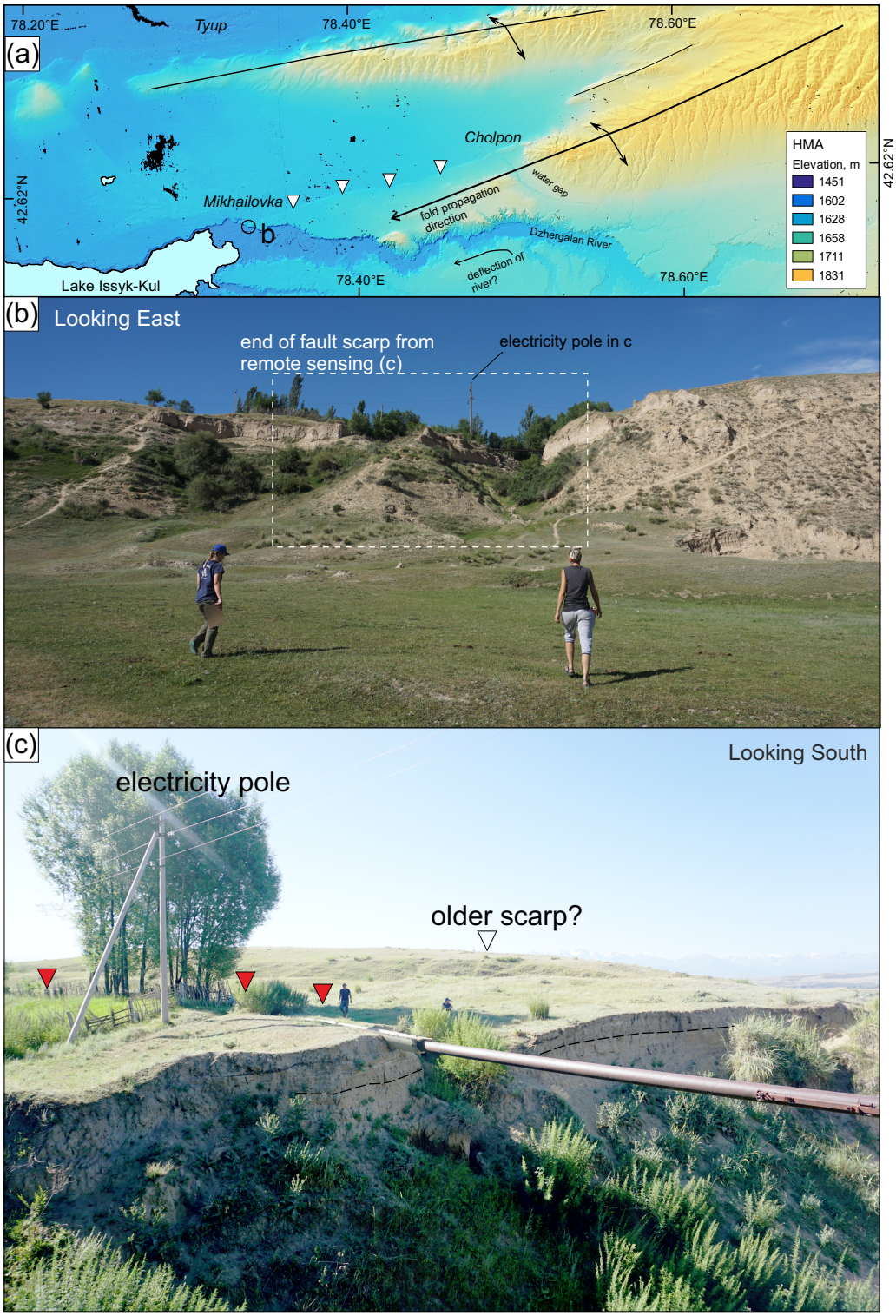


Figure 2.12: Geomorphology of the Cholpon fold. a) Shaded HMA DEM of eastern Issyk-Kul with the white triangles pointing to the scarp extending from the Cholpon fold in the east to the edge of Mikhailovka, near Lake Issyk-Kul, to the west. See text for discussion. b) Canyon wall exposure of the termination of the Mikhailovka scarp as seen from the present-day Dzhergalan River bank. c) Closer view of the outcrop near the top of the canyon, looking south, where the fault trace ends in the west. Mass wasting in the outcrop made it difficult to closely inspect the stratigraphy, however, the lithologies on either side of the projected location of the fault (red triangles) appear the same. Location: 78.3328°E, 42.6036°N.

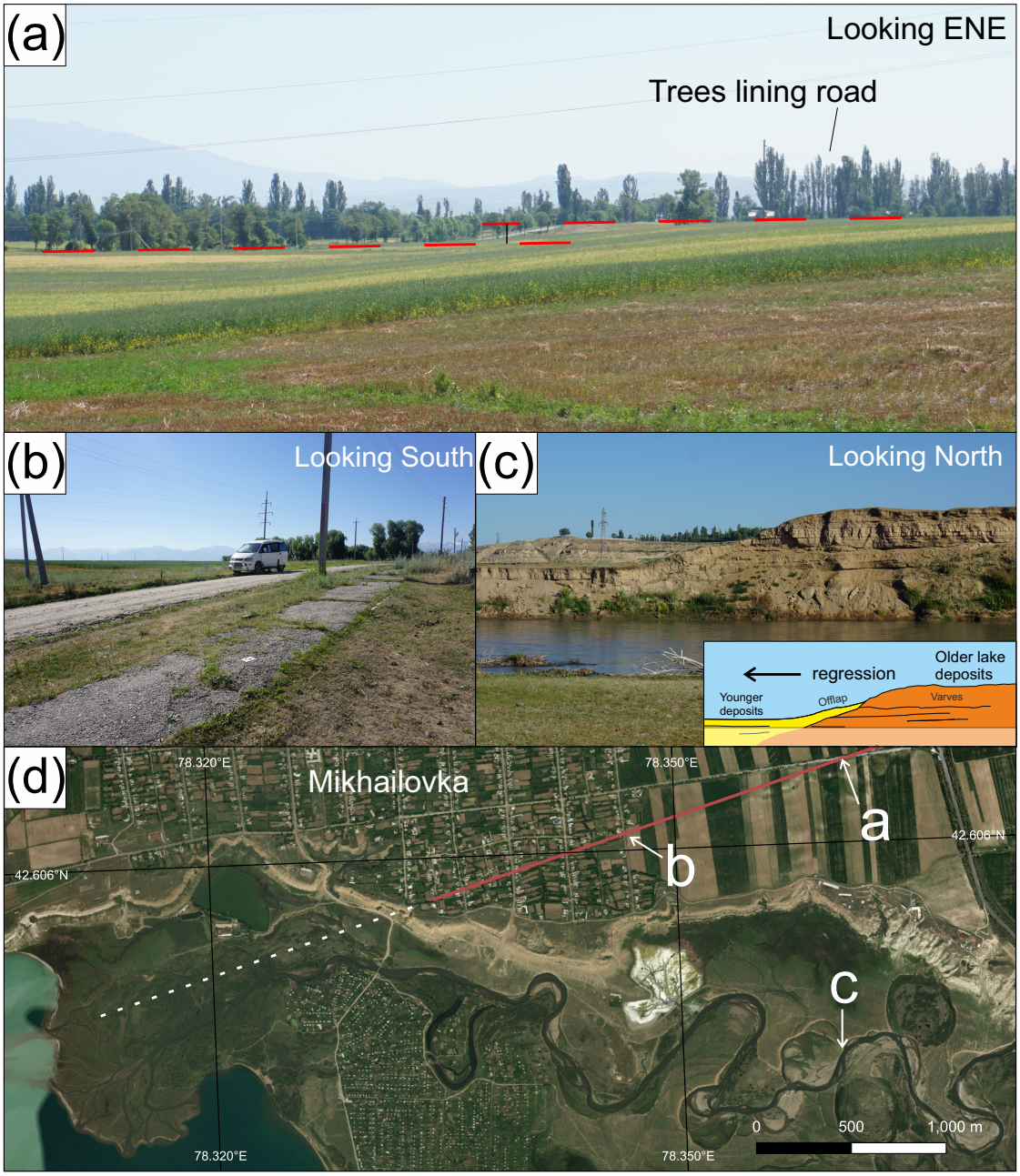


Figure 2.13: a) The fault scarp crossing the fields in Mikhailovka, with a scarp along the road to the village. Photo taken from (b). b) Damaged pavement on the scarp. c) Offlapping deposits on a varve sequence, indicative of a regressive lacustrine environment. Inset shows a simplified interpretation of the outcrop. d) Bing Aerial imagery of Mikhailovka, showing the locations of (a-c) and the scarp (red line). We did not find any apparent scarp-like feature along the dash white line in the field or in the HMA DEM.

2.4.4 Karakudzhur: satellite- and drone-derived DEMs of a centuries old scarp

Evidence of active shortening and seismic activity also exist in the basins southwest of the Issyk-Kul. Downslope of the southern part of the Terskey Range, active faulting in Karakudzhur is marked by scarps and late Quaternary uplift along ∼30 km of the northern basin edge. Satellite imagery shows remarkably fresh-looking scarps that, along with other paleoseismic features, suggest Holocene earthquake activity (in $M \approxeq 7.0$ earthquakes; *Campbell et al.*, 2019). With the Pliocene onset of exhumation of the Paleozoic core (*Macaulay et al.*, 2014) and the construction of mountain ranges reaching 4,000 m in elevation, the shortening here likely manifests as thick-skinned deformation on steep faults, with the shallowest 1-2 km reflecting a degree of flattening in the fault dip (e.g., *Selander et al.*, 2012; *Campbell et al.*, 2019).

The Karakudzhur Fault has a discontinuous trace over 40 km in a high-elevation basin, with the freshest scarps in the east. With the satellite stereo- and drone SfM DEMs, we can identify the scarps detailed in *Campbell et al.* (2019), with the additional benefit of being able to measure the scarp heights at different sections to highlight the small offsets, as summarized in Figure 2.14.

We find scarps as small as 0.4 m in the western site with the SfM DEM, to 3 meters of offset on the eastern end of the scarp from the stereo-DEM (Figures 2.15 and 2.14d, respectively). These scarps appear across small fan deposits and intermittent streams, signifying the relative recency of scarp formation, and are largely sheltered from elements that could promote rapid erosion (e.g., wide streams that have headwaters reaching further into main range). Their non-alignment with the slope in many locations suggest that soil creep or other forms of small-scale mass-wasting cannot account for the genesis of the offsets. Differences in slope between the hanging wall and foot wall of the scarps across alluvial fans may indicate a degree

of degradation. In any case, we find that the slope irregularities do not affect the vertical separation measurements greatly for most profiles (Figure 2.15c and d). The large discrepancy between the measurements assuming the same and different slopes near a small gully, displayed in Figure 2.16c, is likely due to erosion at the foot of the scarp, hence we consider the estimate assuming uniform slope to be more reliable.

A cumulative scarp on an uplifted terrace on the thrust front reaches around 31 m in height, with the estimated vertical separation across the fault from the stereo-DEM and drone SfM providing similar results (Figure 2.16). In the field, the single event ruptures are seen alongside and generally parallel to cumulative scarps (Figure 2.17). We are unable to provide new reliable slip-rate estimates as dating these high terraces is challenging, especially that the regional environment has largely been erosional (alluvial and glacial). Our only useful luminescence dating results in Karakudzhur, from a pit on a 31-meter high terrace on the hanging wall is inconclusive because we likely sampled a post-abandonment sandy silt cap (at 0.5 m depth; burial age of $\sim 930 \pm 100$ years) (Figure 2.17b–d). Not enough suitable grains were obtained in a lower gravelly unit.

Table 2.2: Summary of samples submitted for IRSL dating.[1] FW: Foot wall side. HW: Hanging wall side.

Sample ID	Lab Code	Location	Elevation, m	Depth, cm	Aliquots used (total analyzed)	Stratigraphy	Age, ka	
KGZ18-03	19044	Karakudzhur (76.225$°E, 41.949°N)	2,777	180	*6 (8)*	Gravel	*38,100*	*3,000*
KGZ18-04	19045			85	6 (26)	Gravelly mud	39,200	6,100
KGZ18-05	19046			45	22 (116)	Loess	930	100
KGZ18-06	19047	Naryn: Tash-Bashat (76.371°E, 41.478°N)	2,288	105	11 (12)	Loess, FW	4,200	470
KGZ18-07	19048			60	*7 (9)*	Matrix-supported gravel (colluvium), FW	*3,780*	*510*
KGZ18-08	19049			60	3 (3)	Sand lens in terrace gravel, HW	11,200	1,800
KGZ18-09	19050			55	*11 (15)*	Terrace loess cap, HW	*11,600*	*1,100*
KGZ18-10	19051	Naryn: Dobulu (76.235°E, 41.458°N)	2,168	40	14 (120)	Loess	420	70

[1]Dating was done by Ed Rhodes at the University of Sheffield.

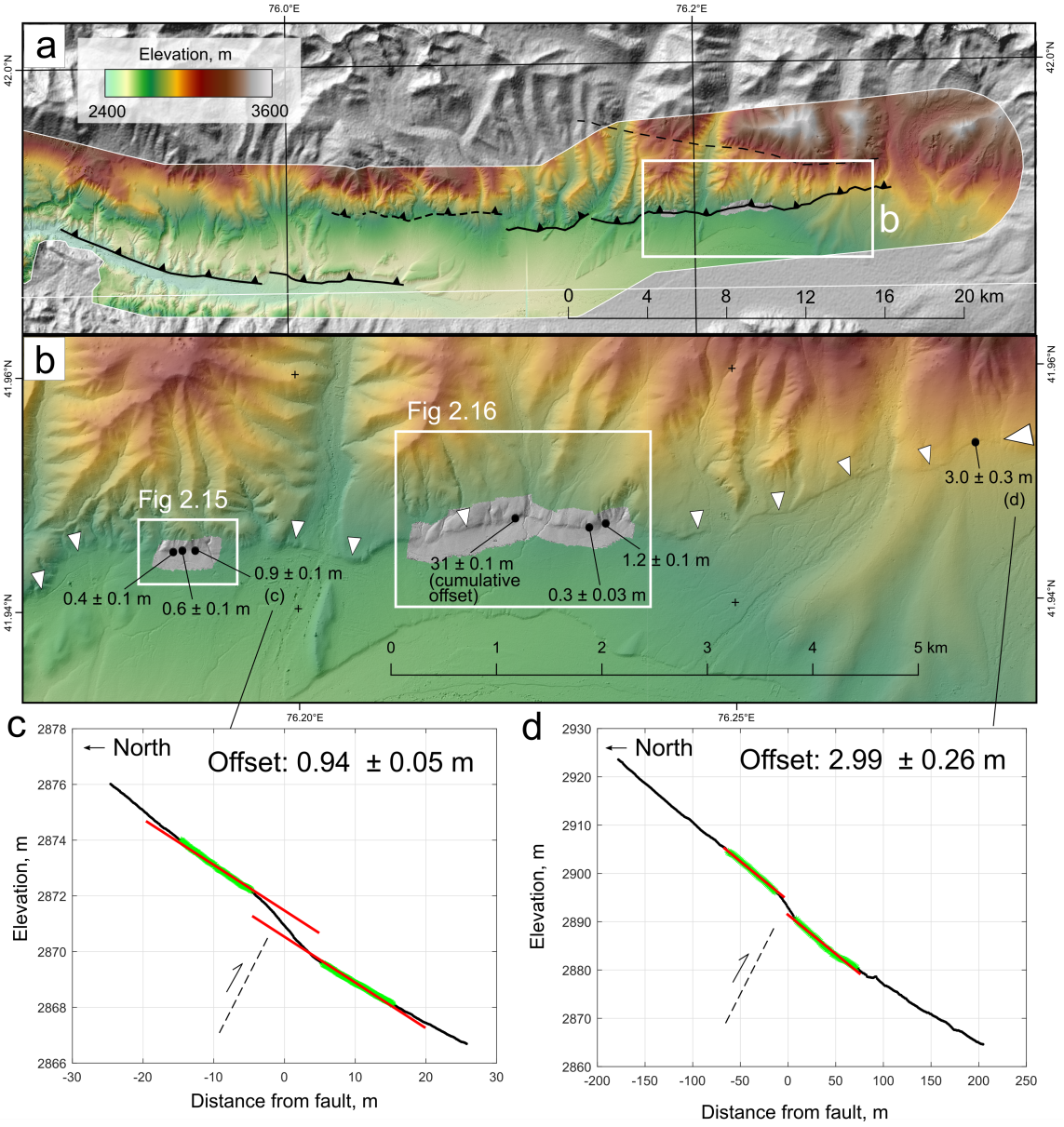


Figure 2.14: Morphology and profiles of the possible paleoearthquake rupture scarp in Karakudzhur. a) Shaded stereo-DEM elevation map overlain on the SRTM hillshade. b) Vertical separation at different sections of the fault. c) Elevation profile across a small alluvial fan (note the gradual steepening upslope of the hanging wall). d) Elevation profile near the easternmost end of the fresh-looking scarp. Error bars indicate the root-mean-square residual between the points and best-fit lines. In (c) and (d), red lines show the offset best-fit surface based on uniform slope fit to the selected elevation points (green) on the upslope and downslope side of the scarp profiles. Inclined dashed line and arrow is a schematic of the underlying thrust fault, with the northern side being the upthrown block.

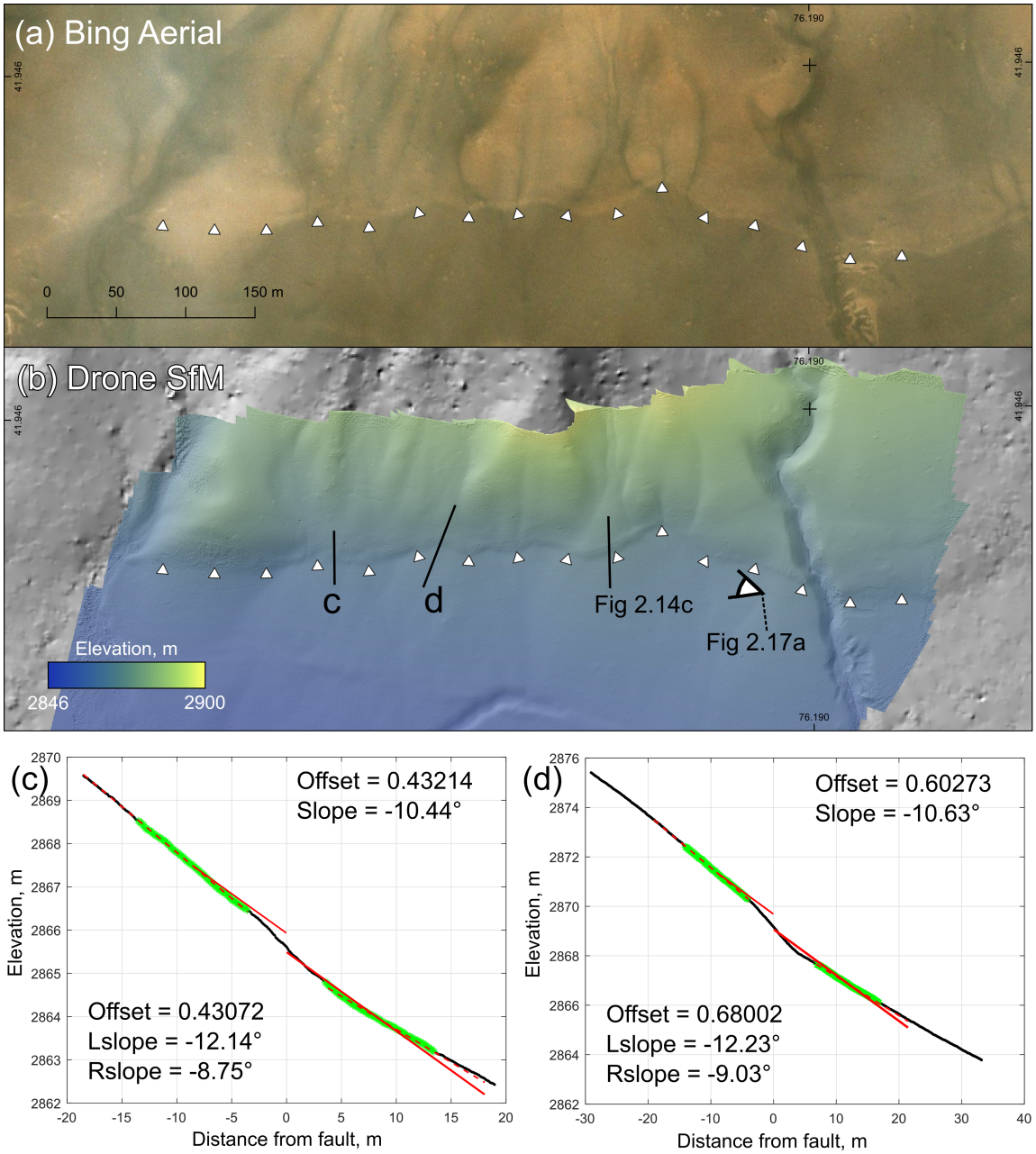


Figure 2.15: (a) Bing Aerial imagery, (b) shaded drone SfM elevation map, and (c-d) profiles showing the vertical separation (offset) of likely-single event scarps. (see Figure 2.14b for location). White triangles in (a) and (b) point to the youngest scarp of the Karakudzhur Fault. In (c) and (d), continuous and dashed red lines show the uniform and variable slope fits, respectively, to the selected elevation points (green).

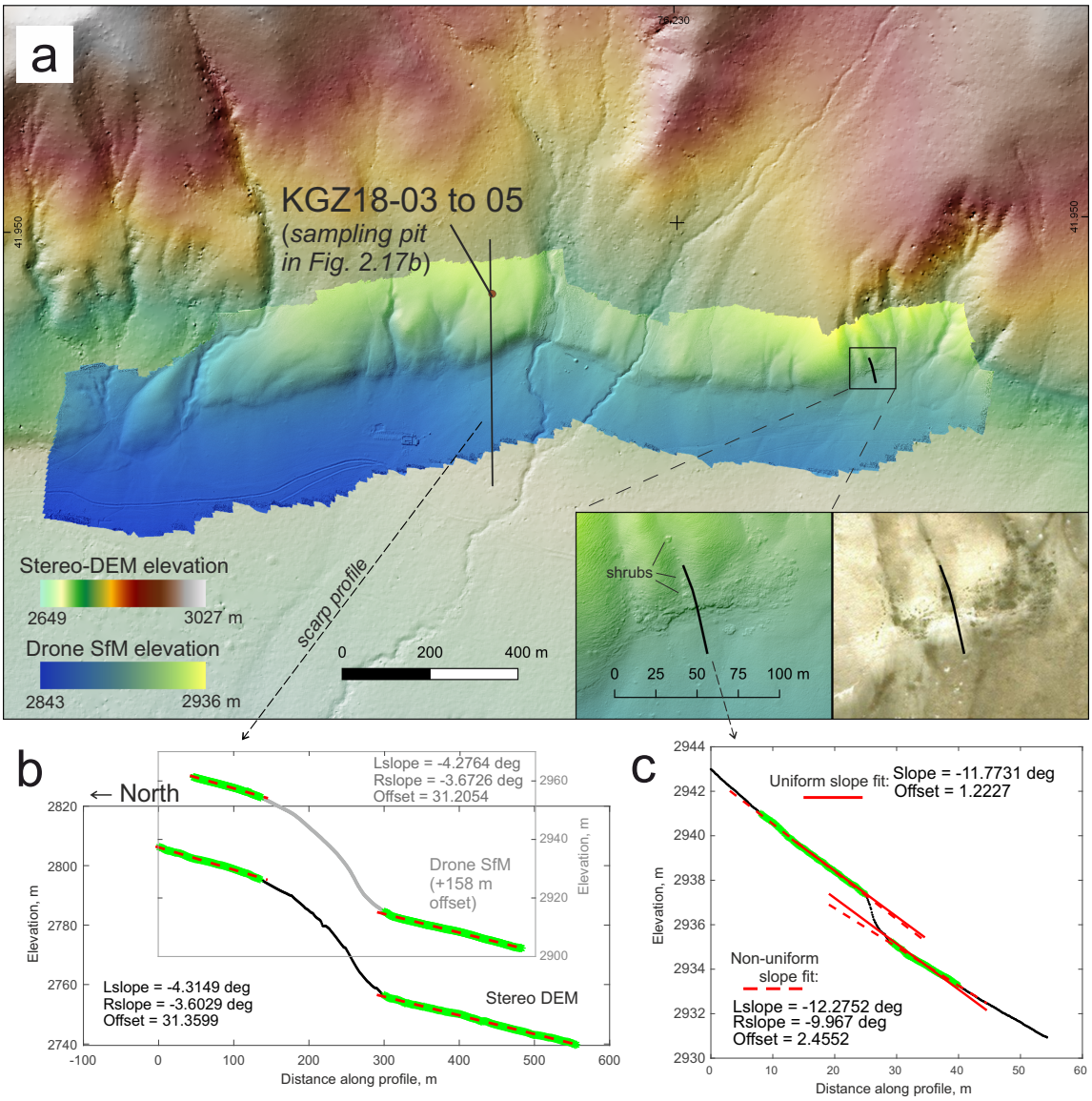


Figure 2.16: Comparison of the cumulative and possible single-event scarps in the eastern section of the Karakudzhur Fault. a) Shaded drone SfM DEM overlain on the satellite stereo-DEM. Inset shows a close-up view of the single-event scarp from the drone SfM and Bing Aerial imagery. Purple dot indicates location of IRSL sampling pit described (Figure 2.17b). b) Cumulative scarp profile, comparing the vertical separation measured from the satellite stereo-DEM (black) and the drone SfM DEM (gray). c) Scarp profile along a young stream, with vertical separation estimates based on fitting a uniform slope and non-uniform slope on the hanging wall (Lslope) and footwall (Rslope).

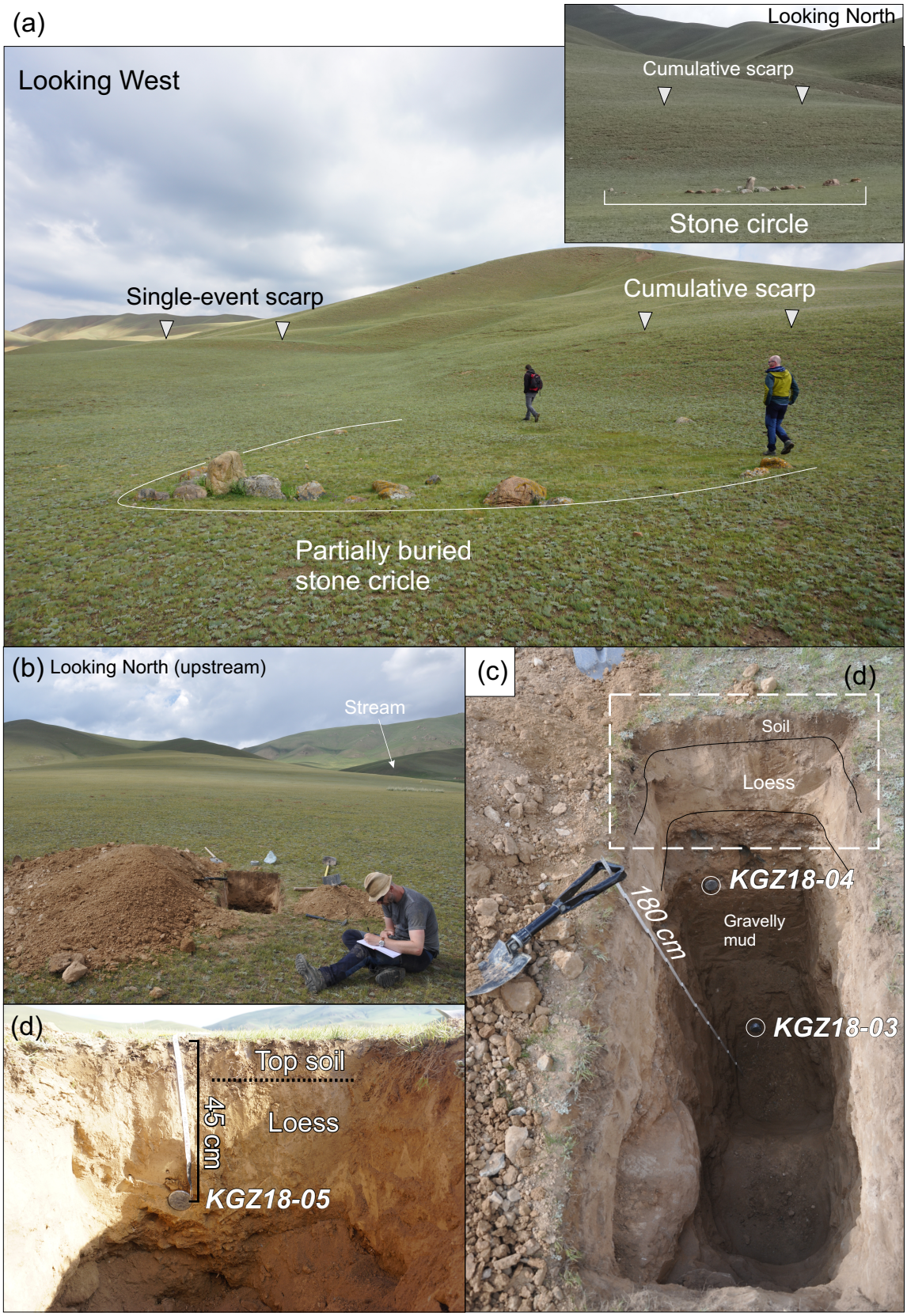


Figure 2.17: a) Photo of a partially buried prehistoric burial circle, with a single event scarp and cumulative scarp in the background. Inset: View looking north of the same site (76.1895°E, 41.9448°N). b) Sampling pit on top of cumulative scarp on top of the 31-m high cumulative scarp (Figure 2.16) (76.2250°E, 41.9484°N). c-d) Top view and profile of the sampling pit in (b).

2.4.5 Naryn: fresh scarps and paleoseismic evidence

The Cenozoic tectonics of the Naryn Basin has been subject of several studies (e.g., *Burbank et al.*, 1999; *Thompson et al.*, 2002; *Goode et al.*, 2011), however, discussion on the paleoseismology of faults is lacking. From satellite imagery and stereo-DEMs, we can identify fresh-looking scarps in the eastern side of the basin suggesting an active thrust front parallel to the Naryn River flood plain. We can trace around 50 km of the fault in the stereo-DEM. This trace is contiguous with the Central Naryn Fault in *Thompson et al.* (2002), an E–W striking, north-dipping thrust fault that goes further west of the Naryn town center (Figure 2.18a), to a total length of 75 km. We also find uphill-facing scarps that appear to follow the Paleozoic-Cenozoic contact (e.g., *Macaulay et al.*, 2014) (Figure 2.18b–d), which might suggest the reactivation of existing structures, although we are unable to constrain the kinematics of recent slip due to unsuitable field conditions. Below, we discuss in detail the evidence for surface rupturing slip on the thrust front.

Paleoseismic evidence on the Tash-Bashat section

The stratigraphy of a terrace exposure north of Tash-Bashat, near the eastern end of the active thrust front, shows convincing evidence of Holocene activity (Figure 2.19, location in Figure 2.18). We interpret the outcrop to be composed of a clast-supported gravelly (terrace) unit overthrusting a light brown fine-sand (loess) unit, capped by a matrix-supported gravelly mud colluvium, and a sandy top soil (Figure 2.19). It is difficult to constrain the amount of slip due to the lack of piercing points, i.e., we do not see the terrace gravel unit on the foot wall side. However, the separation between the top of the terrace unit on the fault contact and the bottom of the exposure indicates at least one meter of dip slip. The DEM also does not show any evidence that the terraces at lower elevations are offset (Figure 2.19a).

We collected samples for IRSL dating of the different units (Table 2.2), and the

results suggest that thrust faulting we observe is younger than ∼4.2 ± 0.5 ka. This is based on the age from the sample of the loess unit (KGZ18–6) in the foot wall. The sample (KGZ18–9) from the base of the loess cap of the terrace gravel in the hanging wall side, 15 meters north of the fault, is 11.6 ± 1.1 ka. The ages for the colluvial wedge and the terrace units are poorly constrained due to the insufficient number of suitable aliquots, i.e., less than 10 feldspar grains, though estimating the age from the preliminary estimates from existing best grains still generally follow the observed relative stratigraphic succession. The tentative age of the colluvium sample is 3.8 ± 0.5 ka (KGZ18–7). The fine sand lens sample within the terrace gravel unit has an age of 11.2 ± 1.8 ka (KGZ18–8), which is slightly lower than the loess cap. This suggests that the age from the terrace gravel unit, while only based on three grains, might be a plausible estimate within its uncertainties. If we consider that all the reported ages are reliable, it appears that the age of the last surface rupturing thrust earthquake in the outcrop is at ∼4 ka (i.e., between the burial ages of the foot wall loess unit and the colluvium).

Small scarps and the geological features of the fault zone (Dobulu)

Near the village of Dobulu, 15 km west of Tash-Bashat, the scarp is around ∼0.5 m high (Figure 2.20). It is continuous with the fault trace to the east and west, making it stand out from the abandoned channels that are also visible in the drone DEM. In the field, outcrops in a nearby quarry show that the scarp goes across gravelly fluvial deposits. A natural cross-section of the fault on the eastern end of the scarp, by the side of the river, shows fragments of dark volcanic rock (basalt?) in a white crystalline matrix, which is a feature we find in another part of the thrust front (see Section 2.4.5).

IRSL dating results of the best grains from a silt layer overlying the gravels suggest a burial age of 0.4 ± 0.7 ka for the fluvial deposit (KGZ18-10, Table 2.2)

Interpreting the age of the scarp offset is complicated by the large scatter of apparently older grains, which may be due to inheritance or incomplete bleaching prior to burial in the environment of deposition (likely fluvial). Hence, we consider the reported age as the upper limit of scarp formation, i.e., faulting may be at the same time or older.

Bashnura River section: Holocene slip rate and fault geometry

The Late Quaternary deformation rates and geological manifestation of faulting suggest thrusting along the whole length of the Naryn fault. A differential GPS elevation profile across an uplifted terrace of the Bashnura River (Figure 2.22) shows a vertical separation of 25.6 ± 0.1 m on the fault scarp, representing the cumulative offset on the fault. From the pre-abandonment sedimentary cap of the uplifted terrace (Figure 2.22d), one fresh water shell has an age of 10,116–9,689 years cal BP (95% probability; K17-NA in Table 2.1). The age of a separate shell fragment in the same layer is older (∼16,000 years cal BP, K17-NA2); we consider this a less reliable indicator of the terrace age due to possible detrital component. A modern shell sample from the soil returns an age of 465-300 years cal BP (K17-NA4).

The fault slip rate, accounting for the potential variability in fault dip at depth by considering a uniform probability from 40° to 60° dip through Monte Carlo sampling (e.g., *Mackenzie and Elliott*, 2017; *Ainscoe et al.*, 2019), suggests a Holocene slip rate between 2.9 to 3.7 mm/yr at the upper and lower limit, respectively, of the 95% probability radiocarbon age. The upper bound in the dip helps us to account for the possibility that the fault may steepen at depth (i.e., following thick-skinned tectonics). In the field, the fault dip appears to be around 45° on the ∼75-m high outcrop in Bashnura River (Figure 2.22b). In any case, this estimated range of slip rates is slightly higher than the slip rate in central Naryn ($2.3^{+0.3}_{-0.4}$ mm/yr; *Thompson et al.*, 2002). The difference may reflect along-strike variability of shortening owing

to different styles of faulting in different parts of the Naryn Basin.

The north-dipping Kadjerty Fault (slipping at 1.2-1.9 mm/yr, *Thompson et al.*, 2002) is concurrently active along with the Naryn Fault in central Naryn, more than 20 km west of our study area (Figure 2.18). The Kadjerty Fault extends even further west where the basin widens to around 50 km between ranges (Profile N-N‘ in Figure 2.5) and where shallow south-dipping blind thrusts are also thought to be present (*Goode et al.*, 2011, 2014).

Our slip rate estimate of the Naryn Fault translates to shortening of 2.6 mm/yr (with a fixed 45° dip), which is 65% to 85% of the internal N–S shortening of the basin as measured from the GPS data in western Naryn (*Zubovich et al.*, 2010, and Profile N-N‘ in Figure 2.5) The uphill-facing scarps on the Paleozoic-Cenozoic contact may also be recently active based on the scarp that appears along the contact (Figure 2.18b-d). However, the more limited extent of the uphill-facing scarps may mean that it does not accommodate as much of the basin shortening as the Naryn Fault, at least in the Holocene.

Finally, as seen in Figure 2.22b, the thrusting of the red Neogene sedimentary sequence over Quaternary deposits (similar to those observed by *Thompson et al.*, 2002, in central Naryn) further suggests that the Naryn Fault has been active throughout the Holocene. We also find similar basalt structures in the Dobulu quarry scarp on an outcrop on the western bank of the Bashnura River near the fault (Figure 2.22c). Basalts sporadically founds across the central Tien Shan, including sites close to our study area, are believed to be from a shallow mantle plume of Paleogene age at the latest (e.g., *Sobel and Arnaud*, 2000; *Simonov et al.*, 2008). While we do not have age constraints for the basalts in our study area, the Naryn Fault may have either acted as a conduit for the emplacement of shallow basaltic intrusives or has formed along an existing structure (e.g., dikes). Both cases suggest that the Naryn fault is connected to the deeper crust, i.e., faulting across the seismogenic zone.

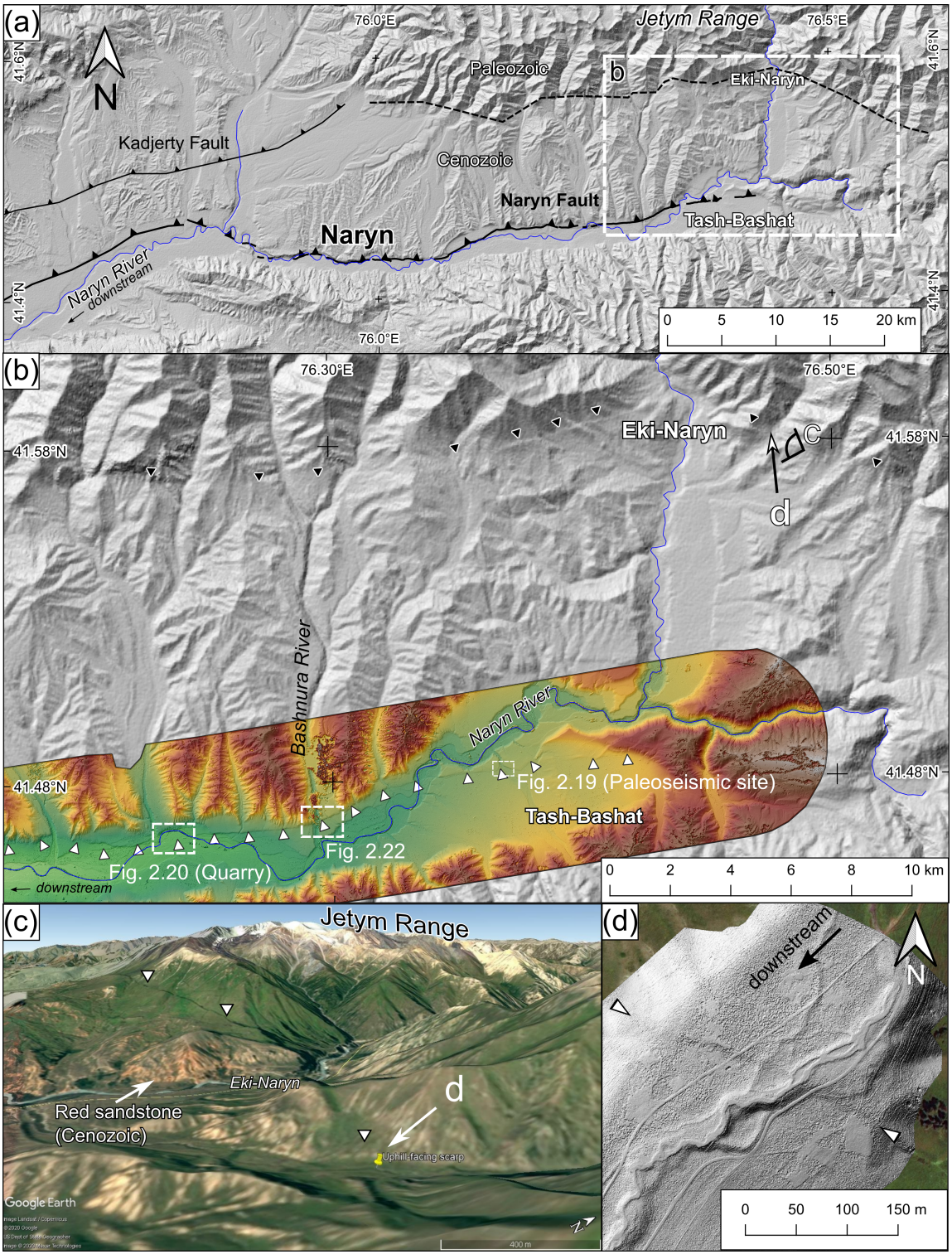


Figure 2.18: Active faulting in eastern Naryn Basin. a) Shaded SRTM DEM highlighting the major structures with evidence for Late Quaternary activity: the Naryn Fault (e.g., *Thompson et al.*, 2002, and this work) and Kadjerty Fault (e.g., *Thompson et al.*, 2002). The contact between the Paleozoic-cored Jetym Range and Cenozoic sedimentary sequences is based on evidence of Cenozoic exhumation from *Macaulay et al.* (2014). b) Closer view of distributed faulting on the eastern margin, with uphill-facing scarps in Eki-Naryn (black triangles), following the trend of the aforementioned contact, and the thrust front (white triangles) covered by the Pleiades stereo-DEM (in color). Also shown is the viewing direction of (c). c) Perspective view looking WNW towards the scarps and geology in Eki-Naryn from Google Earth. d) Shaded drone SfM DEM showing the scarp crossing a stream valley east of Eki-Naryn, as located in (c).

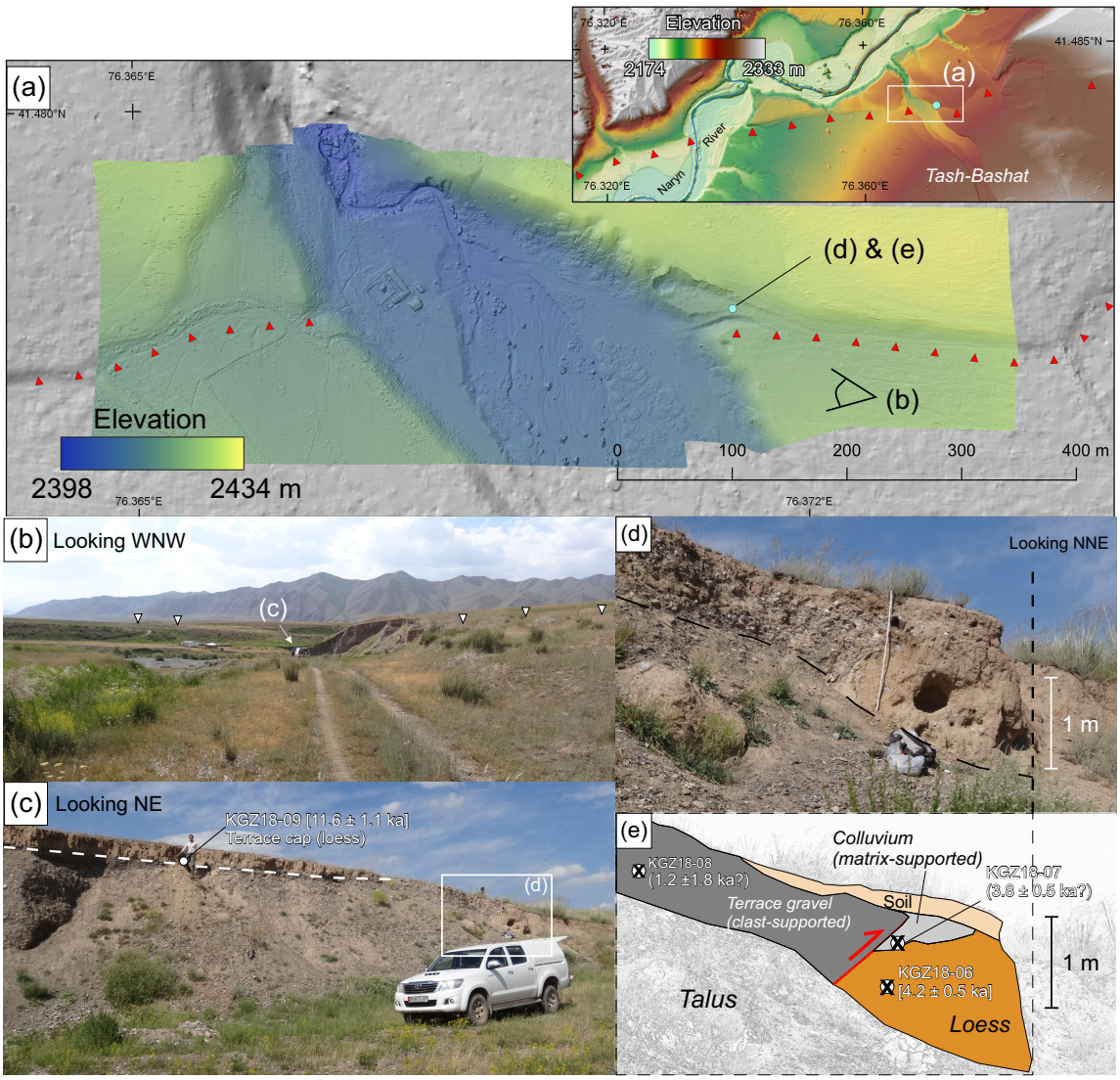


Figure 2.19: Paleoseismic section of a north-dipping surface-rupturing thrust fault in Tash-Bashat (eastern Naryn) on a terrace of the tributary of the Naryn River. a) Shaded drone SfM DEM overlain on shaded satellite stereo-DEM. Cyan dot shows the location of the fault exposure (d,e). Red triangles point ot the fault scarp. Inset: Shaded elevation map from stereo-DEM showing the site location (white box), relative to the Naryn River. b) View of the scarp, traced by the white triangles, in the field. c) Section view of the terrace deposit, highlighting the loess cap of the terrace gravel and the collected sample (KGZ18-19). d) Photo showing the thrust contact between the terrace gravel deposits and the hanging wall loess unit. e) Interpretative log of stratigraphic units and faulting in (d).

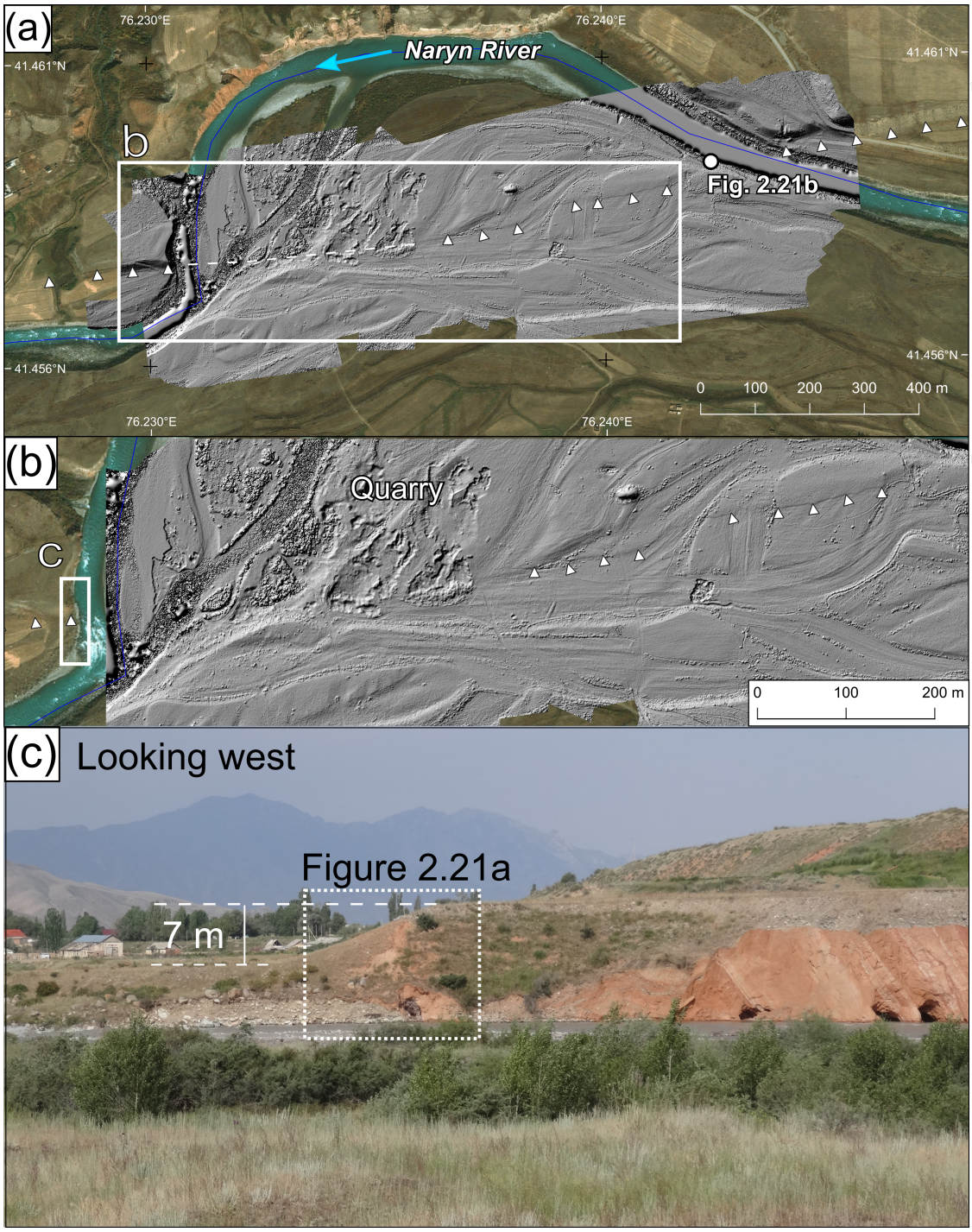


Figure 2.20: The Dobulu scarp in eastern Naryn, to the south of the river. a) Shaded drone DEM overlain on Bing satellite imagery. White triangles point to the scarp showing the trace of the Naryn fault that crosses the river. The dashed white line is the inferred continuation of the fault between the mappable fault scarps. b) Closer view of the scarp adjacent to the quarry area. No fault scarp is visible in lower terraces closer to the banks opposite to the fault outcrop in (c). c) Exposure of the Naryn fault in the field and a seven-meter high uplifted terrace. See Figure 2.21a for a closer view of the enclosed dotted section area.

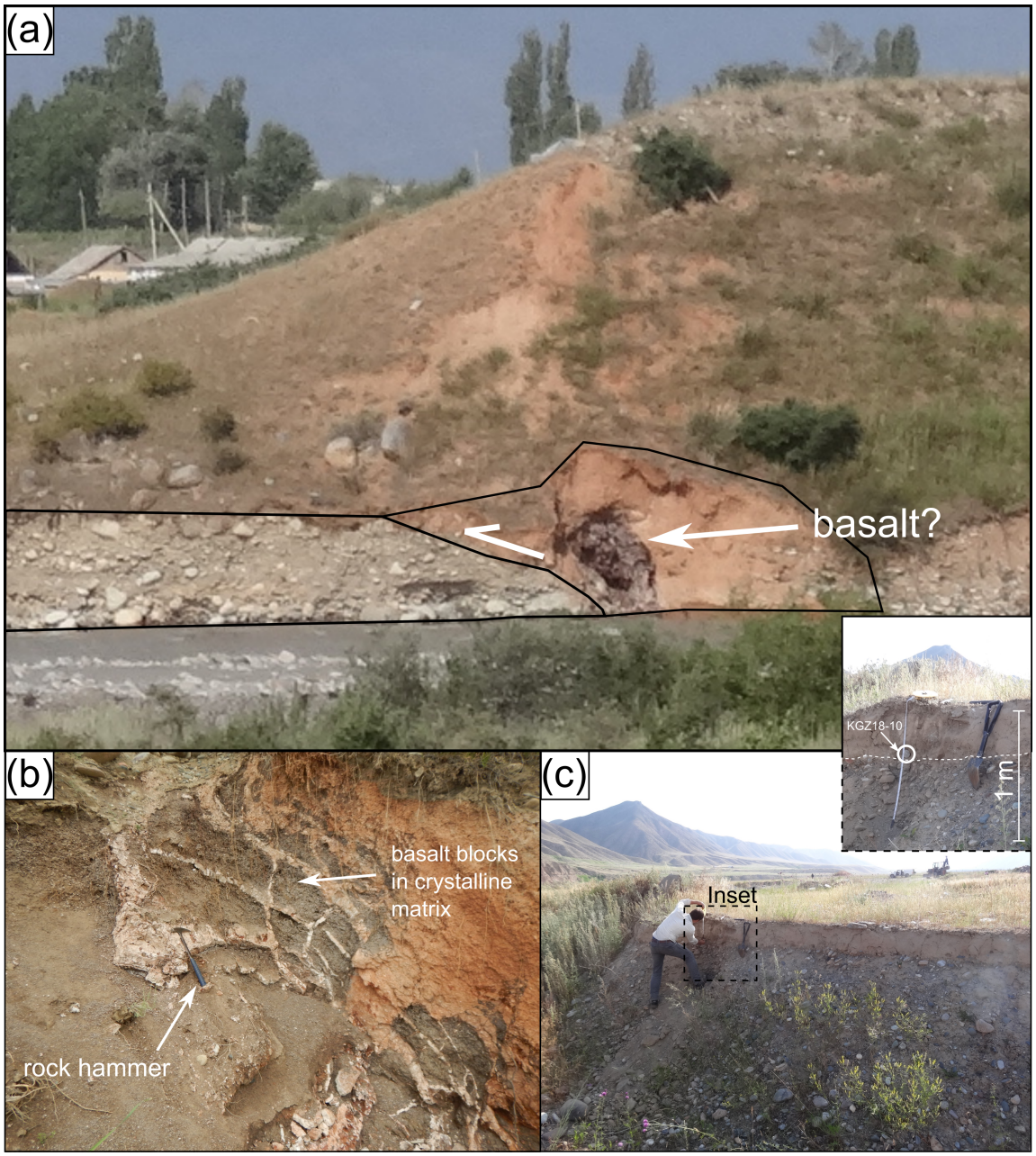


Figure 2.21: a) Closer view of the Naryn Fault exposure in Figure 2.20c, showing the thrusting faulting. b) Outcrop of basalt blocks in the fault zone, found on the eastern end of the quarry scarp (as located in Figure 2.20a). c) Deposits in the quarry on the upthrown side of the scarp. Inset: Location of the sample (KGZ18-10; 0.4 ± 0.7 ka, Table 2.2) collected for IRSL dating, 0.45 m from the top of the silt layer.

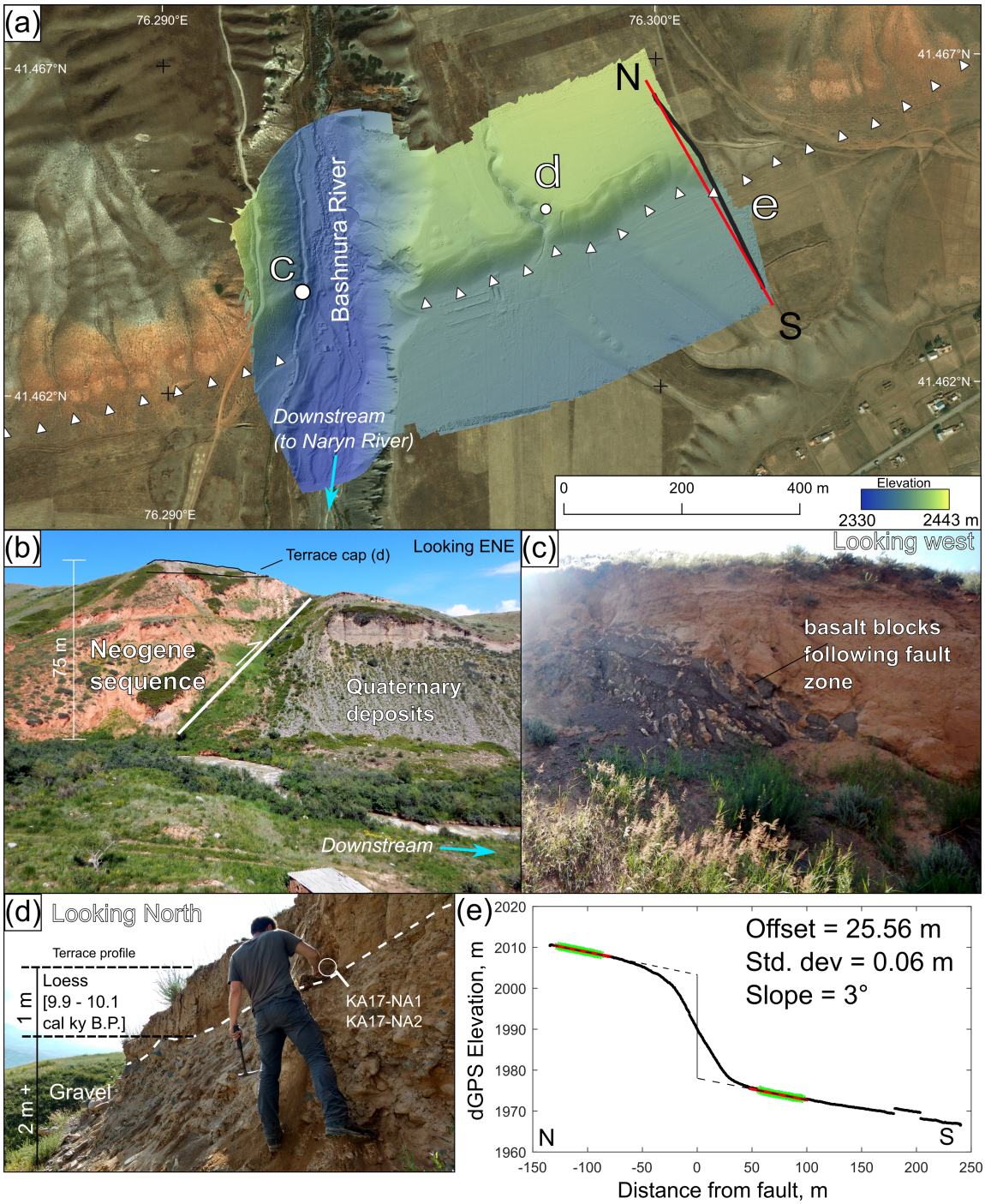


Figure 2.22: Fault scarp along the Bashnura River section. a) Shaded drone DEM overlain on Bing satellite imagery. White triangles point to the scarp showing the trace of the Naryn fault that crosses Bashnura River. Red line indicates projection N–S profile of dGPS survey points (black) across the terrace scarp. b) Section view of the Naryn fault from (c), showing the thrusting of the Neogene sequence over the Quaternary deposits. c) Outcrop of basalt in the Neogene sandstone along the fault zone. d) Geologist collecting freshwater shells from the loess cap of the terrace gravel overlying the uplifted Neogene strata. Located along a gulley in the hanging wall side of the fault, as shown in (a). e) Elevation profile of the cumulative scarp from a dGPS survey. Green indicates points used to fit the upslope and downslope surfaces used to fit the lines representing the offset surface (red).

2.5 Discussion

2.5.1 Seismogenic faults in the central Tien Shan and potential seismic hazard

The high-resolution imagery and DEMs provide an improved picture of the nature of ongoing deformation in the central Tien Shan (Figure 2.23). Our paleoseismic investigation along the scarps show that there is no record of surface slip later than ~1,400 years ago north of the Karkara (Kazakhstan). In Naryn, the fault exposure in Tash-Bashat provides convincing evidence of at least one meter of slip postdating ~4,200 years ago. Dating of the colluvial wedge on the same exposure needs to be constrained better, though the preliminary age provides an indication that the slip event is ~4,000 ago. Another upper limit age is the ~400-500 year-old offset quarry terrace in Dobulu if the offset in the two locations are due to the same event, given possible variability of along-strike surface rupture of faults. Alternatively, the younger age may indicate a later event. In any case, we did not find any evidence of offset in lower terraces continuous with our youngest offsets, which would otherwise be an indicator of surface creep on the faults that we have dated.

The extent of the fault scarps in Karakudzhur and Naryn and their semblance to known ruptures associated with thrust faulting earthquakes in the Tien Shan (e.g., *Bogdanovich et al.*, 1914; *Ghose et al.*, 1997; *Arrowsmith et al.*, 2016; *Ainscoe et al.*, 2019) and globally (e.g., *Philip et al.*, 1992; *Kaneda et al.*, 2008), suggest that we can expect these faults to be the source of surface rupturing earthquakes. If the dated offsets in Naryn represent the most recent earthquakes, the long period of quiescence is a manifestation of the slow deformation in intracontinental regions (e.g., *Grützner et al.*, 2017).

Empirical relationships between fault rupture parameters and earthquake magnitude suggest that the faults in Karkara, Karakudzhur, and Naryn could be the

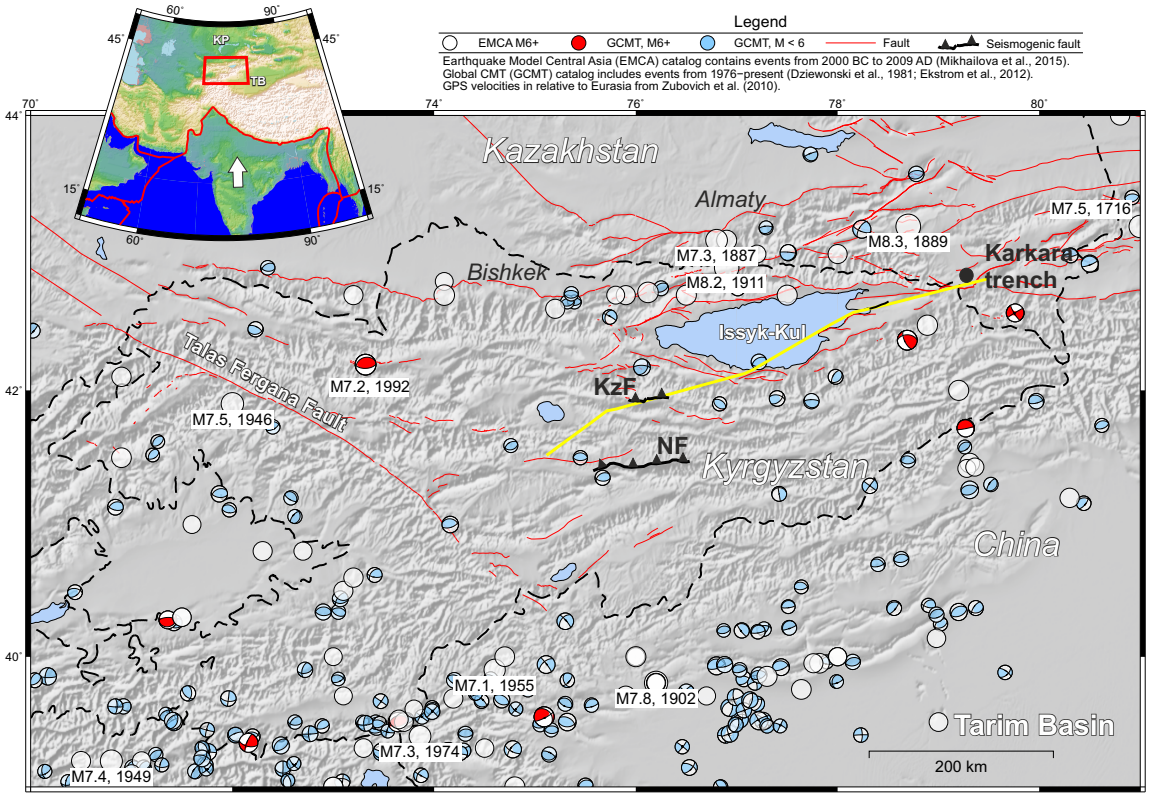


Figure 2.23: Similar to Figure 2.1, but now showing the faults explored in this study to be potential sources of earthquakes with magnitudes ≥ 6.7, but far from any known historically- or instrumentally-recorded events with magnitude > 6 (white circles and red focal mechanisms). KzF: Karakudzhur Fault. NF: Naryn Fault. Also shown is the location of the paleoseismic trench in Karkara. Yellow line is the 'E-M line' (from *England and Molnar*, 2015) referenced thorughout the main text.

potential sources of earthquakes unknown from the existing historical record. According to the linear scaling model between surface rupture length (L_E) and slip rate (S_F) with moment magnitude (M_w) by *Anderson et al.* (2017), where,

$$M_w = 5.12 + 1.15 \log L_E + 0.264 \log \frac{S_F}{1.1}, \tag{2.1}$$

for reverse faults, a 40-km long rupture on the Karakudzhur Fault (the whole trace of the fault) could result to a $M_w \approx 7.1$ to 7.2 earthquake (using the minimum and maximum slip rates in *Campbell et al.*, 2019, resepctively). Similarly, rupturing of the whole 75-km long Naryn Fault can result to an earthquake of $M_w \approx 7.4$. If

we assume a shear modulus of 30 GPa, seismogenic thickness of 20 km (based on seismicity in the Tien Shan; *Sloan et al.*, 2011), and constant 45° dip on the Naryn fault, 1-meter average slip (based on the paleoseismic exposure in Tash-Bashat) on the fault is equivalent to the slip in a M_w 7.2 event.

For the fault in Karkara, our only offset measurement is in the trenchwhere the inferred slip of ∼0.5 m, may be from a seismic rupture that generated a M_w = 6.7 earthquake, based on the magnitude–average displacement equation for reverse faults in *Wells and Coppersmith* (1994). While exceptions to regressions between earthquake magnitude and rupture parameters are not uncommon (e.g., *Ainscoe et al.*, 2019; *Rimando et al.*, 2019), these estimates give an indication of the potential seismic hazard to surrounding regions.

2.5.2 Distributed shortening across intermontane basins

The geomorphic indicators of deformation in eastern Issyk-Kul and western Naryn suggest distributed deformation along series of thrust faults. Both of these basins are estimated to have several kilometers of Cenozoic sedimentary infill (*De Batist et al.*, 2002; *Buslov et al.*, 2007). This likely promotes thin-skinned type deformation on basement-involved or shallow decollément-type thrust faulting in the middle of the basin, similar to the basinward propagation of low-angle splay faults faulting into foreland fold-and-thrust belts and orogens (e.g., *Davis et al.*, 1983; *Selander et al.*, 2012; *Pfiffner*, 2017).

Elastic dislocation modeling by *Goode et al.* (2011) suggest that the creeping blind thrusts in western Naryn accommodate most of the internal shortening. We can speculate that the deformation in eastern Issyk-Kul might be a similar mechanism given their shared basin characteristics; however, we are unable to constrain whether individual faults in Issyk-Kul are creeping or not with the existing GPS data and field observations. Nevertheless, Profile I–I' in Figure 2.3 shows that folds related to

thrust faults in the middle of the basin—the Cholpon and Tyup thrusts–may each accommodate between 1 to 1.5 mm/yr of shortening, based on the velocity gradient across stations TYUP, NTP4, and SRB4. Combined, they account for at most two-thirds of the shortening rate across Issyk-Kul basin as well as on the Karkara Rangefront in the east. The rest of the shortening in Issyk-Kul is accommodated on the range bounding faults (Main Terskey Fault and Kungey Fault).

On the other hand, faulting in the interior of narrow contractional basins appears to be accommodated mostly on the thrust fronts in the basin interior. As discussed in Section 2.4.5, the late Quaternary shortening on the Naryn Fault in eastern Naryn accounts for 65% to 85% of the geodetic shortening rate (estimated from the western side of the basin). *Campbell et al.* (2019) present a similar case where the the Karakudzhur Fault takes up most of the shortening in its basin (between 2.3 to 5.3 mm/yr late Quaternary shortening on the fault). Balanced cross-sections in *Goode et al.* (2011) show that the Naryn Fault forms part of the low-angle splay of the main range-bounding fault. From our mapping of fault scarps, the along-strike continuity and extent of the Naryn Fault indicates that shallow thrust faulting in the basin interior has been more active recently than on the Cenozoic-Paleozoic contact along the Jetym Rangefront. The scarp of the extant rangefront does not appear to be that of a straightforward north-dipping reverse fault on the surface, which may indicate complex slip partitioning due to reactivated oblique slip at depth (e.g., *Selander et al.*, 2012).

2.6 Summary and conclusions

Our combined geologic and geodetic exploration in the central Tien Shan reveals that the apparent 'creep' signal in the GPS velocity field mapped by *England and Molnar* (2015), and further by (*Mackenzie et al.*, 2018) in Karkara, near the eastern Kazakh-Kyrgyz border, does not appear to be clear in the intermontane basins of

the Tien Shan. Instead, the shortening gradient in the wide basins of Issyk-Kul (3–5 mm/yr over 50 km) and Naryn (3 mm/yr over 30 km) appear to be distributed across multiple Quaternary faults. We document the evidence of faults in these basins using high-resolution digital elevation models and dating, and find that thrust faults in the narrower basins in Karakudzhur and Naryn have relatively young and fresh-looking surface ruptures. The Karakudzhur and Naryn faults may be sources of M_w ~7 earthquakes (see also *Campbell et al.*, 2019, for the Karakudzhur Fault). Instead of a simple structure that creeps to the surface, the gradient in the velocity profiles in *England and Molnar* (2015) probably reflects regional creep or aseismic contraction in the lithosphere that variably translates to both aseismic and seismogenic deformation in the shallow crust.

The contrast in the inferred mode of shortening in different sections of the Naryn basin highlight how Holocene shortening in the narrow, eastern side of the basin involves strain accumulation in the seismogenic zone, while faults in the basin-interior of the wider, western side may be creeping (*Goode et al.*, 2011). Detailed studies on the active deformation and basin stratigraphy need to be done as indicators of active deformation on faults in wide basins may be buried in sedimentary deposits, leading to underestimation of potential seismic hazard.

Chapter 3

Conjugate blind and surface fault ruptures of the October–December 2019 southern Mindanao seismic sequence due to shallow crustal heterogeneity

3.1 Introduction

In the rapidly deforming plate boundary setting of the Philippines, a series of four moment magnitude (M_w) 6.4 to 6.7 earthquakes, within a 30 km radius, struck the southern Mindanao island in October and December 2019 (Figure 3.1a). The first three events–October 16th (10/16) M_w 6.4, 10/29 M_w 6.6, and 10/31 M_w 6.5–have epicenters in the province of Cotabato. The latest, on December 15th (12/15) M_w 6.7 occurred in the neighboring Davao del Sur province (Figure 3.1b). While some of the largest instrumental earthquakes in the Philippines are known to be from

the Cotabato subduction zone, the late 2019 seismic sequence includes the strongest known upper-plate onshore earthquakes in almost a century on the island. Focal mechanism solutions of the four earthquakes in the sequence suggest NW-striking and NE-striking nodal planes. Regional NW-SE faults in the vicinity (*Pubellier et al.*, 1991, 1994) might suggest similarly trending sources for the earthquakes, but deformation maps from interferometric synthetic aperture radar (InSAR) data suggests that the rupture geometry is complex (*Li et al.*, 2020, and also this work). Recent maps from the Philippine Institute of Volcanology and Seismology (PHIVOLCS) show discontinuous traces of NW- and NE-striking faults in the epicentral area. However, published information on these faults is non-existent, hence, the source of the earthquakes and their relationship to regional tectonics are poorly understood.

In this paper, we constrain the geometry and kinematics of slip of the rupturing faults in the October–December 2019 sequence using ALOS-2 and Sentinel-1 InSAR observations. Along with parameters derived from body waveform modeling and field investigation, we present evidence for surface rupturing that has not been previously reported. Mindanao is a 500 km wide island in a tropical setting where numerous structures accommodate the convergence of the Philippine Sea Plate and the Eurasian Plate. However, published slip partitioning analysis is based on very sparse geodetic data (see *Rangin et al.*, 1999; *Rangin*, 2016), though the complex structural manifestation of continental–island arc collision on the island has been the subject of several earlier studies (*Rangin and Silver*, 1990; *Pubellier et al.*, 1994; *Quebral et al.*, 1996). With satellite InSAR, imaging earthquake deformation in various settings has become ubiquitous, thanks to the global coverage and complementary capabilities of different satellites (*Simons and Rosen*, 2007; *Elliott et al.*, 2016). Our ability to map fault geometries from earthquake ruptures has vastly improved with the spatial coverage afforded by satellite-based geodesy, especially with multi-fault ruptures (e.g., *Hamling et al.*, 2017), including the cross-fault rupture in the 2019 Ridgecrest

earthquakes (California, USA) (e.g., *Barnhart*, 2017). *Li et al.* (2020) have suggested a conjugate rupture for the 2019 southern Mindanao sequence based on Sentinel-1 data only. A combined analysis with ALOS-2 data, as we present in this study, provides unprecedented detail on the rupture location of the 2019 sequence, which provides new insight to the mechanics of the distributed deformation.

3.2 Regional tectonic setting

The present-day tectonics of the Philippines involves the interplay of rapid deformation along a broad plate boundary zone and a complex geologic history (*Rangin*, 1991; *Aurelio et al.*, 2013). The Sundaland microcontinent began rifting from the southeastern margin of Eurasia at the beginning of the Cenozoic and started to collide with Philippine island arcs in the Miocene (*Taylor and Hayes*, 1980; *Pubellier et al.*, 1991; *Hall*, 2002). Evidence of this collision exists in suture zones exposed in the central Philippines and in Mindanao (e.g., *Yumul et al.*, 2004). At present, with the oblique convergence of the Philippine Sea Plate (PSP) and the Eurasian Plate (EU) (*DeMets et al.*, 2010) (Figure 3.1a), strain is thought to be mostly partitioned on the oppositely-verging subduction zones—to the west and east of the archipelago—and the 1,200-km long left-lateral Philippine Fault (*Barrier et al.*, 1991; *Aurelio*, 2000b). While convergence rates along individual subduction zones are poorly understood, kinematic and geodetic studies show that the Philippine Fault slips at around at 2–3.5 cm/yr (*Barrier et al.*, 1991; *Duquesnoy et al.*, 1994; *Hsu et al.*, 2016).

The 2019 earthquake sequence occurred in the Cotabato Basin, a triangular basin in south central Mindanao. Around 100 km to the east, the southern segments of the Philippine Fault has been the source of surface rupturing earthquakes (e.g., on the Surigao segment *Perez and Tsutsumi*, 2017; *PHIVOLCS*, 2018). West of the basin, there is subduction along the Cotabato Trench, with the latter being the source of the 1976 Moro Gulf earthquake, a deadly tsunamigenic event with an

estimated moment magnitude (M_w) of 8.1 (*Stewart and Cohn*, 1979; *Beck and Ruff*, 1985). Onshore, the NW-SE striking Sindangan-Cotabato Fault marks the inferred boundary between the continental block (Zamboanga Peninsula, Kulaman Plateau, and Sarangani Peninsula) and the Philippine arc (*Pubellier et al.*, 1991) (Figure 3.1a). However, while the Sindangan Fault offers clear geological and tectonic evidence of the suturing (*Pubellier et al.*, 1994; *Yumul et al.*, 2004), the Cotabato Fault is much more poorly understood. *Pubellier et al.* (1994) suggest that NW-SE trending drainage anomalies in the low-lying Cotabato Basin correlate with the tectonics of the Sindangan Fault, and that the perpendicular NE-SW trends reflect blind normal faulting that accommodates subsidence of the basin. The mantling of Quaternary volcanic deposits across central Mindanao and the generally flat Cotabato Basin both make mapping offsets challenging, on top of the tropical environment. As the largest known onshore earthquakes in southern Mindanao, the events in the late 2019 earthquake sequence provide an opportunity to study the kinematics of the faults in the area.

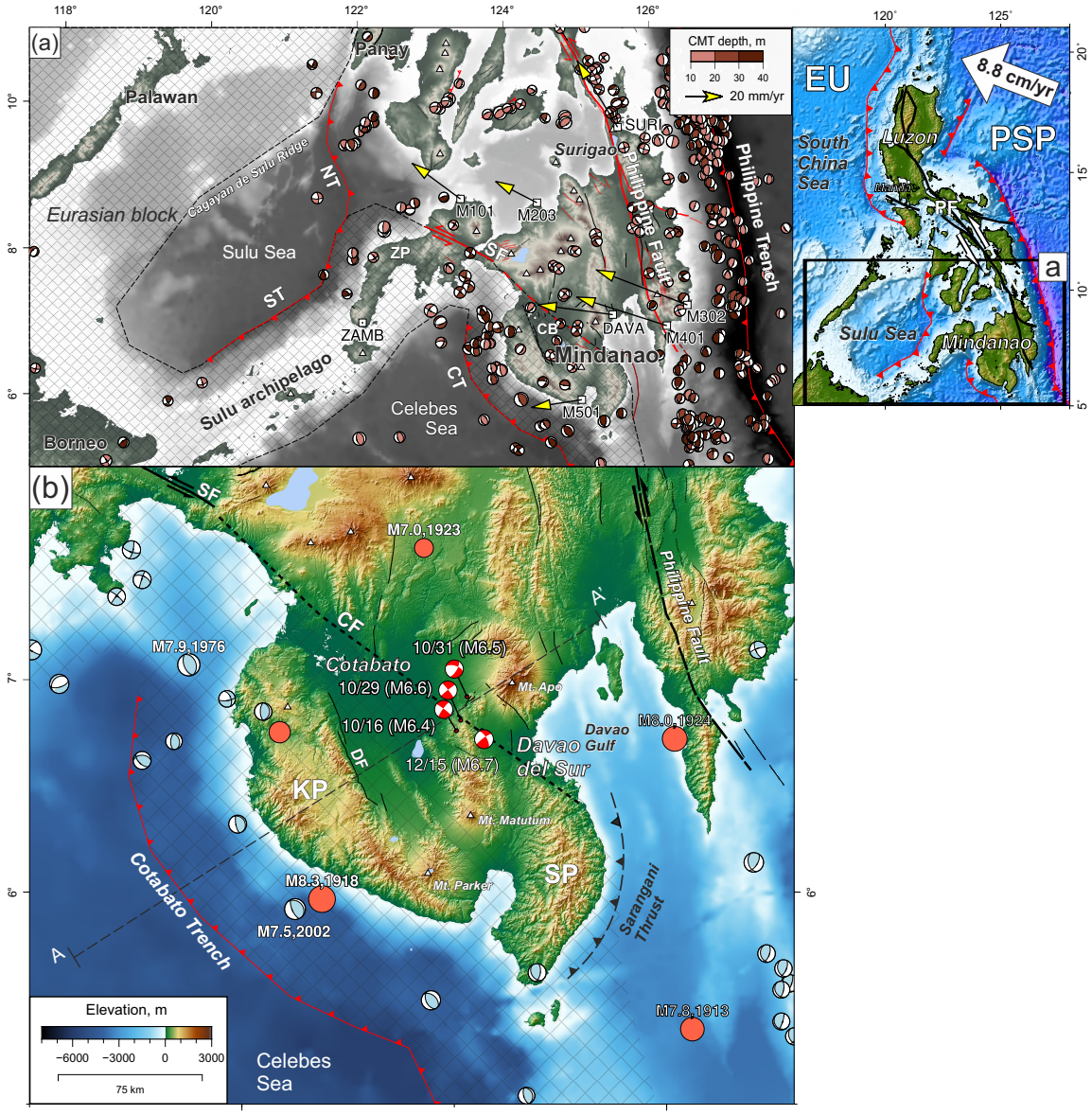


Figure 3.1: a) Tectonic setting of Mindanao island, with the dotted area highlighting the microcontinental terrane of Eurasian affinity, from Palawan island, Zamboanga peninsula (ZP), Kulaman Plateau (KP), and Sarangani Peninsula (SP), and major faults in red. Sawtooth indicate thrust faults, including the subduction zones (Cotabato Trench, CT; Sulu Trench, ST, and; Negros Trench, NT). Onshore strike-slip faults include the Philippine Fault, and the Sindangan (SF), Daguma (DF), and Cotabato Faults (CF) marking the inferred boundary of the continental block with the Philippine Mobile Belt (*Rangin*, 1991; *Pubellier et al.*, 1991). Yellow vectors represent GPS velocity data from (*Aurelio et al.*, 1998). Inset: the location of Mindanao with respect to the Philippine Sea Plate (PSP) and Eurasia (EU). Black rectangle shows extent of (a). b) Seismotectonics of southern Mindanao, with the focal mechanisms of the $M_w > 6$ earthquakes in the October 2019 sequence (from Global CMT, *Ekström et al.*, 2012; *Dziewonski et al.*, 1981, darker shades indicate later events). Also shown are historical earthquakes with $M_w > 7$ from the USGS catalog (orange circles) and Global CMT (light blue focal mechanisms), and the three closest Quaternary volcanoes (Mt. Apo, Mt. Matutum, and Mt. Parker). Shaded digital elevation and bathymetry models are from SRTM 1-arc second topographic data (*NASA*, 2013) and General Bathymetric Chart of the Oceans (*GEBCO*, 2020), respectively.

3.3 Body-wave seismology

To estimate the focal mechanism, centroid depth, moment, and source time functions of the events, we performed a joint inversion of teleseismic *P* and *SH* waveforms to obtain the best-fitting focal parameters of the October–December 2019 earthquakes[1]. Seismograms from stations at epicentral distances of 30-90° were band-pass filtered to 15-100 s and converted to the response of a WWSSN (World-Wide Standardized Seismograph Network) long-period seismometer. These were then inverted using the MT5 program of *Zwick et al.* (1994) (based on the algorithm of *McCaffrey and Abers*, 1988; *McCaffrey*, 1991). The method is well established and described elsewhere (e.g., *Molnar and Lyon-Caent*, 1989; *Maggi et al.*, 2000; *Craig et al.*, 2014). Stations were weighted to account for the uneven distribution of their azimuths, and *P* seismograms were given double the weight of *SH* seismograms to account for their relative amplitudes. Due to the absence of local information of the velocity structure, we use a half-space velocity model with Vp = 6.5 km/s, Vs = 3.8 km/s, and a density of 2800 kg/m3. While this is likely to be fast relative to the uppermost crustal layers, it represents a good average for the bulk crustal properties, and at the frequency range used, the waveforms are not sensitive to short-length scale variations in the shallow velocity structure.

As summarized in Table 3.1, the best-fitting parameters show strike-slip moment tensors for all earthquakes, with nodal planes of all events in the sequence striking along the NW–SE and NE–SW. They are in general agreement with GCMT parameters (e.g., *Dziewonski et al.*, 1981; *Ekström et al.*, 2012). The primary difference is in the depth of the October 31st (10/31) event, which is 7 km in our inversion and 12 km in the GCMT. This difference is likely to be due to our use of body waveforms in the inversions, which are more sensitive to the depth than surface waves. The GCMT algorithm also imposes a minimum depth of 12 km (*Ekström et al.*, 2012). In con-

[1]Inversions done by Alex Copley, University of Cambridge

trast, our solution obtains the same 12 km depth for the December 12th (12/15) event, and the October 16th (10/16) and October 29th (10/29) earthquakes are also consistently at 17 and 18 km, respectively. The P and T directions from the focal mechanisms strike consistently E–W and N–S, respectively.

Table 3.1: Source parameters of the October–December 2019 southern Mindanao earthquakes from the PHIVOLCS and Global CMT catalogs, and from body waveform inversion (this study).

		M^a	$M_0{}^b$	Lat^c	Lon^d	d^e	Strike 1	Dip 1	Rake 1	Strike 2	Dip 2	Rake 2
	PHIVOLCS	6.3	-	6.76	125.01	9	-	-	-	-	-	-
10/16	GCMT	6.4	5.36	6.86	125.01	17.1	307	81	3	217	87	171
	This study	**6.4**	**4.78**	**-**	**-**	**17**	**307**	**85**	**17**	**217**	**87**	**175**
	PHIVOLCS	6.6	-	6.81	125.03	7	-	-	-	-	-	-
10/29	GCMT	6.6	1.03	6.87	125.05	18	323	81	5	232	85	171
	This study	**6.6**	**8.02**	**-**	**-**	**18**	**322**	**86**	**3**	**231**	**87**	**176**
	PHIVOLCS	6.5	-	6.92	125.06	8	-	-	-	-	-	-
10/31	GCMT	6.5	6.30	6.98	125.1	12	303	73	-23	40	68	-162
	This study	**6.5**	**5.13**	**-**	**-**	**7**	**286**	**59**	**333**	**31**	**67**	**-146**
	PHIVOLCS	6.9	-	6.76	125.13	9	-	-	-	-	-	-
12/15	GCMT	6.7	16.0	6.72	125.14	12	320	74	13	226	77	163
	This study	**6.7**	**12.5**	**-**	**-**	**12**	**329**	**66**	**12**	**234**	**79**	**156**

[a]Moment magnitude (M_w) except for PHIVOLCS, which reports surface wave magnitudes (M_s).
[b]Seismic moment in $\times 10^{18} Nm$.
[c,d]North latitude and east longitude location of centroid, respectively.
[e]Centroid depth in kilometers.

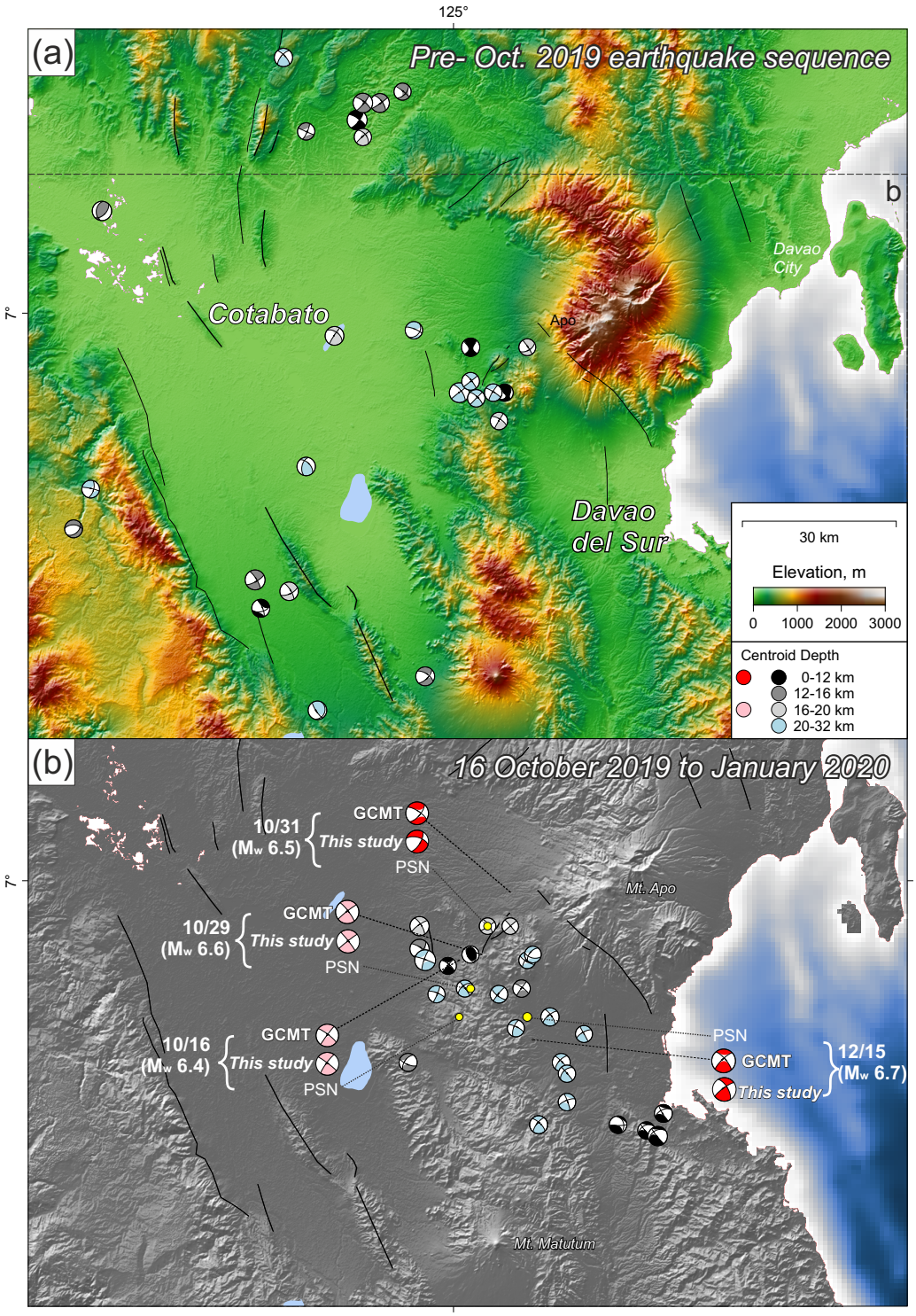


Figure 3.2: Seismotectonics of the Cotabato basin and comparison of focal mechanism solutions. a) Global CMT (GCMT) solutions of pre-October 2019 earthquakes overlain on a shaded elevation model of the Cotabato Basin. Compressional quadrants of focal mechanisms are white, while extensional quadrants are colored according to depth (darker colors indicating shallower depths). Moment tensors of the late 2019 sequence are highlighted as shades of red. Also shown are the Pliocene-Pleistocene antiforms (thicker lines: hinge), and prominent lineaments (thinner lines). b) Same as (a), but showing focal mechanisms of the late 2019 sequence (shades of red) from this study and the GCMT catalog, and the aftershocks up to 31 January 2020 from GCMT. Yellow circles are the epicentral locations from the Philippine Seismic Network (PSN) operated by PHIVOLCS. Outside of the events in the sequence, all earthquakes shown have M_w ranging between 4.7 and 5.8.

3.4 InSAR observations of rupture geometry

We generated a set of interferograms and line-of-sight (LOS) displacement maps from ALOS-2 and Sentinel-1 data to measure the coseismic displacement field and identify potential surface ruptures. As summarized in Table 3.2, we have data from opposing look directions for all earthquakes in the sequence; however, there is no SAR acquisitions from any satellite between the 10/29 and 10/31 events. For the Sentinel-1 data, we used the GAMMA InSAR processing software from coregistration to unwrapping, with an airborne SAR-derived digital terrain model from the Philippines' National Mapping and resource Information Authority (NAMRIA) for topographic phase removal and geocoding (as in *Dianala et al.*, 2020). The ALOS-2 data was processed with GSISAR (e.g., *Morishita*, 2019) and unwrapped using SNAPHU (*Chen and Zebker*, 2002)[2]. We applied Generic Atmospheric Correction Service (GACOS; *Yu et al.*, 2018) corrections to remove weather model-based tropospheric perturbation from the SAR data. Additionally, an ionospheric phase component was estimated and removed from the ALOS-2 data, using a split-spectrum method (*Gomba et al.*, 2016). L-band SAR data (e.g., from ALOS-2, $\lambda \approx 24$ cm) is likely to be more distorted by the ionosphere compared to C-band data (e.g., Sentinel-1, $\lambda \approx 5$ cm) (*Gomba et al.*, 2016). While the final interferograms (Figure 3.3) appear to have residual non-tectonic noise, the earthquake deformation signals are generally distinguishable and not correlated to topography. We also mask out areas of low coherence. The ALOS-2 InSAR data have generally good coherence, allowing us to infer the trend of fault ruptures. The Sentinel-1 data, especially the 12-day baseline interferograms, have relatively poorer coherence near the epicenters.

The wrapped and unwrapped interferograms suggest that both NE- and NW-trending faults ruptured in the October–December 2019 earthquake sequence. With

[2]Processing of ALOS-2 interferograms done by Yu Morishita, GSI Japan, former COMET Visting Fellow.

the ALOS-2 data, we can trace possible NE-trending ground ruptures in the late October interferograms of the 10/29 and 10/31 events, which we investigated in the field (see Section 3.6). Closely-spaced fringes and phase discontinuities are present near the 10/31 epicenter (Figure 3.3f), with unwrapped displacements showing around 45 cm of offset in the ALOS-2 ascending track (A136) LOS across the discontinuity. In Figure 3.3h, blue areas indicate movement away from the satellite (a combination of eastward movement and subsidence) and the red areas show displacement in the opposite direction (westward motion and uplift), while relative displacements in the opposing LOS of the Sentinel-1 descending pass (D163) consistently in the opposite direction (Figure 3.3g). A closer view of the wrapped interferogram shows the location of the phase discontinuities just west of Mount Apo (Figure 3.5). The Sentinel-1 data does not show this due to decorrelation near the epicenter (Figure 3.3e).

It is unclear from the InSAR data alone if we can associate the surface ruptures with only one or both of the 10/29 and 10/31 events. *Li et al.* (2020) infer that both events are due to NE striking faults based on Sentinel-1 data only, with the 10/29 rupture west of the 10/31 event, in agreement with their respective epicenters. However, masking out low coherence areas makes inferring a possible fault orientation for the 10/29 event ambiguous with the Sentinel-1 data alone. In the ALOS-2 A136 wrapped interferograms, many small short wavelength signals are probably due to surficial environmental effects (e.g., landslides and liquefaction; *PHIVOLCS*, 2019). The broad fringe west of the closely spaced fringes across the possible surface rupture might be deformation due to the 10/29 earthquake (Figure 3.5b).

The 10/16 event registers as an elongated bullseye-like pattern in Sentinel-1 D163 and as a broad lobe in the ALOS-2 A136 interferograms (Figures 3.3a and 3.3b, respectively). None of the interferograms suggest that the 10/16 earthquake produced a ground rupture. D163 wrapped data shows an elliptical deformation lobe east of the epicenter, with up to 8 cm of displacement away from the satellite line-of-

sight (Figures 3.3a and 3.3c). The A136 unwrapped interferogram indicates up to 5 cm of displacement towards LOS north of the epicenter (Figures 3.3b and 3.3d). While the Sentinel-1 data suffers decorrelation near the epicentral area, likely due to dense vegetation, the ALOS-2 data has good coherence and shows that there are no distinct discontinuities on the surface deformation field. This suggests that slip did not rupture the surface. Determining the rupture strike just from the images of surface deformation of the 10/16 event is not straightforward due to the residual non-tectonic noise.

Interpreting the rupture geometry from the interferograms of the 12/15 event is less ambiguous, with the butterfly fringe pattern in the Sentinel-1 D136 and ALOS-2 A163 interferograms consistent with a NW-striking fault (Figures 3.3i and 3.3j, respectively). Unlike the data of the October events of similar temporal baseline (12 days), the deformation signal of the 12/15 earthquake is clearer in the Sentinel-1 ascending track InSAR (track 069) (Figure D.2). In any case, no interfergram shows clear evidence of the presence (or absence) of ground surface rupture, due to decorrelation near the epicenter. Nevertheless, the unwrapped interferogram suggest left-lateral slip with up to 60 cm of surface LOS displacement across oppositely displaced areas in A163 LOS (Figures 3.3j and 3.3l, respectively).

Table 3.2: Epochs of interferograms covering the October–December 2019 earthquakes in southern Mindanao, with track number indicated for each satellite track. Italicized date pairs indicate observations that are not considered in this study due to the predominance of atmospheric noise (Appendix D).

		Event date (moment magnitude)			
		10/16 (M_w 6.4)	**10/29** (M_w 6.6)	**10/31** (M_w 6.5)	**12/15** (M_w 6.7)
Sentinel-1	Descending (163)	10/14 - 10/26	10/26 - 11/07		12/13 - 12/19
	Ascending (69)	*10/14 - 10/26*	*10/26 - 11/07*		12/13 - 12/25
ALOS-2	Descending (24)	*10/14-11/11*			-
	Ascending (136)	10/05 - 10/19	10/19 - 11/02		12/14 - 12/28

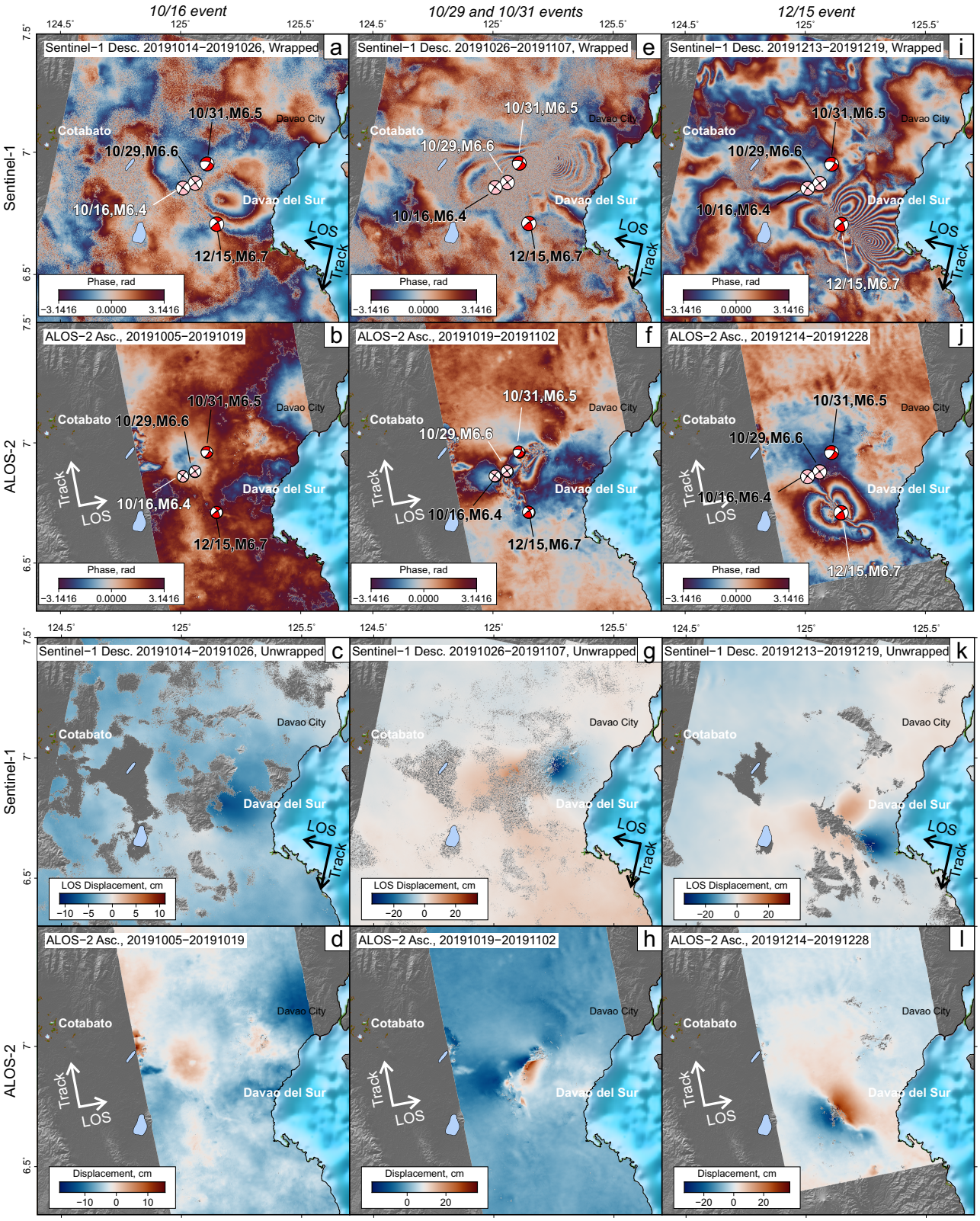


Figure 3.3: Sentinel-1 descending track 163 (D163) and ALOS-2 ascending track (A136) interferograms covering the October-December 2019 earthquake sequence. a-d) 16th October earthquake wrapped (a,b) and unwrapped (c,d) displacements. e-h) Same, but for late October earthquakes, and; i-l) for 15th December earthquake. For reference, focal mechanisms of source earthquakes are shown, with extensional quadrants colored red for events captured by the interferogram, and black or gray for preceding or succeeding events, respectively. Long arrow is the satellite flight direction (track) while the short arrow indicates the line-of-sight. Positive unwrapped displacement is movement towards the satellite.

3.5 Inversion for fault geometry from InSAR data

The surface deformation shown by the InSAR data provides compelling evidence for the rupturing of conjugate NW-SE and NE-SW faults, similar to the focal mechanism solutions. However, the noise in the interferograms imposes some ambiguity in inferring the fault orientation of the deeper 10/16 earthquake and the possibility of a surface rupture for the 12/15 event. To help us constrain the geometry of the source faults of these earthquakes, we combined the InSAR observations in a non-linear inversion for source parameters that takes into account the noise as weights in the modeling.

We used *Pyrocko/Grond* to perform a direct-search bootstrap optimization to sample a defined parameter space for a model with minimum misfit (`https://pyrocko.org`; *Heimann et al.*, 2018). The downsampled data and 'best-fit' model predictions are shown in Figure 3.4. The advantage with *Grond* is that while the sampling progressively converges to low-misfit regions, multiple minima in the parameter space can be sampled by parallel bootstrap chains, visualized as sequence plots, according to a 'high-score' list of evaluated models with low misfits (`https://pyrocko.org/grond/docs/current/method/index.html`). The data covariance, estimated empirically from the spatial correlation of the noise pattern in the interferograms (e.g., *Sudhaus and Jónsson*, 2009), are used as weights for the misfit calculation.

We set the algorithm to explore different configurations of uniform slip models similar to the nodal planes in the focal mechanism solutions (the bounds used are summarized in Table 3.3). To improve the efficiency of the inversions, we downsampled each InSAR dataset using a quadtree algorithm (*Jónsson et al.*, 2002). Further, we masked out data points that have obvious elevation-related and non-tectonic signals away from the epicenter and deformation lobes. We used a pre-calculated PSGRN/PSCMP Green's function (*Wang et al.*, 2003, 2006) of a layered

Table 3.3: Boundary and best-fitting parameters for the 10/16 and 12/15 earthquakes with the standard deviation in parentheses. More details on the distribution statistics are shown in Appendix E, Tables E.2, E.4, and E.3.

Parameter	10/16, free strike[a]		10/16, NE-strike forced		12/15	
	Bounds	Best-fit	Bounds	Best-fit	Bounds	Best-fit
depth[b], km	[2,10]	8.8 (0.9)	[1,10]	9.9 (1.2)	[0,5]	2.8 *(0.1*)*
length, km	[1,20]	19.3 (0.9)	[1,20]	8.1 (0.9)	[10,30]	18.0 (0.2)
width, km	[2,20]	7.2 (3.2)	[2,20]	16.6 (1.8)	[2,20]	13.6 (0.7)
slip, m	[0,2]	1.1 (0.3)	[0,2]	1.5 (0.3)	[0,2]	1.9 *(0.1*)*
strike, °	[200,340]	307 (1)	[180,270]	217 (2)	[290,340]	316 *(1*)*
dip, °	[60,90]	72 (3)	[60,90]	90 *(1*)*	[50,90]	69 (1)
rake, °	[0,180]	6 (1)	[0,180]	169 (3)	[-30,90]	9 *(1*)*

[a]Preferred model.
[b]Depth to the top of the fault.
*Rounded up to the nearest significant figure.

half-space based on CRUST2.0 (https://greens-mill.pyrocko.org/crust2_ib_static-149c71; Table E.1), with an average velocity structure similar to focal mechanism inversion (Section 3.3). We discuss below the results pertaining to the fault geometry, while the details of statistics of the sampling can be found in Appendix E.

For the 10/16 event, the best-fitting model is a NW-striking fault (307° azimuth) with one meter of left-lateral slip (6° rake), with the top of the fault at 9 km depth, 19-km long along-strike and 7-km wide down-dip, and dipping 72° to the NE (Figure 3.4a and b). The joint parameter distribution plots show a negative correlation between width and depth, slip and width, and a positive correlation between slip and depth across the parameter space, but higher values in all of them consistently show lower misfit (Figure E.1). The sequence plots of the inversion show that while a NW strike provides the best fit, the algorithm also narrowed down to a NE-SW fault that eventually had a higher misfit than the best-fit solution (Figure E.4). We conducted a test with narrower bounds for the strike to force the inversion to determine the best-fitting NE-striking fault geometry. This results to a model that largely predicts the InSAR displacements, with a uniform slip model that is 8 km long and 17 km wide down-dip (Table 3.3). We consider the NW-striking geometry

as our preferred model given the lower misfit in the less constrained inversion, and the aspect ratio of the NE-striking model also seems unlikely.

The modeling also returns a NW-trending fault for the 12/15 earthquake, with a strike, dip, and rake that are similar to the 10/16 model (316°, 69° to the NE, and 9°, respectively (Figure 3.4c and d). However, the depth to the top of the fault is much shallower (3 km). This corresponds with the seismological and InSAR observations. For both earthquakes, the model prediction in the Sentinel-1 descending track (D163) and ALOS-2 ascending track (A136) LOS displacement approximates the pattern and magnitude of deformation (Figure 3.4). There are some residuals in near-fault areas, which could indicate distributed slip not captured by the uniform slip model or turbulent atmospheric noise.

We are unable to derive a slip model for either the 10/29 and 10/31 events as none of our tests for these events converged to a solution. This is likely due to their combined signals in the available data. We further discuss the possible source parameters of the 10/29 and 10/31 earthquakes in Section 3.7.

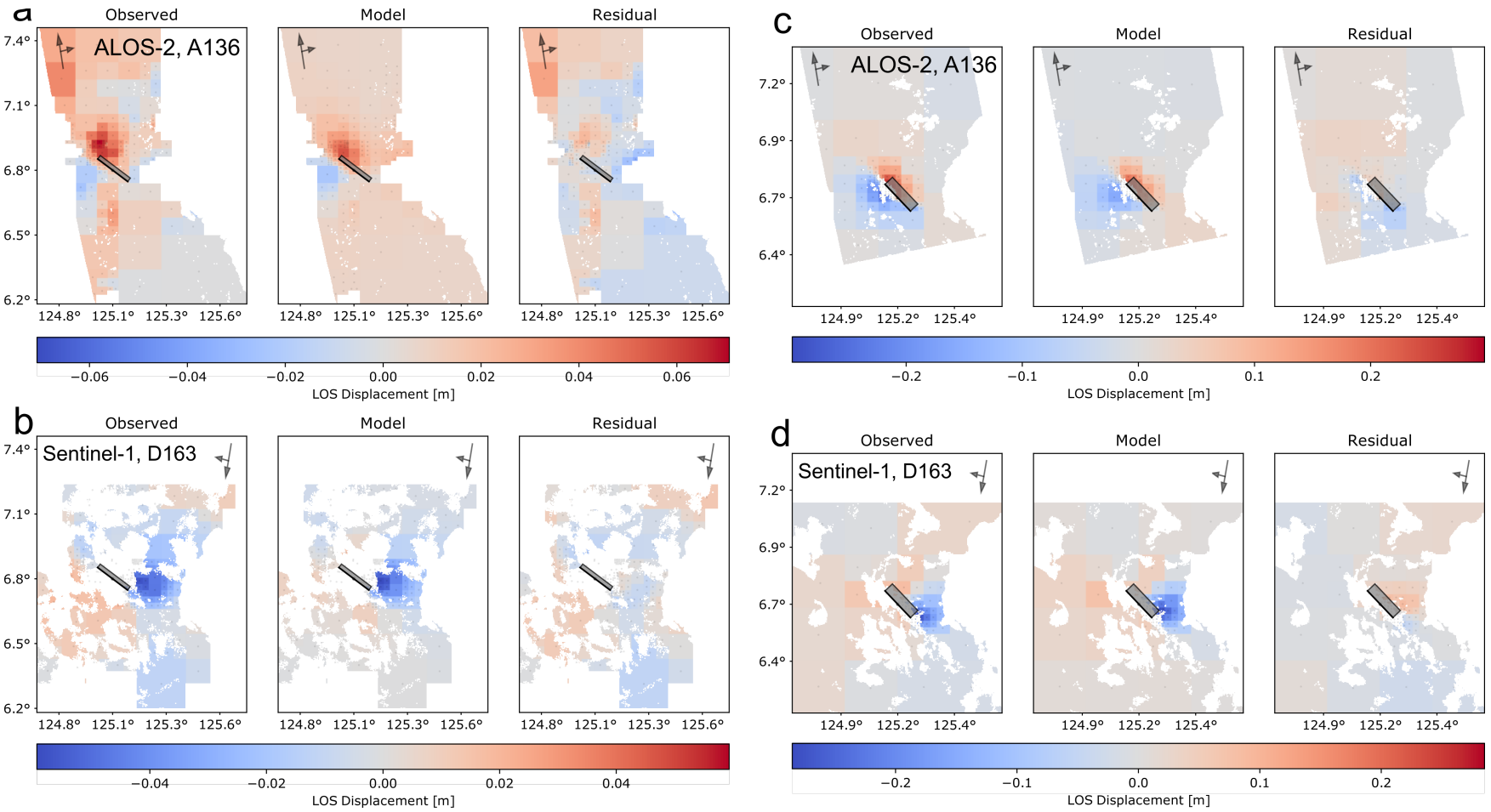


Figure 3.4: Data, model prediction, and residuals of the 'best-fit' uniform slip models for the 16 October M_w 6.4 earthquake source fault in (a) ALOS-2 ascending track 136 (A136), and (b) the Sentinel-1 descending track 163 (D163). (c-d) Same, but for the 15 December M_w 6.4 earthquake source fault in A136 and D163, respectively. Long arrows indicate path of satellite, and the arrow attached to it is the satellite line-of-sight. Positive displacement indicates movement towards the satellite.

3.6 Field evidence of surface rupturing

Guided by our interpretation of possible surface ruptures from the ALOS-2 InSAR data, we coordinated a reconnaissance field investigation in early November 2019 to investigate the ground deformation along the phase discontinuities[3].

From visiting several accessible sites in the rugged, densely vegetated volcanic terrain, a NE-trending zone of fissuring was found at Biangan village, on flat farmland near the eastern end of the possible ground rupture trace from InSAR (Figure 3.5). The fissures appeared to be spaced 1 to 4 meters apart and were mapped to be distributed along a 60-meter long zone generally parallel to the trace from InSAR. The pattern of fissuring, reconstructed with the help of an orthorectified drone photomosaic, evokes Riedel shears formed by right-lateral faulting from analog and natural examples (e.g., *Dooley and Schreurs*, 2012; *Lin and Chiba*, 2017); hence, given that they colocate with the InSAR observations, we associate the fissuring to earthquake rupture that reached the surface. Landslides and extensive surficial effects have been documented in surrounding areas as well, but no other surface rupture has been reported from the field thus far (*PHIVOLCS*, 2019).

[3]Thesis note: Field surveys were done by Richard Ybañez, Mahar Lagmay, and Mario Aurelio, in coordination with the thesis author, along with other team members from the University of the Philippines

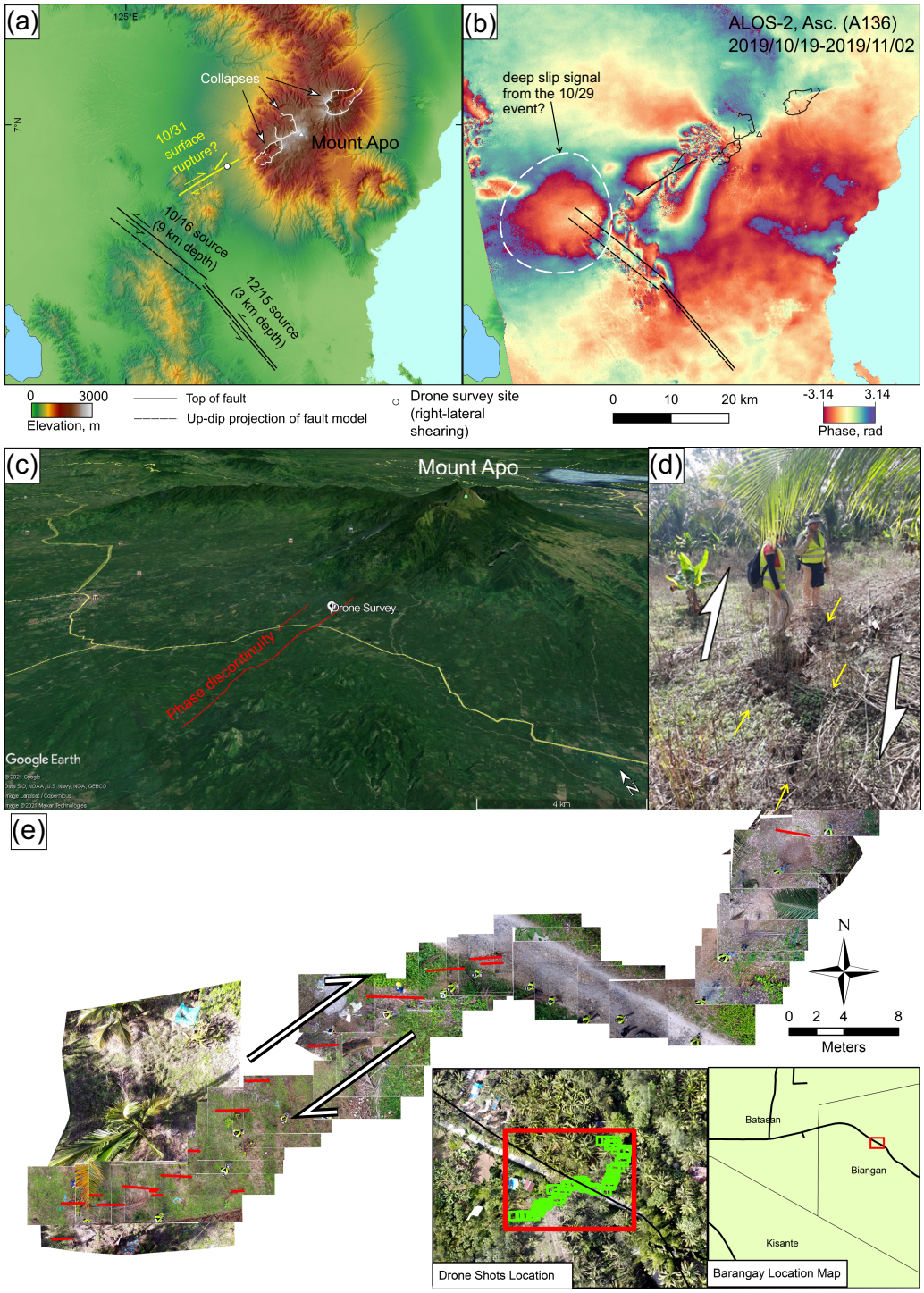


Figure 3.5: a) Extent of rupturing faults in the October–December 2019 sequence. Solid lines: location of fault top at depth based on the uniform slip models, projected to the surface. Dashed lines: up-dip surface projection of source faults. White hachures: sector collapses around Mount Apo. b) Same as (a), but overlain on the ALOS-2 ascending track 136 interferogram (spanning 2019 10/19 to 11/02). c) Perspective view of the location of the InSAR phase discontinuity/possible surface ruptures (red) and the drone survey (white marker) from Google Earth. 1.5x vertical exaggeration. d) Fissures (between yellow arrows) observed in the village of Biangan, resembling Riedel shears formed by a narrow zone of right-lateral faulting. Location: 125.1595°E, 6.9370°N. e) Photomosaic of drone imagery with fissures (red) as mapped from the field. Captured using DJI Mavic Air and Mavic Pro 2 drones. Uninterpreted high-resolution version is found in Appendix G.

3.7 Discussion

3.7.1 Locating surface and buried ruptures

Mapping of surface ruptures from previously unmapped faults after an earthquake in remote tropical areas is often challenging. For the case of the 2019 southern Mindanao sequence, the InSAR data has allowed us an opportunity to identify sites that were investigated in more detail in the field. We also encounter difficulty in obtaining a uniform slip model for the 10/29 and 10/31 earhtquakes due to of what may be combined signals of two earthquakes in the interferograms that span the two events; hence, we consider below the differences of parameters obtained from seismology to narrow down possible source parameters.

The depths for all earthquakes reported by PHIVOLCS are between 7-9 km, however the shallower centroid depth of the 10/31 event (7 km), compared to the 10/29 earthquake (18 km) supports the idea that the 10/31 earthquake is more likely to have slip that reached surface, and hence ruptured the ground. The deeper 10/29 event might correspond with the broad deformation lobe that can be seen southwest of the more closely-spaced fringes along the ground rupture (Figure 3.5b). The right-lateral NE-striking nodal plane of the 10/32 focal mechanism, and the correspondence of the InSAR observations with the orientation of the ground fissures (Section 3.6), both suggest that the dextral shear on the ground surface may be associated with the 10/31 event.

If we take into consideration the similarly deep centroid depths of the 10/16 and 10/29 events, the spatial wavelength of their respective wrapped phase signals should be similar, and differ only with the fault strike and rake (see Figure F.1 in Appendix F for forward models of the 10/29 deformation field using uniform slip models based on the focal mechanism nodal planes). Assuming a NE-trending rupture for the latter connects the 10/31 and 10/16 source faults (as in *Li et al.*, 2020), and suggests

that we have a case of blind and shallow slip on the NE conjugate fault.

3.7.2 Geological controls of seismic slip

Depth-varying lithology

If the uniform slip models represent the average slip area, the 10/16 and 12/15 earthquakes appear to have ruptured a contiguous fault along-strike, i.e., the same fault but at different sections (Figure 3.5a). The 12/15 rupture is just south of the 10/16 event, and they have similar azimuths (316° for the former and 307° for the latter) and dips (within 3° of each other; see Table 3.3). Models by *Li et al.* (2020) also reflect the southward kink in the fault with the 12/15 fault rupture and the depth difference in the distributed slip between the two events. If slip from both earthquakes did occur on different segments of the same fault, the change in strike could have played a role in the spatio-temporal distribution of seismic slip as fault bends may impede seismic slip (e.g., *Wesnousky*, 2008; *Biasi and Wesnousky*, 2017, and references therein).

The shallow slip deficit in earthquakes is sometimes attributed to the rate-strengthening friction at the shallowest parts of fault zones (*Scholz*, 1998). Additionally, buried coseismic slip also tends to get distributed on overlying sedimentary cover (e.g., *Zinke et al.*, 2014). For the northwestward fault rupture, we find it notable that while the 12/15 event involved slip from 3–16 km down-dip, the 10/16 earthquake slip was confined from 9–16 km down-dip. This variation in depth extent of seismic slip may be related to the heterogeneous local geology. In the Cotabato Basin, the Cretaceous basement is overlain by five-kilometer thick Cenozoic marine sedimentary sequences (*Ranneft et al.*, 1960; *Tamesis*, 1981; *Pubellier et al.*, 1994; *Aurelio*, 2000a) (Figure 3.6). The GCMT catalog shows that most events with M_w 4.7 and greater, including aftershocks of the late 2019 sequence, especially those with strike-slip focal mechanisms, have centroid depths greater than 16 km (light colored

FMS in Figure 3.2). Whether the source of the smaller earthquakes are the same or different from the late 2019 sequence is unknown; nevertheless, the depths support the idea of the confinement of faulting to the basement. The shallower fault top of the 12/15 earthquake may indicate a shallowing of the basement towards Sarangani Peninsula (Figure 3.1).

The depth-variation might also apply to the NE-trending conjugate fault. However, unlike the NW trends,northeasterly structures are less prominent in the vicinity of the earthquakes. While *Pubellier et al.* (1994) suggest blind northeasterly normal faulting that accommodates the formation of the basin, most appear strike-slip (Figure 3.2). Only a few events in the basin have oblique normal mechanisms, and some even indicate thrust faulting at different depths, supporting the complex depth variability discussed above.

Volcano-tectonic structures and mechanics

Recent maps from PHIVOLCS show NE-trending faults on the surface (`https://faultfinder.phivolcs.dost.gov.ph/`), which are visible as lineaments in the five-meter resolution NAMRIA DEM (thin black lines in Figure 3.2). Mount Apo also has features that suggest the existence of NE-trending structures. First, the peaks in the Apo volcanic area—a composite of three cones—follow a northeasterly trend (Figure 3.5a and 3.5b). This suggests that their formation might be controlled by NE-oriented feeder dikes (e.g., *Nakamura et al.*, 1977; *Paulsen and Wilson*, 2009). Second, prominent amphitheater-shaped scarps surrounding the peak of Mount Apo resemble sector collapses. The northeastern and southwestern scarps, in particular, appear elongated along the NE-SW and continue the trend of the mapped 10/31 rupture. Hence, the congruence of the fault rupture with the collapse features may be an indication of instability that is caused by volcano-crossing basal faults (*Tibaldi*, 1995; *Lagmay et al.*, 2000)

We also find that the location of the northeastern end of the 10/31 rupture right on the flanks of Mount Apo may be related to the rheological changes and the topographic load of Mount Apo. In a study of the coincidence of the rupture limit and postseismic deformation of the 2016 M_w7.1 Kumamoto earthquake with Mount Aso (Japan), *Yue et al.* (2017) suggest that active volcanoes can act as material or stress barriers to coseismic slip. In Mount Apo, geophysical exploration has revealed a shallow high-temperature geothermal fluid resource in the volcano (300°C at 0 m above sea level), along with several sites of surface thermal manifestation (*Los Baños et al.*, 2010), which is currently being exploited for energy production. In a similar setting, *Dianala et al.* (2020) explain how these factors promote aseismic slip on the creeping segment of the Philippine Fault. Additionally, the ∼ 2.9-km relief of Mount Apo could locally induce higher normal stress on the fault plane, helping prevent the propagation of seismic slip.

3.7.3 Implications for tectonics: regional stress field and active deformation of a complex suture zone

Available GPS data in Mindanao from campaign surveys is sparse (*Aurelio et al.*, 1998) . Nevertheless, the station velocities, relative to a fixed ZAMB station (Figure 3.1a), show the westward motion of the island arc section of the Mindanao, i.e., from the Philippine Fault in the east to the Sindangan Fautl in the west, towards the stable continental block. The slight N–S divergence of the velocity vectors between the northenmost and southernmost stations (e.g., M203 and M501, respectively) may further indicate some internal N–S extension in Mindanao, including the Cotabato Basin. These stress directions are conducive for conjugate NW-SE and NE-SW faulting, in agreement with the focal mechanism solutions of the 2019 earthquake sequence (all have N–S compressional and E–W extentional directions (Section 3.3).

According to *Pubellier et al.* (1991), NNE and E–W shortening in the region has

been ongoing since the Late Pliocene. The NNE-SSW shortening appears to be localized to the southwest of the Cotabato Fault. NW-striking folds can only be found across the southern part of the Cotabato Basin, and the Cotabato Trench bends from a NNW-SSE strike to a more WNW-ESE trend, south of 6°N latitude. On the other hand, the N–S folds and the NE-conjugate ruptures in the 2019 earthquake sequence are found north and east of the Cotabato Fault, respectively. Long-term interseismic coupling on the Cotabato subduction zone could be inducing the localization of shortening to the SW of the Cotabato Fault and driving the post-Pliocene uplift of the Kulaman Basin (*Tamesis*, 1981), while regional E–W shortening governs shortening in central Mindanao.

The location and extents of regional structures in southern Mindanao, alongside the late 2019 earthquake sequence, suggests that active deformation is distributed across the continental margin–island arc convergence zone, under a regime of regional E–W shortening. The northwestward fault models align with the Cotabato Fault, which forms part of the inferred suture zone of the Eurasian block and the Philippine Mobile Belt (*Pubellier et al.*, 1991; *Yumul et al.*, 2004). Unlike the Philippine Fault, which has been the source of earthquakes exceeding magnitude 7.0 from ruptures over 100-km long, the smaller event magnitudes in the 2019 Mindanao sequence may indicate the immaturity of the Cotabato Fault, resulting to more segmented displacement (e.g., *Manighetti et al.*, 2015; *Perrin et al.*, 2019). The Cotabato subduction zone, where there is a history of four magnitude 7.4–8.3 earthquakes in the instrumental record (Figure 3.1b), may be accommodating most of the elastic strain in southern Mindanao. While more scrutiny of the onshore tectonics is required, the broad deformation in the form of conjugate faulting revealed by the 2019 sequence may be analogous to distributed intraplate deformation, where earthquakes are not concentrated on a single fault defining a plate boundary (*Landgraf et al.*, 2017).

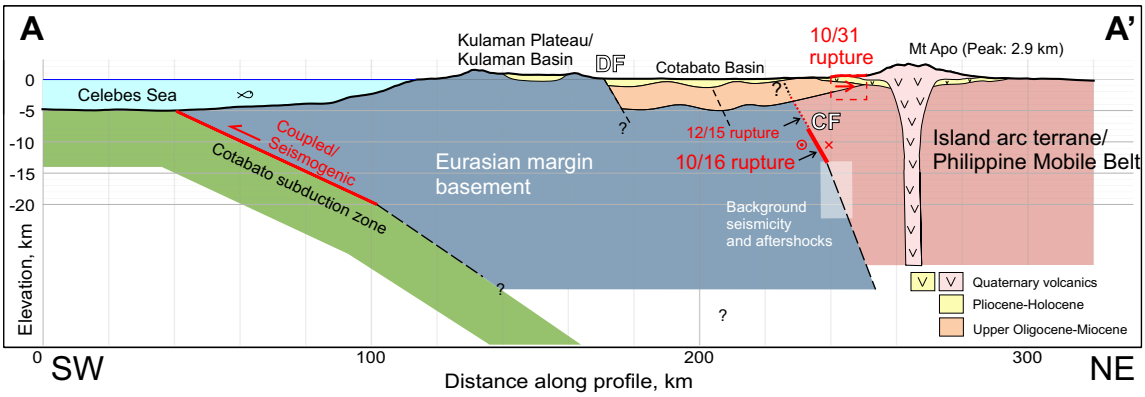


Figure 3.6: Schematic cross-section of the tectonic terranes in southern Mindanao and the Cotabato Basin, emphasizing the Cotabato Fault (CF), the basement of Eurasian affinity (blue), and the Philippine Mobile Belt (dark pink). Known seismogenic faults (solid red lines) and zones of seismicity discussed in the text are highlighted, inferred where dashed. Basin stratigraphy and geometry of the Daguma Fault (DF) is based on previous studies (e.g., *Tamesis*, 1981; *Aurelio*, 2000a). Coupling of the Cotabato subduction zone is based on the rupture width of the 1976 earthquake (80-km; *Beck and Ruff*, 1985) on the Slab2 geometry (*Hayes et al.*, 2018). Bathymetric–topographic profile is from the GEBCO global DEM (*GEBCO*, 2020).

3.8 Conclusion

Our analysis of the seismological, InSAR, and field observations of the 2019 southern Mindanao earthquake sequence suggests that the conjugate rupture involved deep NW-trending faults that are likely buried beneath the thick sedimentary section of the Cotabato Basin. Further, the limits of the surface rupture of the NE conjugate fault may be related to the structures in Mount Apo. The extent of seismic slip may be limited by the rheological and stress contrast induced by the volcano (as in *Yue et al.*, 2017). We infer that the ruptures form part of the Cotabato Fault, an extension of the suture zone of the fragmented continental Sundaland block and the predominantly island arc Philippine Mobile Belt.

The distribution of these active faults highlight the regional E–W compression, with possible N–S extension, and the complex deformation of ongoing terrane accretion along the southeastern margin of Eurasia. Similar to recent significant earthquakes within the Philippibe Mobile Belt (e.g., *Aurelio et al.*, 2017; *Rimando et al.*,

2019), the 2019 earthquakes on the Cotabato Fault are clear evidence of elastic, seismogenicw deformation on structures away from the more well-known plate-boundary features involved in the oblique convergence of the Philippine Sea Plate and Eurasia.

Chapter 4

The relationship between seismic and aseismic slip on the creeping segment of the Philippine Fault

4.1 Introduction

Whereas the relative aseismicity of faults in the Tien Shan and onshore Mindanao in the historical record appears to be due to the lack of observations that can constrain how strain is accommodated in areas with distirbuted faulting, the Leyte island section of the Philippine Fault has primarily been thought to be aseismic due to long-term fault creep (*Duquesnoy et al.*, 1994). Faults that slip aseismically, as opposed to locked faults, are often considered less likely to generate large earthquakes due to the lack of long-term strain accumulation. Hence, the seismogenic potential of faults can be assessed by appraising the degree and extent of locking on faults and by exploring the relationship between seismic and aseismic slip (*Avouac*, 2015; *Harris*, 2017). Geodetic and seismological observations show that fault segments that appear to slip aseismically on the surface may host locked sections at depth. This

has been made apparent on relatively well-studied faults in California (USA) (e.g., *Tse et al.*, 1985; *Burgmann et al.*, 2000; *Lienkaemper et al.*, 2012; *Johnson*, 2013; *Chaussard et al.*, 2015; *Jolivet et al.*, 2015b), most strikingly along the central section of the San Andreas Fault, where the Parkfield segment has hosted repeated strong earthquakes on a locked asperity (e.g., *Bakun et al.*, 2005). Continental faults in other settings, including the Longitudinal Valley Fault (Taiwan) and the Alto Tiberina Fault (Italy), also show a similar behavior of partial locking with a potential for strong earthquakes (e.g., *Thomas et al.*, 2014a; *Anderlini et al.*, 2016, respectively). In addition, numerical models based on rate-and-state friction suggest that seismic ruptures may propagate across sections of faults that host aseismic slip during the interseismic period (e.g., *Noda and Lapusta*, 2013; *Thomas et al.*, 2017). Isolating seismogenic asperities and documenting how far seismic slip propagates into sections that slip aseismically is therefore key in estimating seismic hazard, especially when these faults run across populated regions.

Many advances in understanding the diverse spatial and temporal nature of aseismic slip on continental faults have been brought about by interferometric synthetic aperture radar (InSAR) (*Bürgmann*, 2018; *Jolivet and Frank*, 2020). Thanks to its fine resolution, global coverage, and convenient access to the data, space geodesy using InSAR has become a powerful tool for studying earthquakes and active tectonics (*Elliott et al.*, 2016). The earliest InSAR observations of the seismic cycle revolutionized our ability to explore fault and crustal mechanics (e.g., *Massonnet et al.*, 1993; *Price and Sandwell*, 1998; *Deng*, 1998; *Wright et al.*, 2001; *Peltzer et al.*, 2001). Continuous monitoring through interseismic periods has further enabled us to delineate aseismic slip on remote and less well-instrumented faults (e.g., *Cavalié et al.*, 2008; *Jolivet et al.*, 2013; *Cetin et al.*, 2014; *Thomas et al.*, 2014a; *Fattahi and Amelung*, 2016; *Pousse Beltran et al.*, 2016; *Tong et al.*, 2018). This allows us to discover and explore potential earthquake sources that might not be well known, like on faults

sometimes referred to as "creeping faults" (e.g., *Jolivet et al.*, 2015b).

For two decades, shallow aseismic slip of more than 2.0 cm/yr on the Leyte island section of the Philippine Fault has been measured using sparse GPS surveys alone (*Duquesnoy et al.*, 1994; *Duquesnoy*, 1997) (Figure 4.1). The similarity of these estimates to the long-term slip rate, along with the lack of induced seismicity from injection experiments, has led to the notion that this portion of the fault is primarily aseismic (*Prioul et al.*, 2000). However, on 6 July 2017, a moment magnitude (M_w) 6.5 earthquake occurred in Leyte (*PHIVOLCS Quick Response Team*, 2019; *Yang et al.*, 2018; *Fukushima et al.*, 2019). With up to 1.1 meters of slip on the surface, most prominently in the village of Tongonan, within the city of Ormoc, the M_w 6.5 earthquake registered Intensity VIII shaking (on the PHIVOLCS Earthquake Intensity Scale) near the epicenter (*Llamas et al.*, 2017; *PHIVOLCS Quick Response Team*, 2019). The temblor happened in populated areas, resulting to three deaths and widespread economic disruption (*PHIVOLCS Quick Response Team*, 2019). InSAR has been used to model the extent of seismic slip (*Yang et al.*, 2018) and to juxtapose the seismogenic section with the surface manifestation of aseismic slip in the interseismic (*Fukushima et al.*, 2019). However, anthropogenic subsidence adjacent to the fault and the coeseismic area has hindered detailed comparisons of interseismic and coseismic slip distribution (*Fukushima et al.*, 2019). Furthermore, abundant geothermal resources in Leyte have spurred more than 30 years of detailed geological investigations on and near the fault, even up to around 2 km depth (e.g., *Reyes*, 1990; *Scott*, 2001; *Caranto and Jara*, 2015), allowing the rare opportunity to directly correlate *in-situ* physical conditions of an active fault with its behavior.

In this study, we constrain deformation from fault and anthropogenic subsidence sources in Leyte, and analyze the relationship between aseismic and seismic slip modes. The distributed slip models that we present are the first of their kind on the Philippine Fault, as we invert for the subsidence parameters and slip rates

through probabilistic (Bayesian) approaches. This permits us to explore how fault zone geometry and geological conditions correlate and might control the distribution of the slip modes, adding to a rich body of literature on fault and earthquake mechanics. Independent of the available InSAR data, we incorporate information from leveling surveys (from *Apuada et al.*, 2005) to understand the anthropogenic subsidence source. For coseismic displacements, we isolate the slip of the July 2017 mainshock from that of a M_w 5.8 aftershock, which are combined in previous coseismic slip models (*Yang et al.*, 2018; *Fukushima et al.*, 2019), and this shows how the spatiotemporal distribution of seismic slip might relate to geometrical complexity of the fault. Finally, we provide a physics-based framework for estimating the earthquake return time in a probabilistic sense and check this against the possibility of the July 2017 earthquake as a repeat of a surface magnitude (M_s) 6.9 event in 1947 (*Fukushima et al.*, 2019), which is of societal importance.

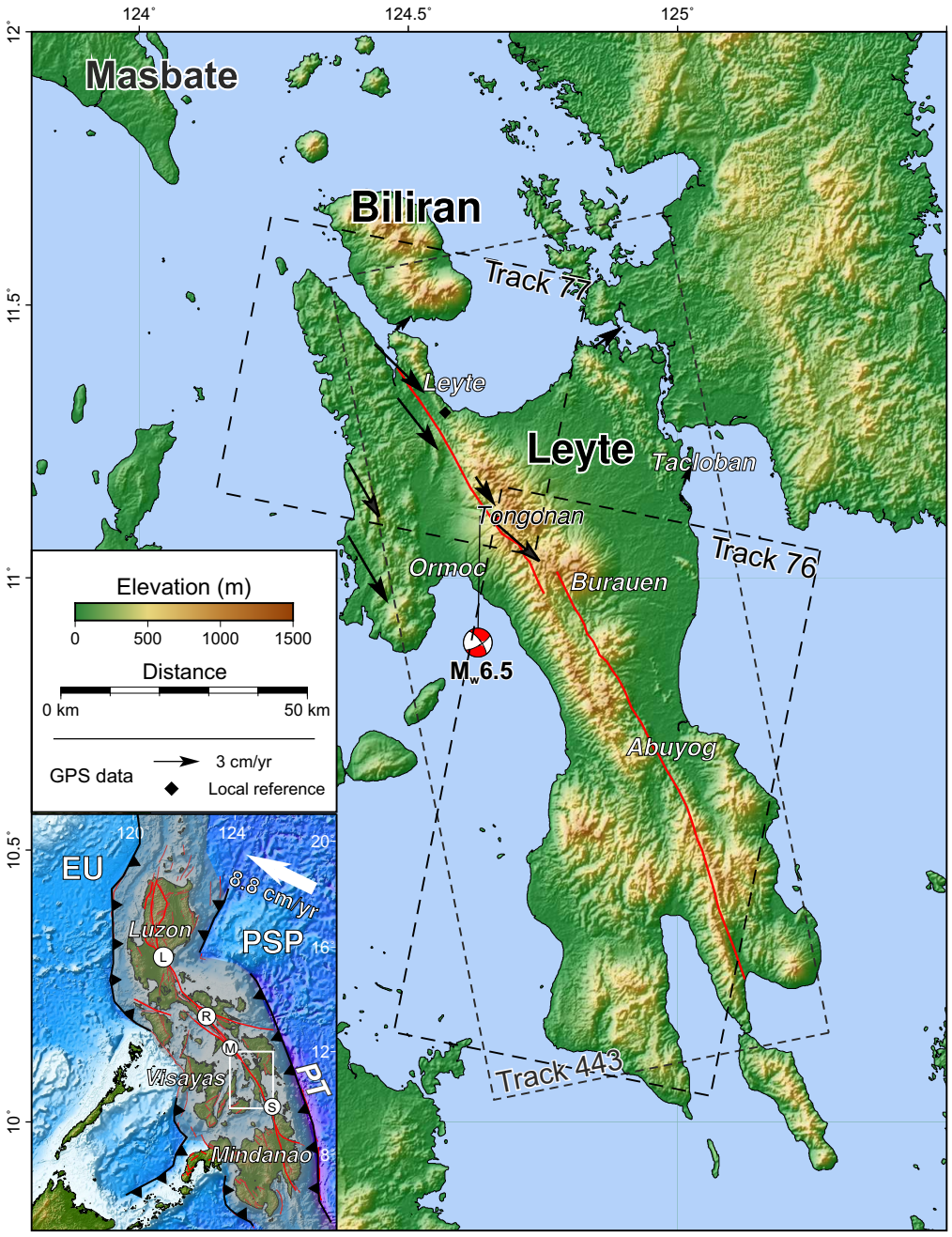


Figure 4.1: Active tectonics of the island of Leyte in the Philippines. Shaded relief map is based on SRTM 30-m resolution elevation data. Surface trace of the Philippine Fault (red, modified from *Tsutsumi and Perez*, 2013) is based on observations from AirSAR-derived DEM and InSAR. Arrows are GPS-derived velocities from *Duquesnoy* (1997) relative to a local reference station (black diamond). Red 'beach-ball' indicates the mechanism of the 6 July 2017 M_w 6.5 earthquake (USGS). Long and short black dashed lines indicate spatial coverage of ALOS data in ascending (track 443) and descending (tracks 76 and 77) passes, respectively. Inset: Geographic location of Leyte (white box) with respect to regional tectonic features around the Philippine Mobile Belt (shaded area) (modified from *Aurelio et al.*, 2013). White circles: epicenters of known historical and recent surface-rupturing earthquakes (see text for discussion) – L - Luzon, magnitude M_w 7.7, 1990; R - Ragay Gulf, M_s 7.3, 1973; M - Masbate, M_s 6.2, 2003; S - Surigao, M_s 6.9, 1879 and M_w 6.5, 2017. White arrow indicates the velocity of the Philippine Sea Plate (PSP) relative to the Eurasian Plate (EU) (*DeMets et al.*, 2010). Sawtooth pattern: subduction zones, with PT denoting the Philippine Trench.

4.2 Tectonic setting

4.2.1 The Philippine Fault: geodynamic and seismic context

The Philippine Fault is an approximately 1,200-km long left-lateral strike-slip fault (*Allen*, 1962; *Tsutsumi and Perez*, 2013). It accommodates part of the the oblique convergence between the Philippine Sea Plate and the Philippine Mobile Belt, on the margin of the Eurasian Plate, in a strain partitioning regime (*Barrier et al.*, 1991; *Aurelio*, 2000b) (Figure 4.1). The Philippine Sea Plate moves northwestwards at around 8.8 cm/yr relative to a fixed Eurasian Plate (*DeMets et al.*, 2010). Regional Euler pole rotation suggests that the Philippine Fault has a long-term strike-slip rate of 1.9–2.5 cm/yr (*Barrier et al.*, 1991). In the northern Philippines, 100–150 km long GPS transects indicate a long-term slip rate of 2.4–4.0 cm/yr on the Philippine Fault (*Galgana et al.*, 2007; *Yu et al.*, 2013). These estimates, however, go across several branches of the fault on Luzon island. More detailed block models from campaign surveys suggest interseismic slip rates of around 0.7 to 3.1 cm/yr on individual branches of the Philippine Fault in Luzon (*Hsu et al.*, 2016).

Geologic, geodetic, and seismotectonic studies have shown a spectrum of fault slip behavior along different sections of the Philippine Fault. The location of several major modern and historical earthquakes are associated with northern and southern splays of the Philippine Fault (*Bautista and Oike*, 2000). However, as shown inthe inset of Figure 4.1, only a handful have been determined to have produced surface ruptures, like the 1990 magnitude M_w 7.7 Luzon (*Punongbayan et al.*, 1992; *Silcock and Beavan*, 2001), the 1973 M_s 7.3 Ragay Gulf (southern Luzon) (*Tsutsumi et al.*, 2015), and the 1879 M_s 6.9 and 2017 M_w 6.5 Surigao (Mindanao) (*Perez and Tsutsumi*, 2017; *PHIVOLCS*, 2018) earthquakes. The central section of the fault (from 10°–12.5°N) is known for clusters of moderate to strong earthquakes ($\sim$ M 5–6), including the surface-rupturing 2003 M_s 6.2 Masbate earthquake (*Bacolcol et al.*,

2005). It has also been suggested that the Masbate earthquake was followed by post-seismic afterslip (*Besana and Ando*, 2005). In addition, directly south of Masbate, aseismic slip on the island of Leyte was first quantified from campaign GPS surveys around the Tongonan geothermal area in northern Leyte. Fault-parallel aseismic slip rates on the surface range from 2.6 cm/yr (*Duquesnoy et al.*, 1994) to 3.5 cm/yr (*Duquesnoy*, 1997; *Prioul et al.*, 2000). As previously mentioned, the 6 July 2017 M_w 6.5 earthquake ruptured the section of the fault where these surveys were conducted.

4.2.2 Seismotectonics of Leyte Island

The Philippine Fault goes through the island of Leyte from its northern to its southern shores, with a marked 150-km-long onshore trace. At the latitude of the island, the fault crosses the volcanic arc associated with the Philippine Trench subduction zone (Barrier et al., 1991) (inset of Figure 4.1). The fault is especially clear on narrow linear valleys, and portions that cut through Quaternary volcanoes and the central highlands (*Willis*, 1944; *Allen*, 1962; *Aurelio et al.*, 1993; *Lagmay et al.*, 2003; *Tsutsumi and Perez*, 2013). Active fault maps, based on topographic data from aerial photos and 90-m resolution global digital elevation models (*Tsutsumi and Perez*, 2013), reflect the main fault trace as a linear feature along the length of the island, with a bend near Tongonan village. There, sub-parallel secondary faults east of the main trace demarcate a 2- to 2.5-kilometer-wide relay zone that, further south (west of Burauen in Figure 4.2a), becomes a 4-kilometer-wide left-stepping step-over at around 11°N. Structural field observations and tectonic models expound on localized extension and secondary faulting along this releasing bend (*Aurelio et al.*, 1993; *Duquesnoy et al.*, 1994) and the sigmoidal stuctures that result from long-term volcano-tectonic interactions (*Lagmay et al.*, 2003). The Leyte Geothermal Production Field in Tongonan has been exploiting the abundant geothermal resources related to the Quaternary volcanoes for commercial energy production since the 1980s.

Geothermal exploitation within the fault bend leads to subsidence of up to 3 cm/yr (*Apuada et al.*, 2005). South of Tongonan, a rift-like morphology can be observed on the wide valleys west of Burauen, which *Willis* (1944) attributes to be a part of a "Visayan Rift". Subsequent mapping by *Allen* (1962) describes the active left-lateral strike-slip kinematics. The most recent work by *Tsutsumi and Perez* (2013) does not map out structures west of the main trace as active.

Several studies focusing on geothermal energy exploration suggest that the faulting (e.g., *Aurelio et al.*, 1993; *Lagmay et al.*, 2003) and continuous aseismic slip (*Caranto and Jara*, 2015) on the Philippine Fault in the volcanic area enhances the permeability in the shallow crust, allowing for the outflow of geothermal fluids. *Duquesnoy et al.* (1994) propose that the high heat flow and the clay alteration of volcanic rocks, due to the hydrothermal activity, might affect the rheology of the fault zone. They postulate that this causes the weakening of the fault zone, which, in turn, promotes aseismic slip. The ophiolitic basement is also exposed on the surface in Leyte (*Cole et al.*, 1989; *Aurelio et al.*, 1993; *Suerte et al.*, 2005; *Dimalanta et al.*, 2006; *Guotana et al.*, 2018), as shown in Figure 4.2. While the mineralogy of serpentinites from ophiolites along the San Andreas Fault has been considered to explain aseismic slip (e.g. *Moore and Rymer*, 2007), this has yet to be suggested for the Philippine Fault, so we expound on this in detail in the Discussion (Section 4.5). *Fukushima et al.* (2019) show the along-strike variability of surface aseismic slip rates based on the step-change of InSAR-derived surface velocity. However, due to the large magnitude of subsidence in the geothermal area, they are unable to estimate the rate of interseismic aseismic slip where the 2017 earthquake happened.

We focus this paper on two main segments of the Philippine Fault in Leyte, which are primarily based on distinct continuous surface traces: the Northern Leyte Segment (the section of the fault from Leyte town to Ormoc), and the Central Leyte Segment (from Burauen to Abuyog) (Figure 4.2a). Plotting the reviewed catalog of

the International Seismological Centre (ISC; *Storchak et al.*, 2017) of seismic events from 1964 to just before the July 2017 earthquake shows a clustering of seismicity in northern Leyte, which contrasts with what can be seen in central Leyte (Figure 4.2b). *Besana and Ando* (2005) have implied that a "large" earthquake in 1608 ruptured the Central Leyte Segment, and may suggest that a "seismic gap" exists between Burauen and Abuyog. The review of *Bautista and Oike* (2000) of pre-instrumental historical record of earthquakes in the Philippines, however, suggests that the 1608 earthquake had a M_s of 5.0 and a poorly constrained location (i.e., this event only has two reports that could be used as basis for the equivalent Modified Mercalli intensity). In southern Leyte, seismicity broadly clusters to the east of the fault trace.

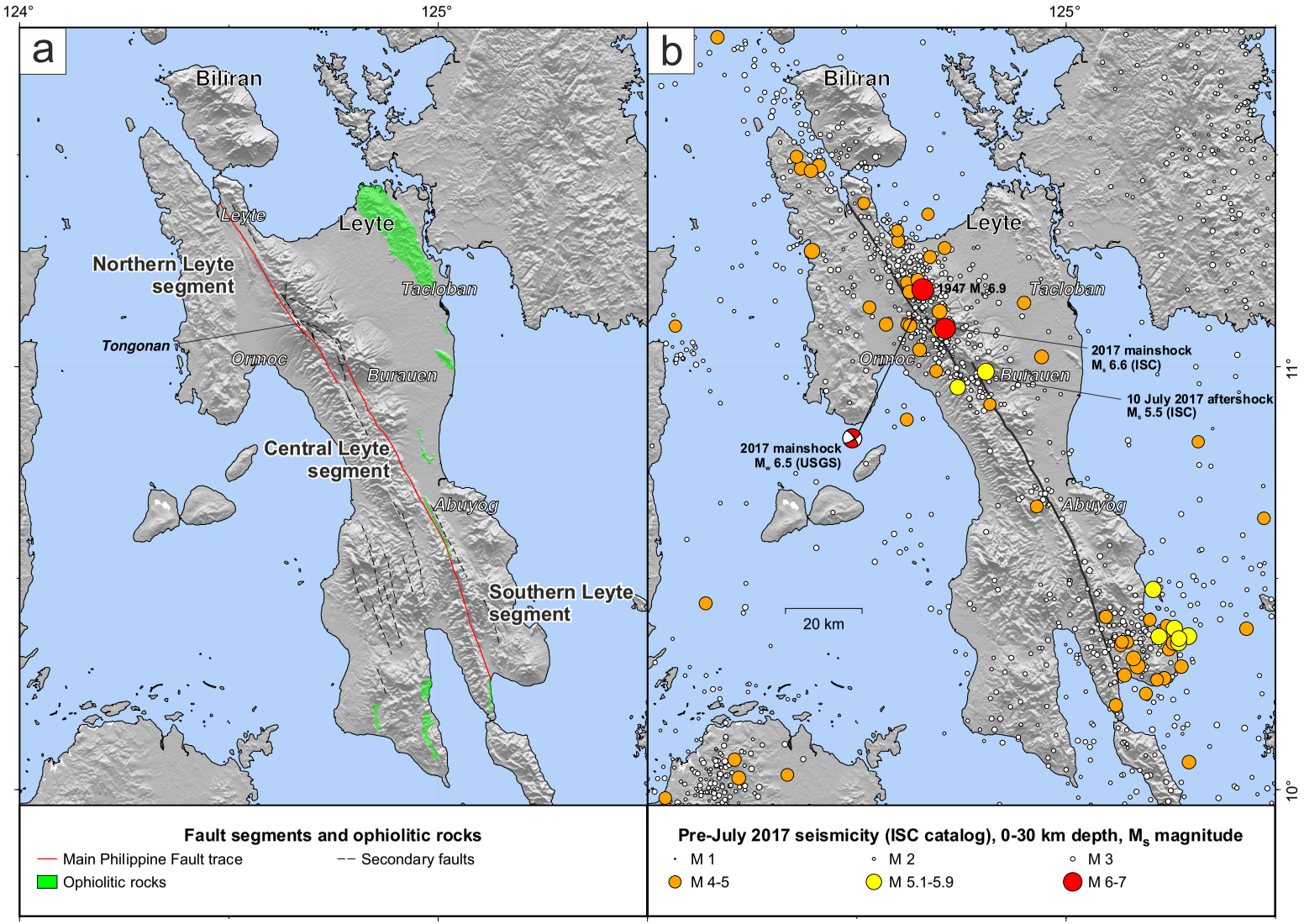


Figure 4.2: Seismotectonics of Leyte island. a) Main Philippine Fault segments referred to in the text (red line), along with secondary structures (dashed black lines) and surface exposures of ophiolitic rocks (*Aurelio et al.*, 1993; *Suerte et al.*, 2005; *Guotana et al.*, 2018). b) Instrumental seismicity (1984–July 2017) in Leyte based on the rebuilt International Seismological Centre (ISC) catalog (*Storchak et al.*, 2017). Symbol sizes are scaled according to surface wave magnitude (M_s). The mechanism and location of the July 2017 mainshock reported by the USGS is shown for reference (red beachball).

4.3 Interseismic (2007-2011) velocity field and aseismic fault slip

In this section, we explore the aseismic slip throughout the fault in Leyte including where the anthropogenic subsidence occurs. By deriving high-resolution velocity maps from InSAR data and including a subsidence source in the kinematic inversions, we are able to isolate the strike-slip fault deformation. We generated line-of-sight velocity maps with a spatial resolution of around 100 meters in radar range (nominally of higher resolution compared to the 1,500-meter resolution velocity maps in *Fukushima et al.*, 2019). This allows us not only to to revisit the surface manifestation of shallow aseismic slip on the fault, but also to capture the anthropogenic subsidence in enough detail that corresponds to data from local leveling surveys (*Apuada et al.*, 2005).

4.3.1 InSAR data processing

Using available synthetic aperture radar (SAR) data from ascending and descending passes of the ALOS satellite (Table 4.1), we analyze the surface deformation on Leyte during the 2007 to 2011 interseismic period. Because there has not been any large earthquake in the area in the 70 years prior to the 2017 earthquake, we do not expect significant postseismic transient motion and we can be confident that the ALOS measurements capture only interseismic motion. ALOS L-band SAR data (wavelength, $\lambda = 23.6$ cm) has the advantage of being able to produce coherent interferograms in vegetated areas despite long temporal baselines (e.g., *Sandwell et al.*, 2008; *Pousse Beltran et al.*, 2016), unlike SAR data at shorter wavelengths (e.g., C- and X-band).

We used the GAMMA Software to produce unwrapped interferograms from single-look complex images (SLC). For each track, we coregistered all SLCs to a corre-

Table 4.1: Summary of ALOS SAR data per track used for interseismic time-series analysis and stacking.

Date range	Track	# of acquisitions	# of ifgs[a]	N valid[b]
2006/12 – 2011/01	443, Ascending	25	86	50
2006/10 – 2011/01	76, Descending	5	10	6
2008/09 – 2010/12	77, Descending	3	3	2

[a]Number of interferograms.
[b]Number of required coherent measurements from interferogram network on a pixel to make a velocity estimate.

sponding reference SLC. Reference SLCs for tracks 443, 76, and 77 were chosen as a compromise between the perpendicular baseline of individual interferograms and overall baseline extent of the whole interferogram network. We first generated interferograms and multi-looked them to a pixel size of around 100 m x 100 m in azimuth and range. We used an adaptive spectral filter to improve the signal-to-noise ratio while preserving high-phase gradients (*Goldstein and Werner*, 1998). We unwrapped the interferograms using a minimum cost flow (MCF) algorithm (*Werner et al.*, 2002) and masked decorrelated pixels (i.e., those with coherence less than 0.4). We manually corrected unwrapping errors between adjacent islands with less than 2π phase jumps and no expected relative motion (i.e., islands that are on the same side of the fault). For removal of the topographic phase and generating a lookup table for geocoding the data, we used an airborne SAR-derived "bare-earth" digital elevation model (DEM) from the National Mapping and Resource Information Authority of the Philippines (NAMRIA) (e.g. *Luzon et al.*, 2016). For computational efficiency, we downsampled the 5-m resolution NAMRIA DEM to 10-m resolution.

Estimating surface deformation rates

As the temporal coverage of the ascending and descending passes are not uniform (see Appendix Figures J.1 to J.3 for temporal and spatial baselines, and interferogram pairs), we employed different strategies to measure the surface deformation rate. The

ascending track has 25 acquisitions between December 2006 and February 2011 and covers the whole length of the fault in Leyte. The two descending tracks that cover the fault have fewer acquisitions. Data from track 76 encompasses most of central and southern Leyte and has 5 acquisitions from 2006 to 2011. Track 77, which covers northern Leyte and Biliran, has only 3 acquisitions between 2008 and 2011.

For the ascending track, we followed an N-SBAS (Small Baseline) time-series analysis approach implemented in the Generic InSAR Analysis Toolbox (GIAnT; *Agram et al.*, 2013). This method allows the estimation of velocities in areas that have decorrelated signals in some interferograms but have at least a specific number of coherent measurements (N) in the interferogram network (e.g., *Doin et al.*, 2011; *Jolivet et al.*, 2012). For the time-series inversion, we manually selected 86 interferograms with no apparent non-linear phase ramps, which are usually due to ionospheric perturbations (*Gomba et al.*, 2016). The resulting interferogram network still covers 4 years of data (from 2007-2011, as shown in Appendix Figure J.1). We estimated the LOS velocity for pixels where more than 50 interferograms are unwrapped, assuming a linear rate. We included a step function in time to remove the coseismic signal from a M_w 5.3 earthquake in southern Leyte that has visible surface deformation off the Philippine Fault. Prior to inverting for the LOS velocity, we applied atmospheric corrections based on the European Centre for Medium-Range Weather Forecasting ERA-Interim models (*Jolivet et al.*, 2014). We also removed planar ramps on individual interferograms and corrected for DEM errors. The resulting velocity map has a mean root mean square error of 1.3 cm/yr (Appendix Figure J.4a).

For the descending tracks, we did not perform a complete time-series analysis to derive deformation rates as we do not have enough acquisitions. Instead, we estimated the average LOS displacement rate, $\dot{\phi}_d$, through a simple yet robust *stacking* approach, implemented in GAMMA, from the unwrapped interferograms. For

N number of interferograms, the algorithm uses the temporal baseline, Δt_j, of the respective j interferograms as a weight for LOS displacement, ϕ_j, to derive $\dot{\phi}_d$, as:

$$\dot{\phi}_d = \frac{\sum_{j=1}^{N} \Delta t_j \phi_j}{\sum_{j=1}^{N} \Delta t_j^2}. \tag{4.1}$$

Similar to the N-SBAS time-series approach, this formulation lets us estimate deformation rate on pixels that have coherent signals in N number of interferograms in the stack. We set N to to be more than half the total number of interferograms of each stack (Table 4.1). The mean standard deviation for the descending tracks 76 and 77 stacks are around 1.1 cm/yr and 0.9 cm/yr, respectively (Appendix Figure J.4b).

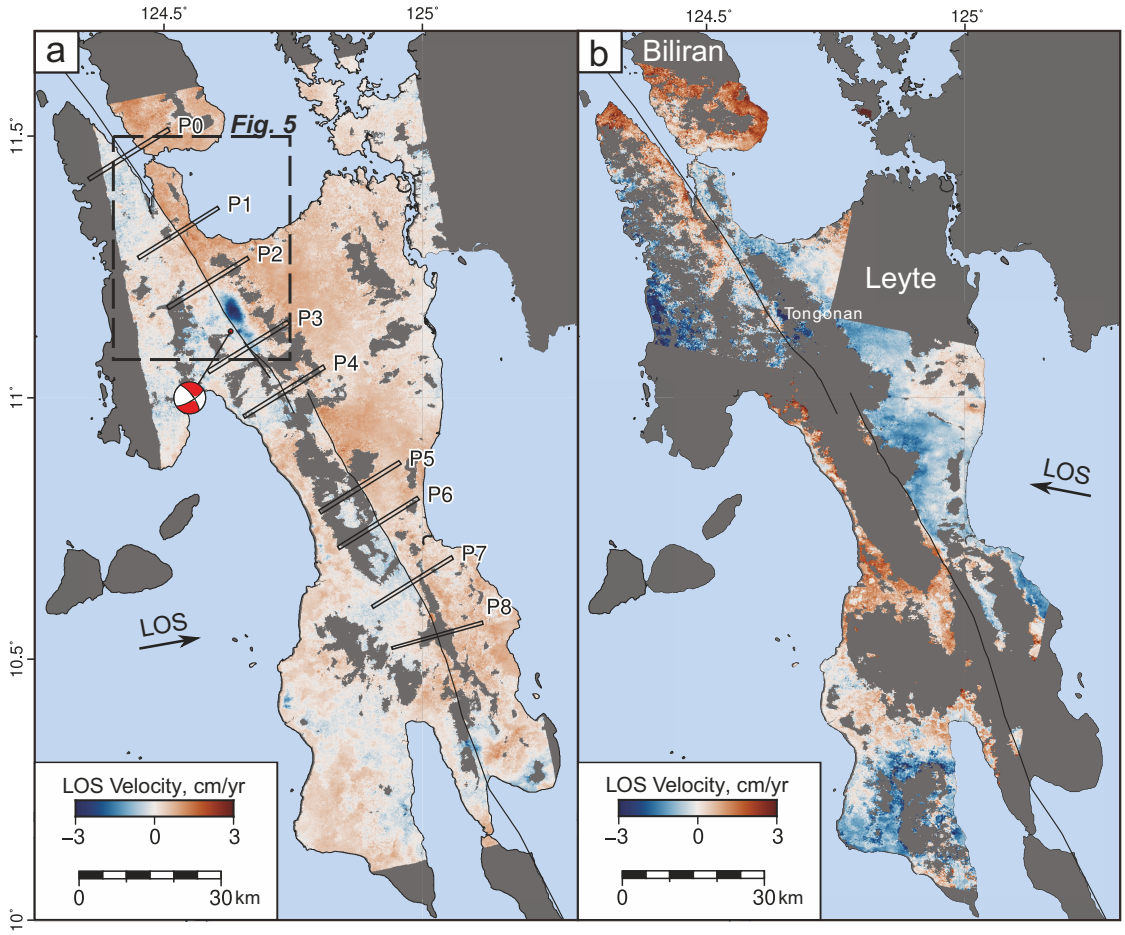


Figure 4.3: Interseismic surface deformation in Leyte in satellite line-of-sight (LOS) with rates in cm/yr (positive values indicate movement towards the satellite), and the Philippine Fault as the solid black line. Gray areas within the velocity field correspond to pixels masked out due to temporal decorrelation. a) Surface deformation from time-series analysis of ascending ALOS data (track 443). 6 July 2017 mainshock (M_w 6.5) location is shown for reference. LOS velocity swath profiles, P0–P8, are in Figure 4.4. b) LOS displacement rate derived from stack of ALOS descending interferograms (tracks 76 and 77).

Deriving subsidence from InSAR

The LOS velocity maps show a sharp velocity gradient across the Philippine Fault (Figure 4.3). We measure 0.2 to 0.9 cm/yr difference in the ascending LOS velocity across the fault with a step-like function right on the fault (Figure 4.4). Motion is compatible with the left-lateral sense of slip on the fault, as shown by the opposite LOS deformation rate observed on ascending versus descending tracks. We also observe an elliptical deformation feature that is most likely related to subsidence adjacent to the fault. Leveling surveys by *Apuada et al.* (2005) indicate up to 18 cm of subsidence in the Leyte Geothermal Production Field between 1997 and 2003. They associate this phenomena with net mass loss from energy production, as extraction rates exceed fluid reinjection rates. Since the geothermal production is ongoing, it is likely that subsidence still occurs in the area.

With InSAR displacements from multiple LOS directions, we can derive horizontal and vertical velocity components, and provide new measurements of subsidence. The off-nadir LOS of the SAR satellites makes InSAR most sensitive to vertical deformation; nonetheless, it is also possible to derive the eastward and northward component of horizontal motion (e.g., *Fialko et al.*, 2001; *Wright et al.*, 2004). As we lack a third velocity vector, however, we are unable to independently constrain the eastward and northward components of horizontal motion. We can instead project the east and north horizontal components of the InSAR LOS to the dominant horizontal direction of movement around the fault (as in *Lindsey et al.*, 2014; *Tymofyeyeva and Fialko*, 2018).

Given the LOS velocity from ascending ($\dot{\phi}_a$) and descending ($\dot{\phi}_d$) tracks, we inverted for vertical and fault-parallel velocity components, V_v and V_f, respectively,

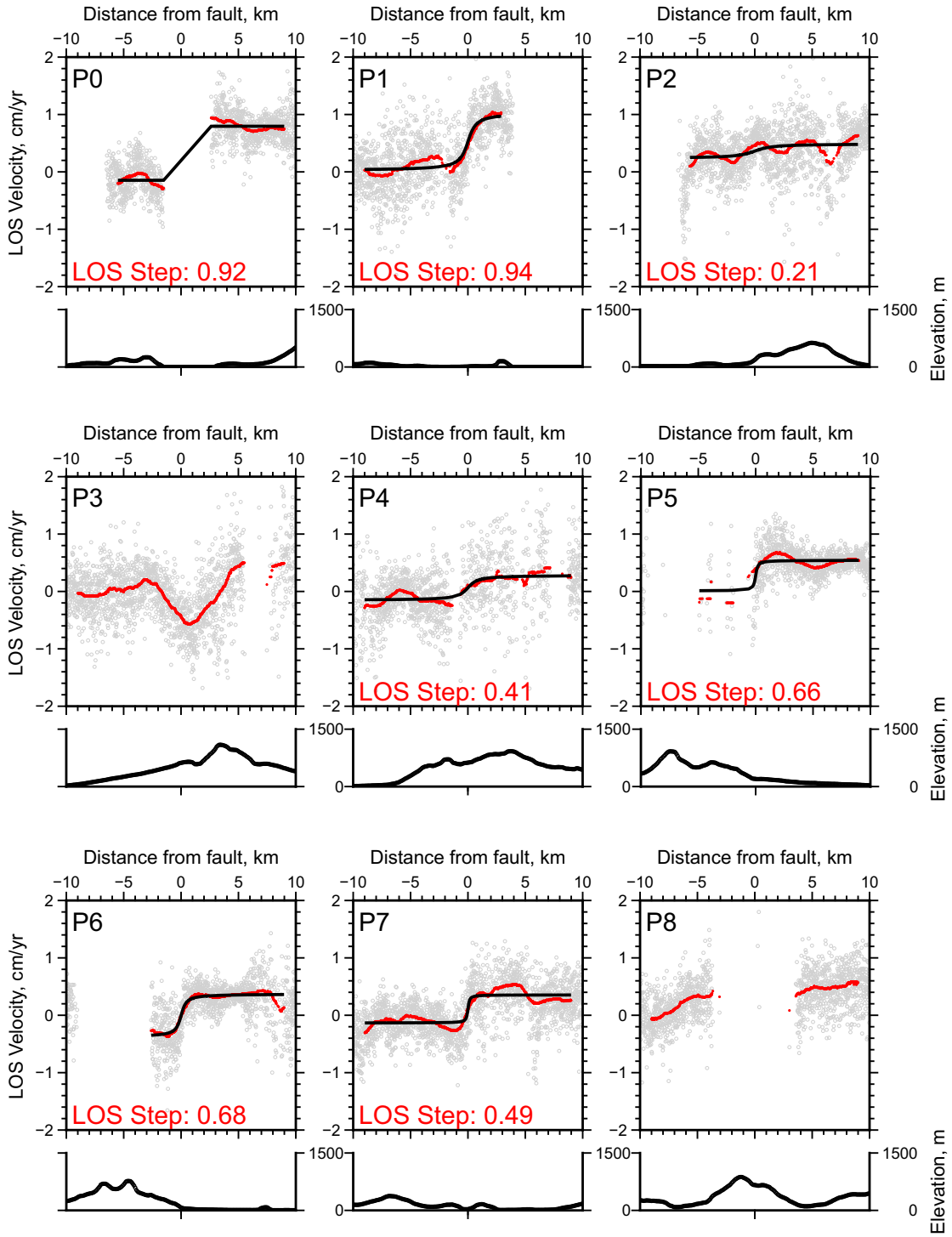


Figure 4.4: ALOS ascending track (443) LOS velocities and step-change (in cm/yr) within 20-km long, 1-km wide swath profiles centered on the Philippine Fault in Leyte (see Figure 4.3 for location). Corresponding elevations are shown below each profile. Gray dots and red line represent the LOS velocity and median value, respectively. Black lines indicate the step-function fit to the median LOS velocity (see Appendix H).

as:

$$\begin{bmatrix} \dot{\phi}_a \\ \dot{\phi}_d \end{bmatrix} = \begin{bmatrix} e_a\ sin(\alpha) + n_a\ cos(\alpha) & u_a \\ e_d\ sin(\alpha) + n_d\ cos(\alpha) & u_d \end{bmatrix} \begin{bmatrix} V_f \\ V_v \end{bmatrix}. \tag{4.2}$$

where e, n, and u are the east, north, and up components, respectively, of the unit vector pointing towards the satellite. α is the average strike of the Philippine Fault (328°), which corresponds to its large-scale strike-slip nature, and is, to first order, consistent with the GPS observations (*Duquesnoy*, 1997) (Figure 4.1).

To maintain temporal consistency, we derived the ascending LOS displacement rate for this inversion from stacking interferograms (as in section 4.3.1) that cover the same time period as the descending track (2008-2010). The derived fault-parallel and vertical velocities are shown in Figure 4.5.

4.3.2 Manifestation of surface aseismic slip

The LOS velocity map from the ALOS ascending track data shows a clear discontinuity across the fault (Figures 4.3a and 4.4, profiles P0, P1, and P4 to P7). This is apparent on a ∼100–km–long section of the fault, albeit discontinuously, between 10.5°N–11.5°N. Comparing the LOS velocity with the elevation on the same profiles suggests that this step change does not correlate to elevation gradients. The contrast in surface velocity, however, coincides with well-preserved fault scarps and most of the mapped surface trace of the Philippine Fault (as in *Tsutsumi and Perez*, 2013) in the northern and central sections of the island. We therefore attribute the velocity step to aseismic slip on the surface. Surface deformation derived from the descending track acquisitions (Figure 4.3b) has a lot more spatial variability and observation gaps. This is likely due to consistent temporal decorrelation of interferograms, resulting to less than the N number of observations required to estimate the average velocity. We nevertheless still observe a contrast in the descending LOS velocity

across the fault, as also noted by *Fukushima et al.* (2019). We describe below in more detail the deformation field, from north to south.

North of 11.4°N, while the Philippine Fault disappears below water in the strait between Leyte and Biliran, we observe a clear difference in velocity between the two islands, which are on opposite sides of the fault (P0 in Figures 4.3 and 4.4). Although unwrapping across water requires the assumption that no significant phase jump exists between landmasses, we are confident that the consistency between surface deformation rates in Leyte and Biliran suggests our velocity field is robust. In the town of Leyte, just north of Profile P1, field observations (Appendix Figures J.5b and J.5c) and anecdotal reports suggest that roads, houses, and other concrete structures show signs of left-lateral displacement even if there are no significant seismic events. Profiles V1 and V2, in Figure 4.5, highlight the fault-parallel motion across the fault between the islands of Leyte and Biliran and onshore in northern Leyte, respectively. They both correspond to left-lateral motion, which on Profile V2 is a clear step function of 2 cm/yr right on the fault. This signifies that, for this time-period at least, the northern section of the fault in Leyte slipped aseismically at around the long-term rate near the surface. The GPS fault-parallel velocities from *Duquesnoy* (1997) (black squares in Profile V2) appear to suggest faster motion than the InSAR data across the fault. This may reflect temporal variations on the interseismic slip rate in this location, but the sparse GPS data coverage makes it difficult to make robust inferences.

Contrast in surface velocities across the Philippine Fault is less prominent on Profile P2 (Figure 4.4), north of Tongonan. The derived fault-parallel surface velocity also shows no discontinuity across the fault in this area (Figure 4.5c, Profile V3), possibily indicating that the fault is locked near the surface. Another possibility is that the aseismic slip signal between Profiles P2 and P3, if any, might be obscured by the subsidence-related deformation in Tongonan (Profile V4 in Figure 4.5c). Finally,

significant surface ruptures related to the 6 July 2017 M_w 6.5 earthquake are found just south of Profile V4 (*PHIVOLCS Quick Response Team*, 2019).

Along the central highlands in Leyte, temporal decorrelation leads to gaps in the LOS velocity maps near the fault. Still, LOS velocity steps are visible across the fault from Burauen down to Abuyog, between 11°N and 10.6°N (profiles P4 to P7 in Figure 4.3). In the field, continuous and slow offset of roads in Abuyog have been documented by *Tsutsumi et al.* (2016). One of these roads has been repaved recently, but it appears the pre-repavement displacement has been preserved (Appendix Figure J.5d).

South of Abuyog, no clear contrast in the LOS velocity is observable (e.g. P8 in Figure 4.3). However, it does not necessarily mean that the fault does not slip aseismically near the surface. The ascending track LOS is orthogonal to the fault in this area, which makes fault-parallel deformation, if it exists, unresolvable. Looking at the descending data, which has a LOS oblique to the fault, there does appear to be a difference in the far-field velocities across the fault. However, we lack sufficient coherent data to be able to resolve the deformation rates closer to the fault. The off-main trace faulting in southern Leyte (Figure 4.2a) might also mean that deformation is more distributed across a wider area.

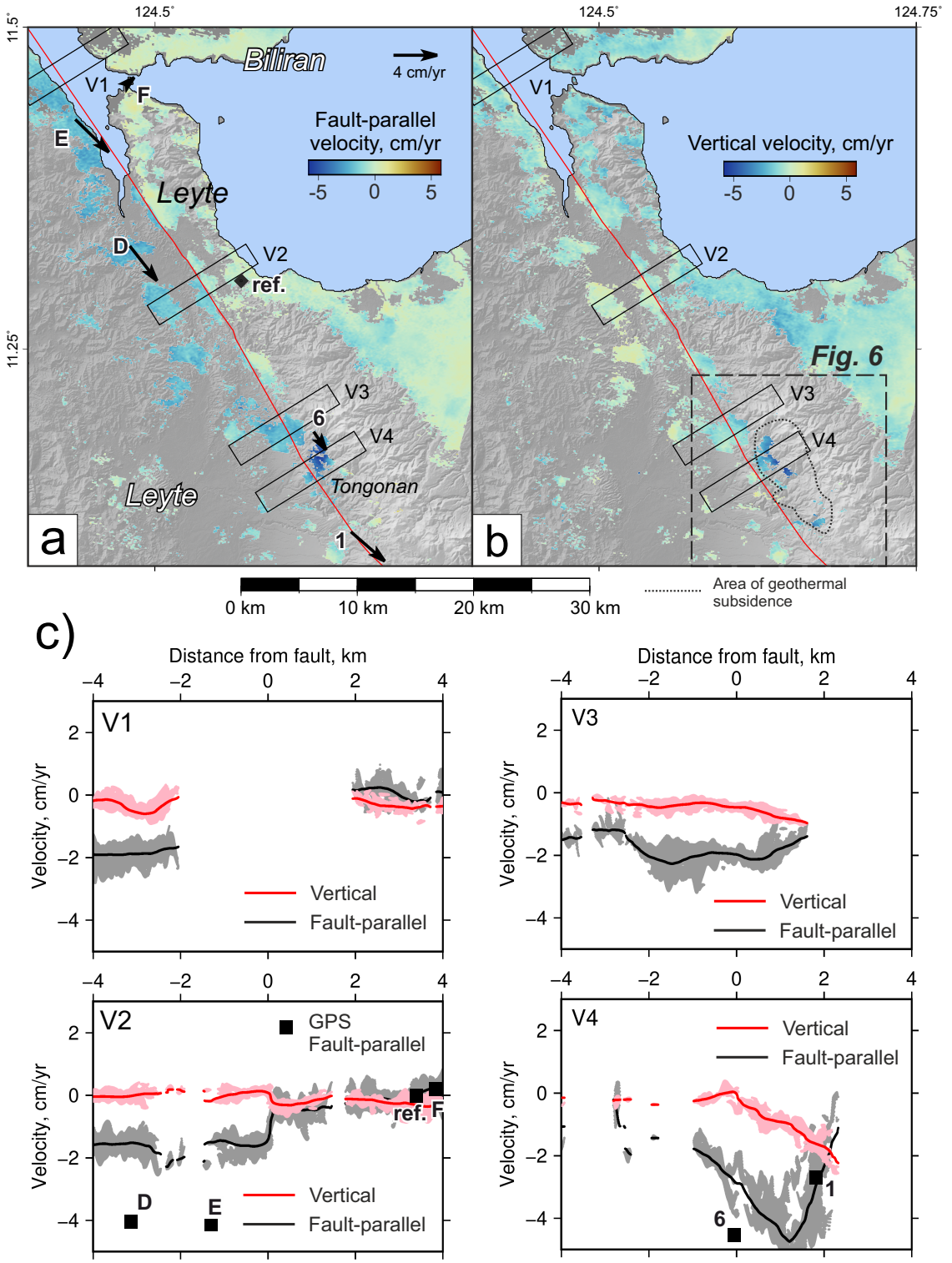


Figure 4.5: Estimated fault-parallel and vertical velocity in northern Leyte. a) Fault-parallel velocity from InSAR analysis. Black boxes show the spatial extent of swath profiles V1 to V4. Black vectors are GPS velocities from *Duquesnoy* (1997) (same as Figure 1) relative to the reference station (black diamond), with station names outlined in white. b) Same, but showing the vertical velocity and the geothermal subsidence area (based on *Apuada et al.*, 2005) in Tongnan (dotted outline. c) Profiles of fault-parallel velocity (gray: data, black: median) and vertical velocity (pink: data, red: median) from swaths V1-V4. V2 shows a clear step function in fault parallel velocity right on the fault, which is absent in V3. This suggests that shallow aseismic slip on the fault occurs near the surface at V2, but not on V3. The fault-parallel component of *Duquesnoy* (1997) GPS data (black squares) are shown in provile V2 for reference.

4.3.3 Subsidence in Tongonan

Our analysis of LOS surface velocities makes it apparent that to delineate the expression of shallow aseismic slip, we need to understand the contribution of the subsidence source to the deformation field adjacent to the fault. The vertical displacement rate, as seen in Figure 4.5b, shows subsidence in an area previously monitored by leveling surveys (*Apuada et al.*, 2005). We estimate up to ∼2.5 cm/yr of subsidence (Profile V4, Figure 4.5c), which is slightly less than the reported ∼3 cm/yr of maximum subsidence from the geothermal survey by (*Apuada et al.*, 2005). This discrepancy may be due to temporal variations in net mass loss, especially as a gradual decrease in extraction rates since the early 2000s has been reported (*Hazel et al.*, 2015). We also note a significant amount of horizontal motion in the subsidence area (profile V4 in Figure 4.4c), but in the opposite direction of that corresponding to left-lateral slip on the fault (see profiles V1 and V2, Figure 4.5c). Since both ascending and descending tracks are not consistently coherent in this area, we cannot derive meaningful horizontal and vertical deformation rate maps there. However, the apparent horizontal motion in Profile V4 may be related to the subsidence, in which case, it represents the surface moving towards the area of peak subsidence.

4.3.4 Modeling deformation sources

Surface observations indicate that the Philippine Fault slips aseismically up to the surface for a significant fraction of its Leyte section. The geothermal production field also leads to surface deformation in Tongonan. Hence, in our attempt to model the distribution of aseismic slip on the fault, we need to account for the contribution of a subsidence source to the interseismic deformation field. We describe in this section the details of our modeling approach, where we first determined a simple horizontal rectangular source for the subsidence from leveling surveys conducted in 1997 and 2003 (Section 4.3.4). While we do not aim to explain the subsidence mechanism,

deflationary elastic source models can be used to explain compacting or deflating geothermal sources (e.g., *Receveur et al.*, 2019). Then, using this subsidence source and a fault geometry based on the known trace of the Philippine Fault, we jointly solved for the rates of subsidence source deflation and aseismic slip on the fault using the LOS velocity maps derived over the 2007–2011 period (Section 4.3.4). Our main assumption is that the geometry of the source of subsidence did not change from the time of early leveling surveys (i.e., the data we use to infer the geometry of the source) to the time of SAR observations.

We followed a probabilistic (Bayesian) approach to invert for the various parameters of our model. The linear problem, $\mathbf{d} = \mathbf{Gm}$, allows us to invert for a vector of unknown model parameters, $\mathbf{m}$, from a vector of surface observations, $\mathbf{d}$ (e.g., InSAR and leveling data), and a Green's function matrix, $\mathbf{G}$, assuming a homogeneous elastic half-space (*Okada*, 1985). With Bayes theorem, we are able to derive the *a posteriori* probability distribution (also called posterior probability density function, PDF), of the model parameters given the data, $p(\mathbf{m}|\mathbf{d})$, as:

$$p(\mathbf{m}|\mathbf{d}) \; \alpha \; p(\mathbf{m}) \; \exp\left[\frac{1}{2}(\mathbf{d}-\mathbf{Gm})^T\mathbf{C}_d^{-1}(\mathbf{d}-\mathbf{Gm})\right], \tag{4.3}$$

where $p(\mathbf{m})$ is the prior PDF of the model parameters, which can be defined from *a priori* understanding of the physics of the problem (e.g., *Minson et al.*, 2013; *Jolivet et al.*, 2015b; *Bagnardi and Hooper*, 2018). For example, to model slip on the Philippine Fault, we can define prior PDFs that correspond to the known kinematics of the fault, i.e., left-lateral strike-slip. $\mathbf{C_d}$ is a variance-covariance matrix that describes the noise in the data (as in *Lohman and Simons*, 2005; *Sudhaus and Jónsson*, 2009; *Jolivet et al.*, 2012, among others). We then can sample models ($\mathbf{m}$) to describe the posterior PDF, and evaluate the model statistics (e.g., in terms of the mean and uncertainties of the PDF). We apply two different approaches to sample two different PDFs in the following sections, first to recover the geometry of the

source of subsidence, and then to derive the distribution of aseismic slip along the fault.

Inversion for the subsidence source geometry

We used the subsidence measured from leveling surveys, done by *Apuada et al.* (2005) between 1997-2003, to infer the geometry of the underground source of subsidence. This allowed us to constrain the source geometry independently from the InSAR data and use the vertical velocity derived from InSAR as verification instead. We avoided inverting for the subsidence source geometry from the derived InSAR velocity maps as this might lead to parameter overfitting to the complex deformation field in the InSAR line-of-sight. We excluded the leveling data in the joint inversion of fault and subsidence deformation rates. As the raw leveling data no longer exists, we digitized the subsidence contours from (*Apuada et al.*, 2005) and interpolated a raster of the subsidence rate using GRASS GIS (*GRASS Development Team*, 2017) (Figure 4.6a). Further, the elongated elliptical shape of the subsidence suggests a northwest-trending source. We therefore inverted for a horizontal rectangular source (sill) in an elastic half-space (*Okada*, 1985) (Figure 4.6b and Table 4.2).

We constrained the source parameters using the Geodetic Bayesian Inversion Software (GBIS; *Bagnardi and Hooper*, 2018). We determined the optimal source parameters, including length, width, depth, strike, position, and rate of opening. GBIS uses a Markov Chain Monte Carlo (MCMC) sampling, controlled by a Metropolis-Hastings algorithm, to approximate the posterior PDF from the parameter space based on *a priori* assumptions of the source (*Bagnardi and Hooper*, 2018, and references therein). The prior PDFs are expressed as uniform probability density functions. As the subsidence source in Tongonan is unknown, we set broad bounds for the prior PDFs to allow exploration of different sill geometries between 0 to 5 km depth (*a priori* bounds are summarized in Table 4.2).

We generated 10^6 samples of the posterior PDFs of the source parameters. The first 20,000 iterations of sampling, wherein the GBIS fine-tunes the ideal step-size for the random walk in the parameter space for the succeeding samples (*Bagnardi and Hooper*, 2018), are excluded from the posterior PDFs. The maximum *a posteriori* probability is taken as the optimal solution from the whole distribution. For spatially continuous data (e.g., InSAR), GBIS also considers the uncertainties of the data in evaluating the posterior probability based on empirical estimation of variance and range (correlation distance) from semi-variograms of the noise outside of deforming areas (e.g., *Lohman and Simons*, 2005; *Sudhaus and Jónsson*, 2009). As our subsidence data is spatially continuous but does not have far-field information, we arbitrarily assumed a variance (σ^2) of 5 cm^2/y^2 and a range (λ) of 1 km. The former is larger than the observed subsidence gradient (~3 cm/yr), while the latter is smaller than the spatial extent of the data.

The results show an optimal sill geometry and negative opening (deflation) that largely captures the magnitude and pattern of subsidence (Figures 4.6). The observed subsidence can be explained by a northwest-striking sill-shaped source at around 1.4 km depth from the surface, with deflation reaching 4.2 cm/yr (Table 4.2). The source depth coincides with the depth of the bottom of most wells in the Leyte geothermal production field (i.e., approximately between 1-2 km; *Apuada et al.*, 2005; *Prioul et al.*, 2000, as displayed in Appendix Figure J.6); hence the probable depth of compaction that can result from geothermal fluid extraction (for a similar geothermal case in Iceland, see *Receveur et al.*, 2019). Based on the joint marginals (Figure 4.7), we observe that the source geometry parameters are well constrained, with only a slight bias (or correlation) between the sill width and its location. The opening parameter negatively correlates with the width, length, and depth (between 1.2 and 2 km) of the source. The negative correlation between depth and opening means that a deeper source with a larger deflation could predict the observations

Table 4.2: *A priori* bounds and inversion results for a horizontal rectangular source for the observed subsidence (from leveling surveys). We give the optimal values[a], and 2.5% and 97.5% percentile bounds of the posterior distributions (shown in Figure 4.7).

	Length, m	Width, m	Depth, m	Strike	Opening, cm/yr	X[b], m	Y[b], m
Lower bound	500	300	100	300°	-0.1	-500	4,000
Upper bound	10,000	5,000	5,000	359°	0.1	4,000	2,500
Optimal[a]	3,516	1,939	1,377	321.2°	-0.042	1,022	577.1
2.5%	1,338	1,838	958.7	302.1°	-0.098	151.2	-1,302
97.5%	8,536	1,737	3,588	356.9°	-0.015	2,436	1,610

[a]Maximum *a posteriori* probability
[b]X and Y refer to the position in Eastings and Northings of the center of the northeastern edge of the sill relative to the reference point (124.641208°E, 11.164502°N). Opening is negative for a deflating source.

on the surface as well as a shallower source with smaller deflation. Such bias is expected from the formulation of elastic dislocations and cannot be resolved with surface deformation data only. The fault-perpendicular profiles in Figure 4.6d show that the extent of the predicted subsidence is slightly wider than the observations, so the source might be slightly shallower. Nevertheless, we find that the extent of deformation and the location of the optimal model's predicted peak subsidence rate is similar to the vertical velocity component derived from the InSAR data (as shown by the red line and gray dots, respectively, in Profile S-S', Figure 4.6d). The root-mean-square of the residuals (Figure 4.6c) is 0.2 cm/yr. These give us some confidence that the sill-like elastic subsidence source is a useful model to adopt for joint inversion with fault slip.

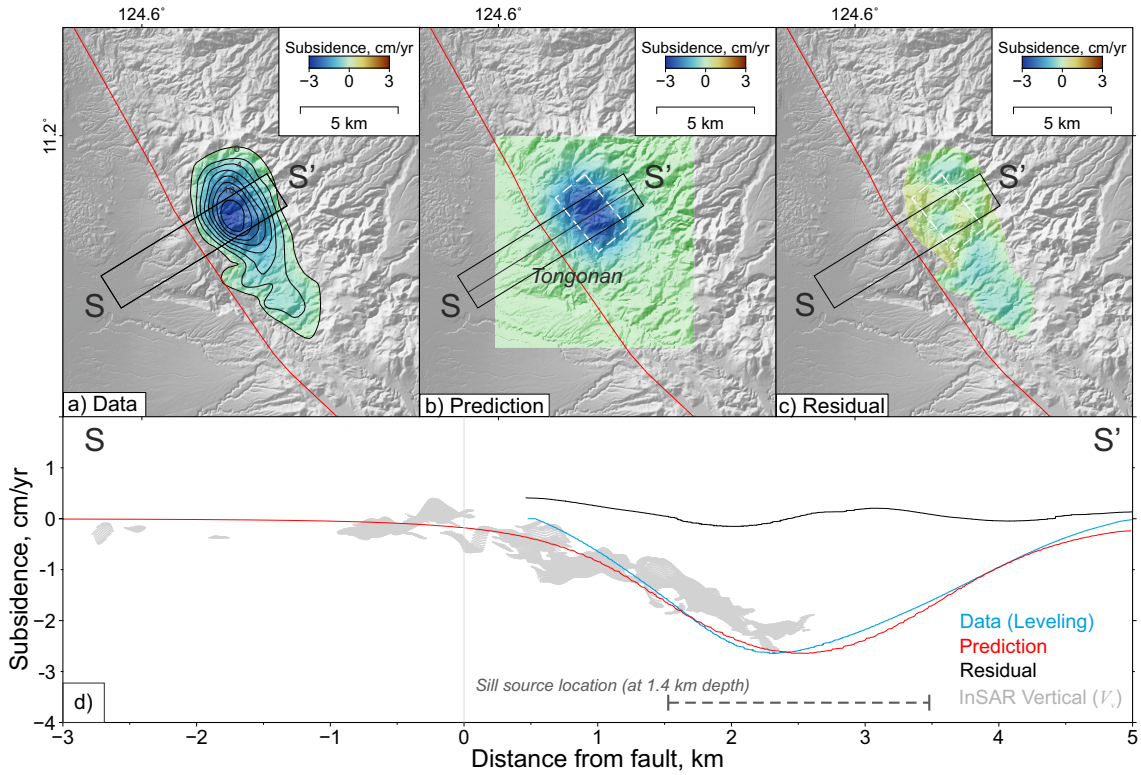


Figure 4.6: Subsidence data, model prediction, and residuals from modeling using leveling data. a) Interpolated subsidence rates based on leveling contours, with extent of swath profile, S-S' (black rectangle). The outermost contour represents zero subsidence as published in *Apuada et al.* (2005), and each contour interval represents 0.2 cm/yr of subsidence. b) Predicted subsidence from the optimal source model geometry, with the surface projection of the sill source (white dashed polygon). c) Residual deformation (the difference between data and predictions). d) Profiles of median subsidence data (blue), prediction (red), and residuals (black) in swath S-S'. Vertical surface velocity (V_v) in the swath from InSAR decomposition (gray points) and the location of the sill (dashed line) at the swath midsection also shown for reference.

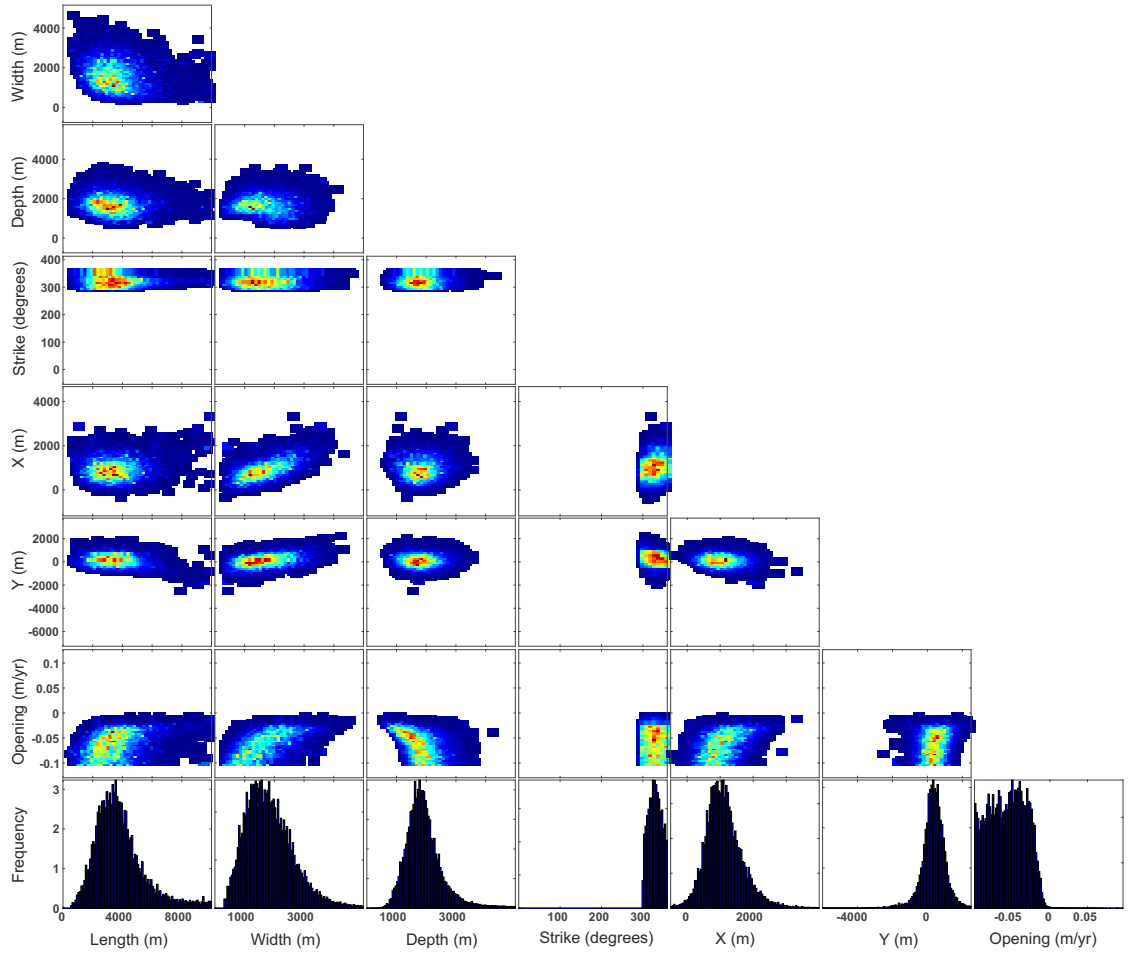


Figure 4.7: Posterior distribution and joint probabilities of subsidence source parameters from inversion with leveling data. Parameters include length, width, depth, strike, position (X and Y) relative to reference point, and rate of opening. Cooler colors correspond to lower frequency and warmer colors indicate higher frequency. See Table 4.2 for the summary of the statistics of the inversion.

Fault parametrization

We then defined the geometry of the fault in the joint inversion for aseismic slip and subsidence deformation rate. Given the regional-scale strike slip nature of the Philippine Fault, we assumed a vertical fault with the along-strike geometry based on existing active fault maps (*Tsutsumi and Perez*, 2013), modified to match the fault scarps and linear valleys observable from the five-meter resolution NAMRIA DEM. We reflected the left-stepping nature of the fault as two separate segments–the Northern Leyte and the Central Leyte segments.

From 0 to 15 km depth, we divided the fault into rectangular patches with increasing patch sizes in three rows (see Figure 4.8 for the shallow fault geometry). We explored different discretizations through qualitative trial-and-error tests (e.g., *Sagiya and Thatcher*, 1999), increasing the size variability from uniform 2 x 2 kilometer square patches. We adopted the variable patch size distribution that balances the ability to capture the heterogeneity at the shallowest sections of the fault (represented by smaller patches at the surface), the decreasing resolution with depth of inversion from surface data, and the convergence of the Bayesian sampling algorithm (*Jolivet et al.*, 2015b; *Gombert et al.*, 2018). The down-dip widths are 2 km on the top row, 5 km on the middle row, and 8 km on the bottom row. For the Northern Leyte Segment, the along-strike length from the top, middle, and bottom rows are 2 km, 10 km, and 30 km, respectively. We set slightly longer patches on the deeper rows of the Central Leyte Segment to account for the gaps in the surface data along the central highlands. The middle and bottom rows of the Central Leyte Segment have 12- and 40-km long patches, respectively. At depths greater than 15 km, we introduced a single vertical fault with fewer but much larger patches to effectively mimic surface displacements related to an infinitely deep dislocation source, to capture deep-slip below the seismogenic zone (*Savage and Burford*, 1973). Slip on the 'deep' patch reflects the secular rate and predicts far-field displacements due to plate

motion across a strike-slip boundary.

Joint modeling of aseismic slip and deflation from InSAR data

We used AlTar (e.g., *Jolivet et al.*, 2014; *Gombert et al.*, 2018) to jointly solve for the PDF of slip on the fixed fault geometry and deflation rate on the subsidence source. AlTar is a parallel MCMC solver based on the early CATMIP algorithm (*Minson et al.*, 2013) that benefits from GPU acceleration. This algorithm samples the parameter space, imposed by the prior PDF, using a Bayesian formalism. The sampling provides an ensemble of probable models that fit the data within its uncertainties. Furthermore, it does not involve any form of arbitrary smoothing of the solution, often used to regularise the inverse problem. Smoothing of slip between adjacent fault patches is usually a source of discrepancies between deterministic slip models (*Minson et al.*, 2013, 2014; *Duputel et al.*, 2015; *Gombert et al.*, 2018).

We first downsampled the InSAR-derived surface deformation rates with a resolution-based algorithm (*Lohman and Simons*, 2005). We masked out points within 500 meters from the fault to account for uncertainty in the geometry of the fault near the surface. Finally, we excluded data south of 10.6°N where left-lateral slip is likely poorly resolved because the ascending track line-of-sight is orthogonal to the fault fault strike (as discussed in Section 4.3.2). We used empirical exponential function fits to the noise covariograms of each InSAR dataset to build the variance-covariance matrix ($\mathbf{C_d}$ in Equation 4.3), as in *Jolivet et al.* (2012). The empirical standard deviations and correlation lengths, respectively, were 0.1 cm/yr and 6 km for ascending track 443; 0.2 cm/yr and 4 km for descending track 76; and 0.3 cm/yr and 3 km for descending track 77. The covariograms are shown in Appendix Figure J.7.

We assumed a uniform prior PDF for the deflation rate and slip parameters, reflecting our *a priori* understanding of the left-lateral nature of the Philippine Fault. The fault patches at depths shallower than 15 km had a uniform prior PDF between

−0.01 and 4 cm/yr, with positive values denoting left-lateral slip. The negative lower bound was set to allow efficient sampling of zero values. We assigned a normal (Gaussian) prior PDF to the deeper patches, with a mean of 3.0 cm/yr and a standard deviation of 0.25 cm/yr, to reflect the range of published farther-field and long-term slip rates (*Duquesnoy et al.*, 1994; *Duquesnoy*, 1997; *Barrier et al.*, 1991). As far-field displacement data (i.e., further than ∼20 km) is sparse, slip rate on the deeper patches may be less well-constrained. Therefore, in order to speed up the sampling and to study only the distribution of aseismic slip consistent with current plate models, we used the Gaussian distribution with rather small standard deviation as the prior PDF.

We obtained more than 100,000 probable models that approximate the posterior PDF. For simplicity, in the following section, we primarily cite the mean and 1-σ of the posterior distribution of the parameters (the 'mean model', as shown in Figure 4.8), unless otherwise specified. The mode, skewness, and kurtosis of the posterior marginals (Figure 4.9) give us further indication of the robustness of inversion results as qualitative indicators of the "shape" of the posterior distribution.

4.3.5 Results: Variable aseismic slip rate and apparent locked section

The results of the modeling show varying rates of aseismic slip along-strike, with the mean model showing more than 3 cm/yr of slip on several section of the fault (Figure 4.8). The highest slip rates are present on the onshore Northern Leyte Segment and also along the shallowest patches of the Central Leyte Segment. Along most of the fault, between 2 to 15 km depth, most patches slip rapidly at around 2–3 cm/yr. The model also shows that, below 15 km depth, the fault slips at a rate of 3.3 ± 0.2 cm/yr. This rate is higher than the rates from plate-scale kinematic analysis (2–2.5 cm/yr; *Barrier et al.*, 1991), but is similar to the rates derived from campaign GPS

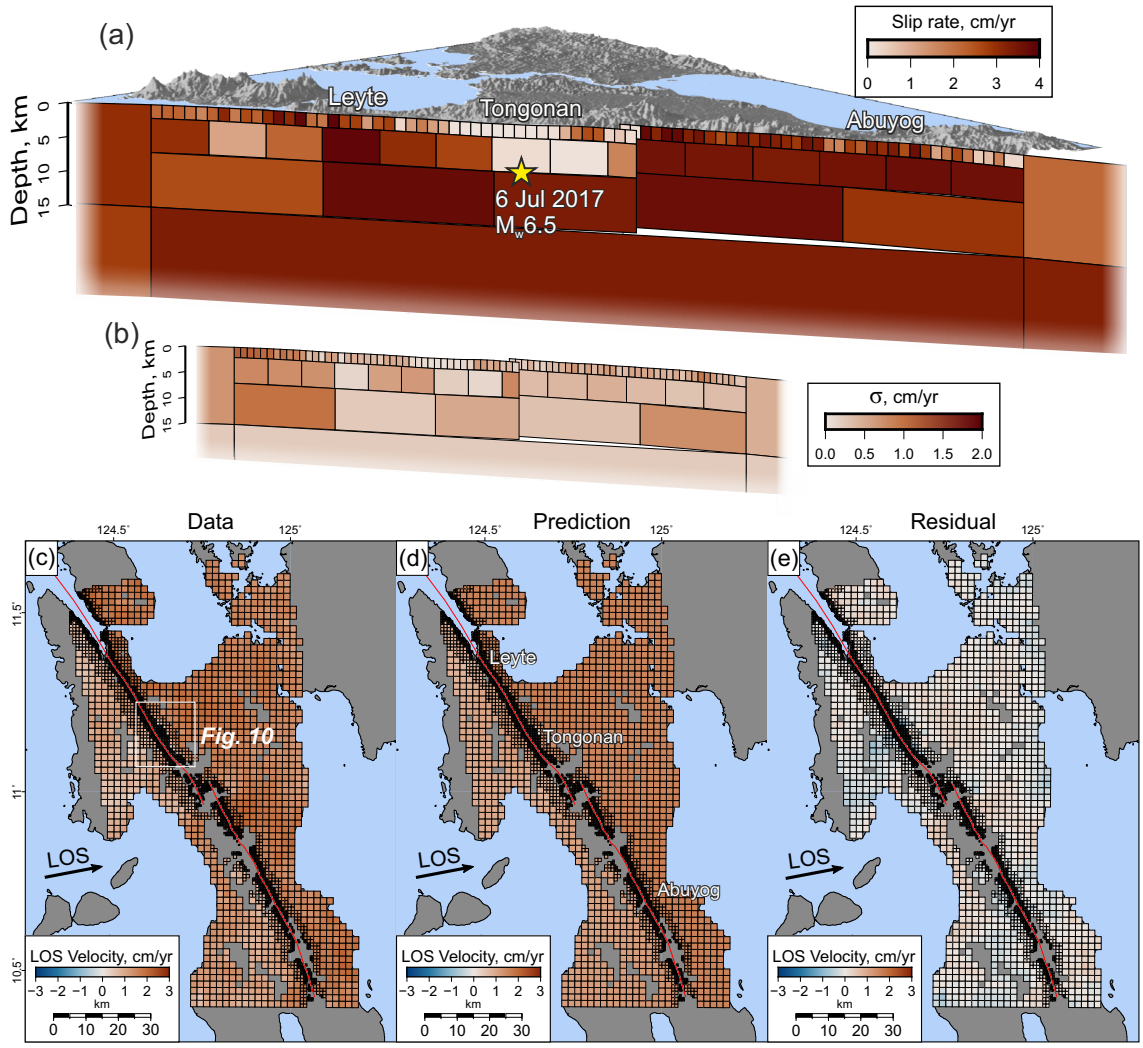


Figure 4.8: Rate and extent of aseismic slip on the Philippine Fault in Leyte and model fit. a) Mean of posterior PDF of aseismic slip, in cm/yr, with darker colors indicating faster slip. Star: hypocenter of the July 2017 M_w 6.5 earthquake. b) Standard deviation of posterior PDF. c-e) Downsampled ALOS ascending track 443 InSAR line-of-sight (LOS) velocity data, mean model prediction, and residuals. White square: Extent of Figure 4.10, which shows fit of model to the data in Tongonan. Red line: Faults included in model inversion. For the fit of model predictions to descending data, see Appendix Figure J.8.

studies in Leyte (*Duquesnoy et al.*, 1994; *Duquesnoy*, 1997, 2.5–3.5 cm/yr;).

In contrast, the southern end of the Northern Leyte Segment, hereafter referred to as the Tongonan Segment, appears to slip at a slower rate compared to the rest of the fault. Figure 4.8a shows that the aseismic slip rate on several contiguous patches from 0 to 7 km depth is close to zero. The small standard deviation (Figure 4.8b), as well as the mode, skewness, and kurtosis of the posterior PDF (Figure 4.9a to 4.9c)

provide further indications of very low slip rate in Tongonan across the ensemble of probable models. This reveals a previously unrecognized section of the fault that has a significant interseismic slip deficit, i.e., a locked asperity, which can be a source of earthquakes. The depth of the hypocenter reported by the USGS for the July 2017 M_w 6.5 earthquake is 9 ± 1.8 km, just at the bottom of the locked section (yellow star in Figure 4.8a). PHIVOLCS, on the other hand, reports a depth of 2 km and a 6.5 surface magnitude (M_s) (*PHIVOLCS Quick Response Team*, 2019). We make further comparisons between the interseismic and coseismic slip models for the July 2017 earthquakes (Section 4.4) in the discussion (Section 4.5).

The resolution matrix indicates that the inversion has resolving power for the majority of the patches (Figure 4.9d, with details on the resolution analysis in Appendix I). The absence of any data points promixal to the shallowest sections of the fault where it goes underwater, in between Leyte and Biliran islands, have much poorer resolution than the patches that correspond to the onshore trace of the Philippine Fault. The far-field model predictions and residuals of LOS velocity show that our model largely captures the gradient of fault deformation across Leyte (Figure 4.8d and 4.8e, respectively). The remaining residuals likely reflect uncorrected atmospheric noise or deformation that is not captured by a simple straight fault model in an elastic half-space.

Closer to the Philippine Fault in Tongonan, however, a linear pattern in residuals is visible, around two kilometers east of the main fault trace (Figure 4.10). This probably is a manifestation of complexity in the deformation field in Tongonan that is not captured by the model. Our sill source model is in this area (dashed black rectangle in Figure 4.10) and has a deflation rate of 5.4 ± 0.4 cm/yr. This estimate appears to be well-constrained as we do not observe obvious trade-offs between the joint marginal PDF of sill deflation and fault slip on adjacent patches (Appendix Figure J.9). We cannot, however, exclude the possibility of a more complex nature

of vertical deformation, like subsidence controlled by minor faults. The residuals also might reflect aseismic slip on a secondary, parallel branch of the Philippine Fault—the Central Fault branch (*Prioul et al.*, 2000; *Aurelio et al.*, 1993) (Figure 4.10f). This seems to be a likely explanation as, when comparing Figure 4.10c and Figure 4.10f, the residual velocities between opposing line-of-sights are of different signs across the Central Fault, denoting horizontal motion. We explore this possibility and its implications in the discussion (Section 4.5).

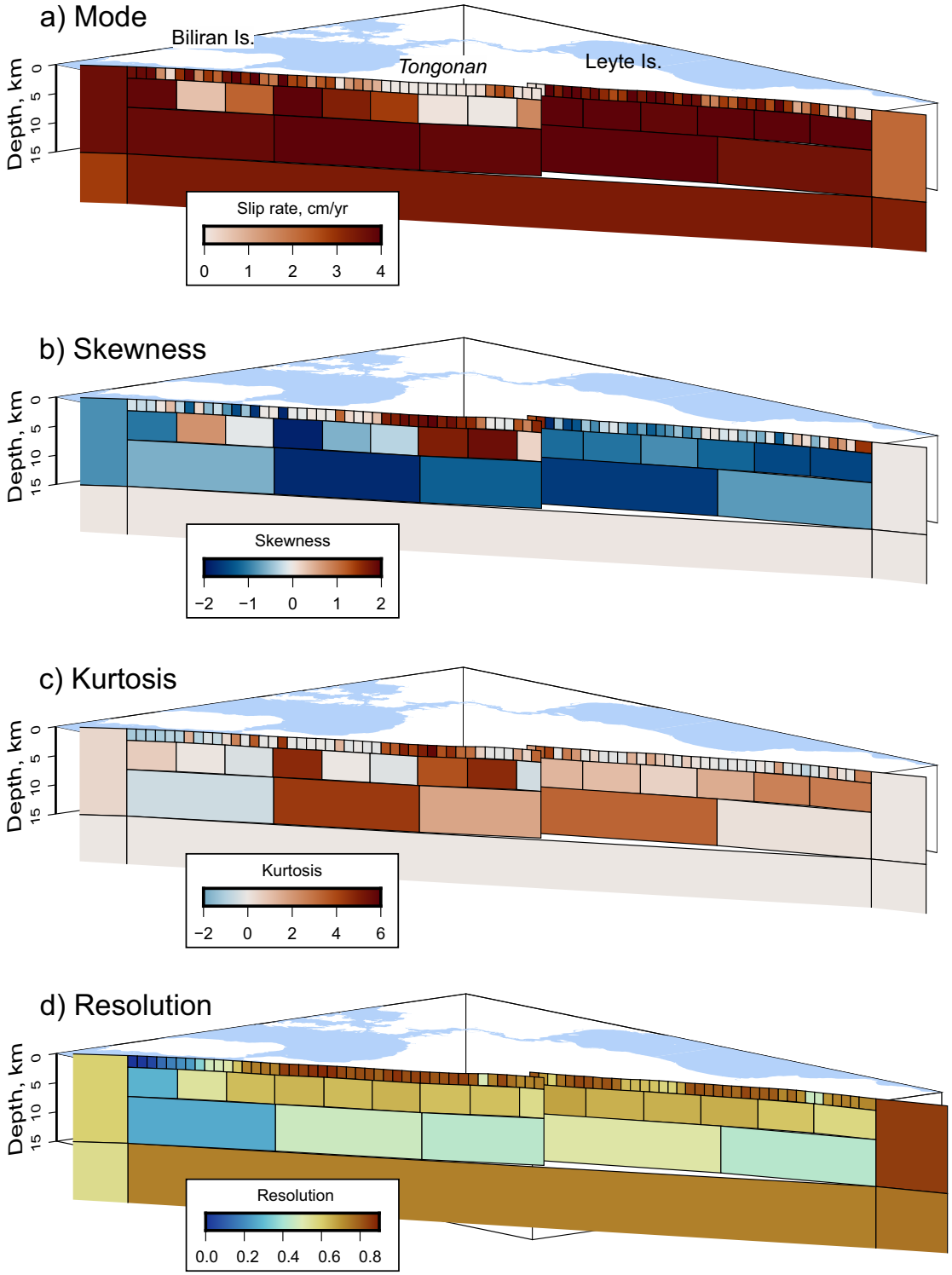


Figure 4.9: a) Mode, b) skewness, and c) kurtosis of the posterior distribution. d) Resolution of the inversion on the fault patches, with higher values indicating better resolution (see Appendix I for the resolution analysis).

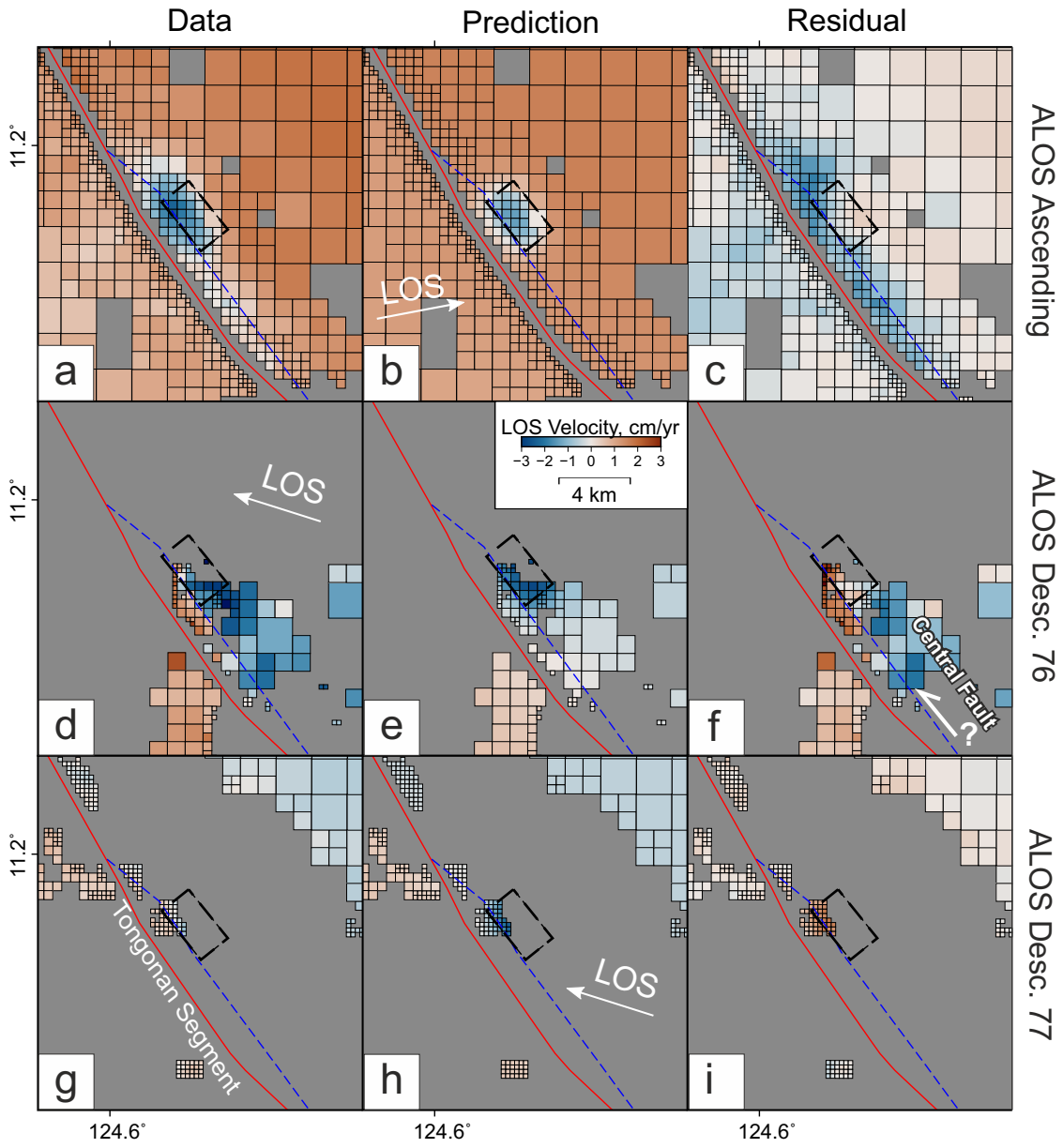


Figure 4.10: Downsampled InSAR LOS velocity data (left column), model prediction (middle column), and residuals (right column) in the Tongonan area, for ALOS ascending track 443 (top row, a-c), descending track 76 (middle row, d-f), and descending track 77 (bottom row, g-i). Red line: trace of the fault model. Dashed blue line: trace of the Tongonan Central Fault (*Aurelio et al.*, 1993; *Prioul et al.*, 2000). Dashed black rectangle: surface projection of the sill source. The residual velocity across the Tongonan Central Fault branch suggests that this fault is active. The opposite signs of LOS velocity between the ascending and descending tracks suggest that this is likely left-lateral deformation. See text for discussion (Section 4.3.5).

4.4 Coseismic: 6 July 2017 M_w 6.5 Mainshock and M_w 5.8 Aftershock

The interseismic model of aseismic slip in Leyte suggests that the Tongonan section of the Philippine Fault could be locked. Following the 6 July 2017 M_w 6.5 earthquake in Leyte, we thus evaluate any potential overlap between seismic and aseismic slip. The M_w 6.5 event produced discontinuous surface ruptures, with quick-response surveys by *PHIVOLCS Quick Response Team* (2019) indicating that slip was distributed along the known traces of the fault in Tongonan (Figure 4.11). Offset of concrete structures show around a maximum of 1.1 m of left-lateral displacement, with around 0.6 m vertical displacement (*Llamas et al.*, 2017) (Figure 4.11b). The earthquake was followed by several aftershocks, the largest of which (a M_w 5.8 event) happened four days later on 10 July 2017, with a similar strike-slip mechanism (orange 'beach-ball' in Figure 4.11a). No historical earthquakes are known to have produced surface ruptures along this fault, although *Besana and Ando* (2005) suggest that earthquakes of magnitudes greater than 6.0 could have occurred in Leyte. More recently, *Fukushima et al.* (2019) highlight the similarity of the recorded waveforms of a M_s 6.9 event in 1947 and the 2017 mainshock.

The recent published slip models of the 6 July 2017 mainshock have used interferograms that span both the mainshock and the aftershock (*Yang et al.*, 2018; *Fukushima et al.*, 2019). Hence, these slip distributions actually show the combined seismic slip from the 6 July mainshock and the 10 July aftershock. As listed in Table 4.3, there is a Sentinel-1 acquisition one day after the mainshock. We therefore propose to constrain the deformation from the mainshock and aftershock independently. However, only one Sentinel-1 acquisition was realized between the two events, so information is available for only one line-of-sight in constraining the separate slip distributions of each event. ALOS-2, on the other hand, has only pre-mainshock and

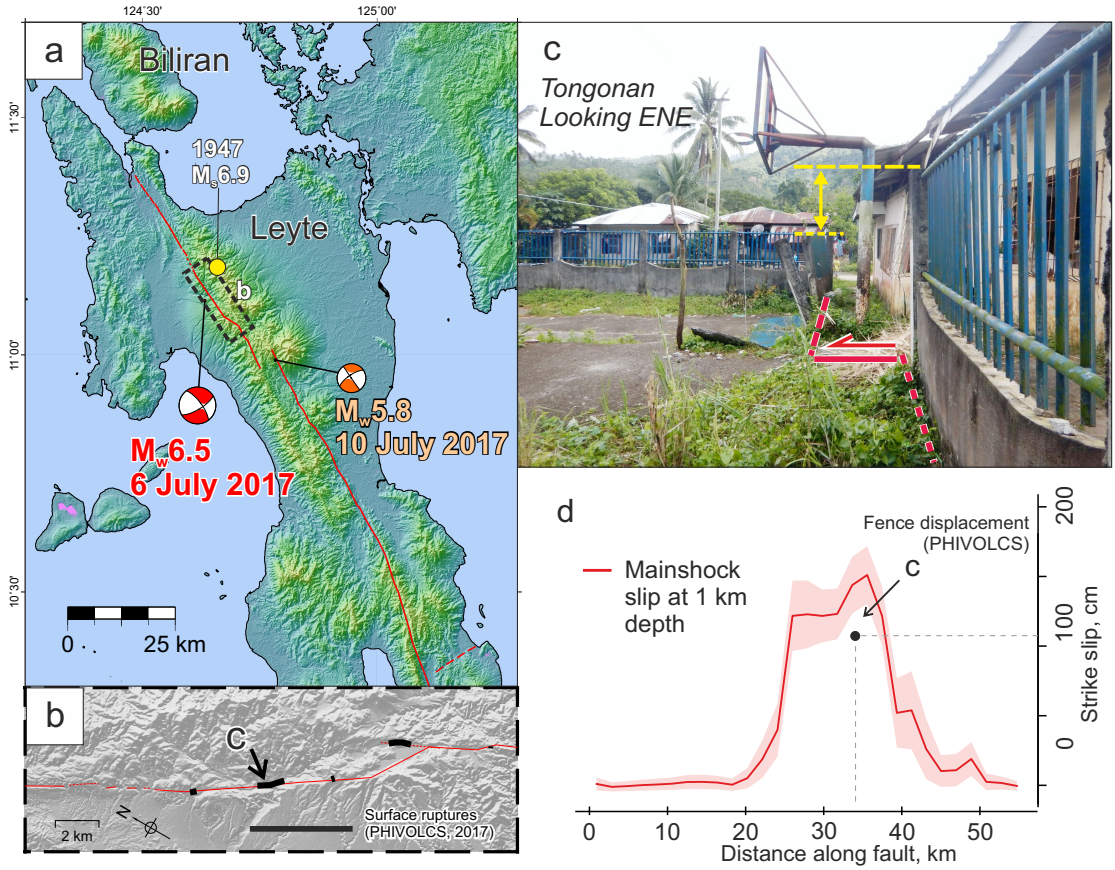


Figure 4.11: July 2017 earthquakes in Leyte. a) Map showing the 6 July 2017 M_w 6.5 mainshock (red) and 10 July 2017 M_w 5.8 aftershock focal mechanisms, obtained from the USGS website. Also shown for reference is the location of the 1947 M_s 6.9 earthquake (yellow) from the ISC-GEM catalog (USGS, https://earthquake.usgs.gov/earthquakes/eventpage/iscgem897883/executive). Dashed boxed indicates location of map in (b). b) Surface ruptures mapped by *PHIVOLCS Quick Response Team* (2019) quick-response team. c) Displaced concrete fence near the village center of Tongonan, showing left-lateral displacement (red) with a vertical component (yellow) associated with the July 2017 earthquakes, as reported by PHIVOLCS. d) Along-strike variation of mean (red) and 1-σ range (pink area) of posterior strike-slip PDF at 1-km depth from the mainshock model (Figure 4.14). Distance, in km, is relative to the northern end of the fault in onshore Leyte. Reported displacement by *PHIVOLCS Quick Response Team* (2019) of the fence shown for reference.

post-aftershock acquisitions, but data is available on both ascending and descending tracks. The modeling strategy we have developed to invert for the mainshock and aftershock slip distributions using all available interferograms (similar to *Ragon et al.*, 2019) is described in the following section. This approach exploits the advantage of using different look geometries from distinct satellite tracks, providing more

constraints to infer fault displacements.

4.4.1 Data and Methods

InSAR data processing

We used Sentinel-1 interferograms generated by the LiCSAR semi-automated processing chain (*González et al.*, 2016). LiCSAR automatically combines bursts and sub-swaths of Sentinel-1 SLC images within pre-defined frames to create interferograms using GAMMA Software with minimal manual input. The interferograms were multi-looked by 20 and 4 in azimuth and range, respectively, roughly equivalent to pixels of around 60 m x 60 m pixels. We took the unfiltered interferograms from LiCSAR frame 061D_07906_131313 (derived from Sentinel-1 descending track 61 data) that covers Leyte. In the processing, we included the NAMRIA IfSAR DEM (the same as in Section 4.3.1) for topographic corrections and geocoding.

The ALOS-2 interferograms, as in *Fukushima et al.* (2019), were processed using the RINC software (*Ozawa et al.*, 2016) with the SRTM1 DEM for topographic phase and geocoding. These interferograms were multi-looked to an equivalent pixel size of 100 m x 100 m in range and azimuth[1].

Table 4.3: Summary of coseismic interferograms used in this study. M: Mainshock, A: Aftershock

Event covered	Date pair	Satellite	Track
Mainshock (M)	2017/07/01—2017/07/07	Sentinel-1	61, Descending
Aftershock (A)	2017/07/07—2017/07/13	Sentinel-1	61, Descending
M and A	2017/07/01—2017/07/13	Sentinel-1	61, Descending
M and A	2017/06/04—2017/07/15	ALOS-2	136, Descending
M and A	2016/02/13—2017/07/15	ALOS-2	24, Ascending

We used an adaptive spectral filter on both datasets to increase the signal-to-noise ratio (*Goldstein and Werner*, 1998, as described in Section 4.3.1). We unwrapped

[1]Initial ALOS-2 InSAR processing done by Yo Fukushima

each interferogram with a region-growing branch-cut algorithm (i.e., *grasses* program in GAMMA). In order to reduce the occurrence of unwrapping errors in the coseismic interferograms, we applied this method iteratively. We initially unwrapped regions with coherences above 0.8 and decreased the coherence threshold on each iteration. This step also flagged branch-cuts to prevent unwrapping between pixels with sudden phase jumps, and then unwrapped small regions with high coherence. Succeeding iterations unwrapped areas with progressively lower coherence adjacent to the previously unwrapped regions. We manually checked for unwrapping errors at each iteration. Finally, from the result of the iteration with minimal unwrapping errors, we made manual corrections where necessary and masked any outstanding unwrapping errors that could not be corrected. For the Sentinel-1 interferograms, we did the filtering twice to make the unwrapping more efficient.

We estimated the noise covariance in each interferogram in regions where no coseismic deformation has been recorded, and downsampled the data for use in the inversion (both methods as described in Section 4.3.4). The empirical standard deviation and correlation length of the Sentinel-1 coseismic data are ∼1.5 cm and ∼6 km, respectively. For the ALOS-2 data, these are ∼1 cm and 2 km, respectively. The covariance functions of the coseismic InSAR datasets can be found in Appendix Figure J.10.

Inverting for mainshock and aftershock slip

In order to obtain models of the mainshock and aftershock slip, we set-up the inverse problem considering the different datasets (Table 4.3). The long temporal baseline of the ALOS-2 interferograms means that they include some interseismic (pre-seismic) and postseismic slip. For example, the pre-mainshock acquisition of the ALOS-2 ascending track 24 is almost 1.5 years prior to the M_w 6.5 event, which means that there could be up to almost six centimeters of left-lateral displacement on sections

that slip aseismically.

To separate the mainshock, aftershock, and pre- and post-seismic slips, we write the direct problem as:

$$\overbrace{\begin{bmatrix} \mathbf{d}^{M}_{Sent1_{d1}} \\ \mathbf{d}^{A}_{Sent1_{d2}} \\ \mathbf{d}^{MA}_{Sent1_{d3}} \\ \mathbf{d}^{MA}_{ALOS2_{d}} \\ \mathbf{d}^{MA}_{ALOS2_{a}} \end{bmatrix}}^{\mathbf{d}} = \overbrace{\begin{bmatrix} \mathbf{G}^{M}_{Sent1_{d1}} & 0 & 0 \\ 0 & \mathbf{G}^{A}_{Sent1_{d2}} & 0 \\ \mathbf{G}^{M}_{Sent1_{d3}} & \mathbf{G}^{A}_{Sent1_{d3}} & 0 \\ \mathbf{G}^{M}_{ALOS2_{d}} & \mathbf{G}^{A}_{ALOS2_{d}} & \mathbf{G}^{P}_{ALOS2_{d}} \\ \mathbf{G}^{M}_{ALOS2_{a}} & \mathbf{G}^{A}_{ALOS2_{a}} & \mathbf{G}^{P}_{ALOS2_{a}} \end{bmatrix}}^{\mathbf{G}} \overbrace{\begin{bmatrix} \mathbf{m}^{M} \\ \mathbf{m}^{A} \\ \mathbf{m}^{P} \\ \\ \\ \end{bmatrix}}^{\mathbf{m}} . \tag{4.4}$$

On the left-hand side, the $\mathbf{d}$ vector contains the five LOS displacement observations including only one or both of the mainshock- and aftershock-related signals (superscripts M and A, respectively), along either the ascending (subscript a) or descending (d) LOS from the ALOS-2 and Sentinel-1 satellites. The $\mathbf{G}$ matrix is a combination of Green's functions that relate slip on the fault from different source patches of the fault ($\mathbf{m}$) to the observations in $\mathbf{d}$. $\mathbf{m}^M$ is the distribution of the mainshock coseismic slip, $\mathbf{m}^A$ is the distribution of the aftershock coseismic slip, and $\mathbf{m}^P$ is the distribution of the sum of pre- and post-seismic slip recorded by the ALOS-2 interferograms. We also include terms in $\mathbf{G}$ and $\mathbf{m}$ that allow us to fit a residual ramp for each individual dataset.

We used the same fault parametrization of the Northern Leyte Segment as in the interseismic model (Section 4.3.4), but use only the onshore patches. Our prior PDF is uniform for all strike-slip parameters, between -5 cm to 300 cm, and Gaussian for the dip-slip component (mean at 0 cm and the 3-σ probability range within -200 cm and 200 cm). Positive values of slip indicate left-lateral and reverse slip for strike-slip and dip-slip, respectively.

As we also modeled the coseismic slip with AlTar, we primarily cite, in the following sections, the mean and standard deviation of the posterior PDF of slip,

unless otherwise stated. We find that the mean and the mode of the posterior PDF are not significantly different (comparisons can be found in Appendix Figure J.11). The fit of the model prediction to the observations are shown in Appendix Figure J.12 for the Sentinel-1 data, and Appendix Figure J.13 for the ALOS-2 data.

4.4.2 Results: Surface deformation and slip on the fault

The interferograms clearly show the left-lateral deformation related to the M_w 6.5 mainshock and the M_w 5.8 aftershock. As respectively displayed in Figure 4.12 and Figure 4.13c, descending track Sentinel-1 and ALOS-2 interferograms show movement away from satellite LOS east of the fault, and displacement in the opposite sense on the west side. This is apparent despite poor coherence in the Sentinel-1 data near the fault. In the ascending track ALOS-2 interferogram (Figure 4.13d), we note an opposite sign of LOS displacement compared to that in the descending track interferogram (Figure 4.13c). Thanks to the good coherence to the west of the fault in all interferograms, we can observe large LOS displacement right along the Tongonan Segment of the fault (white T in Figure 4.12d). This coincides with the location of the largest reported surface displacements in the field (*Llamas et al.*, 2017; *PHIVOLCS Quick Response Team*, 2019).

Comparing the Sentinel-1 wrapped interferograms that include the mainshock and the aftershock separately (Figures 4.12a and 4.12b, respectively) reveals that most of the deformation occurring during the aftershock happened south of the mainshock. Discontinuities in the wrapped phase of both the mainshock and aftershock data appear to be on the same fault trace (the Tongonan Segment). For the aftershock, this discontinuity is just south of the fault bend. These observations strongly suggest that both seismic events ruptured the Tongonan Segment, but at different locations.

The model slip distributions in Figure 4.14 suggest that most of the seismic slip

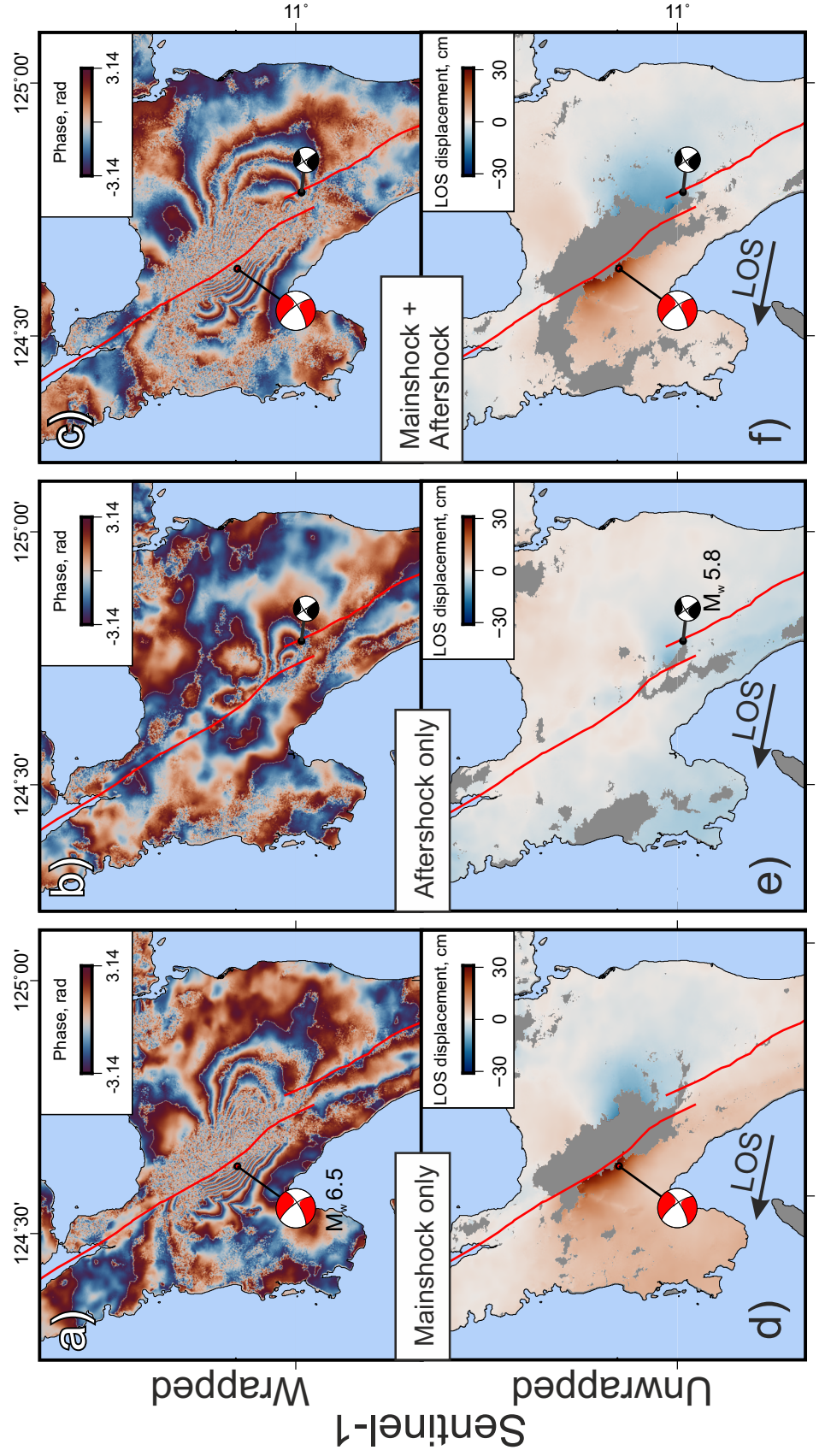


Figure 4.12: Pairs of wrapped and unwrapped coseismic interferograms, from Sentinel-1 data, showing phase change and line-of-sight (LOS) displacement of either the 6 July mainshock (M_w 6.5) or the 10 July aftershock (M_w 5.8), and their combined signal. Each map pair shows filtered wrapped interferogram (top) and unwrapped displacement (bottom). Positive unwrapped LOS displacement indicates movement towards the satellite. Focal mechanisms of the earthquakes are included for reference. T: Tongonan. a,d) Sentinel-1 descending track 61 data, showing mainshock displacement only. b,e) Same track, but showing aftershock displacement only. c-j) Combined mainshock and aftershock displacement from Sentinel-1 descending track 61 (c,f).

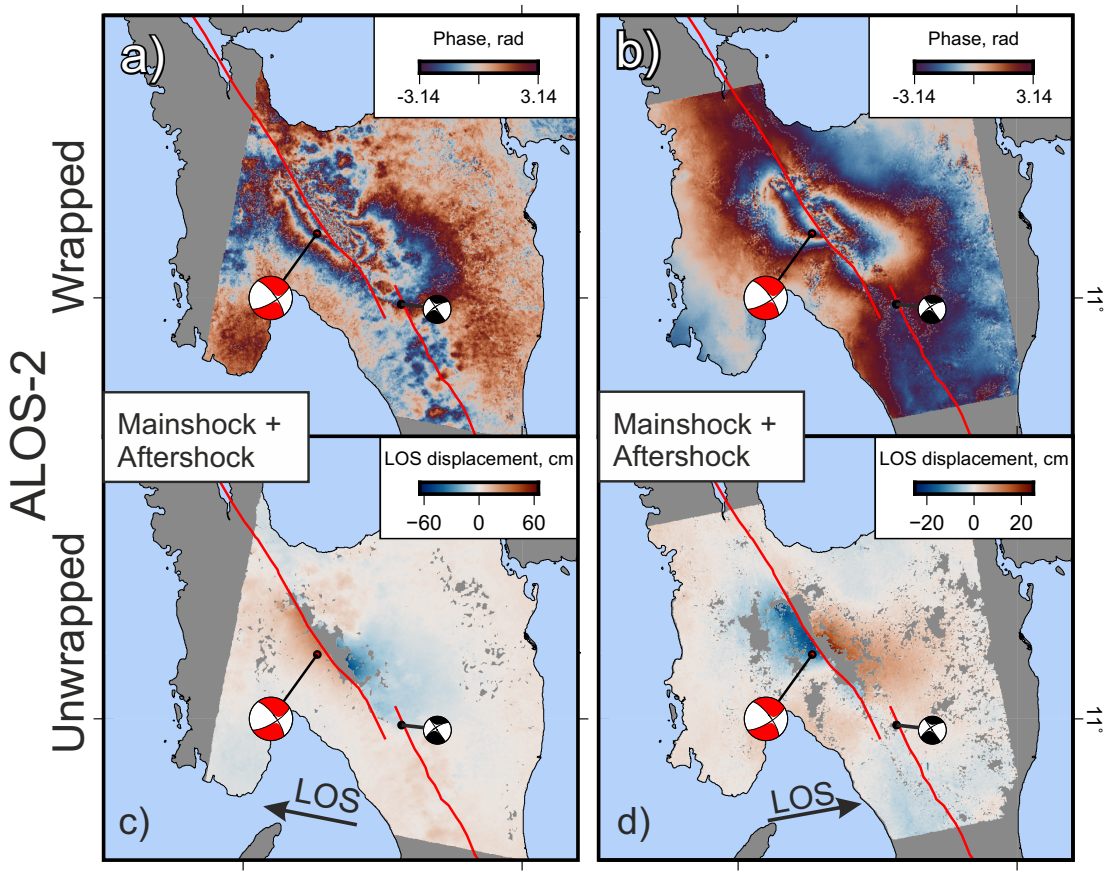


Figure 4.13: Pairs of wrapped and unwrapped coseismic interferograms, from ALOS-2 data, showing phase change and LOS displacement. These interferograms include both the 6 July mainshock (M_w 6.5) and the 10 July aftershock (M_w 5.8). Each map pair shows filtered wrapped interferogram (top) and unwrapped displacement (bottom). Positive unwrapped LOS displacement indicates movement towards the satellite. Focal mechanisms of the mainshock (red) and aftershock (black) are included for reference. ALOS-2 descending track 136 (a,c), and ALOS-2 ascending track 24 (b,d). See Table 4.3 for details of interferogram pairs.

from both events occurred at depths shallower than 7 km. The largest magnitude of slip for the mainshock is confined to the upper 2 km of the fault, with up to 152 ± 21 cm of left-lateral slip (Figure 4.14a). This corresponds well with the location of the mapped surface ruptures in Tongonan (Figure 4.11a and 4.11b). The modeled strike-slip magnitude is only slightly higher than the observed field offsets (*PHIVOLCS Quick Response Team*, 2019, ∼1.1 m,) (Figure 4.11c). Likewise, vertical displacements can also be observed in the field, with the eastern side downthrown

by about 50 cm (*PHIVOLCS Quick Response Team*, 2019) (Figure 4.11b). In our model, dip-slip of 27 ± 33 cm on the patch with the greatest slip reflects this, but is not as well-constrained as the strike-slip (i.e., the standard deviation is larger than the mean). The discrepancies between the field observations and the model may be due to local ground conditions that can attenuate slip, and may also reflect limitations imposed by the size of the model's shallowest patches.

The aftershock model shows slip on fault patches directly south of the mainshock deformation, with a maximum slip of 36 ± 10 cm at depths between 2-7 km (Figure 4.14b). As similarly apparent in the interferograms, it is notable that most of the aftershock slip is located just south of the fault bend. This may indicate that the fault geometry played a role in the spatio-temporal distribution of seismic slip, which is an implication we discuss further in the discussion that follows. Comparing the distribution of total seismic slip with the aseismic slip model shows the coincidence of the seismic slip distribution with the patches that have a significant slip deficit in the interseismic period (Figure 4.14c).

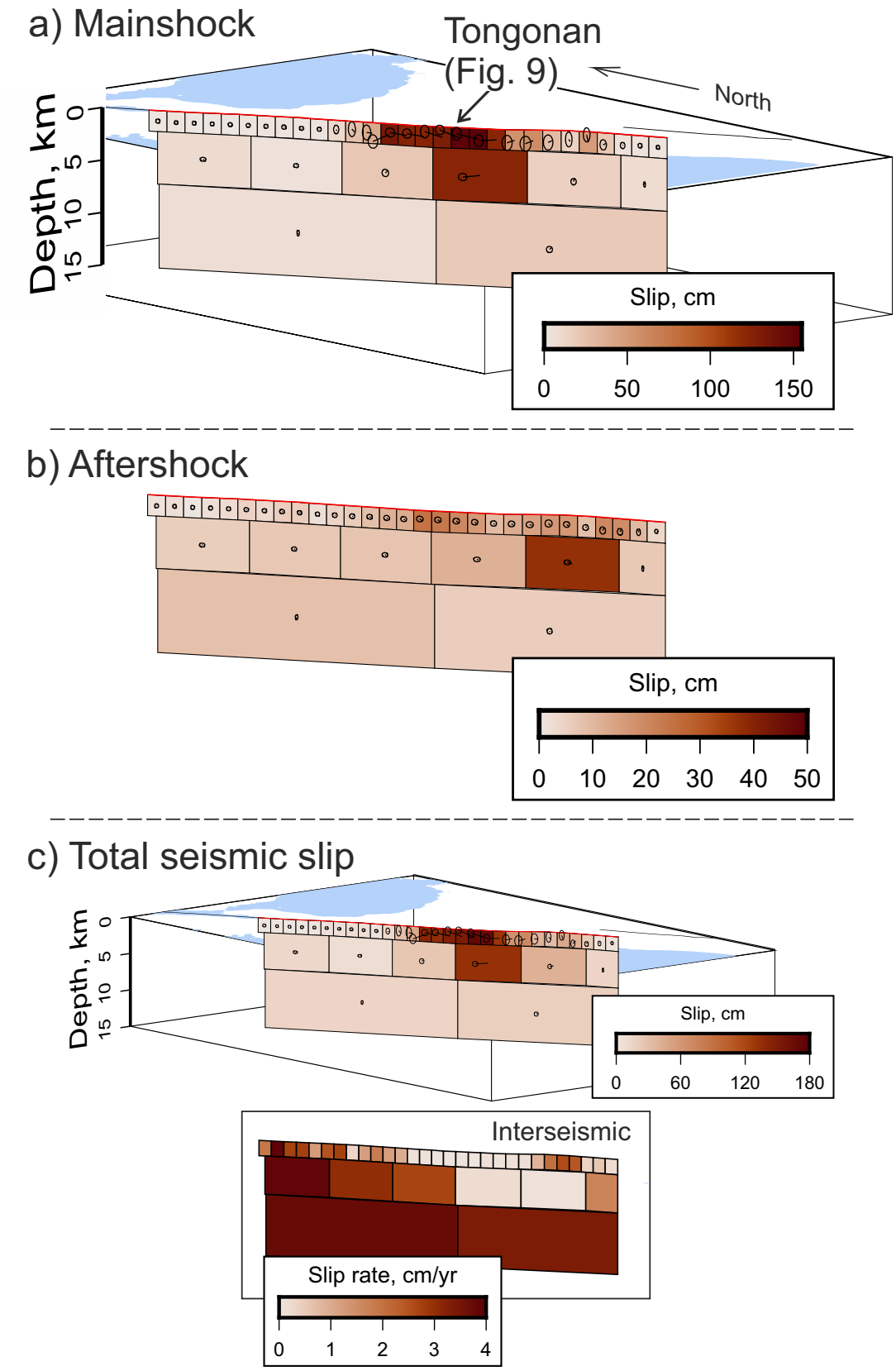


Figure 4.14: a) Posterior mean slip model, in cm, for the 6 July 2017 M_w 6.5 mainshock. Arrows and ellipses show slip direction and 95% confidence interval, respectively. b) The same, but for the 10 July 2017 M_w 5.8 aftershock. c) Combined mainshock and aftershock slip. Inset: Interseismic aseismic slip distribution on the same segment (as in Figure 4.8).

4.5 Discussion

Different lines of evidence have been used to investigate the nature and causes of aseismic fault slip (see reviews by *Avouac*, 2015; *Harris*, 2017; *Bürgmann*, 2018). Our slip models representing different stages of the seismic cycle provide a basis for discussion of the mechanics of faulting, such as what controls seismic rupture extent and why faults slip aseismically, and earthquake recurrence. One important aspect of our modeling, which makes it reasonable to compare the slip distributions for different stages of the seismic cycle, is that we independently derived the interseismic and coseismic models with few *a priori* assumptions on the slip distribution or the relationship of the two modes of slip—our only assumption being the fixed fault geometry.

4.5.1 Complementary distribution of seismic and aseismic slip

Juxtaposing the extent of shallow seismic slip with the along-strike variations of interseismic slip rate, we can observe the clear complementarity between them (Figure 4.15). This is also apparent when comparing the interseismic and coseismic slip models (Figure 4.14c). If we consider a rate-and-state friction perspective, the retardation of seismic slip can be related to the frictional properties of a rate-strengthening (RS) material (*Scholz*, 1998). The existence of such a material along the fault will have two impacts: 1) increase of friction with increasing rate of slip will slow and potentially arrest a rupture propagating at seismic rate; and 2) a RS material favors aseismic slip during the interseismic period. The latter consequence reduces the shear stress available on the fault that could otherwise have helped the seismic rupture to propagate, even in a RS environment (*Kaneko et al.*, 2010; *Thomas et al.*, 2014c).

Figure 4.15 suggests that seismic slip did propagate slightly into the sections that slip aseismically by no more than five kilometers to the north and ten kilometers to the south. As demonstrated by numerical models of fault slip, the stress changes ahead of the rupture tip can permit the coseismic rupture to propagate into RS zones (e.g., *Tse and Rice*, 1986; *Boatwright and Cocco*, 1996; *Thomas et al.*, 2014c). The propagation of seismic slip into sections with low slip deficit may also be attributed to the partial coupling on patches that do not slip aseismically at the full tectonic rate, as this leads to stress accumulation as described above (*Kaneko et al.*, 2010). We note that our ability to resolve slip variability in Leyte is limited by the patch sizes of our discretized fault model, i.e., we only have slip measurements every two kilometers at the surface.

4.5.2 The role of geometry and structural complexity on seismic and aseismic slip distribution

Observations of the relationship between fault geometry and variations in aseismic slip rate are limited. Nevertheless, *Moore and Byerlee* (1992) suggest there is a link between the orientation of secondary structures (e.g. Riedel-type shears) and the sliding dynamics (seismic or aseismic behavior). Observations of aseismic slip on the Haiyuan Fault (China) show that bursts of slow slip are constrained by fault geometry (*Jolivet et al.*, 2015a). *Romanet et al.* (2018) have also demonstrated numerically that a fault with parallel branches and no variations in frictional properties can influence the sliding dynamics. On the other hand, many studies have highlighted how fault bends and stepovers appear to control the extent of seismic ruptures (e.g. *Wesnousky*, 2006; *Biasi and Wesnousky*, 2017, and references therein).

In Leyte, the southern limit of the seismic slip distribution of the M_w 6.5 earthquake coincides with the fault bend, south of Tongonan. The Tongonan Segment ruptured further south of the bend during the M_w 5.8 aftershock, four days after

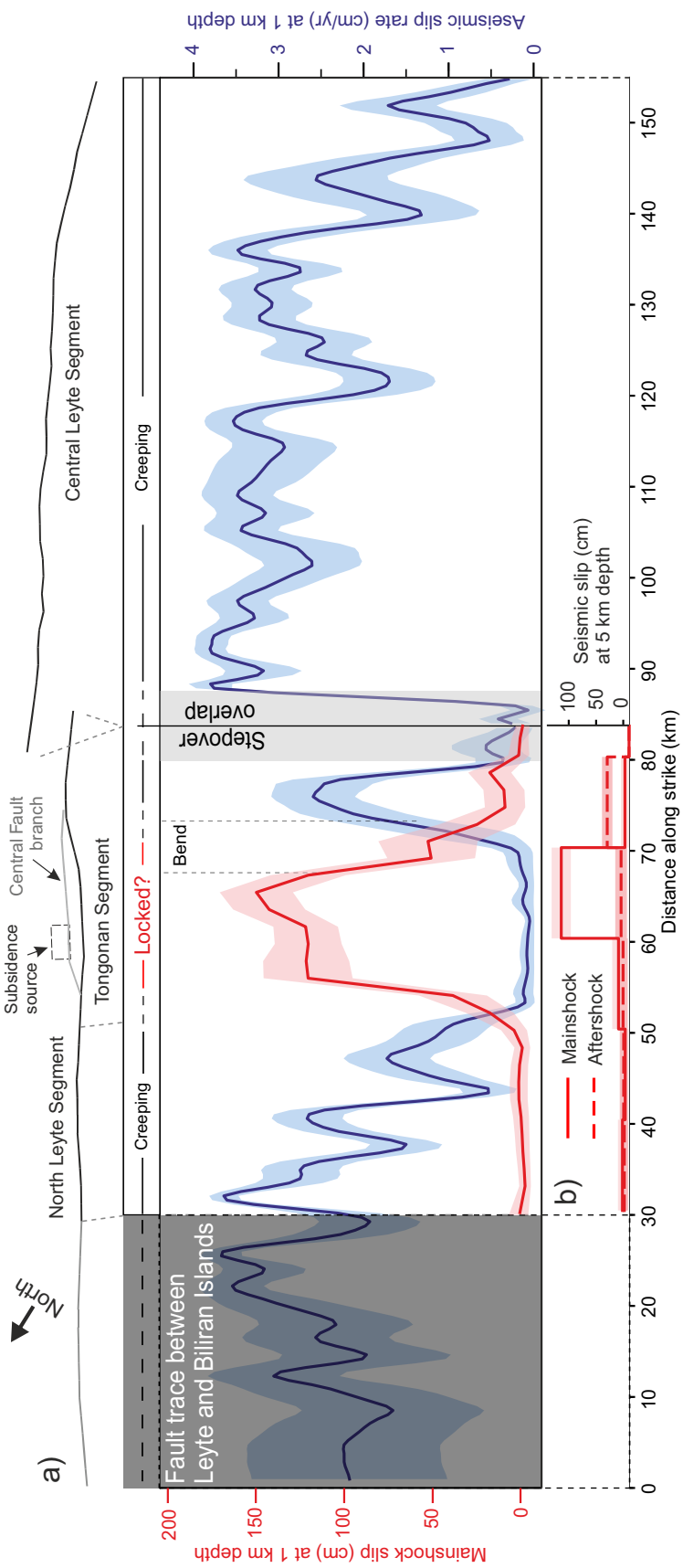


Figure 4.15: Rate and extent of aseismic and seismic slip on the Philippine Fault in Leyte. a) Interseismic slip rate (blue) and strike-slip component of M_w 6.5 mainshock (red) at 1 km depth. Shaded area from 0-30 km distance indicates section of the fault that goes off the coast of Leyte, where slip at 1 km depth may be poorly resolved. Map view of the surface trace of the main Philippine Fault and Central Fault branch, and surface projection of the subsidence source is also shown for reference. Light blue and pink area: 1-σ uncertainty range slip of aseismic and seismic slip, respectively. b) Seismic slip at 5 km depth from the 6 July M_w 6.5 mainshock (red solid line) and the 10 July M_w 5.8 aftershock (dashed line), taken from slip of patches on the middle row of the models (Figure 4.14). Pink area also indicates 1-σ uncertainty range.

the mainshock, at slightly greater depths than during the mainshock (Figures 4.14 and 4.15b). This suggests that, instead of rupturing the whole locked section in one event, the fault bend may have controlled the spatio-temporal distribution of seismic slip during the July 2017 earthquake sequence.

In terms of the interseismic slip distirbution, as we noted in Section 4.3.5, residuals near Tongonan from our interseismic model might be related to the simplicity of the fault geometry used. If we consider faults from detailed maps of structures in the geothermal area, the linear trend in the data and residuals (Figures 4.8c and 4.8e) appears to coincide with the Central Fault Line sub-branch. Detailed structural studies of the geothermal area (e.g., *Aurelio et al.*, 1993; *Caranto and Jara*, 2015) also suggest that there are several other secondary faults in Tongonan, not considered in our model. The presence of these off-main fault structures are consistent with what can be expected along intersegments (e.g., *Manighetti et al.*, 2015; *Perrin et al.*, 2016, and references therein). Thus, strain dissipation may occur across several structures while shallower patches on the main fault in Tongonan remain locked during the interseismic.

To explore the effects of a more complex fault geometry on our results, we perform a separate test with a model that includes a Central Fault branch. We discretize the Central Fault as a vertical strike-slip fault with two-kilometer long patches that extend to two kilometers depth from the surface, and assign broad uniform priors (-4 to 4 cm/yr). While this doesn't completely get rid of the residuals, the model resolves aseismic slip on the Central Fault (Appendix Figures J.14 and J.15, respectively), and the Tongonan Segment appears to remain locked. Including even more secondary faults, based on detailed structural maps, may provide more realistic models and would probably further improve the model predictions, but better data coverage would then be required (e.g., InSAR observations from different look angles with less decorrelation, dense continuous GPS coverage). Moreover, on a broad scale,

large residuals in the near-fault zone are apparent only in Tongonan. Further work may also be done by comparing the inversion results with a detailed cartography of the microstructure around the different fault segments (e.g., damage, lithology, and permeability), something beyond the scope of this study. A complementary investigation of the afterslip will is also needed to understand further the physical parameters that control the spatio-temporal extent of the aseismic and seismic segments, and how they interact with each other.

4.5.3 Physical factors that can lead to aseismic slip

Based on the rich existing literature, several physical parameters, such as lithology, ambient temperatures, local pore pressure, and seismic history, can lead to aseismic slip on faults (e.g., *Avouac*, 2015; *Harris*, 2017; *Bürgmann*, 2018).

The active hydrothermal system in Leyte has been advocated as a factor promoting aseismic slip (*Duquesnoy et al.*, 1994). The circulation of heated fluids causes significant mineral alteration in geothermal systems in the Philippines (*Reyes*, 1990), leading to deposits with RS phyllosilicates, as observed on other comparable structures, e.g., the San Andreas Fault and the Longitudinal Valley Fault (*Moore and Rymer*, 2007; *Thomas et al.*, 2014b, respectively). In Leyte, mineralogical and geochemical analyses of lithologies encountered in geothermal exploration wells in Tongonan show extensive phyllosilicate alteration in the subsurface, with assemblages including talc, chlorite, smectite, and illite (*Reyes*, 1990; *Scott*, 2001). Depending on the ambient temperatures, these minerals and rock formations can display a RS or a rate-weakening (RW) behavior (*Blanpied et al.*, 1991; *Scholz*, 1998; *Saffer and Marone*, 2003; *den Hartog et al.*, 2012; *Okamoto et al.*, 2019). Temperatures in the geothermal wells in Tongonan at depths where these minerals are found range between 100°–300°C (*Reyes*, 1990; *Scott*, 2001). Furthermore, exploration wells drilled into the Quaternary volcanoes in central Leyte show that the volcanic deposits are

generally andesitic, and that the underlying Leyte ultramafic basement is as shallow as 800–1,600 m depth (*Ramos and Rigor*, 2005). They report that these basement rocks are serpentinized—with secondary minerals like talc, chlorite, actinolite, and antigorite—and have poor permeability for geothermal resource interests. As noted in Section 4.2.2, serpentinites, particularly those bearing talc, have been correlated to aseismic slip on creeping sections of the San Andreas Fault (*Moore and Rymer*, 2007). Related laboratory experiments further tested how the shearing of serpentinites against quartz-bearing rocks promotes aseismic slip (*Moore and Lockner*, 2013). The shallow occurrence of serpentinized rocks across Leyte (e.g., *Cole et al.*, 1989; *Suerte et al.*, 2005, as shown in Figure 4.2) alongside young andesitic volcanism could thus explain the inferred aseismic slip in our model at depth.

The presence of fluids can also favor pressure-solution creep as observed along the Parkfield segment (*Gratier et al.*, 2011) and on the Longitudinal Valley Fault (*Thomas et al.*, 2014b). In central Leyte, fluid upflow through the impermeable basement from depth is believed to be restricted to existing structural channels like andesitic dikes and faults (*Ramos and Rigor*, 2005). Besides, fluids can induce elevated pore-pressure conditions on the fault, thus reducing effective normal stress, which, if maintained for a long time, will further aseismic slip.

That being said, the above suggestions make it difficult to explain why the Tongonan Segment is locked, despite its location near the largest geothermal power plant of the Philippines, where extensive alteration and higher pore-pressures from the abundant amount of geothermal fluids can be expected. Geothermal resource surveys have indicated that the Tongonan Segment has poor permeability and low resource potential (*Caranto and Jara*, 2015). In that case, fluid circulation, and therefore mineral alteration and/or pressure-solution can be limited, thus favoring a RW type of behavior. In addition, one cannot exclude possible along-strike variations of lithology. The potential influence of the net fluid loss from geothermal production on the

stress field also needs to be carefully considered. If the removal of fluids from the geothermal reservoir causes fluid-saturated faults to drain (lowering pore pressure), then normal stress on the fault will increase. This may be the case for the shallowest faults close to the subsidence source. However, whether anthropogenic activity in the upper two kilometers can affect the stresses at deeper patches (i.e., greater than two kilometers depth) or not is an open question, given that we can expect natural circulation of hydrothermal fluids across the volcanic arc. Detailed analysis of fault zone lithology and geophysical data will be needed before we can directly correlate the myriad of conditions in Leyte with the behavior of the fault.

4.5.4 Seismic and aseismic slip budget: probabilistic return period of significant earthquakes on the Tongonan Segment

Our modeling results allow the estimation of the relative proportion of coseismic and interseismic slip on the Leyte segment of the Philippine Fault, and, thus, permit us to draw inferences regarding the return period of earthquakes in this area. It is important to note the large uncertainties involved in this discussion, as all possible sources of errors, arising from measurement errors and modeling assumptions, are difficult to fully follow through. Furthermore, we can only compare the coseismic strike-slip component with our interseismic model, as the latter does not include dip-slip. However, it is still worth illustrating the kind of questions that can be addressed based on the probabilistic modeling presented in this paper.

From our ensemble of probable coseismic slip models, we can draw a probability distribution of seismic moment (M_o) (e.g., *Minson et al.*, 2014). As shown in Figure 4.16, if we consider only the patches below Tongonan, the mainshock moment follows a Gaussian distribution with a mean of 4.34×10^{18} N m ($\sim M_w$ 6.4) and a standard deviation of 0.67×10^{18} N m (hereafter referred to as $4.34 \pm 0.67 \times 10^{18}$ N m). Equiv-

alently, the aftershock moment is $1.20 \pm 0.48 \times 10^{18}$ N m ($\sim M_w$ 5.9). The seismic moments reported by the USGS for the mainshock and the aftershock are higher and lower, respectively, though the moment magnitudes do not differ greatly (Table 4.4). Our moment magnitude estimates for the mainshock are slightly smaller than the magnitudes from existing slip models also derived from InSAR data (Table 4.4 *Fukushima et al.*, 2019; *Yang et al.*, 2018). However, as previously mentioned in Section 4.4, it is important to note that the interferograms used in these studies span the 10 July aftershock deformation as well. Discrepancies may also exist due to different fault parameterizations (e.g., Yang et al., 2018 and Fukushima et al., 2019 both suggest steep east-dipping faults) and assumptions on the shear modulus of the fault, which for our estimates we set to 30 GPa. If we include the dip-slip component, the moment magnitude we obtain for both the mainshock and aftershock are only slightly higher (Table 4.4).

We can then compare the seismic moment of the July 2017 earthquakes with the slip deficit accumulated during interseismic period. Interseismic strain may translate to an accumulation of seismic moment deficit at a certain rate ($\dot{M}_{o_{deficit}}$). Similar to calculations of interseismic fault coupling (e.g., *Mccaffrey*, 2002), this can be computed by integrating the slip rate deficit over the locked fault area (the slip potency deficit; e.g., *Thomas et al.*, 2014a) and assuming a shear modulus (μ), as:

$$\dot{M}_{o_{deficit}} = \mu \sum_i \left(V_{LG} - V_{int_i}\right) A_i \tag{4.5}$$

where A_i is the area of the fault patch, V_{LG} is the long-term slip rate, and V_{int_i} is the slip rate during the interseismic period. Obtaining a PDF of $\dot{M}_{o_{deficit}}$ from our posterior PDF of interseismic slip (e.g., *Michel et al.*, 2017) suggests that seismic moment deficit accumulates at a rate of $1.49 \pm 0.44 \times 10^{17}$ Nm/yr ($\sim M_w$ 5.4 per year) along the Tongonan Segment (Figure 4.16c), assuming that our model of interseismic slip deeper than 15 km depth (3.3 ± 0.2 cm/yr) is representative of V_{LG}.

Table 4.4: Seismic moment (M_o) and moment magnitude (M_w) estimates of the July 2017 earthquakes. M_o uncertainties and M_w ranges are based on the standard deviation and the 2.5 and 97.5 percentile of the marginals, respectively.

	Seismic Moment, in $\times 10^{18}$ N m and Magnitude				
	Seismological	Geodetic			
		This study			
	USGS	Strike-slip only[a]	SS + DS[b]	F2019[c]	Y2018[d]
Mainshock	7.06 (M_w 6.5)	4.34 ± 0.67 (M_w 6.3–6.4)	5.38 ± 0.49 (M_w 6.4–6.5)	6.80 (M_w 6.5)	7.78 (M_w 6.6)
Aftershock	0.721 (M_w 5.8)	1.20 ± 0.48 (M_w 5.7–6.2)	1.73 ± 0.46 (M_w 5.9–6.2)	-	-

[a]Seismic moment obtained from strike-slip component only.
[b]Seismic moment from total slip (combined strike-slip and dip-slip component).
[c]From *Fukushima et al.* (2019), using only ALOS-2 data.
[d]From *Yang et al.* (2018), using both Sentinel-1 and ALOS-2 data spanning both the mainshock and aftershock.

The return period (T) of earthquakes like the July 2017 events can be estimated, given that:

$$T = \frac{M_{o_{July2017}}}{\dot{M}_{o_{deficit}}}. \tag{4.6}$$

Through random sampling of the interseismic slip rate and coseismic slip probability distributions, we obtain a probability distribution for the return period. In Tongonan, events with the same seismic moment as the mainshock can have a return period of any span between 16 and 63 years (based on the 95% confidence interval of the PDF; blue distribution in Figure 4.16d). For the combined moment of the mainshock and aftershock strike-slip ($5.54 \pm 0.57 \times 10^{18}$ N m), the likely return period range becomes 22–79 years (orange PDF in Figure 4.16d). The 70-year interval between the June 1947 M_s 6.9 and July 2017 M_w 6.5 earthquakes is at the upper end of the tail of the PDF for the mainshock only return period, while it is within the 2-σ bounds of the PDF for the combined mainshock-aftershock case (orange PDF in Figure 4.16d). In principle, accurate assessments of earthquake recurrence should also include the cumulative moment released during the afterslip period, which we have not isolated in this study. If the Philippine Fault in Leyte behaves similarly to the Longitudinal Valley Fault after the M_w 6.8 2003 Chengkung earthquake, this is not a negligible amount (e.g., 75% of the coseismic moment; *Thomas et al.*, 2014a). Therefore, including afterslip in the calculation could significantly increase the return period of M_w 6.5 earthquakes in the area (shifting our return period PDFs to higher values). Smaller aftershocks would only slightly increase the return period (i.e., the next largest ones, other than the aftershock we model, are mb 5.0 and mb 5.3 events that may increase the return period PDF by a few years), and we also do not account for the possibility of off-fault earthquakes. Finally, we note that, while we have assumed a value for the shear modulus to determine the equivalent interseismic moment deficit and coseismic moment, Equation 4.6 shows that our estimates

of the return period are independent of the value of the shear modulus.

The aforementioned considerations, along with the complementarity of the aseismic and seismic slip distributions from our models (Figures 7 and 12), and the similarity of the waveforms of the 1947 and 2017 earthquakes (*Fukushima et al.*, 2019), support the possibility that the Tongonan Segment may indeed be a site of repeating earthquakes with M_w about 6.5. The seismic catalog of smaller earthquakes may warrant a closer look. If we were to compare the modern instrumental record (Figure 4.2) with the slip deficit and locking on the fault (Figure 4.15), there is a stark difference in the clustering of $M_s > 1$ seismicity between the partially locked Northern Leyte Segment and the generally uncoupled Central Leyte Segment. However, the location of the epicenters don't exactly plot directly on the main fault trace. Event relocation (e.g., *Waldhauser and Ellsworth*, 2000, among others) will be needed for a robust analysis to distinguish earthquakes that might be related to diffuse faulting in the vicinity of the relay zone from possible smaller asperities on the fault (*Tse et al.*, 1985).

4.5.5 Limitations of assuming elastic homogeneity

Our models and the correlation of the slip modes with different local geological features has led us to several physical explanations for the observed behavior of the Philippine Fault in Leyte. Nonetheless, the homogeneous elastic modeling approach, useful in understanding fault behavior to first order, has limitations in representing possible structural complexity. Microstructural studies suggest that well-developed fault damage zones can modify the elastic properties of the material surrounding the fault compared to background values (*Walsh*, 1965a,b; *Faulkner et al.*, 2006), resulting in lower S-wave and P-wave velocities in the damage zone (e.g., *Froment et al.*, 2014). These lower values of the elastic moduli will have an impact on the amount of energy stored in the medium during the interseismic period. Furthermore,

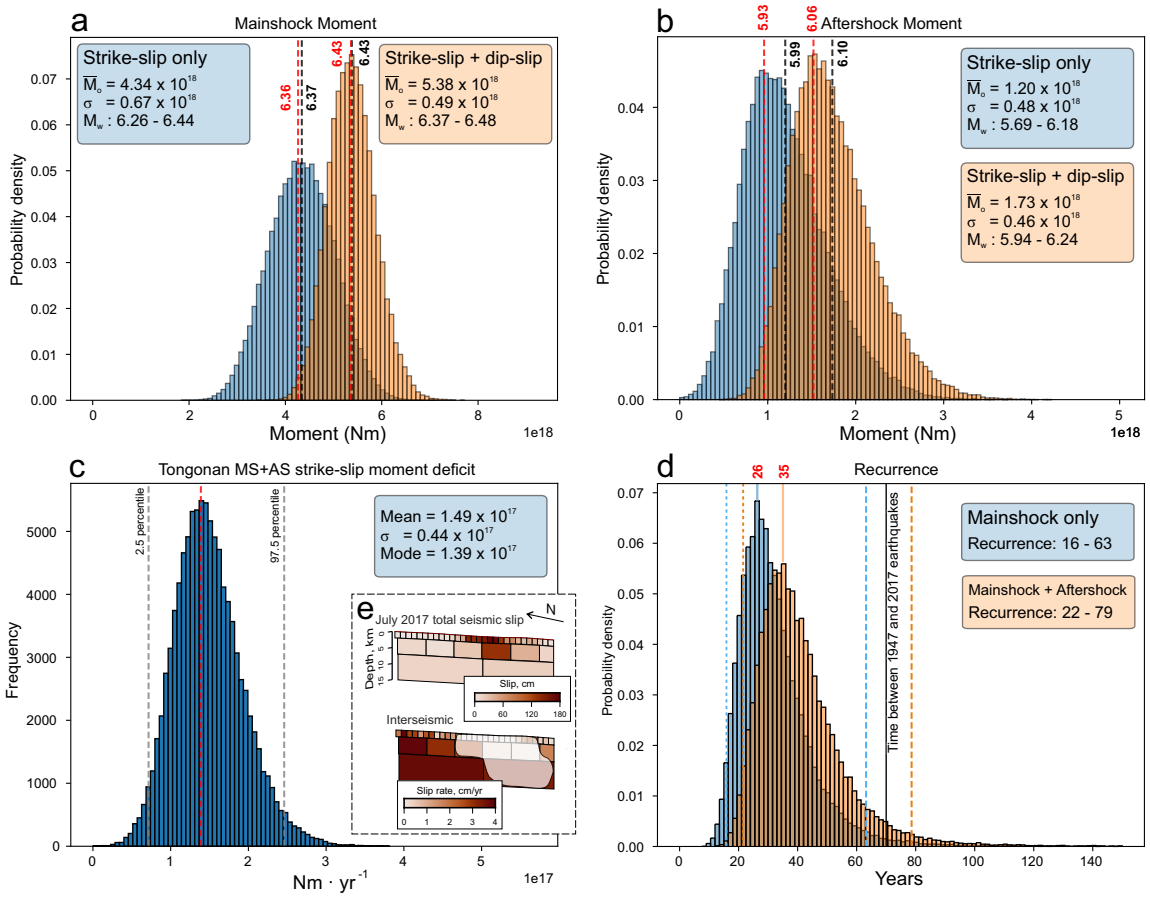


Figure 4.16: Probability distribution of seismic and aseismic slip budget, and return period. a) Seismic moment of 6 July 2017 mainshock. Blue PDF corresponds to the seismic moment if we include only the strike-slip component. Orange PDF shows the seismic moment when we include both strike-slip and dip-slip components. Red and black dashed lines indicate the mode and the mean of the PDF, respectively, labeled with the equivalent moment magnitude. b) The same as (a) but for the 10 July 2017 aftershock. c) Interseismic strike-slip moment deficit rate. Interval between dotted and dashed lines indicates the 95% confidence interval. d) Return period PDF for events similar to the mainshock only (blue) and combined moment of the mainshock and the aftershock (orange). Recurrence range is based on the lower and upper bounds of the return period 95% confidence interval. e) Coseismic and interseismic models, with white shaded area showing patches used in the slip budget calculation.

using a stratified elastic structure generally requires higher slip values near the surface to match geodetic observations (*Jolivet et al.*, 2015b). Careful evaluation of the 3D elastic structure is therefore needed here to further evaluate the effect of elastic heterogeneities on the distribution of seismic and aseismic slip, and therefore on the the return period of large earthquakes in the area.

4.6 Summary and Conclusions

We present the first probabilistic models of aseismic and coseismic slip along the Philippine Fault, specifically on Leyte island where the fault was generally thought of as aseismic prior to the earthquakes in July 2017. We highlight the spatial variations of aseismic slip rate along-strike and at depth, on around 100 km of the fault, with certain sections of the fault slipping aseismically at rates that match the long-term slip rate. We also identify the 20-km long Tongonan Segment that accumulates significant slip deficit. This segment may represent a locked asperity that can be the site of recurring earthquakes, similar to the M_w 6.5 and M_w 5.8 earthquakes in July 2017. In this paper, we have drawn observations from geothermal exploration work—primarily, the presence of hydrothermal fluids and rate-strengthening minerals—that can explain the propensity of the Philippine Fault in Leyte to slip aseismically. Detailed mapping and laboratory analysis, however, are required to draw any steady conclusions especially when considering that part of the fault appears to be locked and seismogenic.

The role played by the complex fault architecture—like the bend, parallel branches, and secondary faults in Tongonan—needs to be investigated using better surface deformation data, along with a more detailed analysis of the reported low permeability on the Tongonan segment (*Caranto and Jara*, 2015). The coincidence of these factors could influence the slip dynamics and stressing rate on the locked fault patches (e.g., *Ghosh et al.*, 1992; *Romanet et al.*, 2018). This has implications for the estimation of earthquake recurrence, and, more generally, to our understanding of the factors that drive aseismic and seismic slip on faults.

More broadly, in the regional tectonic sense, the July 2017 earthquakes in Leyte fall within the ideas of slip decoupling and strain partitioning across the Philippine Mobile Belt (*Fitch*, 1972; *Barrier et al.*, 1991; *McCaffrey*, 1996; *Aurelio*, 2000b). Our models provide a detailed look on the heterogeneity of the mode of deformation on

the Philippine Fault and give new insights to the active tectonics of the Philippines.

Chapter 5

Summary and concluding remarks

This thesis has investigated faults in different tectonic settings–an intracontinental mountain belt (Tien Shan), an intra-arc convergence zone (Mindanao), and a large-scale transcurrent fault (Philippine Fault)–with an emphasis on analyzing geologic and geodetic evidence of seismic and/or aseismic slip in detail. I have identified and characterized previously unknown sources of seismic hazard, improved our understanding of sparsely studied structures, and evaluated how faults in the central Tien Shan and the Philippines could be the source of earthquakes with magnitudes from 6.5 to 7.4–large enough to cause considerable damage to nearby developing communities. At the same time, I correlate the mode of fault slip to the geologic parameters around the faults, which may indicate how the geology controls the behavior of faulting.

In doing so, two related threads emerge from the findings in each of the case studies: 1) the role of shallow crustal heterogeneity in controlling the extent of seismic slip and the observed relationship between seismic and aseismic slip, and 2) that inferring aseismicity with sparse geodetic observations underestimates the seismogenic potential of faults in diffuse fault zones. These are borne out of observations that are correlative and do not necessarily mean causality. In any case, these findings generally echo the hypotheses developed from studies of faults that have undergone

more scrutiny (see review by *Bürgmann*, 2018). Hence, it is valuable to highlight these two threads to better put them in the context of our existing knowledge of fault and earthquake mechanics, and seismic hazard.

5.1 The relationship between shallow crustal heterogeneity and seismic ruptures

The shortening across the intermontane basins in the Tien Shan appears to happen differently between the wide and the narrow basins. In the narrow basins, like Karakudzhur and eastern Naryn, and in other mapping efforts in other narrow basins like Chon-Aksu and Chon-Kemin (*Bogdanovich et al.*, 1914; *Arrowsmith et al.*, 2016), generally E–W trending thrust surface ruptures are clearly present. Most of the wider basins that have been surveyed in some detail do not have any known evidence of earthquake-related ruptures. Whether this is due to strain being accommodated aseismically, as *Goode et al.* (2011) suggest in western Naryn and (*Mackenzie et al.*, 2018) imply in Karkara, or because the fault ruptures are buried in the basin sediments, is unresolvable with the existing geodetic data.

The study on the 2019 southern Mindanao earthquake sequence gives us a reference on how blind faults in basins can be the source of earthquakes, with thanks to studies on the basin stratigraphy (e.g., *Tamesis*, 1981; *Pubellier et al.*, 1991). Also, it allows the exploration of how seismic faulting could be limited by a local rheological and stress perturbation due to volcanism (Apo Volcano).

The Philippine Fault on Leyte island shows how InSAR data analysis greatly improves our understanding of the seismogenic potential of faults by mapping the rate and extent of fast and slow slip on the same fault, and how the locking of the fault manifests in a specific section of the fault—along the relay zone. Only a handful of faults in the world have measurements of their geodetic behavior at

different parts of the earthquake cycle along with the observed physical properties of the fault zone (*Harris*, 2017). Whether there are other sources of heterogeneity on the fault in Leyte that can promote locking only along the Tongonan segment needs to be investigated further. Nevertheless, the existing knowledge on the geology of Leyte anchors several discussion points.

5.2 Using geodesy with geology to characterize fault behavior, apparent aseismicity, and seismic hazard

The methods of geodetic analyses (GPS, InSAR, and photogrammetry) that I have adapted to study the faults in the Tien Shan and the Philippines have become much more widely used in the past two decades (as reviewed by *Avouac*, 2015, among others). However, studying strain accumulation and earthquakes is more common on plate boundary settings due to the more obvious seismic risk (*England and Jackson*, 2011). Further, less complex fault systems provide practical means for establishing analytical solutions for fault mechanics, i.e., it is easier to observe fast tectonic deformation and uncomplicated fault geometries simplifies physical modeling. Hence, the seismogenic potential of faults far from 'major' structures are poorly known and maybe underestimated. The exploration for active faults can sometimes be biased by our knowledge of historical seismicity, which may be incomplete, and in favor of prominent structures on the surface.

Mapping the faults that have evidence of Holocene ruptures in the central Tien Shan and the 2019 earthquakes in southern Mindanao highlights how seismic hazard sources may not always have a clear geomorphic expression, and is also dependent on that availability of high-resolution data. Faulting in these areas that have broad deformation zones is closely linked with complex tectonics. Active shortening is

distributed across several structures in these regions and involves the reactivation of existing ones. Like other work in these regions (e.g., *Campbell et al.*, 2019; *Rimando et al.*, 2019), none of the results in this thesis would be apparent without pointing out evidence from careful juxtaposition of the geodetic data with geologic mapping of faults a regional and local scales.

Even on the creeping section of the Philippine Fault, which is a zone of concentrated deformation unlike my other study areas, interseismic deformation is not uniformly accommodated along it. With the high resolution InSAR data, I even show how parallel locked and creeping branches of the same fault may exist alongside each other.

5.3 The way forward

While the enigma behind earthquake occurrence is rooted in our limited ability to directly observe fault slip in the Earth's crust, this thesis shows the continued importance of geodetic and geologic exploration of active faults in their natural setting. Diversifying the catalog of real-world faults for which we have data on the spatio-temporal variability of the manifestation of slip provides a wider array of examples that we can draw from to understand the mechanics of earthquakes and faulting. More widely, this endeavor also provides insight to regional tectonics and has important implications to anticipating the fault-related hazards–whether seismic or aseismic–to human society.

Further work in the Tien Shan and Mindanao could focus on careful interseismic deformation analysis with continuous GPS and InSAR time-series data. This will allow the characterization of fault behavior across and around the different basins . On the Philippine Fault, lateral lithological variability alongside the fault must be mapped to help constrain the contributing factors to frictional properties based on the fault zone materials. Further, continued monitoring of the mode of slip might

show temporal variability of slip rates on the fault, as seen on other 'major' strike-slip faults in the world (e.g., *Jolivet et al.*, 2013; *Rousset et al.*, 2016, 2019)

Bibliography

Abdrakhmatov, K. E., R. T. Walker, G. E. Campbell, A. S. Carr, A. Elliott, C. Hillemann, J. Hollingsworth, A. Landgraf, D. Mackenzie, A. Mukambayev, M. Rizza, and R. A. Sloan (2016), Multisegment rupture in the 11 July 1889 Chilik earthquake (Mw 8.0-8.3), Kazakh Tien Shan, interpreted from remote sensing, field survey, and paleoseismic trenching, *Journal of Geophysical Research: Solid Earth*, *121*(6), 4615–4640, doi:10.1002/2015JB012763. 2.1, 2.2, 2.3

Abdrakhmatov, K. Y., S. A. Aldazhanov, B. H. Hager, M. W. Hamburger, T. A. Herring, K. B. Kalabaev, V. I. Makarov, P. Molnar, S. V. Panasyuk, M. T. Prilepin, R. E. Reilinger, I. S. Sadybakasov, B. J. Souter, Y. A. Trapeznikov, V. Y. Tsurkov, and A. V. Zubovich (1996), Relatively recent construction of the Tien Shan inferred from GPS measurements of present-day crustal deformation rates, *Nature*, *384*(6608), 450–453, doi:10.1038/384450a0. 2.2

Agram, P., R. Jolivet, B. Riel, Y. Lin, M. Simons, E. Hetland, M. Doin, and C. Lasserre (2013), New Radar Interferometric Time Series Analysis Toolbox Released, *EOS Transactions*, *94*(7), 69–76, doi:10.1029/2011JB008731. 4.3.1

Ainscoe, E. A., K. E. Abdrakhmatov, S. Baikulov, A. S. Carr, A. J. Elliott, C. Grützner, and R. T. Walker (2019), Variability in surface rupture between successive earthquakes on the Suusamyr Fault, Kyrgyz Tien Shan: Implications for palaeoseismology, *Geophysical Journal International*, *216*(1), 703–725, doi:10.1093/gji/ggy457. 2.2, 2.4.1, 2.4.1, 2.4.5, 2.5.1, 2.5.1

Allen, C. R. (1962), Circum-Pacific faulting in the Philippines-Taiwan Region, *Journal of Geophysical Research*, *67*(12), 4795–4812, doi:10.1029/JZ067i012p04795. 4.2.1, 4.2.2

Anderlini, L., E. Serpelloni, and M. E. Belardinelli (2016), Creep and locking of a low-angle normal fault: Insights from the Altotiberina fault in the Northern Apennines (Italy), *Geophysical Research Letters*, *43*(9), 4321–4329, doi:10.1002/2016GL068604. 4.1

Anderson, J. G., G. P. Biasi, and S. G. Wesnousky (2017), Fault-scaling relationships depend on the average fault-slip rate, *Bulletin of the Seismological Society of America*, *107*(6), 2561–2577, doi:10.1785/0120160361. 2.5.1

Apuada, N. A., R. E. R. Olivar, and N. D. Salonga (2005), Repeat Microgravity and Leveling Surveys at Leyte Geothermal Production Field, North Central Leyte, Philippines, in *Proceedings of the Thirtieth Workshop on Geothermal Reservoir Engineering*, vol. 30, pp. 403–411, Stanford University, Stanford Geothermal Program, Stanford, California. 4.1, 4.2.2, 4.3, 4.3.1, 4.5, 4.3.3, 4.3.4, 4.6, J.6

Arrowsmith, R., C. Crosby, A. Korjenkov, E. Mamyrov, I. Povolotskaya, B. Guralnik, and A. Landgraf (2016), Surface rupture of the 1911 Kebin (Chon-Kemin) earthquake, Northern Tien Shan, Kyrgyzstan, in *Seismicity, Fault Rupture and Earthquake Hazards in Slowly Deforming Regions, Geological Society of London, Special Publications*, vol. 432, edited by A. Landgraf, S. Kübler, E. Hintersberger, and S. Stein, pp. 233–253, doi:10.1144/SP432.10. 1.2, 2.1, 2.2, 2.5.1, 5.1

Atzori, S., and A. Antonioli (2011), Optimal fault resolution in geodetic inversion of coseismic data, *Geophysical Journal International*, *185*(1), 529–538, doi:10.1111/j.1365-246X.2011.04955.x. I

Aurelio, M. A. (2000a), Tectonics of the Philippines Revisited, *Journal fo the Geological Society of the Philippines*, *55*(1-2), 119–186. 3.7.2, 3.6

Aurelio, M. A. (2000b), Shear partitioning in the Philippines: Contraints from the Philippine fault and global positioning system data, *Island Arc*, *9*(4), 584–597, doi:10.1046/j.1440-1738.2000.00304.x. 3.2, 4.2.1, 4.6

Aurelio, M. A., E. S. Pagado, and H. J. Tebar (1993), Kinematics of Philippine Fault system at the Tongonan Geothermal Field, N. Leyte: Implications for Geothermal Exploration and Development, *Journal of the Geological Society of the Philippines*, *48*(1-2), 1–20. 4.2.2, 4.2, 4.3.5, 4.10, 4.5.2, J.13

Aurelio, M. A., W. J. Simons, R. Almeda, and EC-Philippine GPS Team (1998), Present-Day Plate Motions in the Philippines: Interpretation of GPS Results of GEODYSSEA. 3.1, 3.7.3

Aurelio, M. A., R. E. Peña, and K. J. L. Taguibao (2013), Sculpting the Philippine archipelago since the Cretaceous through rifting, oceanic spreading, subduction, obduction, collision and strike-slip faulting: Contribution to IGMA5000, *Journal of Asian Earth Sciences*, *72*, 102–107, doi:10.1016/j.jseaes.2012.10.007. 3.2, 4.1

Aurelio, M. A., J. D. B. Dianala, K. J. L. Taguibao, L. R. Pastoriza, K. Reyes, R. Sarande, and A. Lucero (2017), Seismotectonics of the 6 February 2012 Mw 6.7 Negros Earthquake, central Philippines, *Journal of Asian Earth Sciences*, *142*, 93–108, doi:10.1016/j.jseaes.2016.12.018. 3.8

Avouac, J.-p. (2015), From Geodetic Imaging of Seismic and Aseismic Fault Slip to Dynamic Modeling of the Seismic Cycle, *Annual Review of Earth and Planetary Sciences*, *43*(1), 150223150959,000, doi:10.1146/annurev-earth-060614-105302. 1.1, 4.1, 4.5, 4.5.3, 5.2

Bacolcol, T., E. Barrier, T. Duquesnoy, A. Aguilar, R. Jorgio, R. de la Cruz, and M. Lasala (2005), GPS Constraints on Philippine Fault slip rate in Masbate island, central Philippines, *Journal of the Geological Society of the Philippines*, *60*(1-2), 1–7. 4.2.1

Bagnardi, M., and A. Hooper (2018), Inversion of Surface Deformation Data for Rapid Estimates of Source Parameters and Uncertainties: A Bayesian Approach, *Geochemistry, Geophysics, Geosystems*, *19*(7), 2194–2211, doi:10.1029/2018GC007585. 4.3.4, 4.3.4

Bakun, W. H., B. Aagaard, B. Dost, W. L. Ellsworth, J. L. Hardebeck, R. A. Harris, C. Ji, M. J. Johnston, J. Langbein, J. J. Lienkaemper, A. J. Michael, J. R. Murray, R. M. Nadeau, P. A. Reasenberg, M. S. Reichle, E. A. Roeloffs, A. Shakal, R. W. Simpson, and F. Waldhauser (2005), Implications for prediction and hazard assessment from the 2004 Parkfield earthquake, *Nature*, *437*(7061), 969–974, doi:10.1038/nature04067. 4.1

Bande, A., E. R. Sobel, A. Mikolaichuk, A. Schmidt, and D. F. Stockli (2017), Exhumation history of the western Kyrgyz Tien Shan: Implications for intramontane basin formation, *Tectonics*, *36*(1), 163–180, doi:10.1002/2016TC004284. 2.2

Barnhart, W. D. (2017), Fault creep rates of the Chaman fault (Afghanistan and Pakistan) inferred from InSAR, *Journal of Geophysical Research: Solid Earth*, *122*(1), 372–386, doi:10.1002/2016JB013656. 3.1

Barnhart, W. D., M. J. Willis, R. B. Lohman, and A. K. Melkonian (2011), InSAR and optical constraints on fault slip during the 2010-2011 New Zealand earthquake sequence, *Seismological Research Letters*, *82*(6), 815–823, doi:10.1785/gssrl.82.6.815. 1.2

Barrier, E., P. Huchon, and M. A. Aurelio (1991), Philippine Fault: a key for Philippine kinematics, *Geology*, *19*(1), 32–35, doi:10.1130/0091-7613(1991)019¡0032:PFAKFP¿2.3.CO;2. 3.2, 4.2.1, 4.3.4, 4.3.5, 4.6

Bautista, M. L. P., and K. Oike (2000), Estimation of the magnitudes and epicenters of Philippine historical earthquakes, *Tectonophysics*, *317*, 137–169, doi:10.1016/S0040-1951(99)00272-3. 4.2.1, 4.2.2

Beck, S. L., and L. J. Ruff (1985), The rupture process of the 1976 Mindanao Earthquake, *Journal of Geophysical Research*, *90*(B8), 6773, doi:10.1029/jb090ib08p06773. 3.2, 3.6

Besana, G. M., and M. Ando (2005), The central Philippine Fault Zone: Location of great earthquakes, slow events, and creep activity, *Earth, Planets and Space*, *57*(10), 987–994, doi:10.1186/BF03351877. 4.2.1, 4.2.2, 4.4

Biasi, G. P., and S. G. Wesnousky (2017), Bends and Ends of Surface Ruptures, *Bulletin of the Seismological Society of America*, doi:10.1785/0120160292. 3.7.2, 4.5.2

Blanpied, M., D. Lockner, and D. Byerlee (1991), Fault stability at hydrothermal conditions, *Geophysical Research Letters*, *18*(4), 609–612. 4.5.3

Blanpied, M., C. Marone, and D. Lockner (1998), Quantitative measure of the variation in fault rheology due to fluid-rock interactions, *Journal of Geophysical Research*, *103*(B5), 9691–9712, doi:10.1029/98JB00162. 1.1

Blanton, C. M., T. K. Rockwell, A. Gontz, and J. T. Kelly (2020), Refining the spatial and temporal signatures of creep and co-seismic slip along the southern San Andreas Fault using very high resolution UAS imagery and SfM-derived topography, Coachella Valley, California, *Geomorphology*, *357*, 107,064, doi:10.1016/j.geomorph.2020.107064. 2.1

Boatwright, J., and M. Cocco (1996), Frictional constraints on crustal faulting, *Journal of Geophysical Research*, *101*, 13,895, doi:10.1029/96JB00405. 4.5.1

Bogdanovich, K., I. Kark, B. Korolkov, and D. Mushketov (1914), Earthquake in the Northern Districts of Tien Shan, 22 December 1910 (January 4, 1911). 2.2, 2.5.1, 5.1

Brace, W. F., and J. D. Byerlee (1966), Stick-slip as a mechanism for earthquakes, *Science*, *153*(3739), 990–992, doi:10.1126/science.153.3739.990. 1.1

Burbank, D. W., J. K. McLean, M. Bullen, K. Y. Abdrakhmatov, and M. M. Miller (1999), Partitioning of intermontane basins by thrust-related folding, Tien Shan, Kyrgyzstan, *Basin Research*, *11*(1), 75–92, doi:10.1046/j.1365-2117.1999.00086.x. 2.4.5

Burgette, R. J. (2017), Timing and process of lake and river terrace formation in the Kyrgyz Tien Shan, *Quaternary Science Reviews*, *159*, 15–34, doi:10.1016/j.quascirev.2017.01.003. 2.4.3

Bürgmann, R. (2018), The geophysics, geology and mechanics of slow fault slip, *Earth and Planetary Science Letters*, *495*, 112–134, doi:10.1016/j.epsl.2018.04.062. 1.1, 1.1, 1.2, 4.1, 4.5, 4.5.3, 5

Burgmann, R., D. Schmidt, R. M. Nadeau, M. D'Alessio, E. Fielding, D. Manaker, T. V. McEvilly, and M. H. Murray (2000), Earthquake potential along the Northern Hayward fault, California, *Science*, *289*(5482), 1178–1182, doi:10.1126/science.289.5482.1178. 4.1

Burtman, V. S., S. F. Skobelev, and P. Molnar (1996), Late Cenozoic slip on the Talas-Ferghana fault, the Tien Shan, central Asia, *Bulletin of the Geological Society of America*, *108*(8), 1004–1021, doi:10.1130/0016-7606(1996)108¡1004:LCSOTT¿2.3.CO;2. 2.2

Buslov, M. M., J. De Grave, E. A. Bataleva, and V. Y. Batalev (2007), Cenozoic tectonic and geodynamic evolution of the Kyrgyz Tien Shan Mountains: A review

of geological, thermochronological and geophysical data, *Journal of Asian Earth Sciences*, *29*(2-3), 205–214, doi:10.1016/j.jseaes.2006.07.001. 2.2, 2.3, 2.5.2

Campbell, G. E., R. T. Walker, K. Abdrakhmatov, S. Carolin, A. S. Carr, J. R. Elliott, J. Jackson, D. Mackenzie, M. Rizza, and A. Rodes (2019), Rapid Late Quaternary Slip, Repeated Prehistoric Earthquake Rupture, and Widespread Landsliding Associated With the Karakudzhur Thrust, Central Kyrgyz Tien Shan, *Tectonics*, pp. 3740–3764, doi:10.1029/2018TC005433. 2.1, 2.3, 2.4.4, 2.5.1, 2.5.2, 2.6, 5.2

Caranto, J. A., and M. P. Jara (2015), Factors Controlling Reservoir Permeability at the Leyte Geothermal Production Field, Tongonan, Philippines, in *Proceedings: World Geothermal Congress 2015*, Melbourne, Australia. 4.1, 4.2.2, 4.5.2, 4.5.3, 4.6

Cavalié, O., C. Lasserre, M. P. Doin, G. Peltzer, J. Sun, X. Xu, and Z. K. Shen (2008), Measurement of interseismic strain across the Haiyuan fault (Gansu, China), by InSAR, *Earth and Planetary Science Letters*, *275*(3-4), 246–257, doi:10.1016/j.epsl.2008.07.057. 1.2, 4.1

Cetin, E., Z. Cakir, M. Meghraoui, S. Ergintav, and A. M. Akoglu (2014), Extent and distribution of aseismic slip on the Ismetpaa segment of the North Anatolian Fault (Turkey) from Persistent Scatterer InSAR, *Geochemistry, Geophysics, Geosystems*, *15*(7), 2883–2894, doi:10.1002/2014GC005307. 4.1

Chaussard, E., R. Bürgmann, H. Fattahi, C. W. Johnson, R. Nadeau, T. Taira, and I. Johanson (2015), Interseismic coupling and refined earthquake potential on the Hayward-Calaveras fault zone, *Journal of Geophysical Research: Solid Earth*, *120*(12), 8570–8590, doi:10.1002/2015JB012230. 4.1

Chen, C. W., and H. A. Zebker (2002), Phase unwrapping for large SAR interferograms: Statistical segmentation and generalized network models, *IEEE Transactions on Geoscience and Remote Sensing*, *40*(8), 1709–1719, doi:10.1109/TGRS.2002.802453. 3.4

Cole, J., R. McCabe, T. Moriarty, J. A. Malicse, F. G. Delfin, H. Tebar, and H. P. Ferrer (1989), A preliminary Neogene paleomagnetic data set from Leyte and its relation to motion on the Philippine fault, *Tectonophysics*, *168*(1-3), 205–220, doi:10.1016/0040-1951(89)90376-4. 4.2.2, 4.5.3

Collettini, C., T. Tesei, M. Scuderi, B. Carpenter, and C. Viti (2019), Beyond Byerlee friction, weak faults and implications for slip behavior, *Earth and Planetary Science Letters*, *519*, 245–263, doi:10.1016/j.epsl.2019.05.011. 1.1

Craig, T. J., A. Copley, and J. Jackson (2014), A reassessment of outer-rise seismicity and its implications for the mechanics of oceanic lithosphere, *Geophysical Journal International*, *197*(1), 63–89, doi:10.1093/gji/ggu013. 3.3

Davis, D., J. Suppe, and F. A. Dahlen (1983), Mechanics of Fold-and-Thrust Belts and Accretionary Wedges, *Journal of Geophysical Research*, *88*(B2), 1153–1172. 2.5.2

De Batist, M., Y. Imbo, P. Vermeesch, J. Klerkx, S. Giralt, D. Delvaux, V. Lignier, C. Beck, I. Kalugin, and K. E. Abdrakhmatov (2002), *Bathymetry and Sedimentary Environments of Lake Issyk-Kul, Kyrgyz Republic (Central Asia): A Large, High-Altitude, Tectonic Lake*, pp. 101–123, Springer Netherlands, Dordrecht, doi:10.1007/978-94-010-0491-6$_9$. 2.5.2

Deev, E., A. Korzhenkov, I. Turova, T. L. Pavlis, D. Luzhanskii, J. Mažeika, S. Abdieva, and A. Yudakhin (2018), Large ancient earthquakes in the western Issyk-Kul basin (Kyrgyzstan, northern Tien Shan), *Journal of Asian Earth Sciences*, *166*, 48–65, doi:10.1016/j.jseaes.2018.07.019. 2.2

DeMets, C., R. G. Gordon, and D. F. Argus (2010), Geologically current plate motions, *Geophysical Journal International*, *181*(1), 1–80, doi:10.1111/j.1365-246X.2009.04491.x. 3.2, 4.1, 4.2.1

den Hartog, S. A., A. R. Niemeijer, and C. J. Spiers (2012), New constraints on megathrust slip stability under subduction zone P-T conditions, *Earth and Planetary Science Letters*, *353-354*, 240–252, doi:10.1016/j.epsl.2012.08.022. 4.5.3

Deng, J. (1998), Viscoelastic Flow in the Lower Crust after the 1992 Landers, California, Earthquake, *Science*, *282*(5394), 1689–1692, doi:10.1126/science.282.5394.1689. 4.1

Dianala, J. D. B., R. Jolivet, M. Y. Thomas, Y. Fukushima, B. Parsons, and R. Walker (2020), The relationship between seismic and aseismic slip on the Philippine Fault on Leyte Island: Bayesian modeling of fault slip and geothermal subsidence, *Journal of Geophysical Research: Solid Earth*, *125*(12), doi:10.1029/2020jb020052. 3.4, 3.7.2

Dimalanta, C. B., L. O. Suerte, G. P. Yumul, R. A. Tamayo, and E. G. L. Ramos (2006), A Cretaceous supra-subduction oceanic basin source for Central Philippine ophiolitic basement complexes: Geological and geophysical constraints, *Geosciences Journal*, *10*(3), 305–320, doi:10.1007/BF02910372. 4.2.2

Doin, M.-P., F. Lodge, S. Guillaso, R. Jolivet, C. Lasserre, G. Ducret, R. Grandin, E. Pathier, and V. Pinel (2011), Presentation of the small baseline NSBAS processing chain on a case example: the Etna deformation monitoring from 2003 to 2010 using Envisat data, in *Proceedings: ESA Fringe 2011 Workshop*, ESA, Frascati, Italy. 4.3.1

Dolan, J. F., L. J. McAuliffe, E. J. Rhodes, S. F. McGill, and R. Zinke (2016), Extreme multi-millennial slip rate variations on the Garlock fault, California: Strain super-cycles, potentially time-variable fault strength, and implications for system-level earthquake occurrence, *Earth and Planetary Science Letters*, *446*, 123–136, doi:10.1016/j.epsl.2016.04.011. 1.2

Dooley, T. P., and G. Schreurs (2012), Analogue modelling of intraplate strike-slip tectonics: A review and new experimental results, *Tectonophysics*, *574-575*, 1–71, doi:10.1016/j.tecto.2012.05.030. 3.6

Duputel, Z., J. Jiang, R. Jolivet, M. Simons, L. Rivera, J. P. Ampuero, B. Riel, S. E. Owen, A. W. Moore, S. V. Samsonov, F. Ortega Culaciati, and S. E. Minson (2015), The Iquique earthquake sequence of April 2014: Bayesian modeling accounting for prediction uncertainty, *Geophysical Research Letters*, *42*(19), 7949–7957, doi:10.1002/2015GL065402. 4.3.4

Duquesnoy, T. (1997), Contribution de la géodésie à l'étude de grands décrochements actifs associés à des zones de subduction à convergence oblique Exemples de la grande faille de Sumatra et de la faille Philippine, Ph.D. thesis, Univ. Paris-Sud, Orsay, France. 4.1, 4.1, 4.2.1, 4.3.1, 4.3.2, 4.5, 4.3.4, 4.3.5

Duquesnoy, T., E. Barrier, M. Kasser, M. Aurelio, R. Gaulon, R. S. Punongbayan, and C. Rangin (1994), Detection of creep along the Philippine Fault: First results of geodetic measurements on Leyte Island, central Philippine, *Geophysical Research Letters*, *21*(11), 975–978, doi:10.1029/94GL00640. 3.2, 4.1, 4.2.1, 4.2.2, 4.3.4, 4.3.5, 4.5.3

Dziewonski, A. M., T.-A. Chou, and J. H. Woodhouse (1981), Determination of earthquake source parameters from waveform data for studies of global and regional seismicity, *Journal of Geophysical Research: Solid Earth*, *86*(B4), 2825–2852, doi:10.1029/JB086iB04p02825. 2.1, 3.1, 3.3

Ekström, G., M. Nettles, and A. M. Dziewoński (2012), The global CMT project 2004-2010: Centroid-moment tensors for 13,017 earthquakes, *Physics of the Earth and Planetary Interiors*, *200-201*, 1–9, doi:10.1016/j.pepi.2012.04.002. 2.1, 3.1, 3.3

Elliott, J. R., R. J. Walters, and T. J. Wright (2016), The role of space-based observation in understanding and responding to active tectonics and earthquakes, *Nature Communications*, *7*, 1–16, doi:10.1038/ncomms13844. 1.2, 3.1, 4.1

England, P., and J. Jackson (2011), Uncharted seismic risk, *Nature Geoscience*, *4*(6), 348–349, doi:10.1038/ngeo1168. 1.2, 2.1, 5.2

England, P., and P. Molnar (2015), Rheology of the lithosphere beneath the central and western Tien Shan, *Journal of Geophysical Research: Solid Earth*, *120*, 3803–3823, doi:10.1002/2014JB011733.Received. 1.3, 2.1, 2.3, 2.2, 2.4, 2.23, 2.6

Fattahi, H., and F. Amelung (2016), InSAR observations of strain accumulation and fault creep along the Chaman Fault system, Pakistan and Afghanistan, *Geophysical Research Letters*, *43*(16), 8399–8406, doi:10.1002/2016GL070121. 1.2, 4.1

Faulkner, D. R., T. M. Mitchell, D. Healy, and M. J. Heap (2006), Slip on 'weak' faults by the rotation of regional stress in the fracture damage zone, *Nature*, *444*(7121), 922–925, doi:10.1038/nature05353. 4.5.5

Fialko, Y., M. Simons, and D. Agnew (2001), The complete (3-D) surface displacement field in the epicentral area of the 1999 Mw 7.1 Hector Mine earthquake, California, from space geodetic observations, *Geophysical Research Letters*, *28*(16), 3063–3066. 4.3.1

Fitch, T. J. (1972), Plate convergence, transcurrent faults, and internal deformation adjacent to Southeast Asia and the Western Pacific, *Journal of Geophysical Research*, *77*(23), 4432–4460. 4.6

Froment, B., J. J. McGuire, R. D. van der Hilst, P. Gouédard, E. C. Roland, H. Zhang, and J. A. Collins (2014), Imaging along-strike variations inmechanical properties of the Gofar transform fault, East Pacific Rise, *Journal of Geophysical Research: Solid Earth*, *119*, 7175–7194, doi:10.1002/2014JB011270.Received. 4.5.5

Fukushima, Y., M. Hashimoto, M. Miyazawa, N. Uchida, and T. Taira (2019), Surface creep rate distribution along the Philippine fault, Leyte Island, and possible repeating of Mw ∼6.5 earthquakes on an isolated locked patch, *Earth, Planets and Space*, *71*(118), 22, doi:10.1186/s40623-019-1096-5. 4.1, 4.2.2, 4.3, 4.3.2, 4.4, 4.4, 4.4.1, 4.5.4, 4.4, 4.5.4

Funning, G. J., B. Parsons, T. J. Wright, J. A. Jackson, and E. J. Fielding (2005), Surface displacements and source parameters of the 2003 Bam (Iran) earthquake from Envisat advanced synthetic aperture radar imagery, *Journal of Geophysical Research*, *110*(9), 1–23, doi:10.1029/2004JB003338. I

Galgana, G., M. Hamburger, R. McCaffrey, E. Corpuz, and Q. Chen (2007), Analysis of crustal deformation in Luzon, Philippines using geodetic observations and earthquake focal mechanisms, *Tectonophysics*, *432*(1-4), 63–87, doi:10.1016/j.tecto.2006.12.001. 4.2.1

GEBCO, C. G. (2020), GEBCO 2020 Grid, doi:10.5285/a29c5465-b138-234d-e053-6c86abc040b9. 3.1, 3.6

Gebhardt, A. C., L. Naudts, L. De Mol, J. Klerkx, K. Abdrakhmatov, E. R. Sobel, and M. De Batist (2017), High-amplitude lake-level changes in tectonically active Lake Issyk-Kul (Kyrgyzstan) revealed by high-resolution seismic reflection data, *Climate of the Past*, *13*(1), 73–92, doi:10.5194/cp-13-73-2017. 2.4.3, 2.4.3

Ghose, S., R. J. Mellors, A. M. Korjenkov, M. W. Hamburger, T. L. Pavlis, G. L. Pavlis, M. Omuraliev, E. Mamyrov, and A. R. Muraliev (1997), The Ms = 7.3 1992 Suusamyr, Kyrgyzstan, earthquake in the Tien Shan: 2. Aftershock focal mechanisms and surface deformation, *Bulletin of the Seismological Society of America*, *87*(1), 23–38. 2.2, 2.5.1

Ghosh, U., A. Mukhopadhyay, and S. Sen (1992), On two interacting creeping vertical surface-breaking strike-slip faults in a two-layer model of the lithosphere, *Physics of the Earth and Planetary Interiors*, *70*(1-2), 119–129, doi:10.1016/0031-9201(92)90166-S. 4.6

Goldfinger, C., Y. Ikeda, R. S. Yeats, and J. Ren (2013), Superquakes and Supercycles, *Seismological Research Letters*, *84*(1), 24–32, doi:10.1785/0220110135. 1.2

Goldstein, R. M., and C. L. Werner (1998), Radar interferogram filtering for geophysical applications, *Geophysical Research Letters*, *25*(21), 4035–4038, doi:10.1029/1998GL900033. 4.3.1, 4.4.1

Gomba, G., A. Parizzi, F. De Zan, M. Eineder, and R. Bamler (2016), Toward operational compensation of ionospheric effects in SAR interferograms: The split-spectrum method, *IEEE Transactions on Geoscience and Remote Sensing*, *54*(3), 1446–1461, doi:10.1109/TGRS.2015.2481079. 3.4, 4.3.1

Gombert, B., Z. Duputel, R. Jolivet, C. Doubre, L. Rivera, and M. Simons (2018), Revisiting the 1992 Landers earthquake: a Bayesian exploration of co-seismic slip and off-fault damage, *Geophysical Journal International*, *212*, 839–852, doi:10.1093/gji/ggx455. 4.3.4, 4.3.4, I

González, P., R. Walters, E. Hatton, K. Spaans, A. McDougall, A. Hooper, and T. Wright (2016), LiCSAR: Tools for automated generation of Sentinel-1 frame interferograms, *Paper presented at AGU Fall Meeting 2016, San Francisco, CA, USA*. 4.4.1

Goode, J. K., D. W. Burbank, and B. Bookhagen (2011), Basin width control of faulting in the Naryn Basin, south-central Kyrgyzstan, *Tectonics*, *30*(6), 1–14, doi:10.1029/2011TC002910. 2.1, 2.3, 2.4.5, 2.4.5, 2.5.2, 2.6, 5.1

Goode, J. K., D. W. Burbank, and C. Ormukov (2014), Pliocene-Pleistocene initiation, style, and sequencing of deformation in the central Tien Shan, *Tectonics*, *33*(4), 464–484, doi:10.1002/2013TC003394. 2.4.5

GRASS Development Team (2017), *Geographic Resources Analysis Support System (GRASS GIS) Software, Version 7.2*, Open Source Geospatial Foundation. 4.3.4

Gratier, J. P., J. Richard, F. Renard, S. Mittempergher, M. L. Doan, G. Di Toro, J. Hadizadeh, and A. M. Boullier (2011), Aseismic sliding of active faults by pressure solution creep: Evidence from the San Andreas fault observatory at Depth, *Geology*, *39*(12), 1131–1134, doi:10.1130/G32073.1. 4.5.3

Grützner, C., E. Carson, R. T. Walker, E. Rhodes, A. Mukambayev, D. Mackenzie, J. Elliott, G. Campbell, and K. Abdrakhmatov (2017), Assessing the activity of faults in continental interiors: palaeoseismic insights from SE Kazakhstan, *Earth and Planetary Science Letters*, *459*, 93–104, doi:10.1016/j.epsl.2016.11.025. 2.1, 2.5.1

Guotana, J. M., B. D. Payot, C. B. Dimalanta, N. T. Ramos, D. V. Faustino-Eslava, K. L. Queaño, and G. P. Yumul (2018), Petrological and geochemical characteristics of the Samar Ophiolite ultramafic section: implications on the origins of the ophiolites in Samar and Leyte islands, Philippines, *International Geology Review*, *60*(4), 401–417, doi:10.1080/00206814.2017.1336944. 4.2.2, 4.2

Gutiérrez-Santolalla, F., E. Acosta, S. Ríos, J. Guerrero, and P. Lucha (2005), Geomorphology and geochronology of sackung features (uphill-facing scarps) in the Central Spanish Pyrenees, *Geomorphology*, *69*(1-4), 298–314, doi:10.1016/j.geomorph.2005.01.012. 2.4.3

Hall, R. (2002), Cenozoic geological and plate tectonic evolution of SE Asia and the SW Pacific: Computer-based reconstructions, model and animations, *Journal of Asian Earth Sciences*, *20*(4), 353–431, doi:10.1016/S1367-9120(01)00069-4. 3.2

Hamling, I. J., S. Hreinsdóttir, K. Clark, J. Elliott, C. Liang, E. Fielding, N. Litchfield, P. Villamor, L. Wallace, T. J. Wright, E. D'Anastasio, S. Bannister, D. Burbidge, P. Denys, P. Gentle, J. Howarth, C. Mueller, N. Palmer, C. Pearson, W. Power, P. Barnes, D. J. Barrell, R. Van Dissen, R. Langridge, T. Little, A. Nicol, J. Pettinga, J. Rowland, and M. Stirling (2017), Complex multifault rupture during the 2016 Mw 7.8 Kaikura earthquake, New Zealand, *Science*, *356*(6334), doi:10.1126/science.aam7194. 3.1

Harris, R. A. (2017), Large earthquakes and creeping faults, *Reviews of Geophysics*, *55*(1), 169–198, doi:10.1002/2016RG000539. 1.1, 1.2, 4.1, 4.5, 4.5.3, 5.1

Havenith, H. B., A. Strom, I. Torgoev, A. Torgoev, L. Lamair, A. Ischuk, and K. Abdrakhmatov (2015), Tien Shan Geohazards Database: Earthquakes and landslides, *Geomorphology*, *249*, 16–31, doi:10.1016/j.geomorph.2015.01.037. 2.1

Hayes, G. P., G. L. Moore, D. E. Portner, M. Hearne, H. Flamme, M. Furtney, and G. M. Smoczyk (2018), Slab2, a comprehensive subduction zone geometry model, *Science*, *362*(6410), 58–61, doi:10.1126/science.aat4723. 3.6

Hazel, M., C. Uribe, D. B. Dacillo, L. M. Dacoag, R. P. Andrino, and E. H. Alcober (2015), 30 Years of Tongonan-1 (Leyte, Philippines) Sustained Production, in *Proceedings: World Geothermal Congress 2015*, Melbourne, Australia. 4.3.3

Heimann, S., M. Isken, D. Kühn, H. Sudhaus, A. Steinberg, H. Vasyura-Bathke, S. Daout, S. Cesca, and T. Dahm (2018), Grond - A probabilistic earthquake source inversion framework, doi:10.5880/GFZ.2.1.2018.003. 3.5

Hsu, Y.-J., S.-B. Yu, J. P. Loveless, T. Bacolcol, R. Solidum, A. Luis, A. Pelicano, and J. Woessner (2016), Interseismic deformation and moment deficit along the Manila subduction zone and the Philippine Fault system, *Journal of Geophysical Research: Solid Earth*, *121*(10), 7639–7665, doi:10.1002/2016JB013082. 3.2, 4.2.1

Ide, S., G. C. Beroza, D. R. Shelly, and T. Uchide (2007), A scaling law for slow earthquakes, *Nature*, *447*(7140), 76–79, doi:10.1038/nature05780. 1.1

Jackson, D. D. (1979), The use of a priori data to resolve nonuniqueness in linear inversion, *Geophysical Journal of the Royal Astronomical Society*, *57*(1), 137–157, doi:10.1111/j.1365-246X.1979.tb03777.x. I

James, M. R., and S. Robson (2012), Straightforward reconstruction of 3D surfaces and topography with a camera: Accuracy and geoscience application, *Journal of Geophysical Research: Earth Surface*, *117*(3), 1–17, doi:10.1029/2011JF002289. 2.4.1

James, M. R., and S. Robson (2014), Mitigating systematic error in topographic models derived from UAV and ground-based image networks, *Earth Surface Processes and Landforms*, *39*(10), 1413–1420, doi:10.1002/esp.3609. 2.4.1

Johnson, K. M. (2013), Is stress accumulating on the creeping section of the San Andreas fault?, *Geophysical Research Letters*, *40*(23), 6101–6105, doi:10.1002/2013GL058184. 4.1

Jolivet, R., and W. B. Frank (2020), The Transient and Intermittent Nature of Slow Slip, *AGU Advances*, *1*(1), doi:10.1029/2019AV000126. 1.2, 1.2, 4.1

Jolivet, R., C. Lasserre, M. P. Doin, S. Guillaso, G. Peltzer, R. Dailu, J. Sun, Z. K. Shen, and X. Xu (2012), Shallow creep on the Haiyuan fault (Gansu, China) revealed by SAR interferometry, *Journal of Geophysical Research: Solid Earth*, *117*(6), 1–18, doi:10.1029/2011JB008732. 4.3.1, 4.3.4, 4.3.4, I, J.7, J.10

Jolivet, R., C. Lasserre, M. P. Doin, G. Peltzer, J. P. Avouac, J. Sun, and R. Dailu (2013), Spatio-temporal evolution of aseismic slip along the Haiyuan fault, China: Implications for fault frictional properties, *Earth and Planetary Science Letters*, *377-378*, 23–33, doi:10.1016/j.epsl.2013.07.020. 4.1, 5.3

Jolivet, R., P. S. Agram, N. Y. Lin, M. Simons, M.-P. Doin, G. Peltzer, and Z. Li (2014), Improving InSAR geodesy using Global Atmospheric Models, *Journal of Geophysical Research: Solid Earth*, *119*(3), 2324–2341, doi:10.1002/2013JB010588. 4.3.1, 4.3.4

Jolivet, R., T. Candela, C. Lasserre, F. Renard, Y. Klinger, and M. P. Doin (2015a), The burst-like behavior of aseismic slip on a rough fault: The creeping section of the Haiyuan fault, China, *Bulletin of the Seismological Society of America*, *105*(1), 480–488, doi:10.1785/0120140237. 4.5.2

Jolivet, R., M. Simons, P. S. Agram, Z. Duputel, and Z. Shen (2015b), Aseismic slip and seismogenic coupling along the central San Andreas Fault, *Geophysical Research Letters*, *42*(2), 297–306, doi:10.1002/2014GL062222. 4.1, 4.3.4, 4.3.4, 4.5.5

Jónsson, S., H. Zebker, P. Segall, and F. Amelung (2002), Fault slip distribution of the 1999 Mw 7.1 Hector Mine, California, earthquake, estimated from satellite radar and GPS measurements, *Bulletin of the Seismological Society of America*, *92*(4), 1377–1389, doi:10.1785/0120000922. 3.5

Kalmetieva, Z. A., A. V. Mikolaichuk, B. D. Moldobekov, A. V. Meleshko, M. M. Jantaev, A. V. Zubovich, and H. B. Havenith (2009), *Atlas of earthquakes in*

Kyrgyzstan, August 2017, ECHO, UNISDR, and CAIAG, Bishkek, Kyrgyzstan. 2.2

Kaneda, H., T. Nakata, H. Tsutsumi, H. Kondo, N. Sugito, Y. Awata, S. S. Akhtar, A. Majid, W. Khattak, A. A. Awan, R. S. Yeats, A. Hussain, M. Ashraf, S. G. Wesnousky, and A. B. Kausar (2008), *Surface rupture of the 2005 Kashmir, Pakistan, earthquake and its active tectonic implications*, vol. 98, 521–557 pp., doi:10.1785/0120070073. 2.5.1

Kaneko, Y., J. P. Avouac, and N. Lapusta (2010), Towards inferring earthquake patterns from geodetic observations of interseismic coupling, *Nature Geoscience*, *3*(5), 363–369, doi:10.1038/ngeo843. 4.5.1

Kulikova, G., and F. Krüger (2015), Source process of the 1911 M8.0 Chon-Kemin earthquake: Investigation results by analogue seismic records, *Geophysical Journal International*, *201*(3), 1891–1911, doi:10.1093/gji/ggv091. 2.1

Lagmay, A. M. F., B. van Wyk De Vries, N. Kerle, and D. M. Pyle (2000), Volcano instability induced by strike-slip faulting, *Bulletin of Volcanology*, *62*(4-5), 331–346, doi:10.1007/s004450000103. 3.7.2

Lagmay, A. M. F. A., A. M. P. Tengonciang, H. V. Marcos, and C. S. Pascua (2003), A structural model guide for geothermal exploration in Ancestral Mount Bao, Leyte, Philippines, *Journal of Volcanology and Geothermal Research*, *122*(1-2), 133–141, doi:10.1016/S0377-0273(02)00501-2. 4.2.2

Landgraf, A., A. Dzhumabaeva, K. Abdrakhmatov, E. Macaulay, M. Strecker, J. Arrowsmith, F. Preusser, G. Rugel, and S. Merchel (2016), Repeated large-magnitude earthquakes in a tectonically active, low-strain continental interior: the northern Tien Shan, Kyrgyzstan, *Journal of Geophysical Research: Solid Earth*, *121*, 3888–3910, doi:10.1002/2015JB012714. 1.2, 2.1, 2.2

Landgraf, A., S. Kübler, E. Hintersberger, and S. Stein (2017), Active tectonics, earthquakes and palaeoseismicity in slowly deforming continents, *Geological Society, London, Special Publications*, *432*(1), 1–12, doi:10.1144/SP432.13. 1.2, 2.1, 3.7.3

Larson, K. M., A. R. Lowry, V. Kostoglodov, W. Hutton, O. Sánchez, K. Hudnut, and G. Suárez (2004), Crustal deformation measurements in Guerrero, Mexico, *Journal of Geophysical Research: Solid Earth*, *109*(4), 1–19, doi:10.1029/2003JB002843. H

Li, B., Y. Li, W. Jiang, Z. Su, and W. Shen (2020), Conjugate ruptures and seismotectonic implications of the 2019 Mindanao earthquake sequence inferred from Sentinel-1 InSAR data, *International Journal of Applied Earth Observation and Geoinformation*, *90*, doi:10.1016/j.jag.2020.102127. 3.1, 3.4, 3.7.1, 3.7.2

Lienkaemper, J. J., G. Borchardt, and M. Lisowski (1991), Historic creep rate and potential for seismic slip along the Hayward Fault, California, *Journal of Geophysical Research*, *96*(B11), doi:10.1029/91jb01589. 2.1

Lienkaemper, J. J., F. S. McFarland, R. W. Simpson, R. G. Bilham, D. A. Ponce, J. J. Boatwright, and S. John Caskey (2012), Long-term creep rates on the Hayward Fault: Evidence for controls on the size and frequency of large earthquakes, *Bulletin of the Seismological Society of America*, *102*(1), 31–41, doi:10.1785/0120110033. 1.2, 4.1

Lin, A., and T. Chiba (2017), Coseismic conjugate faulting structures produced by the 2016 Mw 7.1 Kumamoto earthquake, Japan, *Journal of Structural Geology*, *99*, 20–30, doi:10.1016/j.jsg.2017.05.003. 3.6

Lindsey, E. O., Y. Fialko, Y. Bock, D. T. Sandwell, and R. Bilham (2014), Localized and distributed creep along the southern San Andreas Fault, *Journal of Geophysical Research: Solid Earth*, (May), 7909–7922, doi:10.1002/2014JB011275.1. 4.3.1

Llamas, D. C., B. Marfito, C. Pogay, K. Vitto, R. Mangahas, M. Cahulogan, and J. Perez (2017), Surface Rupture Associated with the 2017 Magnitude 6.5 Leyte Earthquake, *Paper presented at the Geological Society of the Philippines Convention 2017, Makati, Philippines*. 4.1, 4.4, 4.4.2

Lohman, R. B., and M. Simons (2005), Some thoughts on the use of InSAR data to constrain models of surface deformation: Noise structure and data downsampling, *Geochemistry, Geophysics, Geosystems*, *6*(1), doi:10.1029/2004GC000841. 4.3.4, 4.3.4, 4.3.4

Los Baños, C. F., D. M. Rigor, D. B. Layugan, and L. F. Bayrante (2010), The Resistivity Model of the Mindanao Geothermal Project, South Central Mindanao, Philippines, *Proceedings World Geothermal Congress*, (April), 1–6. 3.7.2

Louderback, G. D. (1942), Faults and Earthquakes, *Bulletin of the Seismological Society of America*, doi:10.1201/9781482266283-11. 1.1

Loveless, J. P., and B. J. Meade (2011), Spatial correlation of interseismic coupling and coseismic rupture extent of the 2011 Mw = 9.0 Tohoku-oki earthquake, *Geophysical Research Letters*, *38*(17), 2–6, doi:10.1029/2011GL048561. I

Luzon, P. K., K. Montalbo, J. Galang, J. M. Sabado, C. M. Escape, R. Felix, and A. M. F. Lagmay (2016), Hazard mapping related to structurally controlled landslides in Southern Leyte, Philippines, *Natural Hazards and Earth System Sciences*, *16*(3), 875–883, doi:10.5194/nhess-16-875-2016. 4.3.1

Macaulay, E. A., E. R. Sobel, A. Mikolaichuk, B. Kohn, and F. M. Stuart (2014), Cenozoic deformation and exhumation history of the Central Kyrgyz Tien Shan, *Tectonics*, *33*(2), 135–165, doi:10.1002/2013TC003376. 2.2, 2.4.4, 2.4.5, 2.18

Mackenzie, D., and A. Elliott (2017), Untangling tectonic slip from the potentially misleading effects of landform geometry, *Geosphere*, *13*(4), GES01,386.1, doi:10.1130/GES01386.1. 2.4.5

Mackenzie, D., R. Walker, K. Abdrakhmatov, G. Campbell, A. Carr, C. Gruetzner, A. Mukambayev, and M. Rizza (2018), A creeping intracontinental thrust fault: past and present slip-rates on the Northern edge of the Tien Shan, Kazakhstan, *Geophysical Journal International*, *215*(2), 1148–1170, doi:10.1093/gji/ggy339. 2.1, 2.3, 2.4.1, 2.4.2, 2.6, 5.1

Maggi, A., J. A. Jackson, K. Priestley, and C. Baker (2000), A re-assessment of focal depth distributions in southern Iran, the Tien Shan and northern India: Do earthquakes really occur in the continental mantle?, *Geophysical Journal International*, *143*(3), 629–661, doi:10.1046/j.1365-246X.2000.00254.x. 3.3

Manighetti, I., C. Caulet, L. D. Barros, C. Perrin, F. Cappa, and Y. Gaudemer (2015), Generic along-strike segmentation of Afar normal faults, East Africa: Implications on fault growth and stress heterogeneity on seismogenic fault planes, *Geochemistry, Geophysics, Geosystems*, *16*, 443–467. 3.7.3, 4.5.2

Massonnet, D., M. Rossi, C. Carmona, F. Adragna, G. Peltzer, K. Felgl, and T. Rabaute (1993), The displacement field of the Landers earthquake mapped by radar interferometry, *Nature*, *364*, 138–142. 1.2, 4.1

McCaffrey, R. (1991), Earthquakes and ophiolite emplacement in the Molucca Sea Collision Zone, Indonesia, *Tectonics*, *10*(2), 433–453, doi:10.1029/90TC02553. 3.3

McCaffrey, R. (1996), Slip partitioning at convergent plate boundaries of SE Asia, *Geological Society Special Publication*, *106*, 3–18, doi:10.1144/GSL.SP.1996.106.01.02. 4.6

Mccaffrey, R. (2002), Crustal Block Rotations and Plate Coupling, in *Plate Boundary Zones, Geodynamic Series 30*, edited by S. Stein and J. Freynuekker, pp. 101–122, American Geophysical Union, doi:10.1029/gd030p0101. 4.5.4

McCaffrey, R., and G. Abers (1988), SYN3: A Program for Inversion of Teleseismic Body Wave Forms on Microcomputers. 3.3

Mccalpin, J. P. (1999), Criteria for Determining the Seismic Significance of Sackungen and Other Scarplike Landforms in Mountainous Regions, in *Techniques for identifying faults and determining their origins*, pp. Appendix A, p. A–122 to A–142, U.S. Nuclear Regulatory Commission. 2.4.3

Michel, S., J. Avouac, R. Jolivet, and L. Wang (2017), Seismic and Aseismic Moment Budget and Implication for the Seismic Potential of the Parkfield Segment of the San Andreas Fault, *Bulletin of the Seismological Society of America*, *108*(1), 19–38, doi:10.1785/0120160290. 4.5.4

Middleton, T. A., R. T. Walker, B. Parsons, Q. Lei, Y. Zhou, and Z. Ren (2015), A major, intraplate, normal-faulting earthquake: The 1739 Yinchuan event in northern China, *Journal of Geophysical Research: Solid Earth*, *4*, 293–320, doi:10.1002/2015JB012355.Received. 2.4.1

Middleton, T. A., J. R. Elliott, E. J. Rhodes, S. Sherlock, R. T. Walker, W. Wang, J. Yu, and Y. Zhou (2017), Extension rates across the northern Shanxi Grabens, China, from Quaternary geology, seismicity and geodesy, *Geophysical Journal International*, *209*(2), 535–558, doi:10.1093/gji/ggx031. 2.4.1, B

Mikhailova, N. N., A. Mukambayev, I. L. Aristova, G. Kulikova, S. Ullah, M. Pilz, and D. Bindi (2015), Central Asia Earthquake catalogue from ancient time to 2009, *Annals of Geophysics*, *58*(1), 9. 2.1

Minson, S. E., M. Simons, and J. L. Beck (2013), Bayesian inversion for finite fault earthquake source models I-theory and algorithm, *Geophysical Journal International*, *194*(3), 1701–1726, doi:10.1093/gji/ggt180. 4.3.4, 4.3.4

Minson, S. E., M. Simons, J. L. Beck, F. Ortega, J. Jiang, S. E. Owen, A. W. Moore, A. Inbal, and A. Sladen (2014), Bayesian inversion for finite fault earthquake source models - II: The 2011 great Tohoku-oki, Japan earthquake, *Geophysical Journal International*, *198*(2), 922–940, doi:10.1093/gji/ggu170. 4.3.4, 4.5.4

Molnar, P. (1988), Continental tectonics in the aftermath of plate tectonics, *Nature*, *335*(6186), 131–137, doi:10.1038/335131a0. 1.2

Molnar, P., and H. Lyon-Caent (1989), Fault plane solutions of earthquakes and active tectonics of the Tibetan Plateau and its margins, *Geophysical Journal International*, *99*(1), 123–154, doi:10.1111/j.1365-246X.1989.tb02020.x. 3.3

Moore, D. E., and J. Byerlee (1992), Relationships between sliding behavior and internal geometry of laboratory fault zones and some creeping and locked strike-slip faults of California, *Tectonophysics*, *211*(1-4), 305–316, doi:10.1016/0040-1951(92)90067-G. 4.5.2

Moore, D. E., and D. A. Lockner (2013), Chemical controls on fault behavior: Weakening of serpentinite sheared against quartz-bearing rocks and its significance for fault creep in the San Andreas system, *Journal of Geophysical Research: Solid Earth*, *118*(5), 2558–2570, doi:10.1002/jgrb.50140. 4.5.3

Moore, D. E., and M. J. Rymer (2007), Talc-bearing serpentinite and the creeping section of the San Andreas fault, *Nature*, *448*(7155), 795–797, doi:10.1038/nature06064. 4.2.2, 4.5.3

Morishita, Y. (2019), A systematic study of synthetic aperture radar interferograms produced from alos-2 data for large global earthquakes from 2014 to 2016, *IEEE Journal of Selected Topics in Applied Earth Observations and Remote Sensing*, *12*(7), 2397–2408, doi:10.1109/JSTARS.2019.2921664. 3.4

Mu, C. H., J. Angelier, J. C. Lee, H. T. Chu, and J. J. Dong (2011), Structure and Holocene evolution of an active creeping thrust fault: The Chihshang fault at Chinyuan (Taiwan), *Journal of Structural Geology*, *33*(4), 743–755, doi:10.1016/j.jsg.2011.01.015. 2.1

Nakamura, K., K. H. Jacob, and J. N. Davies (1977), Volcanoes as Possible Indicators of Tectonic Stress Orientation- Aleutians and Alaska, *Pure and Applied Geophysics*, *115*(1), 87–112. 3.7.2

NASA (2013), NASA Shuttle Radar Topography Mission Global 1 arc second [Data set]., doi:doi.org/10.5067/MEaSUREs/SRTM/SRTMGL1.003. 2.1, 2.4.1, 3.1

Noda, H., and N. Lapusta (2013), Stable creeping fault segments can become destructive as a result of dynamic weakening, *Nature*, *493*(7433), doi:10.1038/nature11703. 1.1, 4.1

Okada, Y. (1985), Surface deformation due to shear and tensile faults in a half-space, *Bulletin Seismological Society of America*, *75*(4), 1135–1154. (document), 4.3.4, 4.3.4, F.1

Okamoto, A. S., B. A. Verberne, A. R. Niemeijer, M. Takahashi, I. Shimizu, T. Ueda, and C. J. Spiers (2019), Frictional Properties of Simulated Chlorite Gouge at Hydrothermal Conditions: Implications for Subduction Megathrusts, *Journal of Geophysical Research: Solid Earth*, pp. 1–21, doi:10.1029/2018JB017205. 4.5.3

Okamura, Y., T. Ishiyama, and Y. Yanagisawa (2007), Fault-related folds above the source fault of the 2004 mid-Niigata Prefecture earthquake, in a fold-and-thrust belt caused by basin inversion along the eastern margin of the Japan Sea, *Journal of Geophysical Research: Solid Earth*, *112*(3), 1–14, doi:10.1029/2006JB004320. 1.2

Ozawa, T., E. Fujita, and H. Ueda (2016), Crustal deformation associated with the 2016 Kumamoto Earthquake and its effect on the magma system of Aso volcano, *Earth, Planets and Space*, *68*(1), doi:10.1186/s40623-016-0563-5. 4.4.1

Patyniak, M., A. Landgraf, A. Dzhumabaeva, K. E. Abdrakhmatov, S. Rosenwinkel, O. Korup, F. Preusser, J. Fohlmeister, J. R. Arrowsmith, and M. R. Strecker (2017), Paleoseismic Record of Three Holocene Earthquakes Rupturing the IssykAta Fault near Bishkek, North Kyrgyzstan, *Bulletin of the Seismological Society of America*, *107*(6), 2721–2737, doi:10.1785/0120170083. 2.1, 2.2

Paulsen, T. S., and T. J. Wilson (2009), Structure and age of volcanic fissures on Mount Morning: A new constraint on Neogene to contemporary stress in the West Antarctic Rift, southern Victoria Land, Antarctica, *Bulletin of the Geological Society of America*, *121*(7-8), 1071–1088, doi:10.1130/B26333.1. 3.7.2

Peltzer, G., F. Crampé, S. Hensley, and P. Rosen (2001), Transient strain accumulation and fault interaction in the Eastern California shear zone, *Geology*, *29*(11), 975–978, doi:10.1130/0091-7613(2001)029¡0975:TSAAFI¿2.0.CO;2. 4.1

Peng, Z., and J. Gomberg (2010), An integrated perspective of the continuum between earthquakes and slow-slip phenomena, *Nature Geoscience*, *3*(9), 599–607, doi:10.1038/ngeo940. 1.1

Perez, J. S., and H. Tsutsumi (2017), Tectonic geomorphology and paleoseismology of the Surigao segment of the Philippine fault in northeastern Mindanao Island, Philippines, *Tectonophysics*, *699*, 244–257, doi:10.1016/j.tecto.2017.02.001. 3.2, 4.2.1

Perrin, C., I. Manighetti, J. P. Ampuero, F. Cappa, and Y. Gaudemer (2016), Location of largest earthquake slip and fast rupture controlled by along-strike change in fault structural maturity due to fault growth, *Journal of Geophysical Research: Solid Earth*, *121*(5), 3666–3685, doi:10.1002/2015JB012671. 4.5.2

Perrin, C., F. Waldhauser, and C. H. Scholz (2019), Persistent fine-scale fault structure and rupture development: a new twist in the Parkfield, CA, story, *Earth and Planetary Science Letters*, *521*, 128–138, doi:10.1016/j.epsl.2019.06.010. 3.7.3

Pfiffner, O. A. (2017), Thick-skinned and thin-skinned tectonics: A global perspective, *Geosciences*, *7*(71), doi:10.3390/geosciences7030071. 2.5.2

Philip, H., E. Rogozhin, A. Cisternas, J. C. Bousquet, B. Borisov, and A. Karakhanian (1992), The Armenian earthquake of 1988 December 7: faulting and folding, neotectonics and palaeoseismicity, *Geophysical Journal International*, *110*(1), 141–158, doi:10.1111/j.1365-246X.1992.tb00718.x. 2.5.1

PHIVOLCS (2018), 10 February 2017 Ms 6.7 Surigao Del Norte Earthquake, PHIVOLCS Special Report, *Tech. rep.*, DOST-PHIVOLCS, Quezon City, Philippines. 3.2, 4.2.1

PHIVOLCS (2019), Poster of the October 2019 Series of Earthquakes in Cotabato and Vicinity. 3.4, 3.6

PHIVOLCS Quick Response Team (2019), 06 July 2017 Ms 6.5 Leyte Earthquake: PHIVOLCS Special Report, *Tech. rep.*, DOST-PHIVOLCS, Quezon City, Philippines. 4.1, 4.3.2, 4.3.5, 4.4, 4.11, 4.4.2, 4.4.2

Pousse Beltran, L., E. Pathier, F. Jouanne, R. Vassallo, C. Reinoza, F. Audemard, M. P. Doin, and M. Volat (2016), Spatial and temporal variations in creep rate along the El Pilar fault at the Caribbean-South American plate boundary (Venezuela), from InSAR, *Journal of Geophysical Research: Solid Earth*, *121*(11), 8276–8296, doi:10.1002/2016JB013121. 4.1, 4.3.1, H

Prescott, W. H., M. Lisowski, and J. C. Savage (1981), Geodetic measurement of crustal deformation on the San Andreas, Hayward, and Calaveras faults near San Francisco, California, *Journal of Geophysical Research*, *86*(B11), 10,853–10,869, doi:10.1029/JB086iB11p10853. 1.2

Price, E. J., and D. T. Sandwell (1998), Small-scale deformations associated with the 1992 Landers, California, earthquake mapped by synthetic aperture radar interferometry phase gradients, *Journal of Geophysical Research: Solid Earth*, *103*(B11), 27,001–27,016, doi:10.1029/98jb01821. 4.1

Prioul, R., F. H. Cornet, C. Dorbath, L. Dorbath, M. Ogena, and E. Ramos (2000), An induced seismicity experiment across a creeping segment of the Philippine Fault, *Journal of Geophysical Research*, *105*(B6), 13,595, doi:10.1029/2000JB900052. 4.1, 4.2.1, 4.3.4, 4.3.5, 4.10, J.13

Pubellier, M., R. Quebral, C. Rangin, B. Deffontaines, C. Muller, J. Butterlin, and J. Manzano (1991), The Mindanao collision zone: a soft collision event within a continuous Neogene strike-slip setting, *Journal of Southeast Asian Earth Sciences*, *6A*(3), 239–248, doi:10.1016/0743-9547(91)90070-E. 3.1, 3.2, 3.1, 3.7.3, 5.1

Pubellier, M., B. Deffontaines, R. Quebral, and C. Rangin (1994), Drainage network analysis and tectonics of Mindanao, southern Philippines, *Geomorphology*, *9*(4), 325–342, doi:10.1016/0169-555X(94)90053-1. 3.1, 3.2, 3.7.2

Punongbayan, R. S., R. E. Rimando, J. A. Daligdig, G. M. Besana, A. S. Daag, T. Nakata, and H. Tsutsumi (1992), The 16 July 1990 Luzon Earthquake Ground Rupture, in *The July 16, 1990 Luzon Earthquake: A Technical Monograph*, pp. 1–32. 4.2.1

Quebral, R. D., M. Pubellier, and C. Rangin (1996), The onset of movement on the Philippine fault in eastern Mindanao: A transition from a collision to a strike-slip environment, *Tectonics*, *15*(4), 713–726. 3.1

Ragon, T., A. Sladen, Q. Bletery, M. Vergnolle, O. Cavalié, A. Avallone, J. Balestra, and B. Delouis (2019), Joint Inversion of Coseismic and Early Postseismic Slip to Optimize the Information Content in Geodetic Data: Application to the 2009 Mw6.3 L'Aquila Earthquake, Central Italy, *Journal of Geophysical Research: Solid Earth*, *124*(10), 10,522–10,543, doi:10.1029/2018JB017053. 4.4

Ramos, S. G., and D. M. Rigor (2005), Lobi and Mahagnao: Geothermal Prospects in an Ultramafic Setting Central Leyte, Philippines, in *Proceedings: World Geothermal Congress 2005*, Antalya, Turkey. 4.5.3

Rangin, C. (1991), The Philippine Mobile Belt: a complex plate boundary, *Journal of Southeast Asian Earth Sciences*, *6*(3-4), 209–220, doi:10.1016/0743-9547(91)90068-9. 3.2, 3.1

Rangin, C. (2016), Rigid and non-rigid micro-plates: Philippines and Myanmar-Andaman case studies, *Comptes Rendus - Geoscience*, *348*(1), 33–41, doi:10.1016/j.crte.2015.10.008. 3.1

Rangin, C., and E. Silver (1990), Geological setting of the Celebes and Sulu Seas, *Proceedings of the Ocean Drilling Program, Scientific Results*, *124*, 35–42. 3.1

Rangin, C., X. Le Pichon, S. Mazzotti, M. Pubellier, N. Chamot-Rooke, M. A. Aurelio, A. Walpersdorf, and R. Quebral (1999), Plate convergence measured by GPS across the Sundaland/Philippine Sea Plate deformed boundary: the Philippines and eastern Indonesia, *Geophysical Journal International*, *139*(2), 296–316, doi:10.1046/j.1365-246x.1999.00969.x. 3.1

Ranneft, T. S. M., R. M. Hopkins, A. J. Froelich, and J. W. Gwinn (1960), Reconnaissance Geology and Oil Possibillities of Mindanao, *AAPG Bulletin*, *44*(5), doi:10.1306/0bda6014-16bd-11d7-8645000102c1865d. 3.7.2

Receveur, M., F. Sigmundsson, V. Drouin, and M. Parks (2019), Ground deformation due to steam cap processes at Reykjanes, SW-Iceland: Effects of geothermal exploitation inferred from interferometric analysis of Sentinel-1 images 2015-2017, *Geophysical Journal International*, *216*(3), 2183–2212, doi:10.1093/gji/ggy540. 4.3.4, 4.3.4

Reid, H. F. (1910), The California Earthquake of April 18, 1906: Volume II (The Mechanics of the Earthquake), *Tech. rep.*, State Earthquake Investigation Commission, Washington, D.C. 1.2

Reimer, P., E. Bard, A. Bayliss, J. Beck, P. Blackwell, C. Ramsey, C. Buck, H. Cheng, R. Edwards, M. Friedrich, P. Grootes, T. Guilderson, H. Haflidason, I. Hajdas, C. Hatte, T. Heaton, D. Hoffman, A. Hogg, K. Hughen, K. Felix Kaiser, B. Kromer, S. Manning, M. Niu, R. Reimer, D. Richards, E. Marian Scott, J. Southon, R. Staff, C. S. Turney, and J. van der Plicht (2013), Intcal13 and Marine13 Radiocarbon Age Calibration Curves 050,000 Years Cal Bp, *Radiocarbon*, *46*(1), 1111–1150, doi:10.2458/azu$_j s_r c$.46.4183. 2.1

Reyes, A. G. (1990), Petrology of Philippine geothermal systems and the application of alteration mineralogy to their assessment, *Journal of Volcanology and Geothermal Research*, *43*(1-4), 279–309, doi:10.1016/0377-0273(90)90057-M. 4.1, 4.5.3

Rhodes, E. J. (2015), Dating sediments using potassium feldspar single-grain IRSL: Initial methodological considerations, *Quaternary International*, *362*, 14–22, doi:10.1016/j.quaint.2014.12.012. B

Rimando, J. M., M. A. Aurelio, J. D. B. Dianala, K. J. L. Taguibao, K. M. C. Agustin, A. E. G. Berador, and A. A. Vasquez (2019), Coseismic Ground Rupture of the 15 October 2013 Magnitude (Mw) 7.2 Bohol Earthquake, Bohol Island, Central Philippines, *Tectonics*, *38*(8), 2558–2580, doi:10.1029/2019TC005503. 2.5.1, 3.8, 5.2

Rizza, M., K. Abdrakhmatov, R. Walker, R. Braucher, V. Guillou, A. Carr, G. Campbell, D. McKenzie, J. Jackson, G. Aumaître, D. Bourlès, and K. Keddadouche (2019), Rate of slip from multiple Quaternary dating methods and paleoseismic investigations along the Talas-Fergana Fault: tectonic implications for the Tien Shan Range, *Tectonics*, (Figure 1), 1–29, doi:10.1029/2018TC005188. 2.2

Romanet, P., H. S. Bhat, R. Jolivet, and R. Madariaga (2018), Fast and Slow Slip Events Emerge Due to Fault Geometrical Complexity, *Geophysical Research Letters*, pp. 4809–4819, doi:10.1029/2018GL077579. 4.5.2, 4.6

Rousset, B., R. Jolivet, M. Simons, C. Lasserre, B. Riel, P. Milillo, Z. Çakir, and F. Renard (2016), An aseismic slip transient on the North Anatolian Fault, *Geophysical Research Letters*, *43*(7), 3254–3262, doi:10.1002/2016GL068250. 5.3

Rousset, B., R. Bürgmann, and M. Campillo (2019), Slow slip events in the roots of the San Andreas fault, *Science Advances*, *5*(2), 1–8, doi:10.1126/sciadv.aav3274. 5.3

Rust, D., A. Korjenkov, and A. Tibaldi (2018), Geologic slip-rate determinations on the Talas-Fergana fault: mismatch with geodetic slip rate., *Geophysical Research Letters*, pp. 3880–3888, doi:10.1002/2017GL076990. 2.1

Saffer, D. M., and C. Marone (2003), Comparison of smectite- and illite-rich gouge frictional properties: application to the updip limit of the seismogenic zone along subduction megathrusts, *Earth and Planetary Science Letters*, *215*(1-2), 219–235, doi:10.1016/S0012-821X(03)00424-2. 4.5.3

Sagiya, T., and W. Thatcher (1999), Coseismic slip resolution along a plate boundary megathrust: The Nankai Trough, southwest Japan, *Journal of Geophysical Research: Solid Earth*, *104*(B1), 1111–1129, doi:10.1029/98jb02644. 4.3.4, I, I

Sandwell, D. T., D. Myer, R. Mellors, M. Shimada, B. Brooks, and J. Foster (2008), Accuracy and resolution of ALOS interferometry: Vector deformation maps of the father's day intrusion at Kilauea, *IEEE Transactions on Geoscience and Remote Sensing*, *46*(11), 3524–3534, doi:10.1109/TGRS.2008.2000634. 4.3.1

Savage, J. C., and R. O. Burford (1973), Geodetic determination of relative plate motion in central California, *Journal of Geophysical Research*, *78*(5), 832–845. 2.3, 4.3.4

Scholz, C. H. (1998), Earthquakes and friction laws, *Nature*, *391*(6662), 37–42, doi:10.1038/34097. 1.1, 3.7.2, 4.5.1, 4.5.3

Scott, G. L. (2001), Hydrothermal alteration and fluid geochemistry of the Tongonan Geothermal Field, Philippines, *Resource Geology*, *51*(2), 117–134, doi:10.1111/j.1751-3928.2001.tb00086.x. 4.1, 4.5.3

Selander, J., M. Oskin, C. Ormukov, and K. Abdrakhmatov (2012), Inherited strike-slip faults as an origin for basement-cored uplifts: Example of the Kungey and Zailiskey ranges, northern Tian Shan, *Tectonics*, *31*(4), 1–22, doi:10.1029/2011TC003002. 2.4.4, 2.5.2

Shean, D. (2017), High Mountain Asia 8-meter DEM Mosaics Derived from Optical Imagery, Version 1, *Tech. rep.*, NASA National Snow and Ice Data Center Distributed Active Archive Center., Boulder, Colorado USA. 2.4.1, 2.6

Sibson, R. H. (1977), Fault rocks and fault mechanisms, *Journal of the Geological Society*, *133*(3), 191–213, doi:10.1144/gsjgs.133.3.0191. 1.1

Sieh, K., M. Stuiver, and D. Brillinger (1989), A more precise chronology of earthquakes produced by the San Andreas fault in southern California, *Journal of Geophysical Research*, *94*(B1), 603–623, doi:10.1029/JB094iB01p00603. 1.2

Sieh, K., D. H. Natawidjaja, A. J. Meltzner, C. C. Shen, H. Cheng, K. S. Li, B. W. Suwargadi, J. Galetzka, B. Philibosian, and R. L. Edwards (2008), Earthquake supercycles inferred from sea-level changes recorded in the corals of west Sumatra, *Science*, *322*(5908), 1674–1678, doi:10.1126/science.1163589. 1.2

Silcock, D. M., and J. Beavan (2001), Geodetic constraints on coseismic rupture during the 1990 Ms 7.8 Luzon, Philippines, earthquake, *Geochemistry, Geophysics, Geosystems*, *2*(7), doi:10.1029/2000GC000101. 4.2.1

Simonov, V. A., A. V. Mikolaichuk, S. V. Rasskazov, and S. V. Kovyazin (2008), Cretaceous-Paleogene within-plate magmatism in Central Asia: data from the Tien Shan basalts, *Russian Geology and Geophysics*, *49*(7), 520–533, doi:10.1016/j.rgg.2008.06.009. 2.4.5

Simons, M., and P. A. Rosen (2007), *Interferometric Synthetic Aperture Radar Geodesy*, vol. 3, 391–446 pp., Elsevier B.V., doi:10.1016/B978-044452748-6.00059-6. 3.1

Sloan, R. A., J. A. Jackson, D. Mckenzie, and K. Priestley (2011), Earthquake depth distributions in central Asia, and their relations with lithosphere thickness, shortening and extension, *Geophysical Journal International*, *185*(1), 1–29, doi:10.1111/j.1365-246X.2010.04882.x. 2.5.1

Sobel, E. R., and N. Arnaud (2000), Cretaceous-Paleogene basaltic rocks of the Tuyon basin, NW China and the Kyrgyz Tian Shan: The trace of a small plume, *Lithos*, *50*(1-3), 191–215, doi:10.1016/S0024-4937(99)00046-8. 2.4.5

Sobel, E. R., M. Oskin, D. Burbank, and A. Mikolaichuk (2006), Exhumation of basement-cored uplifts: Example of the Kyrgyz Range quantified with apatite fission track thermochronolgy, *Tectonics*, *25*(2), doi:10.1029/2005TC001809. 2.2

Stein, S., M. Liu, E. Calais, and Q. Li (2009), Mid-continent earthquakes as a complex system, *Seismological Research Letters*, *80*(4), 551–553, doi:10.1785/gssrl.80.4.551. 1.2, 2.1

Steinbrugge, K. V., and E. G. Zacher (1960), Creep on the San Andreas Fault: Fault Creep and Property Damage, *Bulletin of the Seismological Society of America*, *50*(3), 389–396. 1.2

Stewart, G. S., and S. N. Cohn (1979), The 1976 August 16, Mindanao, Philippine earthquake (Ms= 7.8) evidence for a subduction zone south of Mindanao, *Geophysical Journal of the Royal Astronomical Society*, *57*(1), 51–65, doi:10.1111/j.1365-246X.1979.tb03771.x. 3.2

Storchak, D. A., J. Harris, L. Brown, K. Lieser, B. Shumba, R. Verney, D. Di Giacomo, and E. I. Korger (2017), Rebuild of the Bulletin of the International Seismological Centre (ISC), part 1: 19641979, *Geoscience Letters*, *4*(1), doi:10.1186/s40562-017-0098-z. 4.2.2, 4.2

Sudhaus, H., and S. Jónsson (2009), Improved source modelling through combined use of InSAR and GPS under consideration of correlated data errors: Application to the June 2000 Kleifarvatn earthquake, Iceland, *Geophysical Journal International*, *176*(2), 389–404, doi:10.1111/j.1365-246X.2008.03989.x. 3.5, 4.3.4, 4.3.4, J.7, J.10

Suerte, L. O., G. P. Yumul, R. A. Tamayo, C. B. Dimalanta, M. F. Zhou, R. C. Maury, M. Polvé, and C. L. Balce (2005), Geology, geochemistry and U-Pb SHRIMP age of the Tacloban Ophiolite Complex, Leyte Island (Central Philippines): Implications for the existence and extent of the proto-Philippine Sea Plate, *Resource Geology*, *55*(3), 207–216, doi:10.1111/j.1751-3928.2005.tb00242.x. 4.2.2, 4.2, 4.5.3

Tamesis, E. (1981), Hydrocarbon potential of Philippine Basins, *Energy*, *6*(11), 1179–1206, doi:10.1016/0360-5442(81)90032-3. 3.7.2, 3.7.3, 3.6, 5.1

Tapponnier, P., and P. Molnar (1979), Active faulting and Cenozoic tectonics of the Tien Shan, Mongolia, and Baykal regions, *Journal of Geophysical Research*, *84*(B7). 2.2

Tarantola, A. (2005), *Inverse problem theory and methods for model parameter estimation*, SIAM. I

Taylor, B., and D. E. Hayes (1980), The tectonic evolution of the South China Basin, *Geophysical Monograph Series*, *23*(Figure 1). 3.2

Thomas, M. Y., J. P. Avouac, J. Champenois, J. C. Lee, and L. C. Kuo (2014a), Spatiotemporal evolution of seismic and aseismic slip on the Longitudinal Valley Fault, Taiwan, *Journal of Geophysical Research: Solid Earth*, *119*(6), 5114–5139, doi:10.1002/2013JB010603. 4.1, 4.5.4, 4.5.4

Thomas, M. Y., J. P. Avouac, J. P. Gratier, and J. C. Lee (2014b), Lithological control on the deformation mechanism and the mode of fault slip on the Longitudinal Valley Fault, Taiwan, *Tectonophysics*, *632*(C), 48–63, doi:10.1016/j.tecto.2014.05.038. 4.5.3

Thomas, M. Y., N. Lapusta, H. Noda, and J. P. Avouac (2014c), Quasi-dynamic versus fully dynamic simulations of earthquakes and aseismic slip with and without enhanced coseismic weakening, *Journal of Geophysical Research: Solid Earth*, *119*(3), 1986–2004, doi:10.1002/2013JB010615. 4.5.1

Thomas, M. Y., J. P. Avouac, and N. Lapusta (2017), Rate-and-state friction properties of the Longitudinal Valley Fault from kinematic and dynamic modeling of seismic and aseismic slip, *Journal of Geophysical Research: Solid Earth*, *122*(4), 3115–3137, doi:10.1002/2016JB013615. 4.1

Thompson, S. C., R. J. Weldon, C. M. Rubin, K. Abdrakhmatov, P. Molnar, and G. W. Berger (2002), Late Quaternary slip rates across the central Tien Shan,

Kyrgyzstan, central Asia, *Journal of Geophysical Research: Solid Earth*, *107*(B9), ETG 7–1–ETG 7–32, doi:10.1029/2001JB000596. 2.1, 2.2, 2.3, 2.4.5, 2.4.5, 2.4.5, 2.18

Tibaldi, A. (1995), Morphology of pyroclastic cones and tectonics, *Journal of Geophysical Research*, *100*(B12), doi:10.1029/95jb02250. 3.7.2

Tocher, D. (1960), Creep on the San Andreas Fault: Creep Rate and Related Measurements at Vineyard, California, *Bulletin of the Seismological Society of America*, *50*(3), 396–404. 1.2

Tong, X., D. T. Sandwell, and D. A. Schmidt (2018), Surface Creep Rate and Moment Accumulation Rate Along the Aceh Segment of the Sumatran Fault From L-band ALOS-1/PALSAR-1 Observations, *Geophysical Research Letters*, *45*(8), 3404–3412, doi:10.1002/2017GL076723. 4.1

Tse, S. T., and J. R. Rice (1986), Crustal earthquake instability in relation to the depth variation of frictional slip properties, *Journal of Geophysical Research*, *91*(B9), 9452, doi:10.1029/jb091ib09p09452. 4.5.1

Tse, S. T., R. Dmowska, and J. R. Rice (1985), Stressing of locked patches along a creeping fault, *Bulletin of the Seismological Society of America*, *75*(3), 709–736. 4.1, 4.5.4

Tsutsumi, H., and J. S. Perez (2013), Large-scale active fault map of The Philippines based on aerial photograph interpretation, *Active Fault Research*, *39*(39), 29–37. 4.1, 4.2.1, 4.2.2, 4.3.2, 4.3.4

Tsutsumi, H., J. S. Perez, J. U. Marjes, K. L. Papiona, and N. T. Ramos (2015), Coseismic Displacement and Recurrence Interval of the 1973 Ragay Gulf Earthquake, Southern Luzon, Philippines, *Journal of Disaster Research*, *10*(1), 83–90. 4.2.1

Tsutsumi, H., J. S. Perez, and J. J. Lienkaemper (2016), Variation of Surface Creep Rate Along the Philippine Fault Based on Surveys of Alinement Arrays and Offset Cultural Features, *Paper presented at the American Geophysical Union Fall Meeting 2016*, pp. T23A–2907. 4.3.2, J.4, J.5

Tymofyeyeva, E., and Y. Fialko (2018), Geodetic Evidence for a Blind Fault Segment at the Southern End of the San Jacinto Fault Zone, *Journal of Geophysical Research: Solid Earth*, pp. 878–891, doi:10.1002/2017JB014477. 4.3.1

Waldhauser, F., and W. L. Ellsworth (2000), A Double-difference Earthquake location algorithm: Method and application to the Northern Hayward Fault, California, *Bulletin of the Seismological Society of America*, *90*(6), 1353–1368, doi:10.1785/0120000006. 4.5.4

Walker, R. T., M. M. Khatib, A. Bahroudi, A. Rodés, C. Schnabel, M. Fattahi, M. Talebian, and E. Bergman (2015), Co-seismic, geomorphic, and geologic fold growth associated with the 1978 Tabas-e-Golshan earthquake fault in eastern Iran, *Geomorphology*, *237*, 98–118, doi:10.1016/j.geomorph.2013.02.016. 1.2

Walsh, J. B. (1965a), The Effect of Cracks on the Compressibility of Rock, *Journal of Geophysical Research*, *70*(2), 381–389, doi:10.1029/JB083iB09p04459. 4.5.5

Walsh, J. B. (1965b), The effect of cracks in rocks on Poisson's ratio, *Journal of Geophysical Research*, *70*(20), 5249–5257, doi:10.1029/jz070i020p05249. 4.5.5

Wang, R., F. L. Martín, and F. Roth (2003), Computation of deformation induced by earthquakes in a multi-layered elastic crust - FORTRAN programs EDGRN/EDCMP, *Computers and Geosciences*, *29*(2), 195–207, doi:10.1016/S0098-3004(02)00111-5. 3.5

Wang, R., F. Lorenzo-Martín, and F. Roth (2006), PSGRN/PSCMP - A new code for calculating co- and post-seismic deformation, geoid and gravity changes based on the viscoelastic-gravitational dislocation theory, *Computers and Geosciences*, *32*(4), 527–541, doi:10.1016/j.cageo.2005.08.006. 3.5

Wells, D., and K. Coppersmith (1994), New empirical relationships among magnitude, rupture length, rupture width, rupture area, and surface displacement, *Bulletin of the Seismological Society of America*, *84*(4), 974–1002. 2.5.1

Werner, C., U. Wegmüller, T. Strozzi, and A. Wiesmann (2002), Processing strategies for phase unwrapping for INSAR applications, in *Proceedings: European Conference on Synthetic Aperture Radar (EUSAR) 2002*, vol. 1, pp. 353–356. 4.3.1

Wesnousky, S. G. (2006), Predicting the endpoints of earthquake rupture, *Nature*, *444*. 4.5.2

Wesnousky, S. G. (2008), Displacement and geometrical characteristics of earthquake surface ruptures: Issues and implications for seismic-hazard analysis and the process of earthquake rupture, *Bulletin of the Seismological Society of America*, *98*(4), 1609–1632, doi:10.1785/0120070111. 3.7.2

Westoby, M. J., J. Brasington, N. F. Glasser, M. J. Hambrey, and J. M. Reynolds (2012), 'Structure-from-Motion' photogrammetry: A low-cost, effective tool for geoscience applications, *Geomorphology*, *179*, 300–314, doi:10.1016/j.geomorph.2012.08.021. 2.4.1

Willis, B. (1944), Philippine earthquakes and structure, *Bulletin of the Seismological Society of America*, *34*(2), doi:10.2307/1779766. 4.2.2

Wright, T., B. Parsons, and E. Fielding (2001), Measurement of interseismic strain accumulation the North Anatolian Fault by satellite radar interferometry, *Geophysical Research Letters*, *28*(10), 2117–2120, doi:10.1029/2000GL012850. 1.2, 4.1

Wright, T. J., Z. Lu, and C. Wicks (2004), Constraining the slip distribution and fault geometry of the Mw 7.9, 3 November 2002, Denali fault earthquake with Interferometric Synthetic Aperture Radar and Global Positioning System data, *Bulletin of the Seismological Society of America*, *94*(6 SUPPL. B), 175–189, doi:10.1785/0120040623. 4.3.1

Yang, Y., M. Tsai, J. Hu, M. A. Aurelio, M. Hashimoto, J. A. P. Escudero, Z. Su, and Q. Chen (2018), Coseismic slip deficit of the 2017 Mw 6.5 Ormoc Earthquake that occurred along a creeping segment and geothermal field of the Philippine Fault, *Geophysical Research Letters*, *45*, doi:10.1002/2017GL076417. 4.1, 4.4, 4.5.4, 4.4

Yu, C., Z. Li, and N. T. Penna (2018), Interferometric synthetic aperture radar atmospheric correction using a GPS-based iterative tropospheric decomposition model, *Remote Sensing of Environment*, *204*, 109–121, doi:10.1016/j.rse.2017.10.038. 3.4

Yu, S.-B., Y.-J. Hsu, T. Bacolcol, C.-C. Yang, Y.-C. Tsai, and R. Solidum (2013), Present-day crustal deformation along the Philippine Fault in Luzon, Philippines, *Journal of Asian Earth Sciences*, *65*, 64–74, doi:10.1016/j.jseaes.2010.12.007. 4.2.1

Yue, H., Z. E. Ross, C. Liang, S. Michel, H. Fattahi, E. Fielding, A. Moore, Z. Liu, and B. Jia (2017), The 2016 Kumamoto Mw = 7.0 Earthquake: A Significant Event in a FaultVolcano System, *Journal of Geophysical Research: Solid Earth*, *122*(11), 9166–9183, doi:10.1002/2017JB014525. 3.7.2, 3.8

Yumul, G. P., C. B. Dimalanta, R. A. Tamayo, R. C. Maury, H. Bellon, M. Polvé, V. B. Maglambayan, C. L. Querubin, and J. Cotten (2004), Geology of the Zamboanga Peninsula, Mindanao, Philippines: An enigmatic South China continental fragment?, *Geological Society Special Publication*, *226*, 289–312, doi:10.1144/GSL.SP.2004.226.01.16. 3.2, 3.7.3

Zhou, Y., B. Parsons, J. R. Elliott, I. Barisin, and R. T. Walker (2015), Assessing the ability of Pleiades stereo imagery to determine height changes in earthquakes: A case study for the El Mayor-Cucapah epicentral area, *Journal of Geophysical Research: Solid Earth*, *120*(12), 8793–8808, doi:10.1002/2015JB012358. 1.2

Zinke, R., J. Hollingsworth, and J. F. Dolan (2014), Surface slip and off-fault deformation patterns in the 2013 Mw 7.7 Balochistan, Pakistan earthquake: Implications for controls on the distribution of near-surface coseismic slip, *Geochemistry, Geophysics, Geosystems*, *15*(12), 5034–5050, doi:10.1002/2014GC005538. 1.2, 3.7.2

Zubovich, A. V., X. Q. Wang, Y. G. Scherba, G. G. Schelochkov, R. Reilinger, C. Reigber, O. I. Mosienko, P. Molnar, W. Michajljow, V. I. Makarov, J. Li, S. I. Kuzikov, T. A. Herring, M. W. Hamburger, B. H. Hager, Y. M. Dang, V. D. Bragin, and R. T. Beisenbaev (2010), GPS velocity field for the Tien Shan and surrounding regions, *Tectonics*, *29*(6), 1–23, doi:10.1029/2010TC002772. 2.1, 2.2, 2.3, 2.2, 2.4, 2.5, 2.4.5

Zwick, P., R. McCaffrey, and G. Abers (1994), MT5 Program. 3.3

Appendix A

Radiocarbon dating reports

Beta Analytic Inc
4985 SW 74 Court
Miami, Florida 33155
Tel: 305-667-5167
Fax: 305-663-0964
beta@radiocarbon.com

Mr. Darden Hood
President

Mr. Ronald Hatfield
Mr. Christopher Patrick
Deputy Directors

ISO/IEC 17025:2005 Accredited Test Results: Testing results recognized by all Signatories to the ILAC Mutual Recognition Arrangement

August 06, 2018

Prof. Richard Walker
Oxford University
Department of Earth Sciences
Oxford, Oxon OX1 3AN
United Kingdom

RE: Radiocarbon Dating Results

Dear Prof. Walker,

Enclosed are the radiocarbon dating results for 11 samples recently sent to us. As usual, the method of analysis is listed on the report with the results and calibration data is provided where applicable. The Conventional Radiocarbon Ages have all been corrected for total fractionation effects and where applicable, calibration was performed using 2013 calibration databases (cited on the graph pages).

The web directory containing the table of results and PDF download also contains pictures, a cvs spreadsheet download option and a quality assurance report containing expected vs. measured values for 3-5 working standards analyzed simultaneously with your samples.

Reported results are accredited to ISO/IEC 17025:2005 Testing Accreditation PJLA #59423 standards and all chemistry was performed here in our laboratory and counted in our own accelerators here. Since Beta is not a teaching laboratory, only graduates trained to strict protocols of the ISO/IEC 17025:2005 Testing Accreditation PJLA #59423 program participated in the analyses.

As always Conventional Radiocarbon Ages and sigmas are rounded to the nearest 10 years per the conventions of the 1977 International Radiocarbon Conference. When counting statistics produce sigmas lower than +/- 30 years, a conservative +/- 30 BP is cited for the result. The reported d13C values were measured separately in an IRMS (isotope ratio mass spectrometer). They are NOT the AMS d13C which would include fractionation effects from natural, chemistry and AMS induced sources.

When interpreting the results, please consider any communications you may have had with us regarding the samples.

The cost of analysis was previously invoiced. As always, if you have any questions or would like to discuss the results, don't hesitate to contact us.

Sincerely ,



Beta Analytic
RADIOCARBON DATING

Beta Analytic Inc
4985 SW 74 Court
Miami, Florida 33155
Tel: 305-667-5167
Fax: 305-663-0964
beta@radiocarbon.com

Mr. Darden Hood
President

Mr. Ronald Hatfield
Mr. Christopher Patrick
Deputy Directors

ISO/IEC 2005:17025-Accredited Testing Laboratory

REPORT OF RADIOCARBON DATING ANALYSES

Richard Walker — Report Date: August 06, 2018

Oxford University — Material Received: July 17, 2018

Laboratory Number	Sample Code Number	Conventional Radiocarbon Age (BP) or Percent Modern Carbon (pMC) & Stable Isotopes Calendar Calibrated Results: 95.4 % Probability High Probability Density Range Method (HPD)	
Beta - 499690	**S1e**	**780 +/- 30 BP**	IRMS δ13C: -7.8 o/oo IRMS δ18O: -3.9 o/oo
(95.4%)	**1210 - 1281 cal AD**	**(740 - 669 cal BP)**	

Submitter Material: Shell (Freshwater)
Pretreatment: (shell) acid etch
Analyzed Material: Shell
Analysis Service: AMS-Standard delivery
Percent Modern Carbon: 90.75 +/- 0.34 pMC
Fraction Modern Carbon: 0.9075 +/- 0.0034
D14C: -92.54 +/- 3.39 o/oo
Δ14C: -99.97 +/- 3.39 o/oo(1950:2,018.00)
Measured Radiocarbon Age: (without d13C correction): 500 +/- 30 BP
Calibration: BetaCal3.21: HPD method: INTCAL13

Results are ISO/IEC-17025:2005 accredited. No sub-contracting or student labor was used in the analyses. All work was done at Beta in 4 in-house NEC accelerator mass spectrometers and 4 Thermo IRMSs. The "Conventional Radiocarbon Age" was calculated using the Libby half-life (5568 years), is corrected for total isotopic fraction and was used for calendar calibration where applicable. The Age is rounded to the nearest 10 years and is reported as radiocarbon years before present (BP), "present" = AD 1950. Results greater than the modern reference are reported as percent modern carbon (pMC). The modern reference standard was 95% the 14C signature of NIST SRM-4990C (oxalic acid). Quoted errors are 1 sigma counting statistics. Calculated sigmas less than 30 BP on the Conventional Radiocarbon Age are conservatively rounded up to 30. d13C values are on the material itself (not the AMS d13C). d13C and d15N values are relative to VPDB-1. References for calendar calibrations are cited at the bottom of calibration graph pages.

Beta Analytic
RADIOCARBON DATING

Beta Analytic Inc
4985 SW 74 Court
Miami, Florida 33155
Tel: 305-667-5167
Fax: 305-663-0964
beta@radiocarbon.com

Mr. Darden Hood
President

Mr. Ronald Hatfield
Mr. Christopher Patrick
Deputy Directors

ISO/IEC 2005:17025-Accredited Testing Laboratory

REPORT OF RADIOCARBON DATING ANALYSES

Richard Walker — Report Date: August 06, 2018

Oxford University — Material Received: July 17, 2018

Laboratory Number	Sample Code Number	Conventional Radiocarbon Age (BP) or Percent Modern Carbon (pMC) & Stable Isotopes Calendar Calibrated Results: 95.4 % Probability High Probability Density Range Method (HPD)	
Beta - 499691	**S2e**	**10160 +/- 30 BP**	IRMS δ13C: -5.3 o/oo IRMS δ18O: -2.2 o/oo
(95.4%)	**10071 - 9759 cal BC**	**(12020 - 11708 cal BP)**	

Submitter Material: Shell (Freshwater)
Pretreatment: (shell) acid etch
Analyzed Material: Shell
Analysis Service: AMS-Standard delivery
Percent Modern Carbon: 28.23 +/- 0.11 pMC
Fraction Modern Carbon: 0.2823 +/- 0.0011
D14C: -717.70 +/- 1.05 o/oo
Δ14C: -720.02 +/- 1.05 o/oo(1950:2,018.00)
Measured Radiocarbon Age: (without d13C correction): 9840 +/- 30 BP
Calibration: BetaCal3.21: HPD method: INTCAL13

Results are ISO/IEC-17025:2005 accredited. No sub-contracting or student labor was used in the analyses. All work was done at Beta in 4 in-house NEC accelerator mass spectrometers and 4 Thermo IRMSs. The "Conventional Radiocarbon Age" was calculated using the Libby half-life (5568 years), is corrected for total isotopic fraction and was used for calendar calibration where applicable. The Age is rounded to the nearest 10 years and is reported as radiocarbon years before present (BP), "present" = AD 1950. Results greater than the modern reference are reported as percent modern carbon (pMC). The modern reference standard was 95% the 14C signature of NIST SRM-4990C (oxalic acid). Quoted errors are 1 sigma counting statistics. Calculated sigmas less than 30 BP on the Conventional Radiocarbon Age are conservatively rounded up to 30. d13C values are on the material itself (not the AMS d13C). d13C and d15N values are relative to VPDB-1. References for calendar calibrations are cited at the bottom of calibration graph pages.

Beta Analytic
RADIOCARBON DATING

Beta Analytic Inc
4985 SW 74 Court
Miami, Florida 33155
Tel: 305-667-5167
Fax: 305-663-0964
beta@radiocarbon.com

Mr. Darden Hood
President

Mr. Ronald Hatfield
Mr. Christopher Patrick
Deputy Directors

ISO/IEC 2005:17025-Accredited Testing Laboratory

REPORT OF RADIOCARBON DATING ANALYSES

Richard Walker — Report Date: August 06, 2018

Oxford University — Material Received: July 17, 2018

Laboratory Number	Sample Code Number	Conventional Radiocarbon Age (BP) or Percent Modern Carbon (pMC) & Stable Isotopes Calendar Calibrated Results: 95.4 % Probability High Probability Density Range Method (HPD)	
Beta - 499692	**S1w**	**1530 +/- 30 BP**	IRMS δ13C: -7.7 o/oo IRMS δ18O: -4.6 o/oo
(95.4%)	**428 - 598 cal AD**	**(1522 - 1352 cal BP)**	

Submitter Material: Shell (Freshwater)
Pretreatment: (shell) acid etch
Analyzed Material: Shell
Analysis Service: AMS-Standard delivery
Percent Modern Carbon: 82.66 +/- 0.31 pMC
Fraction Modern Carbon: 0.8266 +/- 0.0031
D14C: -173.43 +/- 3.09 o/oo
Δ14C: -180.20 +/- 3.09 o/oo(1950:2,018.00)
Measured Radiocarbon Age: (without d13C correction): 1250 +/- 30 BP
Calibration: BetaCal3.21: HPD method: INTCAL13

Results are ISO/IEC-17025:2005 accredited. No sub-contracting or student labor was used in the analyses. All work was done at Beta in 4 in-house NEC accelerator mass spectrometers and 4 Thermo IRMSs. The "Conventional Radiocarbon Age" was calculated using the Libby half-life (5568 years), is corrected for total isotopic fraction and was used for calendar calibration where applicable. The Age is rounded to the nearest 10 years and is reported as radiocarbon years before present (BP), "present" = AD 1950. Results greater than the modern reference are reported as percent modern carbon (pMC). The modern reference standard was 95% the 14C signature of NIST SRM-4990C (oxalic acid). Quoted errors are 1 sigma counting statistics. Calculated sigmas less than 30 BP on the Conventional Radiocarbon Age are conservatively rounded up to 30. d13C values are on the material itself (not the AMS d13C). d13C and d15N values are relative to VPDB-1. References for calendar calibrations are cited at the bottom of calibration graph pages.

Beta Analytic Inc
4985 SW 74 Court
Miami, Florida 33155
Tel: 305-667-5167
Fax: 305-663-0964
beta@radiocarbon.com

Mr. Darden Hood
President

Mr. Ronald Hatfield
Mr. Christopher Patrick
Deputy Directors

ISO/IEC 2005:17025-Accredited Testing Laboratory

REPORT OF RADIOCARBON DATING ANALYSES

Richard Walker — Report Date: August 06, 2018

Oxford University — Material Received: July 17, 2018

Laboratory Number	Sample Code Number	Conventional Radiocarbon Age (BP) or Percent Modern Carbon (pMC) & Stable Isotopes Calendar Calibrated Results: 95.4 % Probability High Probability Density Range Method (HPD)	
Beta - 499693	**S2w**	**9240 +/- 30 BP**	IRMS δ13C: -7.3 o/oo IRMS δ18O: -6.8 o/oo
(95.4%)	**8561 - 8331 cal BC**	**(10510 - 10280 cal BP)**	

Submitter Material: Shell (Freshwater)
Pretreatment: (shell) acid etch
Analyzed Material: Shell
Analysis Service: AMS-Standard delivery
Percent Modern Carbon: 31.66 +/- 0.12 pMC
Fraction Modern Carbon: 0.3166 +/- 0.0012
D14C: -683.45 +/- 1.18 o/oo
Δ14C: -686.04 +/- 1.18 o/oo(1950:2,018.00)
Measured Radiocarbon Age: (without d13C correction): 8950 +/- 30 BP
Calibration: BetaCal3.21: HPD method: INTCAL13

Results are ISO/IEC-17025:2005 accredited. No sub-contracting or student labor was used in the analyses. All work was done at Beta in 4 in-house NEC accelerator mass spectrometers and 4 Thermo IRMSs. The "Conventional Radiocarbon Age" was calculated using the Libby half-life (5568 years), is corrected for total isotopic fraction and was used for calendar calibration where applicable. The Age is rounded to the nearest 10 years and is reported as radiocarbon years before present (BP), "present" = AD 1950. Results greater than the modern reference are reported as percent modern carbon (pMC). The modern reference standard was 95% the 14C signature of NIST SRM-4990C (oxalic acid). Quoted errors are 1 sigma counting statistics. Calculated sigmas less than 30 BP on the Conventional Radiocarbon Age are conservatively rounded up to 30. d13C values are on the material itself (not the AMS d13C). d13C and d15N values are relative to VPDB-1. References for calendar calibrations are cited at the bottom of calibration graph pages.

Beta Analytic
RADIOCARBON DATING

Beta Analytic Inc
4985 SW 74 Court
Miami, Florida 33155
Tel: 305-667-5167
Fax: 305-663-0964
beta@radiocarbon.com

Mr. Darden Hood
President

Mr. Ronald Hatfield
Mr. Christopher Patrick
Deputy Directors

ISO/IEC 2005:17025-Accredited Testing Laboratory

REPORT OF RADIOCARBON DATING ANALYSES

Richard Walker — Report Date: August 06, 2018

Oxford University — Material Received: July 17, 2018

Laboratory Number	Sample Code Number	Conventional Radiocarbon Age (BP) or Percent Modern Carbon (pMC) & Stable Isotopes Calendar Calibrated Results: 95.4 % Probability High Probability Density Range Method (HPD)	
Beta - 499694	**S3w**	**7630 +/- 30 BP**	IRMS δ13C: -7.7 o/oo IRMS δ18O: -3.7 o/oo
(91.0%)	**6512 - 6429 cal BC**	**(8461 - 8378 cal BP)**	
(2.9%)	**6564 - 6547 cal BC**	**(8513 - 8496 cal BP)**	
(1.5%)	**6528 - 6518 cal BC**	**(8477 - 8467 cal BP)**	

Submitter Material: Shell (Freshwater)
Pretreatment: (shell) acid etch
Analyzed Material: Shell
Analysis Service: AMS-Standard delivery
Percent Modern Carbon: 38.68 +/- 0.14 pMC
Fraction Modern Carbon: 0.3868 +/- 0.0014
D14C: -613.20 +/- 1.44 o/oo
Δ14C: -616.37 +/- 1.44 o/oo(1950:2,018.00)
Measured Radiocarbon Age: (without d13C correction): 7350 +/- 30 BP
Calibration: BetaCal3.21: HPD method: INTCAL13

Results are ISO/IEC-17025:2005 accredited. No sub-contracting or student labor was used in the analyses. All work was done at Beta in 4 in-house NEC accelerator mass spectrometers and 4 Thermo IRMSs. The "Conventional Radiocarbon Age" was calculated using the Libby half-life (5568 years), is corrected for total isotopic fraction and was used for calendar calibration where applicable. The Age is rounded to the nearest 10 years and is reported as radiocarbon years before present (BP), "present" = AD 1950. Results greater than the modern reference are reported as percent modern carbon (pMC). The modern reference standard was 95% the 14C signature of NIST SRM-4990C (oxalic acid). Quoted errors are 1 sigma counting statistics. Calculated sigmas less than 30 BP on the Conventional Radiocarbon Age are conservatively rounded up to 30. d13C values are on the material itself (not the AMS d13C). d13C and d15N values are relative to VPDB-1. References for calendar calibrations are cited at the bottom of calibration graph pages.

Beta Analytic
RADIOCARBON DATING

Beta Analytic Inc
4985 SW 74 Court
Miami, Florida 33155
Tel: 305-667-5167
Fax: 305-663-0964
beta@radiocarbon.com

Mr. Darden Hood
President

Mr. Ronald Hatfield
Mr. Christopher Patrick
Deputy Directors

ISO/IEC 2005:17025-Accredited Testing Laboratory

REPORT OF RADIOCARBON DATING ANALYSES

Richard Walker — Report Date: August 06, 2018

Oxford University — Material Received: July 17, 2018

Laboratory Number	Sample Code Number	Conventional Radiocarbon Age (BP) or Percent Modern Carbon (pMC) & Stable Isotopes Calendar Calibrated Results: 95.4 % Probability High Probability Density Range Method (HPD)	
Beta - 499695	**S4w**	**2010 +/- 30 BP**	IRMS δ13C: -8.1 o/oo IRMS δ18O: -2.4 o/oo
(91.2%)	**61 cal BC - 65 cal AD**	**(2010 - 1885 cal BP)**	
(4.2%)	**92 - 68 cal BC**	**(2041 - 2017 cal BP)**	

Submitter Material: Shell (Freshwater)
Pretreatment: (shell) acid etch
Analyzed Material: Shell
Analysis Service: AMS-Standard delivery
Percent Modern Carbon: 77.86 +/- 0.29 pMC
Fraction Modern Carbon: 0.7786 +/- 0.0029
D14C: -221.37 +/- 2.91 o/oo
Δ14C: -227.75 +/- 2.91 o/oo(1950:2,018.00)
Measured Radiocarbon Age: (without d13C correction): 1730 +/- 30 BP
Calibration: BetaCal3.21: HPD method: INTCAL13

Results are ISO/IEC-17025:2005 accredited. No sub-contracting or student labor was used in the analyses. All work was done at Beta in 4 in-house NEC accelerator mass spectrometers and 4 Thermo IRMSs. The "Conventional Radiocarbon Age" was calculated using the Libby half-life (5568 years), is corrected for total isotopic fraction and was used for calendar calibration where applicable. The Age is rounded to the nearest 10 years and is reported as radiocarbon years before present (BP), "present" = AD 1950. Results greater than the modern reference are reported as percent modern carbon (pMC). The modern reference standard was 95% the 14C signature of NIST SRM-4990C (oxalic acid). Quoted errors are 1 sigma counting statistics. Calculated sigmas less than 30 BP on the Conventional Radiocarbon Age are conservatively rounded up to 30. d13C values are on the material itself (not the AMS d13C). d13C and d15N values are relative to VPDB-1. References for calendar calibrations are cited at the bottom of calibration graph pages.

Beta Analytic
RADIOCARBON DATING

Beta Analytic Inc
4985 SW 74 Court
Miami, Florida 33155
Tel: 305-667-5167
Fax: 305-663-0964
beta@radiocarbon.com

Mr. Darden Hood
President

Mr. Ronald Hatfield
Mr. Christopher Patrick
Deputy Directors

ISO/IEC 2005:17025-Accredited Testing Laboratory

REPORT OF RADIOCARBON DATING ANALYSES

Richard Walker — Report Date: August 06, 2018

Oxford University — Material Received: July 17, 2018

Laboratory Number	Sample Code Number	Conventional Radiocarbon Age (BP) or Percent Modern Carbon (pMC) & Stable Isotopes Calendar Calibrated Results: 95.4 % Probability High Probability Density Range Method (HPD)	
Beta - 499696	**S5w**	**10660 +/- 30 BP**	IRMS δ13C: -6.1 o/oo IRMS δ18O: -2.6 o/oo
(95.4%)	**10751 - 10621 cal BC**	**(12700 - 12570 cal BP)**	

Submitter Material: Shell (Freshwater)
Pretreatment: (shell) acid etch
Analyzed Material: Shell
Analysis Service: AMS-Standard delivery
Percent Modern Carbon: 26.53 +/- 0.10 pMC
Fraction Modern Carbon: 0.2653 +/- 0.0010
D14C: -734.74 +/- 0.99 o/oo
Δ14C: -736.91 +/- 0.99 o/oo(1950:2,018.00)
Measured Radiocarbon Age: (without d13C correction): 10350 +/- 30 BP
Calibration: BetaCal3.21: HPD method: INTCAL13

Results are ISO/IEC-17025:2005 accredited. No sub-contracting or student labor was used in the analyses. All work was done at Beta in 4 in-house NEC accelerator mass spectrometers and 4 Thermo IRMSs. The "Conventional Radiocarbon Age" was calculated using the Libby half-life (5568 years), is corrected for total isotopic fraction and was used for calendar calibration where applicable. The Age is rounded to the nearest 10 years and is reported as radiocarbon years before present (BP), "present" = AD 1950. Results greater than the modern reference are reported as percent modern carbon (pMC). The modern reference standard was 95% the 14C signature of NIST SRM-4990C (oxalic acid). Quoted errors are 1 sigma counting statistics. Calculated sigmas less than 30 BP on the Conventional Radiocarbon Age are conservatively rounded up to 30. d13C values are on the material itself (not the AMS d13C). d13C and d15N values are relative to VPDB-1. References for calendar calibrations are cited at the bottom of calibration graph pages.

Beta Analytic Inc.
4985 S.W. 74 Court
Miami, Florida 33155 USA
PH: 305-667-5167
FAX: 305-663-0964
beta@radiocarbon.com
www.radiocarbon.com

Consistent accuracy delivered on time

Darden Hood
President

Ronald Hatfield
Christopher Patrick
Deputy Directors

September 19, 2017

Richard Walker
Oxford University
Department of Earth Sciences
Oxford, Oxon OX1 3AN
United Kingdom

RE: Radiocarbon Dating Results

Prof. Walker,

Enclosed are the radiocarbon dating results for three samples recently sent to us. As usual, the method of analysis is listed on the report with the results and calibration data is provided where applicable. The Conventional Radiocarbon Ages have all been corrected for total fractionation effects and where applicable, calibration was performed using 2013 calibration databases (cited on the graph pages).

The web directory containing the table of results and PDF download also contains pictures, a cvs spreadsheet download option and a quality assurance report containing expected vs. measured values for 3-5 working standards analyzed simultaneously with your samples.

Reported results are accredited to ISO/IEC 17025:2005 Testing Accreditation PJLA #59423 standards and all chemistry was performed here in our laboratory and counted in our own accelerators here. Since Beta is not a teaching laboratory, only graduates trained to strict protocols of the ISO/IEC 17025:2005 Testing Accreditation PJLA #59423 program participated in the analyses.

As always Conventional Radiocarbon Ages and sigmas are rounded to the nearest 10 years per the conventions of the 1977 International Radiocarbon Conference. When counting statistics produce sigmas lower than +/- 30 years, a conservative +/- 30 BP is cited for the result. The reported d13C values were measured separately in an IRMS (isotope ratio mass spectrometer). They are NOT the AMS d13C which would include fractionation effects from natural, chemistry and AMS induced sources.

When interpreting the results, please consider any communications you may have had with us regarding the samples.

The cost of the analysis was charged to the VISA card provided. Thank you. As always, if you have any questions or would like to discuss the results, don't hesitate to contact us.

Sincerely ,



Beta Analytic
RADIOCARBON DATING
Consistent accuracy delivered on time

DR. M.A. TAMERS and MR. D.G. HOOD
4985 S.W. 74th Court
Miami, Florida, USA 33155
PH: 305-667-5167 FAX: 305-663-0964
beta@radiocarbon.com

REPORT OF RADIOCARBON DATING ANALYSES

Richard Walker

Oxford University

Rerport Date: September 19, 2017

Material Received: August 21, 2017

Sample Information and Data	Sample Code Number	Conventional Radiocarbon Age (BP) or Percent Modern Carbon (pMC) & Stable Isotopes Calendar Calibrated Results: 95.4 % Probability High Probability Density Range Method (HPD)	
Beta - 472013	**K17-NA1**	**8800 +/- 30 BP**	IRMS δ13C: -8.1 o/oo IRMS δ18O: -2.1 o/oo
Submitter Material: Shell (Freshwater)		**(91.6%) 7976 - 7740 cal BC** **(3.8%) 8167 - 8126 cal BC**	**(9925 - 9689 cal BP)** **(10116 - 10075 cal BP)**
Analyzed Material: Shell Pretreatment: (shell) acid etch			
Analysis Service: AMS-Standard delivery Percent Modern Carbon: 33.44 +/- 0.12 pMC Fraction Modern Carbon: 0.3344 +/- 0.0012 D14C: -665.62 +/- 1.25 o/oo Δ14C: -668.32 +/- 1.25 o/oo(1950:2017) Measured Radiocarbon Age: (without d13C correction): 8520 +/- 30 BP Calibration: BetaCal3.21: HPD method: INTCAL13			

Results are ISO/IEC-17025:2005 accredited. No sub-contracting or student labor was used in the analyses. All work was done at Beta in 4 in-house NEC accelerator mass spectrometers and 4 Thermo IRMSs. The "Conventional Radiocarbon Age" was calculated using the Libby half-life (5568 years), is corrected for total isotopic fraction and was used for calendar calibration where applicable. The Age is rounded to the nearest 10 years and is reported as radiocarbon years before present (BP), “present" = AD 1950. Results greater than the modern reference are reported as percent modern carbon (pMC). The modern reference standard was 95% the 14C signature of NIST SRM-4990C (oxalic acid). Quoted errors are 1 sigma counting statistics. Calculated sigmas less than 30 BP on the Conventional Radiocarbon Age are conservatively rounded up to 30. d13C values are on the material itself (not the AMS d13C). d13C and d15N values are relative to VPDB-1. References for calendar calibrations are cited at the bottom of calibration graph pages.

Beta Analytic
RADIOCARBON DATING
Consistent accuracy delivered on time

DR. M.A. TAMERS and MR. D.G. HOOD
4985 S.W. 74th Court
Miami, Florida, USA 33155
PH: 305-667-5167 FAX: 305-663-0964
beta@radiocarbon.com

REPORT OF RADIOCARBON DATING ANALYSES

Richard Walker

Oxford University

Rerport Date: September 19, 2017

Material Received: August 21, 2017

Sample Information and Data	Sample Code Number	Conventional Radiocarbon Age (BP) or Percent Modern Carbon (pMC) & Stable Isotopes Calendar Calibrated Results: 95.4 % Probability High Probability Density Range Method (HPD)
Beta - 472014	**K17-NA2**	**13120 +/- 40 BP** IRMS δ13C: -4.0 o/oo IRMS δ18O: -3.6 o/oo
Submitter Material: Shell (Freshwater)		**(95.4%) 14017 - 13615 cal BC (15966 - 15564 cal BP)**
Analyzed Material: Shell Pretreatment: (shell) acid etch		
Analysis Service: AMS-Micro-sample Analysis; Standard delivery Percent Modern Carbon: 19.53 +/- 0.10 pMC Fraction Modern Carbon: 0.1953 +/- 0.0010 D14C: -804.71 +/- 0.97 o/oo Δ14C: -806.29 +/- 0.97 o/oo(1950:2017) Measured Radiocarbon Age: (without d13C correction): 12780 +/- 40 BP Calibration: BetaCal3.21: HPD method: INTCAL13		

Results are ISO/IEC-17025:2005 accredited. No sub-contracting or student labor was used in the analyses. All work was done at Beta in 4 in-house NEC accelerator mass spectrometers and 4 Thermo IRMSs. The "Conventional Radiocarbon Age" was calculated using the Libby half-life (5568 years), is corrected for total isotopic fraction and was used for calendar calibration where applicable. The Age is rounded to the nearest 10 years and is reported as radiocarbon years before present (BP), “present" = AD 1950. Results greater than the modern reference are reported as percent modern carbon (pMC). The modern reference standard was 95% the 14C signature of NIST SRM-4990C (oxalic acid). Quoted errors are 1 sigma counting statistics. Calculated sigmas less than 30 BP on the Conventional Radiocarbon Age are conservatively rounded up to 30. d13C values are on the material itself (not the AMS d13C). d13C and d15N values are relative to VPDB-1. References for calendar calibrations are cited at the bottom of calibration graph pages.

Beta Analytic
RADIOCARBON DATING
Consistent accuracy delivered on time

DR. M.A. TAMERS and MR. D.G. HOOD
4985 S.W. 74th Court
Miami, Florida, USA 33155
PH: 305-667-5167 FAX: 305-663-0964
beta@radiocarbon.com

REPORT OF RADIOCARBON DATING ANALYSES

Richard Walker

Oxford University

Rerport Date: September 19, 2017

Material Received: August 21, 2017

Sample Information and Data	Sample Code Number	Conventional Radiocarbon Age (BP) or Percent Modern Carbon (pMC) & Stable Isotopes Calendar Calibrated Results: 95.4 % Probability High Probability Density Range Method (HPD)	
Beta - 472016	**K17-NA4**	**310 +/- 30 BP**	IRMS δ13C: -10.4 o/oo IRMS δ18O: -0.6 o/oo
Submitter Material: Shell (Freshwater)		**(95.4%) 1485 - 1650 cal AD**	**(465 - 300 cal BP)**

Analyzed Material: Shell
Pretreatment: (shell) acid etch

Analysis Service: AMS-Standard delivery
Percent Modern Carbon: 96.21 +/- 0.36 pMC
Fraction Modern Carbon: 0.9621 +/- 0.0036
D14C: -37.86 +/- 3.59 o/oo
Δ14C: -45.62 +/- 3.59 o/oo(1950:2017)
Measured Radiocarbon Age: (without d13C correction): 70 +/- 30 BP
Calibration: BetaCal3.21: HPD method: INTCAL13

Results are ISO/IEC-17025:2005 accredited. No sub-contracting or student labor was used in the analyses. All work was done at Beta in 4 in-house NEC accelerator mass spectrometers and 4 Thermo IRMSs. The "Conventional Radiocarbon Age" was calculated using the Libby half-life (5568 years), is corrected for total isotopic fraction and was used for calendar calibration where applicable. The Age is rounded to the nearest 10 years and is reported as radiocarbon years before present (BP), “present" = AD 1950. Results greater than the modern reference are reported as percent modern carbon (pMC). The modern reference standard was 95% the 14C signature of NIST SRM-4990C (oxalic acid). Quoted errors are 1 sigma counting statistics. Calculated sigmas less than 30 BP on the Conventional Radiocarbon Age are conservatively rounded up to 30. d13C values are on the material itself (not the AMS d13C). d13C and d15N values are relative to VPDB-1. References for calendar calibrations are cited at the bottom of calibration graph pages.

BetaCal 3.21

Calibration of Radiocarbon Age to Calendar Years

(High Probability Density Range Method (HPD): INTCAL13)

(Variables: d13C = -8.1 o/oo)

Laboratory number **Beta-472013**

Conventional radiocarbon age **8800 ± 30 BP**

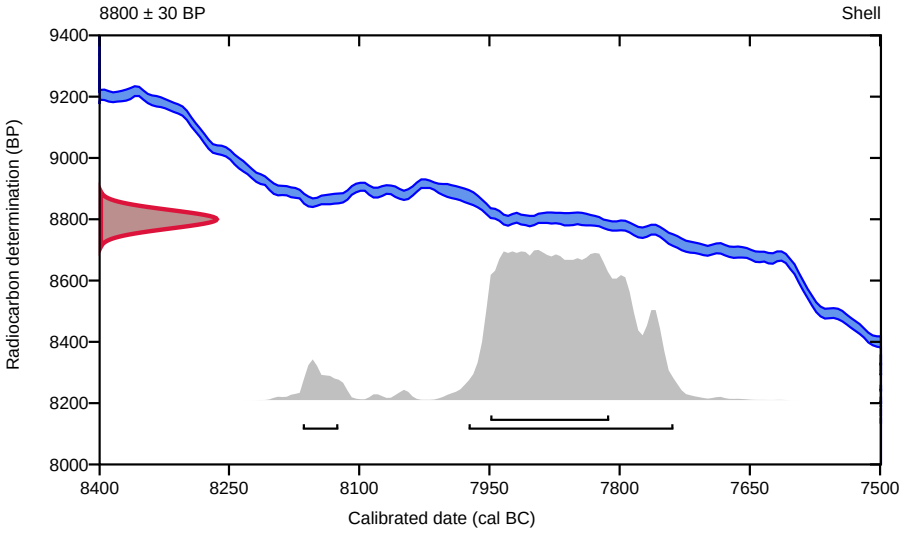
95.4% probability

(91.6%)	7976 - 7740 cal BC	(9925 - 9689 cal BP)
(3.8%)	8167 - 8126 cal BC	(10116 - 10075 cal BP)

68.2% probability

(68.2%)	7951 - 7814 cal BC	(9900 - 9763 cal BP)

K17-NA1



Database used

INTCAL13

References

References to Probability Method

Bronk Ramsey, C. (2009). Bayesian analysis of radiocarbon dates. Radiocarbon, 51(1), 337-360.

References to Database INTCAL13

Reimer, et.al., 2013, Radiocarbon55(4).

BetaCal 3.21

Calibration of Radiocarbon Age to Calendar Years

(High Probability Density Range Method (HPD): INTCAL13)

(Variables: d13C = -4.0 o/oo)

Laboratory number **Beta-472014**

Conventional radiocarbon age **13120 ± 40 BP**

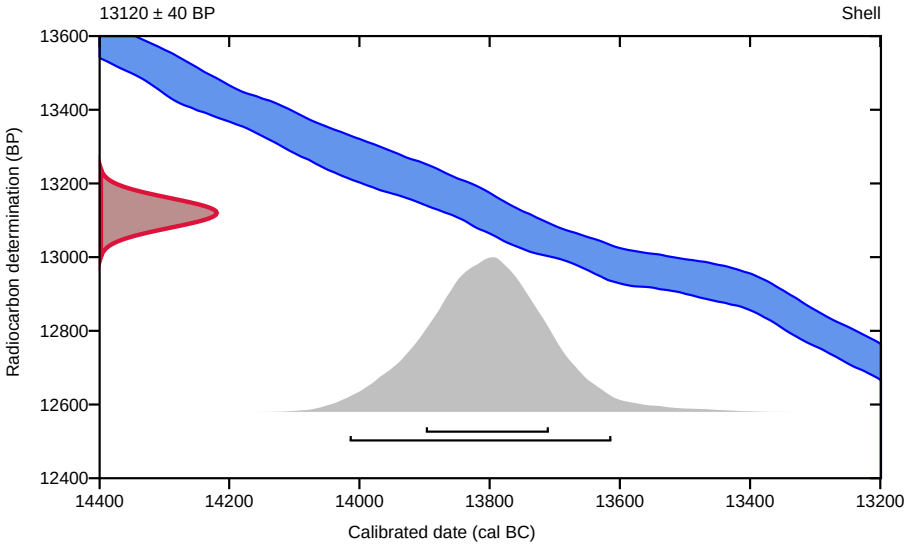
95.4% probability

(95.4%) 14017 - 13615 cal BC (15966 - 15564 cal BP)

68.2% probability

(68.2%) 13900 - 13711 cal BC (15849 - 15660 cal BP)

K17-NA2



Database used

INTCAL13

References

References to Probability Method

Bronk Ramsey, C. (2009). Bayesian analysis of radiocarbon dates. Radiocarbon, 51(1), 337-360.

References to Database INTCAL13

Reimer, et.al., 2013, Radiocarbon55(4).

Beta Analytic Radiocarbon Dating Laboratory

4985 S.W. 74th Court, Miami, Florida 33155 • Tel: (305)667-5167 • Fax: (305)663-0964 • Email: beta@radiocarbon.com

BetaCal 3.21

Calibration of Radiocarbon Age to Calendar Years

(High Probability Density Range Method (HPD): INTCAL13)

(Variables: d13C = -10.4 o/oo)

Laboratory number **Beta-472016**

Conventional radiocarbon age **310 ± 30 BP**

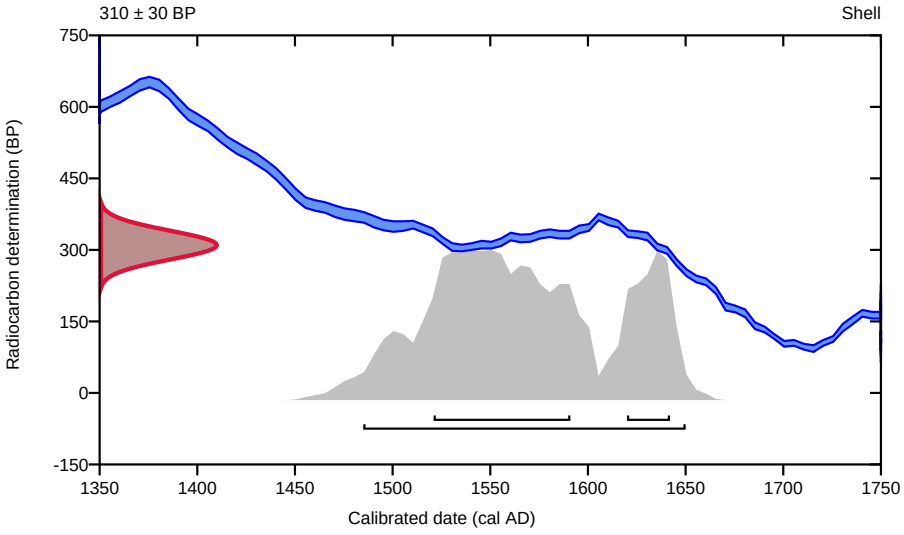
95.4% probability

(95.4%) 1485 - 1650 cal AD (465 - 300 cal BP)

68.2% probability

(51.8%) 1521 - 1591 cal AD (429 - 359 cal BP)
(16.4%) 1620 - 1642 cal AD (330 - 308 cal BP)

K17-NA4



Database used

INTCAL13

References

References to Probability Method

Bronk Ramsey, C. (2009). Bayesian analysis of radiocarbon dates. Radiocarbon, 51(1), 337-360.

References to Database INTCAL13

Reimer, et.al., 2013, Radiocarbon55(4).

Beta Analytic Radiocarbon Dating Laboratory

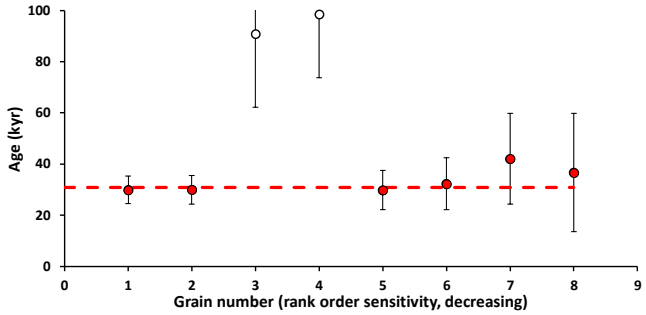
4985 S.W. 74th Court, Miami, Florida 33155 • Tel: (305)667-5167 • Fax: (305)663-0964 • Email: beta@radiocarbon.com

Appendix B

IRSL dating results

The dating results presented here is from work done by Ed Rhodes at the Department of Geography, University of Sheffield, through single grain post-IR IRSL dating of sediment samples from the central Tien Shan. The methodology of sample processing and dose estimation is discussed extensively in previous works (e.g., *Rhodes*, 2015; *Middleton et al.*, 2017). In reporting the burial age, self-consistent ages of at least ten grains (aliquots) at a minimum value, within their errors, are considered reliable estimates (Rhodes, *pers. comm*). Below, these are represented by grains shown in red that are self-consistent at the minimum value on each plot, with the red dashed line showing the combined age estimate.

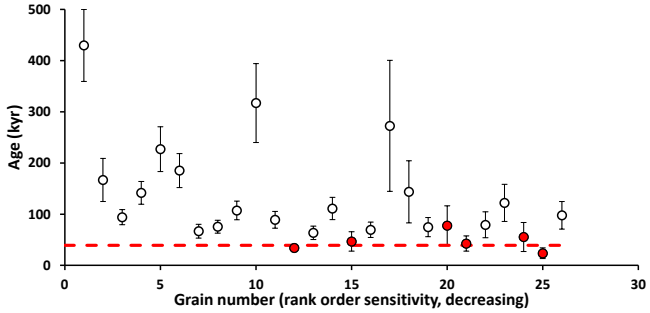
19044 KGZ18-03 depth 180 cm **38,100 ± 3,000 years Measure again?**



Pit on Terrace 3. Pit probably goes into top of Neogene deposits underlying terrace deposits.

Neogene gravels?

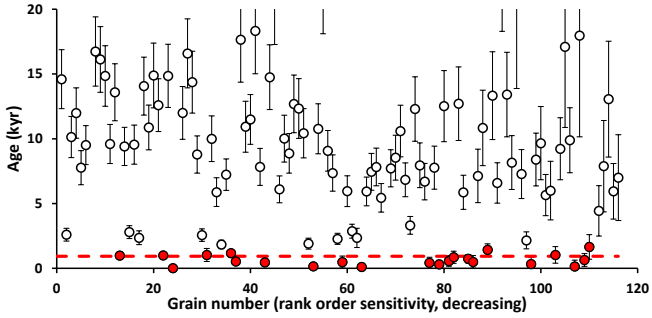
19045 KGZ18-04 depth 85cm **39,200 ± 6,100 years Measure again?**



Pit on Terrace 3. Pit probably goes into top of Neogene deposits underlying terrace deposits.

Neogene mud?

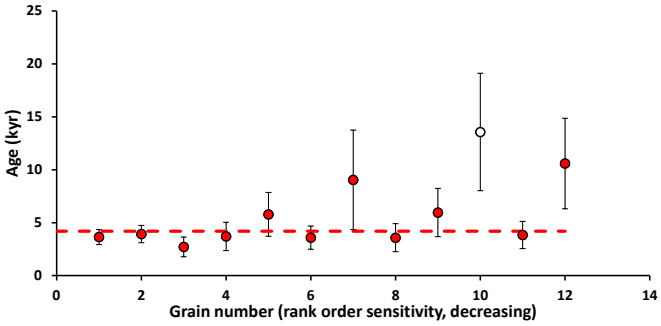
19046 KGZ18-05 depth 45cm **930 ± 100 years**



Pit on Terrace 3. Pit probably goes into top of Neogene deposits underlying terrace deposits.

Bottom of loess layer

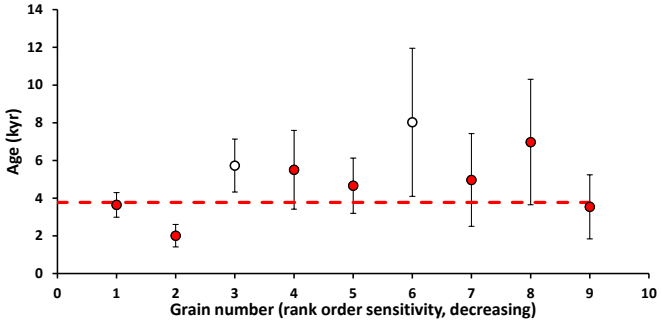
19047 KGZ18-06 depth 105cm **4,200 ± 470 years**



To the south of the Naryn River, although terraces appear to be those of a smaller stream that is now dried up. Nevertheless, the upthrown side is closer to the erosional side of Naryn River river, so very likely uplifted. Scarp is associated with the Central Naryn Fault.

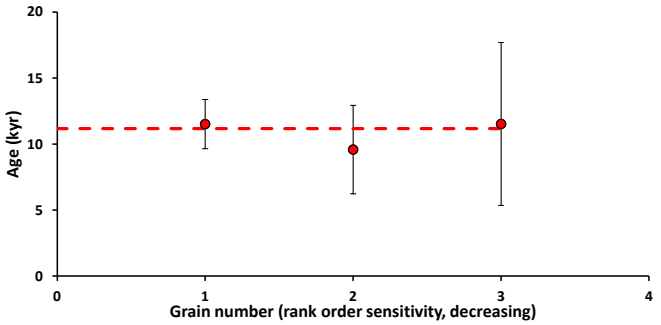
Loess layer overthrust by gravel.

19048 KGZ18-07 depth 60cm **3,780 ± 510 years Remeasure?**



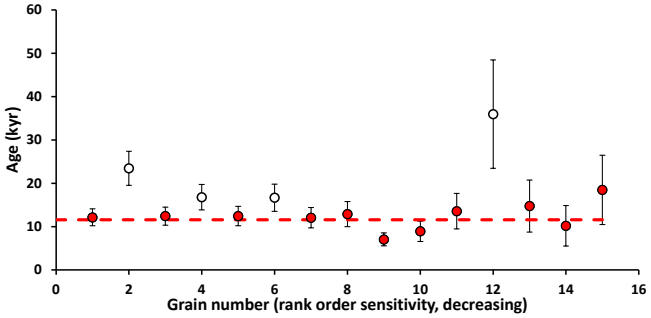
To the south of the Naryn River, although terraces appear to be those of a smaller stream that is now dried up. Nevertheless, the upthrown side is closer to the erosional side of Naryn River river, so very likely uplifted. Scarp is associated with the Central Naryn Fault. Possible colluvial wedge on the downthrown side.

19049 KGZ18-08 depth 60cm **11,200 ± 1,800 years Remeasure?**



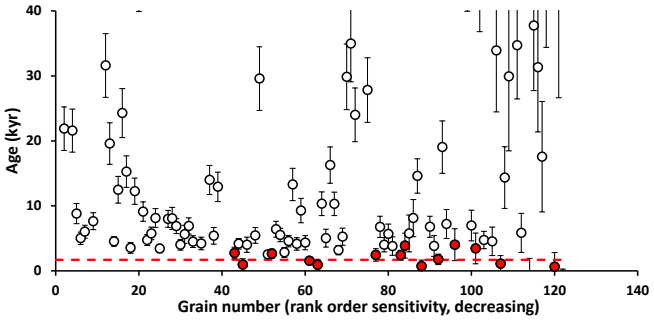
To the south of the Naryn River, although terraces appear to be those of a smaller stream that is now dried up. Nevertheless, the upthrown side is closer to the erosional side of Naryn River river, so very likely uplifted. Scarp is associated with the Central Naryn Fault. Loess layer in gravel, i.e., it does not postdate gravel deposition. Upthrown side.

19050 KGZ18-09 depth 55cm **11,600 ± 1,100 years**



To the south of the Naryn River, although terraces appear to be those of a smaller stream that is now dried up. Nevertheless, the upthrown side is closer to the erosional side of Naryn River river, so very likely uplifted. Scarp is associated with the Central Naryn Fault. Base of loess layer covering the upthrown side.

19051 KGZ18-10 depth 40cm **420 ± 70 years**



This low terrace is displaced by faulting (~50 cm scarp), but even lower terrace is not-- therefore our age will give a limit on abandonment of surface, and will predate the last slip. AKA Quarry Scarp, South of Naryn River.

Base of silt layer overlying gravels.

Appendix C

Best-fit focal mechanism solutions of the October–December 2019 earthquake sequence

The following figures show the minimum misfit solution of the focal mechanisms of each event in the earthquake sequence in Mindanao, as discussed in Chapter 3, Section 3.3 (Bodywave seismology). The summary of the source parameters are listed in Table 3.1.

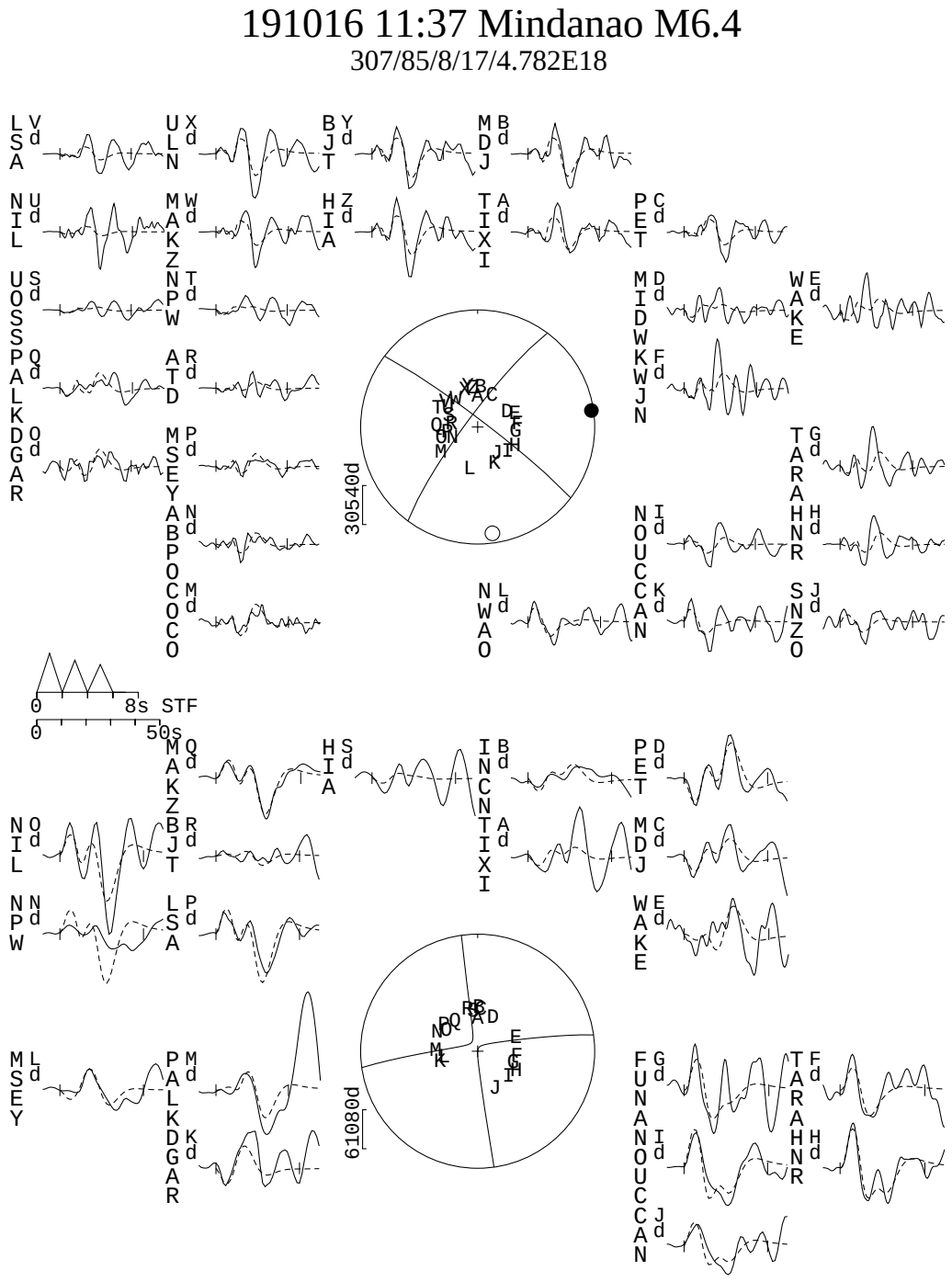


Figure C.1: Minimum misfit solution for the 2019/10/16 southern Mindanao earthquake determined from inversion of *P* and *SH* body-waveforms. The top hemisphere represents the P-wave radiation and the bottom hemisphere represents the *SH* waveforms. Station positions on the focal spheres are identified by capital letters and arranged clockwise from north. Waveforms for each station (identified by a three- or four-letter code, and a capital letter corresponding to those within the focal spheres) are positioned azimuthally around the focal hemispheres. Observed waveforms are shown as solid lines and synthetic waveforms as dashed lines. Numbers beneath the header line are strike, dip, rake, centroid depth (in kilometers) and moment (in Nm). The source-time function and waveform timescale are plotted between the two focal spheres. The P and T axes within the P waveform focal sphere are shown by a solid and an open circle respectively.

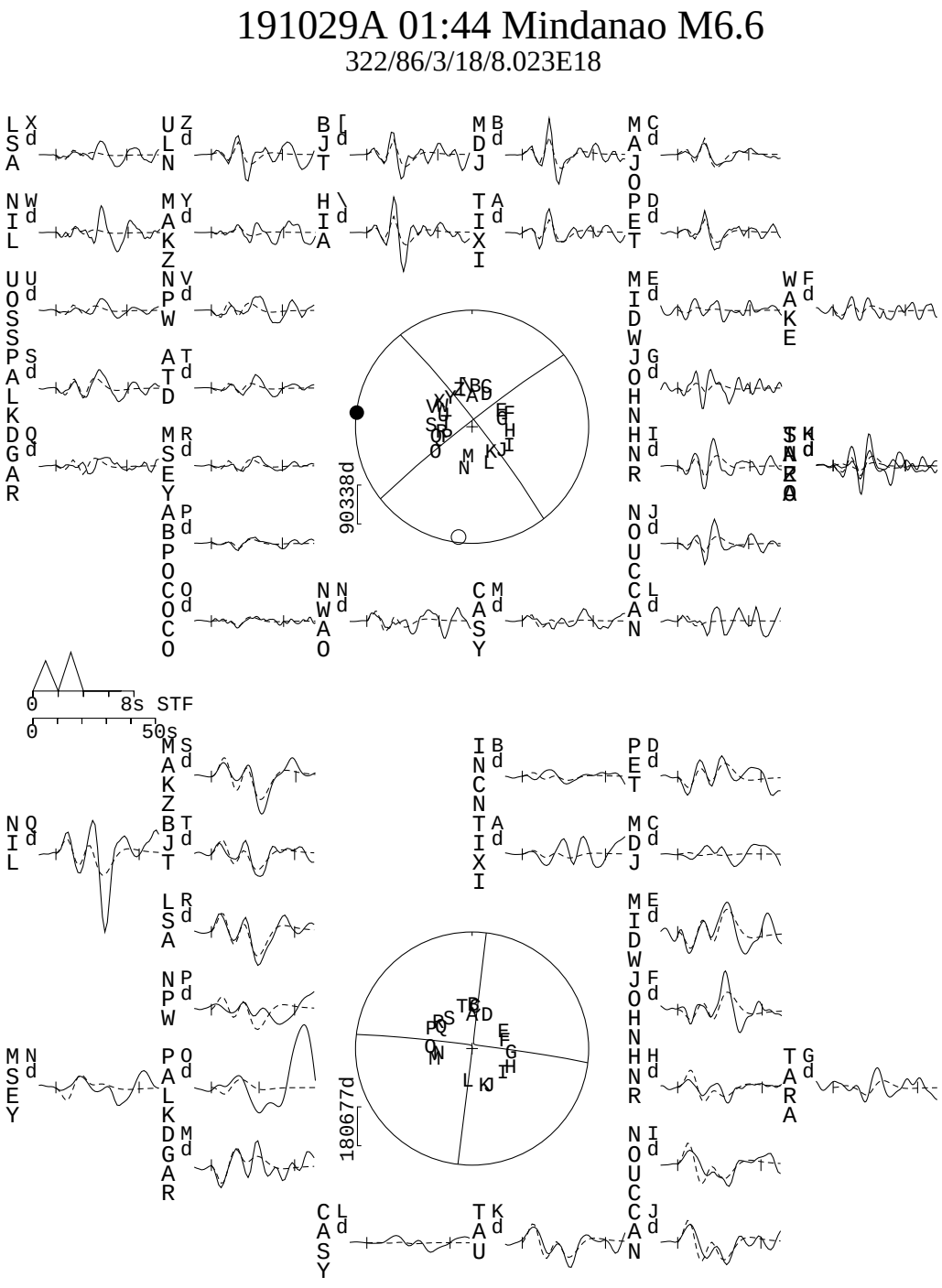


Figure C.2: Same as Figure C.1, but for the 2019/10/29 event.

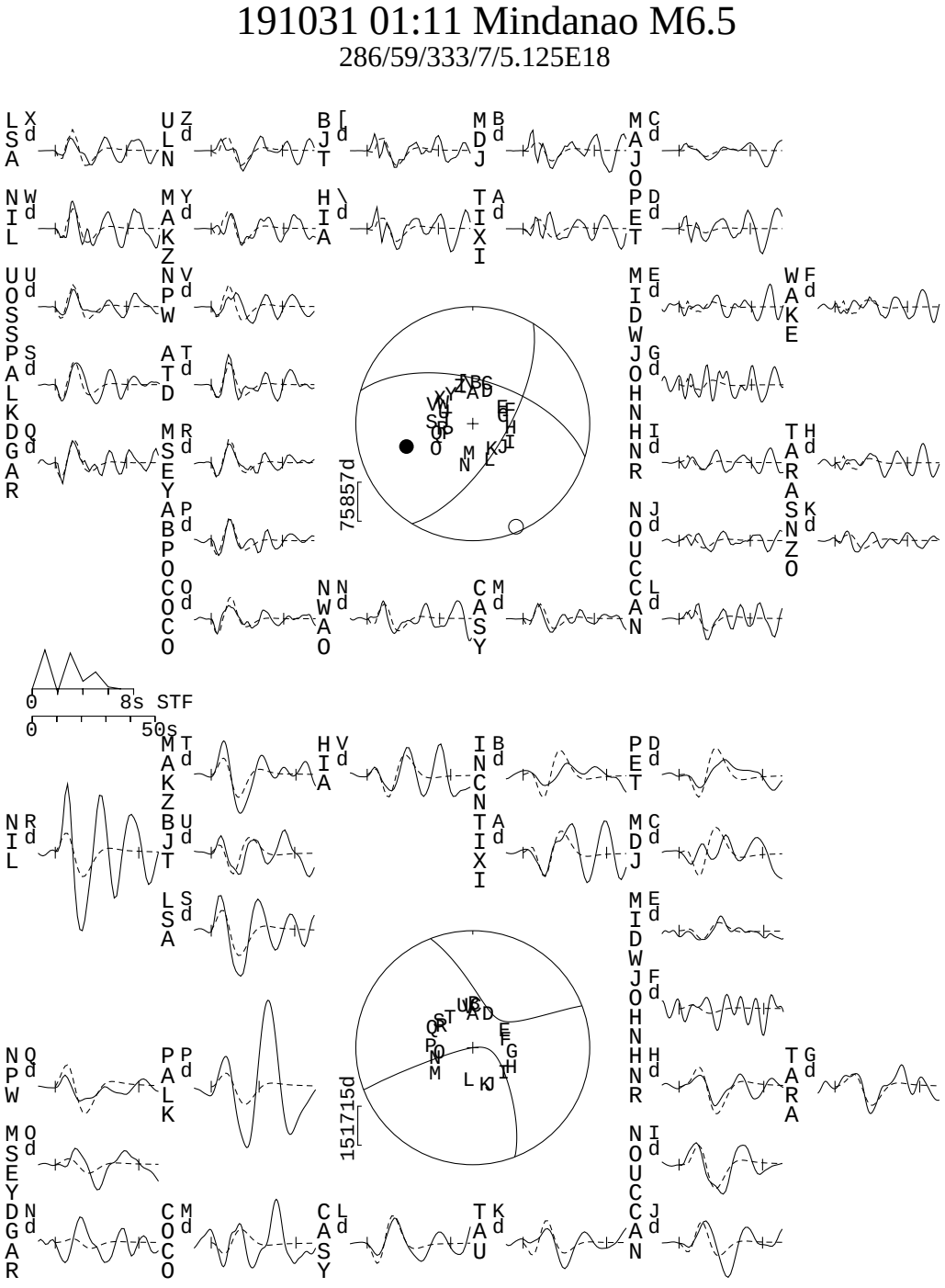


Figure C.3: Same as Figure C.1, but for the 2019/10/31 event.

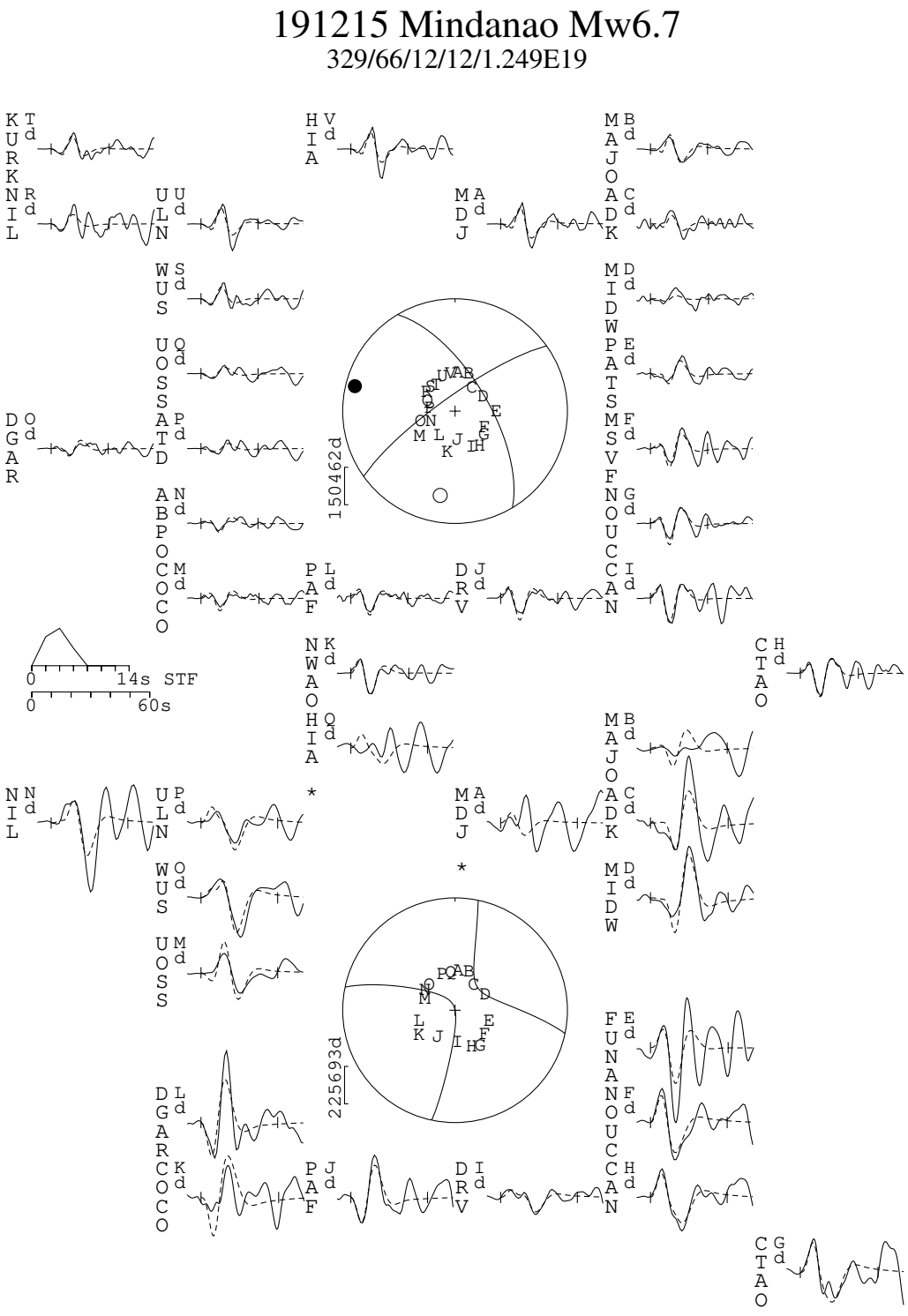


Figure C.4: Same as Figure C.1, but for the 2019/12/15 event.

Appendix D

Sentinel-1 ascending track interferograms of the 2019 southern Mindanao earthquake sequence

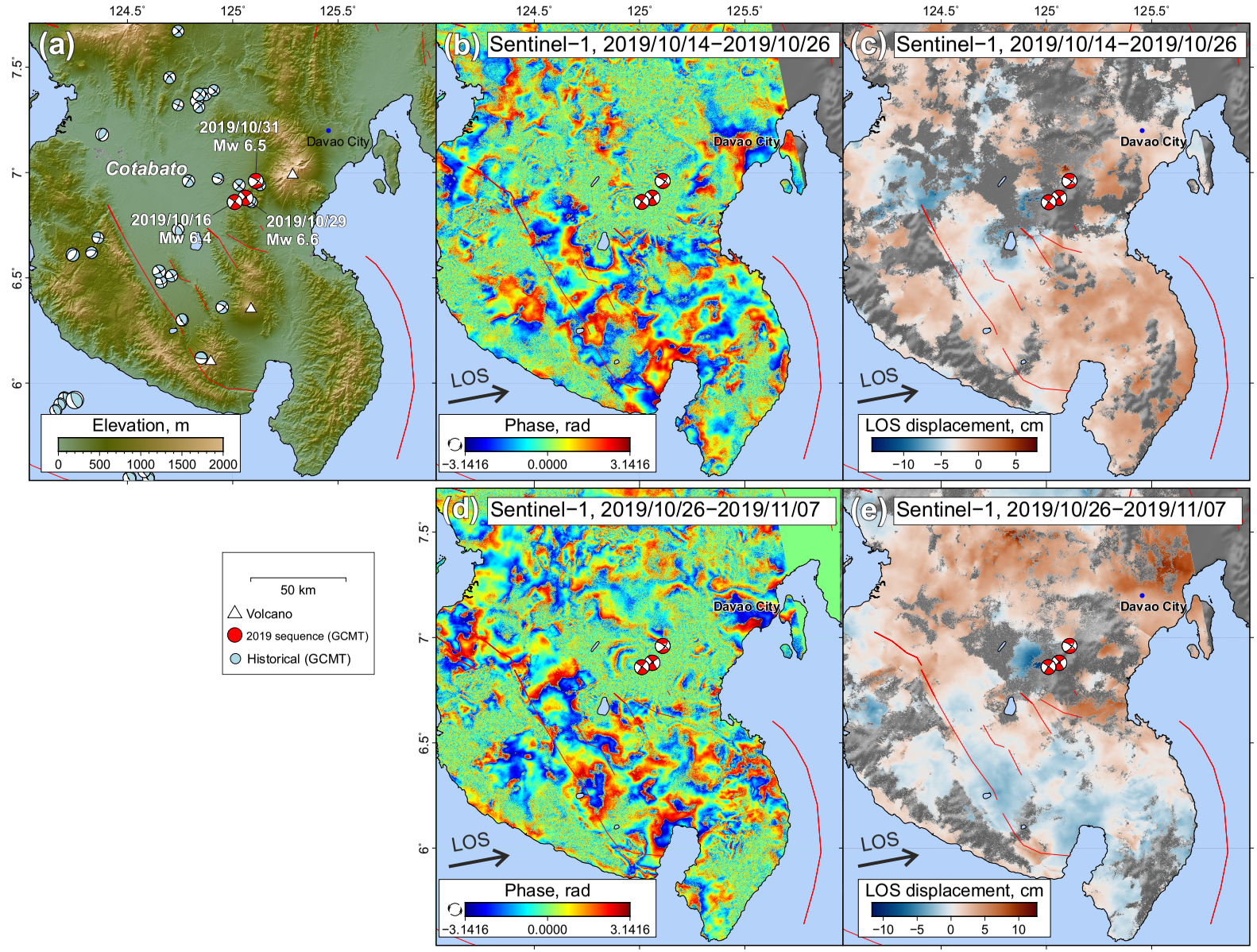


Figure D.1: Sentinel-1 ascending track interferograms covering the October 2019 southern Mindanao earthquakes. a) Shaded elevation map of southern Mindanao with Global CMT focal mechanisms of historical (light blue) and October 2019 earthquake sequence. b, c) Wrapped and unwrapped interferograms spanning the 10/16 event. d, e) Same, but covering the 10/29 and 10/31 events. Positive line-of-sight displacement indicates movement towards the satellite.

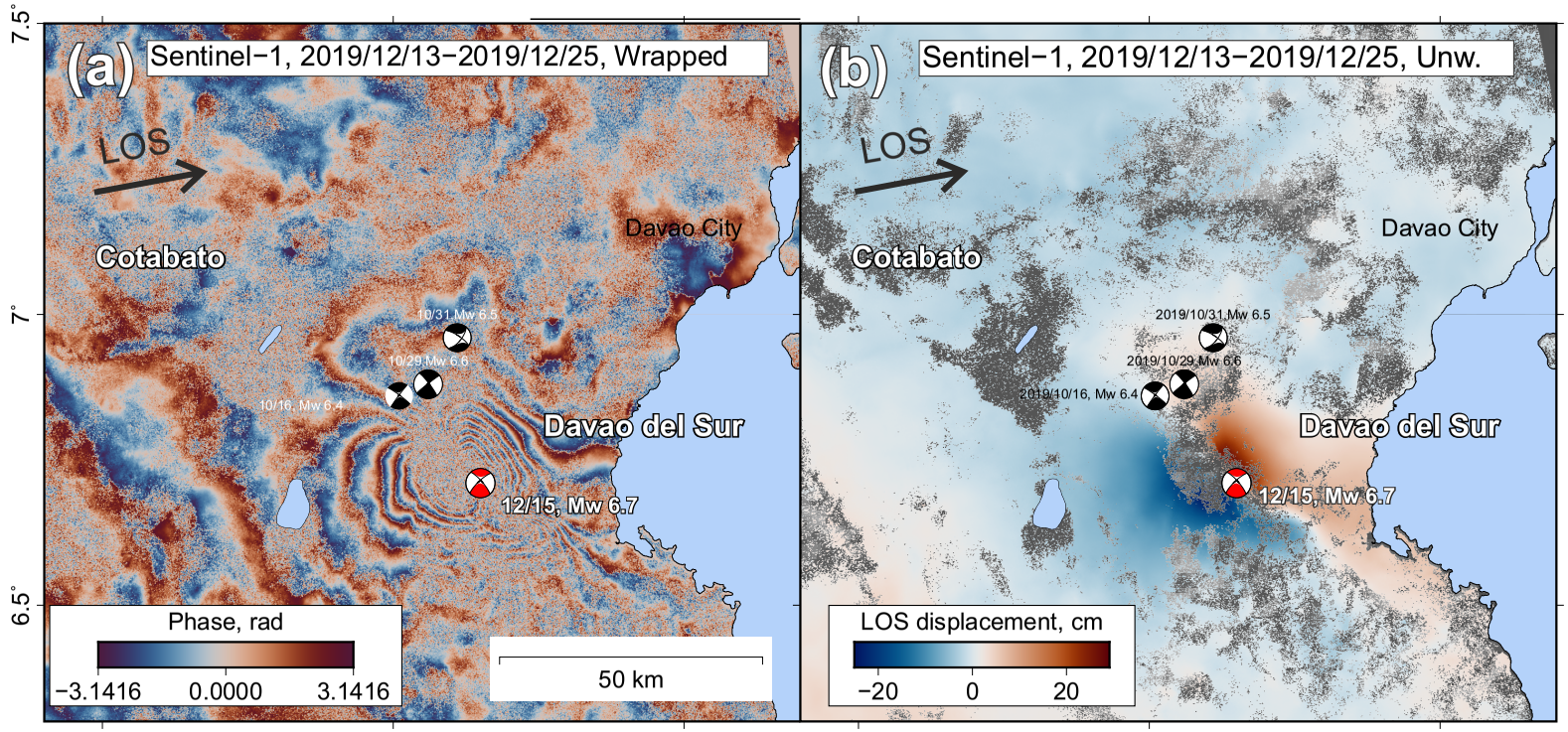


Figure D.2: Sentinel-1 ascending track wrapped (a) and unwrapped (b) interferograms of the 2019/12/15 southern Mindanao earthquake. Positive line-of-sight displacement indicates movement towards the satellite.

Appendix E

Details of the inversion for the 2019 Mindanao fault geometry parameters

The following supplementary material shows the details of the *Grond* bootstrapping results from the inversion for best-fitting fault geometry of the 2019 Mindanao earthquake sequence.

Section E.1 shows the layered velocity structure, based on average CRUST2.0 values, for the inversion (see main text for discussion; Section 3.5).

Section E.2 includes the summary of the posterior distribution of the 10/16 model (Tables E.2), joint parameter distributions showing the correlation between parameters (Figure E.1 to E.3), and sequence plots showing the misfit throughout different iterations of the bootstrapping (Figure E.4).

As discussed in the main text, while the NW-striking solution for the 10/16 event is the best-fitting model, the bootstrapping initially tested NE-striking fault parameters in the earlier iterations (iterations 20,000 to 55,000 in 'Strike' sequence plot in Figure E.4). This was eventually abandoned by the algorithm due to the

lower misfit of a fault model that strikes along the NW-SE (redder points of parallel iterations in the aforementioned plot). Section E.3 shows the posterior distribution for a test that forces the inversion to find the best-fitting NE-striking fault.

For the 12/15 model, Section E.4 displays the posterior distribution (Table E.4), joint parameter distirbution (Figure E.7 to E.9), and sequence plots (Figure E.10).

E.1 Velocity structure of the Green's function

Table E.1: Layered velocity structure of Green's function from Pyrocko, used in the inversion for the fault models of the 2019 southern Mindanao earthquake sequence. Vp: P-wave veolcity, Vs: S-wave velocity, rho: density, Qp and Qs: P- and S-wave attenuation parameters (lower values indicate more attenuation).

[Depth, km]	[Vp, km/s]	[Vs, km/s]	[rho, g/cm3]	[Qp]	[Qs]
0.	2.5	1.2	2.1	50.	50.
0.5	2.5	1.2	2.1	50.	50.
0.5	6.1	3.5	2.75	600.	400.
19.5	6.1	3.5	2.75	600.	400.
19.5	6.6	3.8	2.9	1357.	600.
31.5	6.6	3.8	2.9	1357.	600.
31.5	7.2	4.	3.1	1458.	600.
39.	7.2	4.	3.1	1458.	600.
mantle					
39.	7.9	4.5	3.3	1387.	600.
89.	7.9	4.5	3.3	1387.	600.

E.2 Results of modeling for the 2019/10/16 southern Mindanao earthquake

Table E.2: Best, mean, standard deviation (SD) and percentile bounds of parameters from the fault geometry inversion for the 10/16 earthquake. East and north shift refer to the offset from the epicentral location (125.01°E, 6.86 °N).

Parameter	Best	Mean	SD	5%	16%	84%	95%
East shift, m	6,050	5,740	680	4,660	5,040	6,450	6,840
North shift, m	-5,180	-5,700	510	-6,490	-6,210	-5,190	-4,880
Depth, m	8,750	8,490	900	6,790	7,540	9,390	9,730
Length, m	19,320	19,330	600	18,180	18,810	19,840	19,950
Width, m	7,200	8,600	3,200	4,700	5,400	12,100	14,700
Slip, m	1.13	1.06	0.32	0.61	0.73	1.39	1.61
Strike, °	307	309.9	1.4	307.7	308.5	311.4	312.3
Dip, °	72	80.1	2.8	75.5	77.4	83.1	84.9
Rake, °	6.1	2	1.3	0.2	0.7	3.3	4.4

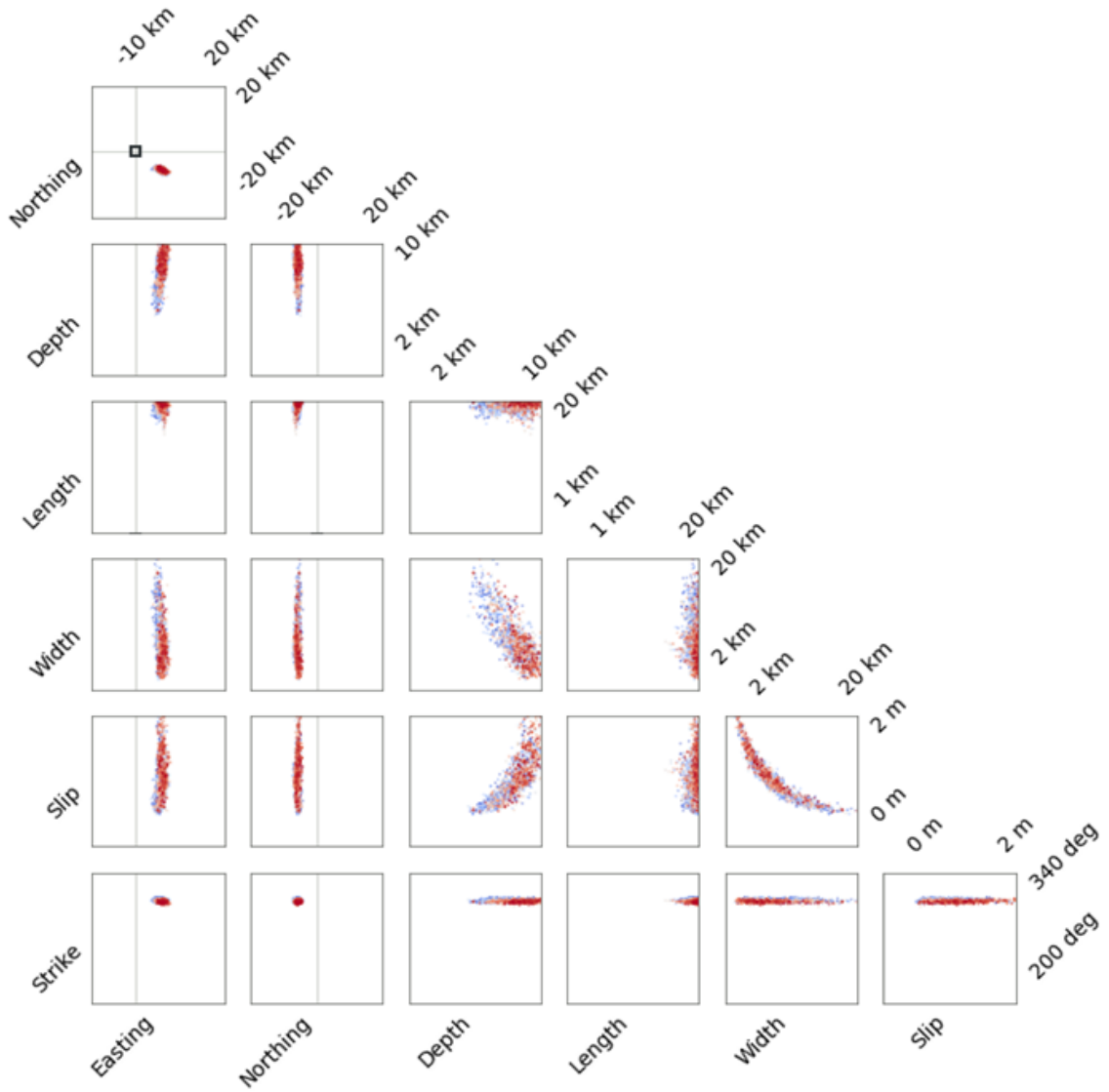


Figure E.1: Joint distributions of 10/16 fault geometry parameters, mainly Northing, Easting, Depth, Length, Width, Slip, Strike, Rake, and a constant offset in the Sentinel-1 and ALOS-2 LOS displacement maps. Darker red indicates lower misfit while darker blue means higher misfit.

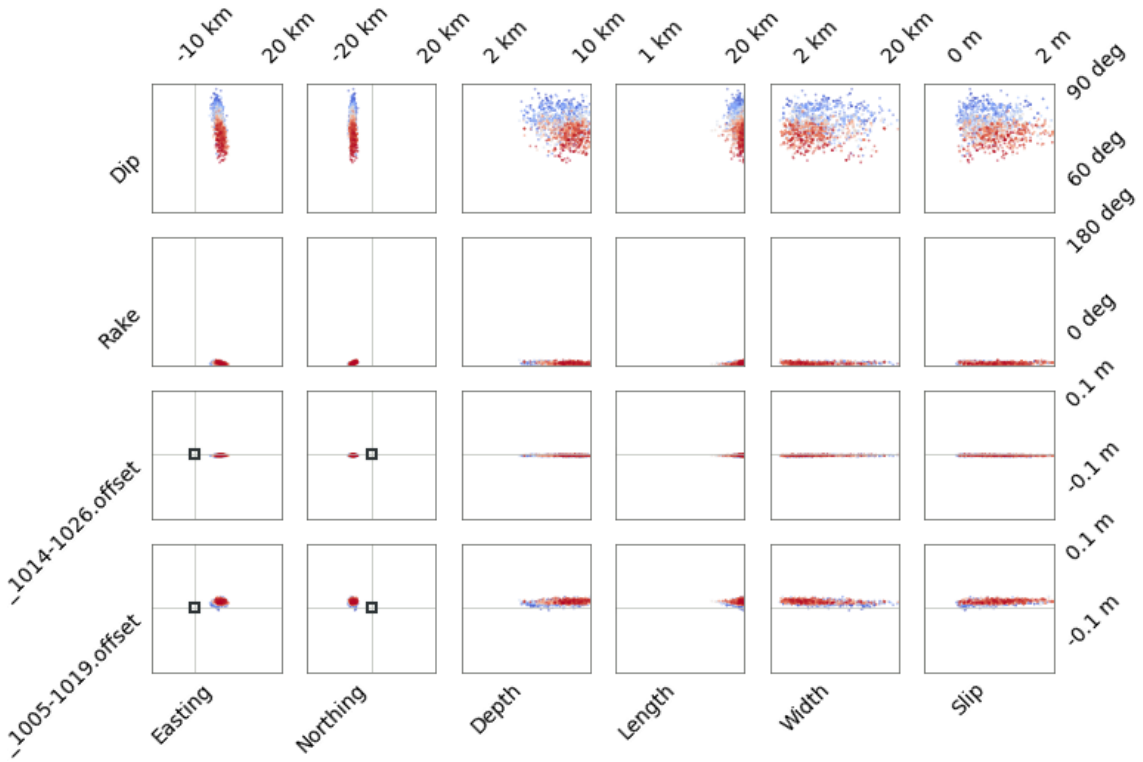


Figure E.2: Continued from E.1.

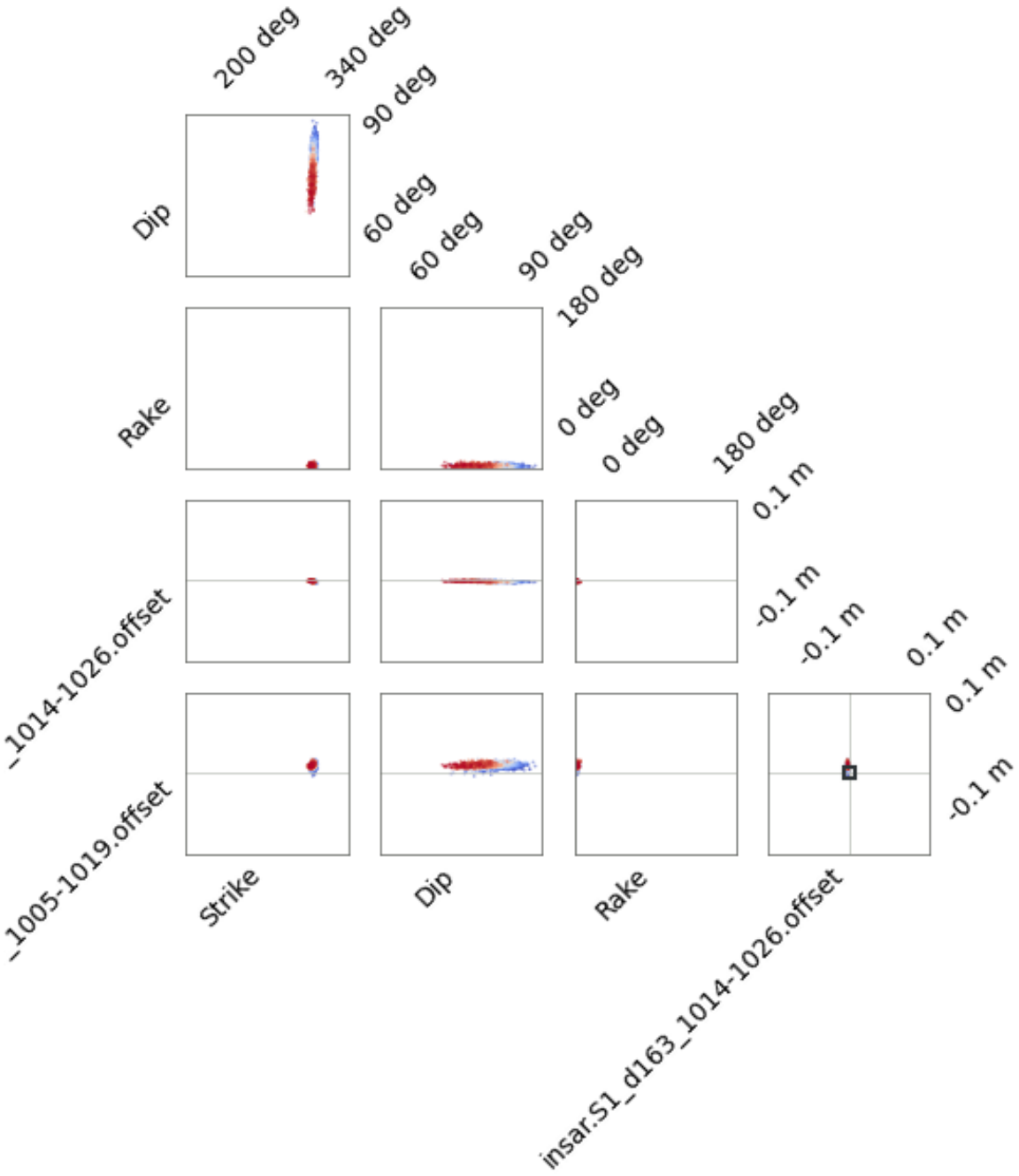


Figure E.3: Continued from E.2.

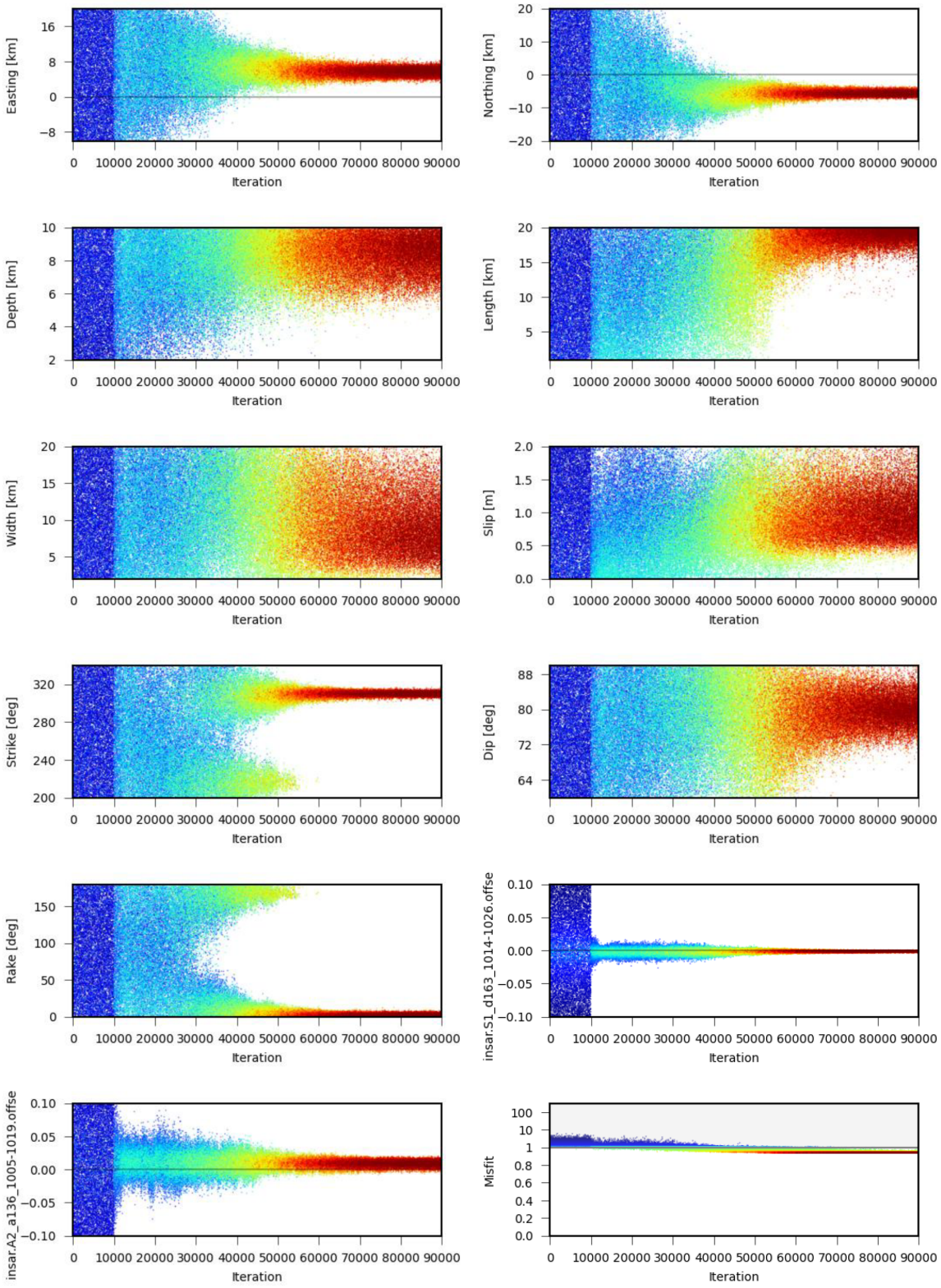


Figure E.4: Sequence plots of the Grond parameter sampling for the 10/16 event, showing the relative misfit at every iteration of each parameter. Warmer colors indicate relatively low misfit while cooler points are iterations with low misfit. The first 10,000 iterations are part of the uniform sampler phase, where models are drawn randomly to define the parameter space for the directed sampling phase (the next 80,000 iterations), based on a 'high-score list' of low misfit models. Note the bimodal sampling of the algorithm for strikes and rakes of a NW- and NE-trending faults between iterations 25,000 to 55,000, but the lower misfit of the NW striking models at around iteration 45,000.

E.3 Forced NE-striking fault model for the 2019/10/16 southern Mindanao earthquake

This section contains the details of optimization for the best-fitting NE-striking fault model for the 10/16. Parameter bounds are summarized in Table 3.3, with the primary difference from the main inversion the strike bounds at [180°, 270°].

Table E.3: Best, mean, standard deviation (SD) and percentile bounds of parameters from the fault geometry inversion for the 10/16 earthquake forced to a NE-SW strike. East and north shift refer to the offset from the epicentral location (125.01°E, 6.86 °N).

Parameter	Best	Mean	SD	5%	16%	84%	95%
East shift, m	6,370	6,840	530	5,840	6,220	7,390	7,600
North shift, m	-6,410	-6,710	390	-7,270	-7,070	-6,330	-6,060
Depth, m	9,900	7,100	1,200	5,400	5,800	8,300	9,100
Length, m	8,100	11,900	2,900	6,500	8,700	14,600	15,900
Width, m	16,600	17,700	1,800	14,300	15,900	19,400	19,900
Slip, m	1.48	0.84	0.33	0.52	0.57	1.12	1.56
Strike, °	217.4	218.4	2	215.3	216.3	220.4	221.8
Dip, °	89.8	89.71	0.29	89.11	89.5	89.94	89.98
Rake, °	168.6	171.1	2.5	167.1	168.7	174	175.6

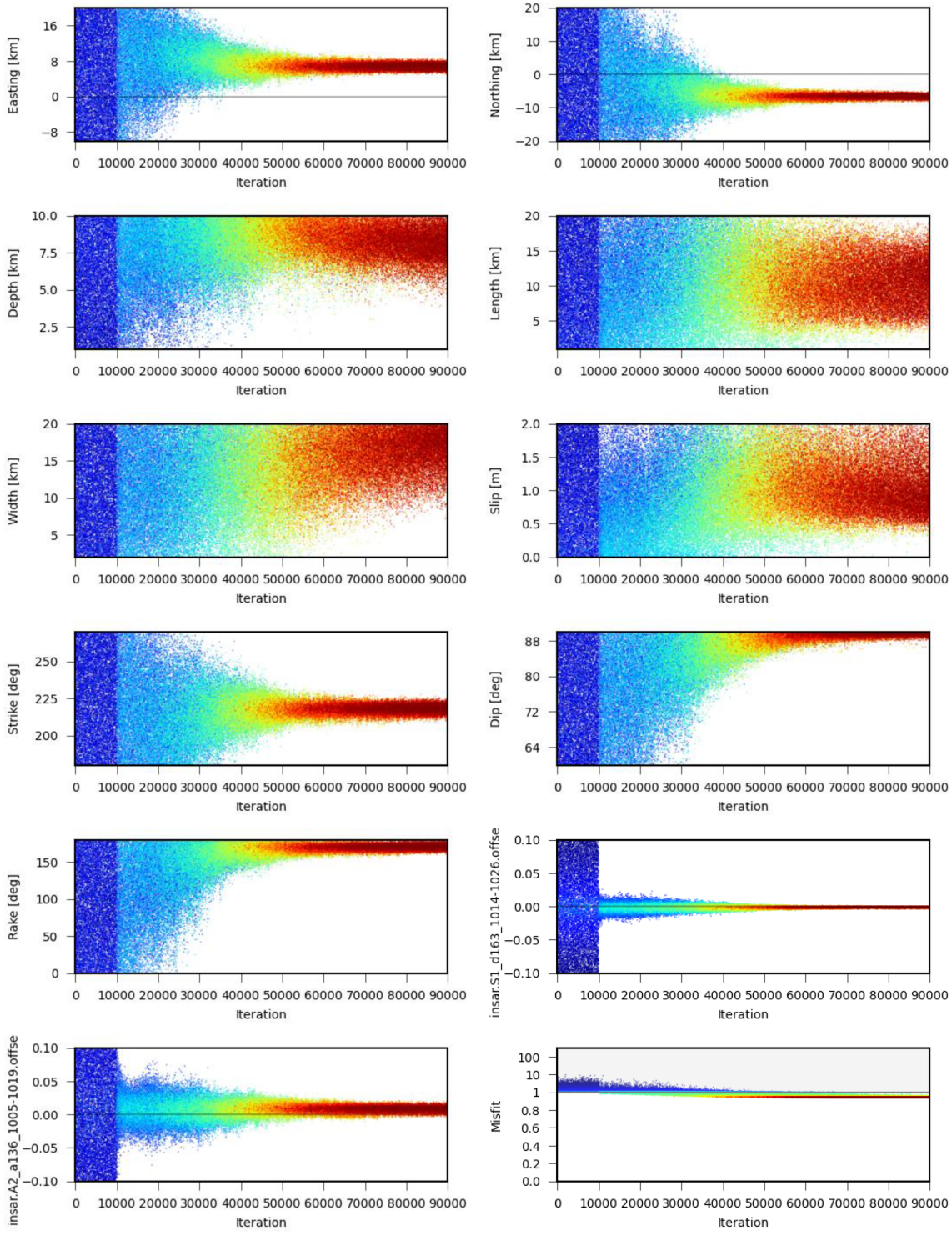


Figure E.5: Same as Figure E.4, but with the strike bounds constrained to NE-trending strikes.

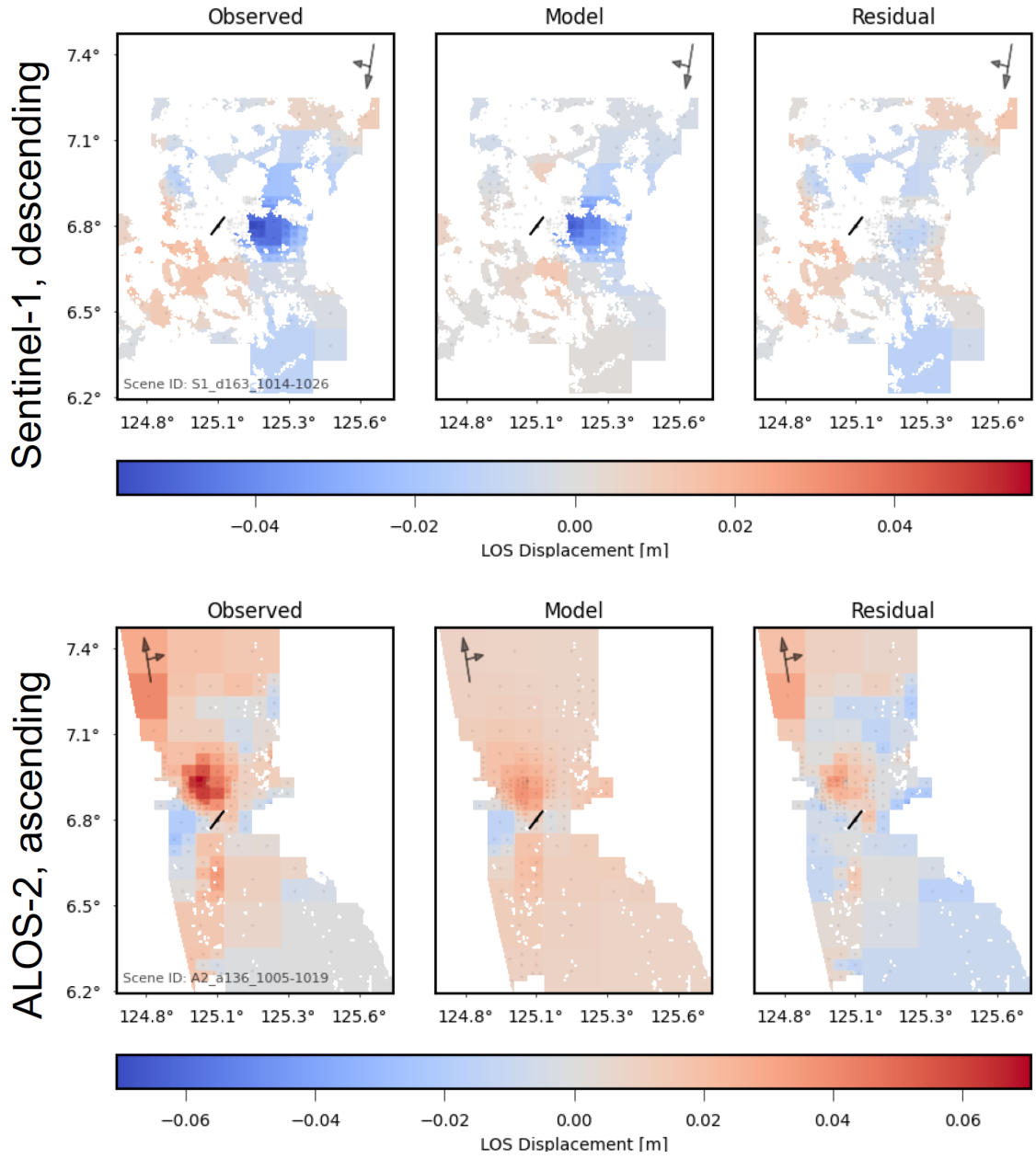


Figure E.6: Downsampled InSAR data (left), model predictions (center), and residual (right) of the best fitting forced NE-strike fault model of the 10/16 earthquake, in Sentinel-1 descending track 163 (top row) and ALOS-2 ascending track 136 (bottom row).

E.4 Results of modeling for the 2019/12/15 southern Mindanao earthquake

Table E.4: Best, mean, standard deviation (SD) and percentile bounds of parameters from the fault geometry inversion for the 12/15 earthquake. East and north shift refer to the offset from the epicentral location (125.16°E, 6.64 °N).

Parameter	Best	Mean	SD	5%	16%	84%	95%
East shift, m	1,909	1,896	76	1,760	1,812	1,975	2,005
North shift, m	5,368	5,329	98	5,197	5,236	5,440	5,542
Depth, m	2,829	2,825	45	2,745	2,777	2,872	2,888
Length, m	17,980	18,400	180	18,180	18,260	18,600	18,750
Width, m	13,590	13,870	690	12,850	13,280	14,520	15,090
Slip, m	1.88	1.829	0.039	1.779	1.79	1.872	1.899
Strike, °	316.46	316.6	0.28	316.18	316.25	316.88	316.99
Dip, °	68.6	68.43	0.57	67.3	67.88	69.05	69.2
Rake, °	9.06	8.58	0.42	7.93	8.15	8.96	9.42

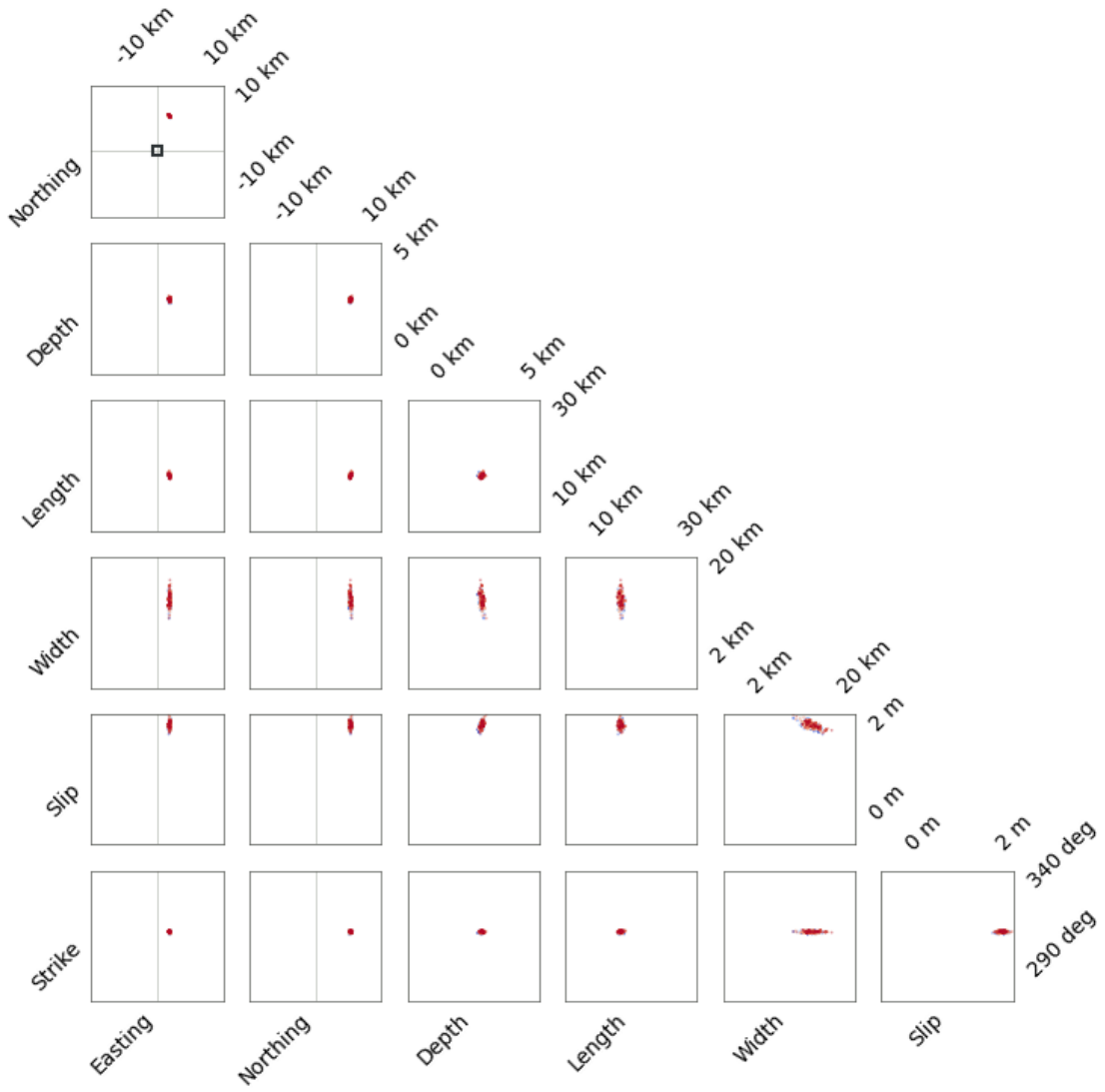


Figure E.7: Joint distributions of 12/15 fault geometry parameters, mainly Northing, Easting, Depth, Length, Width, Slip, Strike, Rake, and a constant offset in the Sentinel-1 and ALOS-2 LOS displacement maps. Darker red indicates lower misfit while darker blue means higher misfit.

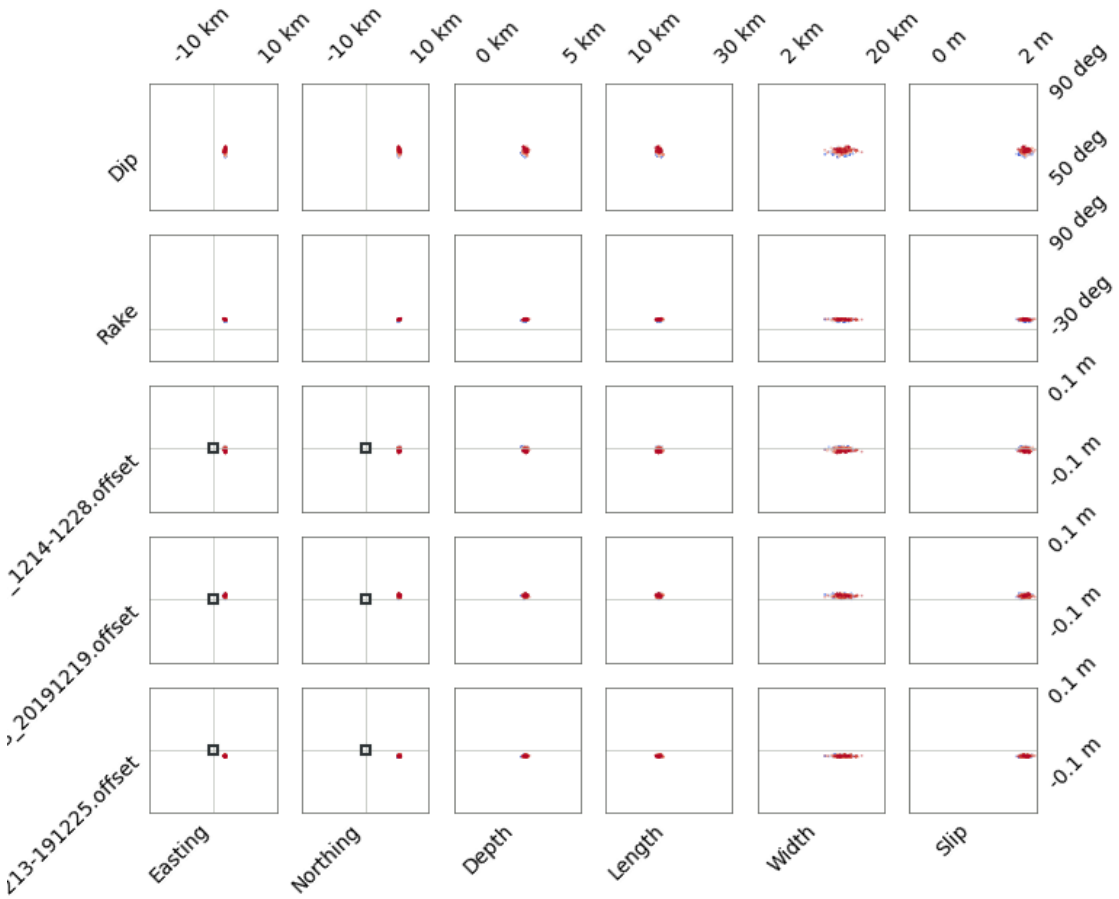


Figure E.8: Continued from E.7.

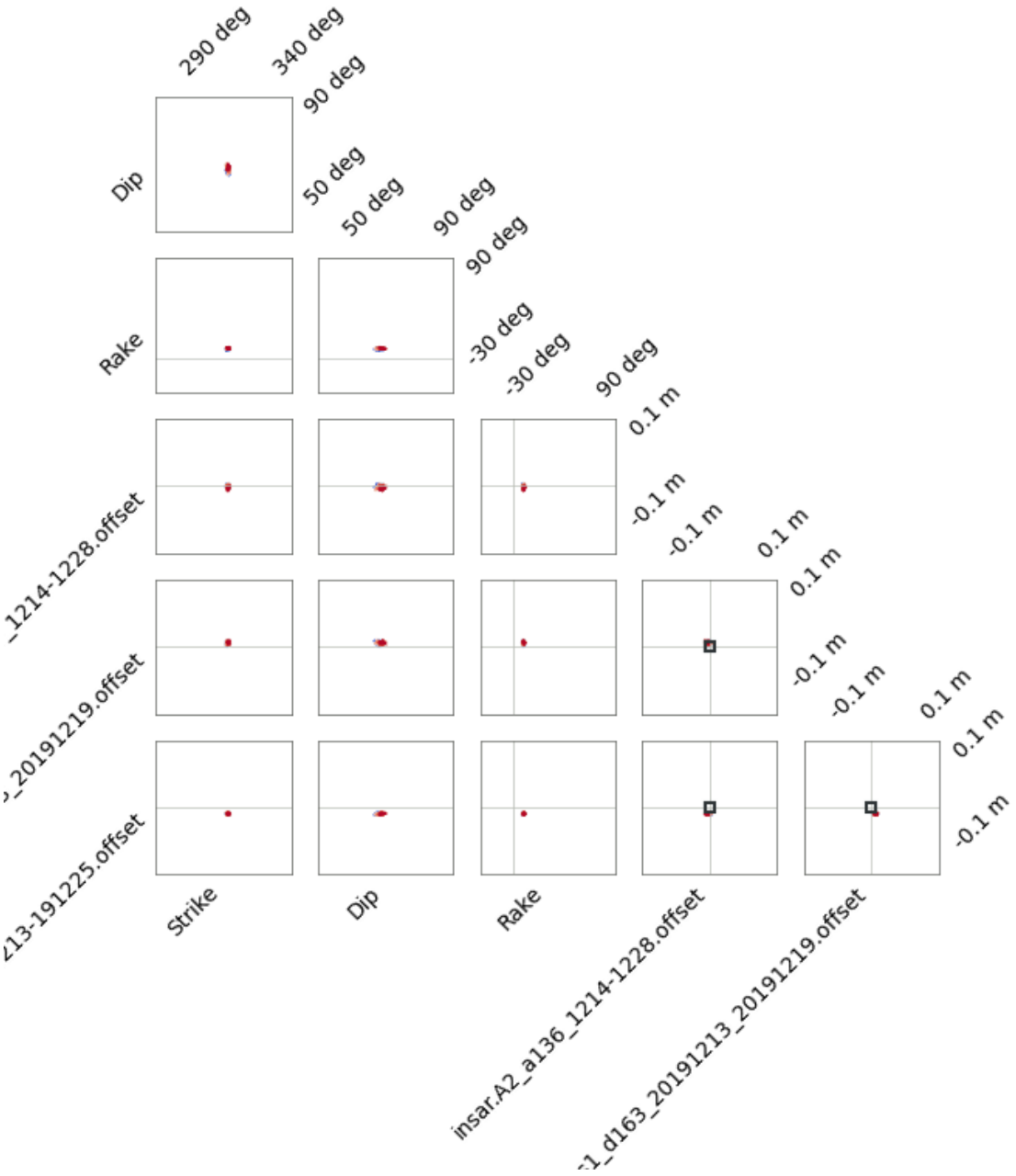


Figure E.9: Continued from E.2.

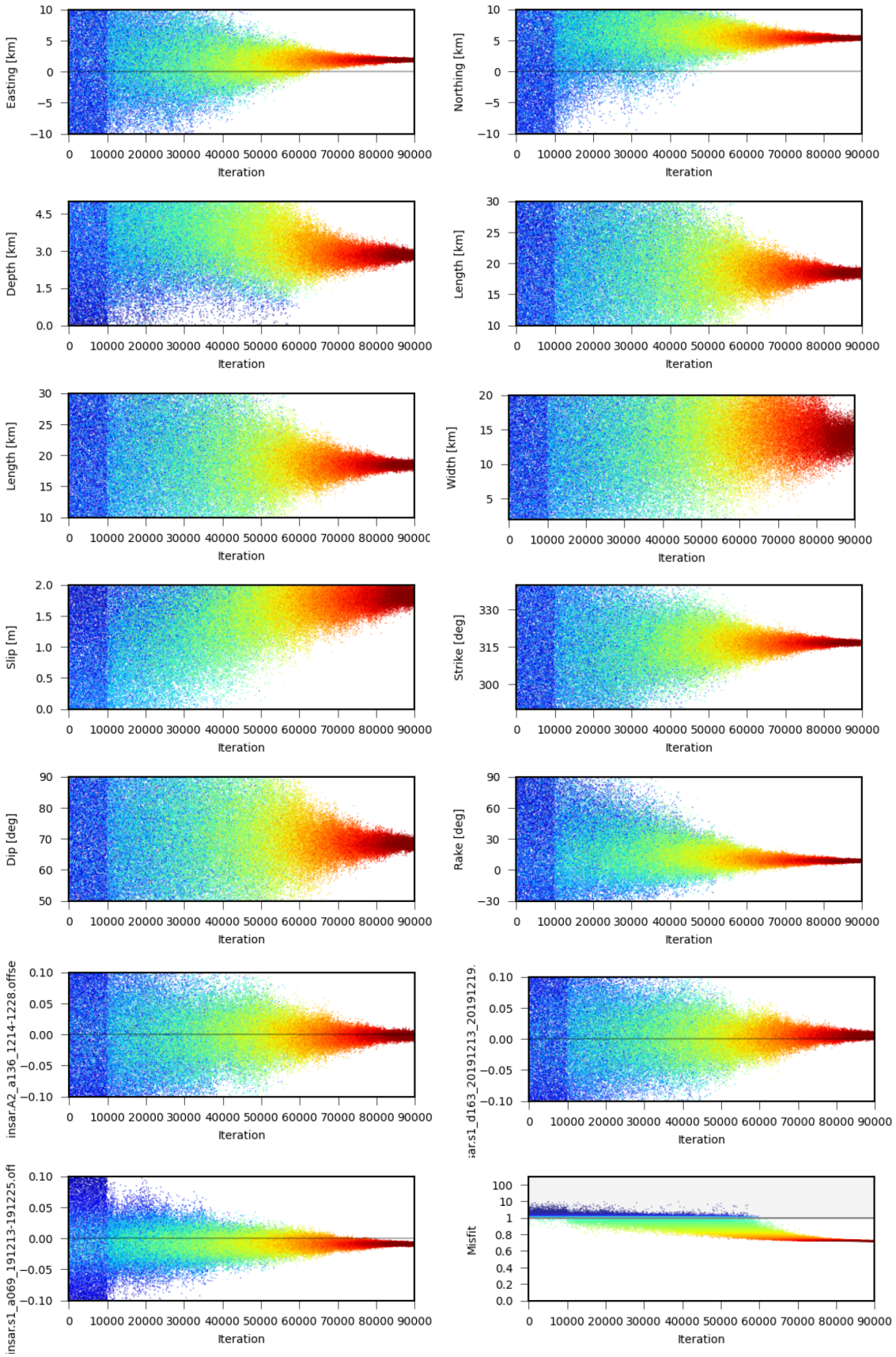


Figure E.10: Same us Figure E.4, but showing sequence plots of modeling for the 12/15 event.

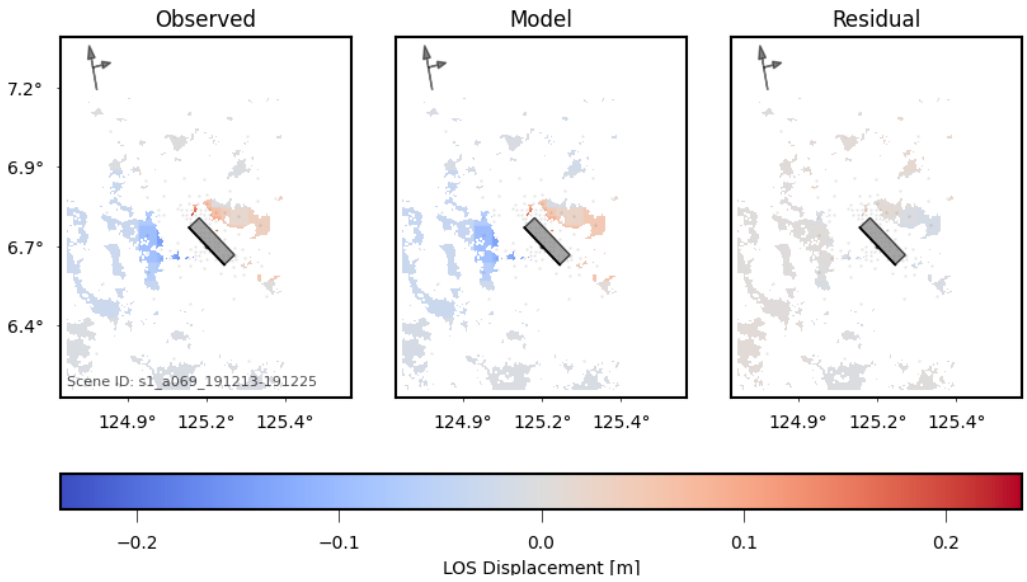


Figure E.11: Downsampled InSAR data (left), model predictions (center), and residual (right) of the best fitting fault parameters of 12/15 earthquake, in Sentinel-1 ascending track 163 line-of-sight.

Appendix F

Simulated interferograms of blind fault ruptures: possible geometry for the 2019/10/29 southern Mindanao earthquake

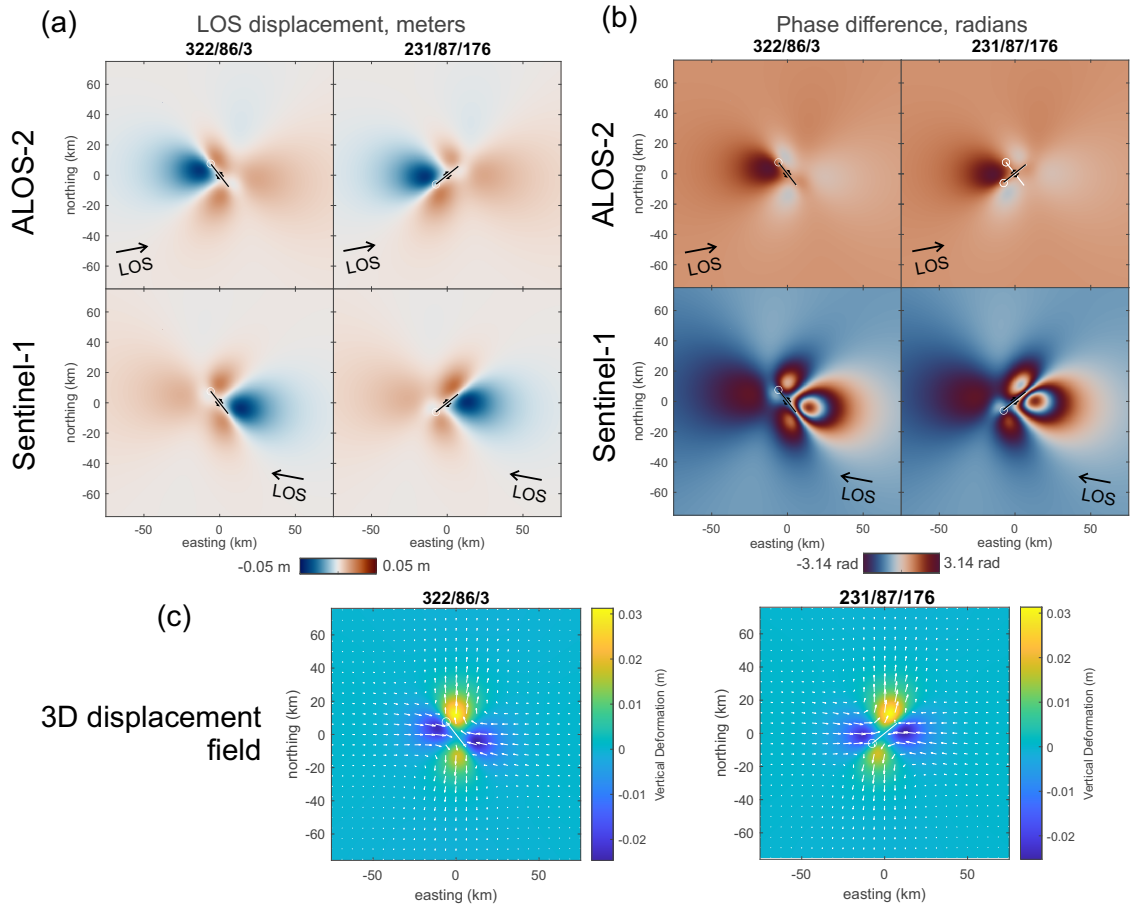


Figure F.1: Forward models of surface deformation based on uniform elastic dislocation models (*Okada*, 1985) of geometries based on the focal mechanism nodal planes of the 10/29 southern Mindanao earthquake. The strike, dip, and rake are based on the focal mechanism nodal planes of the 10/29 event, but with the dimensions of the 10/16 model. a) Displacement in the ALOS-2 (top row) and Sentinel-1 line-of-sight (bottom row). Left column is for a NW-SE left-lateral fault at the origin, and right column is for the NE-SW right-lateral nodal plane. Header of each column indicates the strike, dip, and rake. Positive values indicate movement towards the satellite. b) Same as (a), but showing the simulated differential interferograms, wrapped to $-\pi$ to π radians. Note how the patterns for the two possible geometries are very similar except for slight deviations in the elongation of the phase fringes. c) 3D deformation field, with arrows indicating horizontal displacement, and background colors show vertical displacement.

Appendix G

Drone photomosaic of fissuring associated with the 2019 southern Mindanao earthquake sequence

The following figure contains the complete photomosaic of drone imagery from field surveying of the possible surface ruptures identifiable in the ALOS-2 InSAR data.

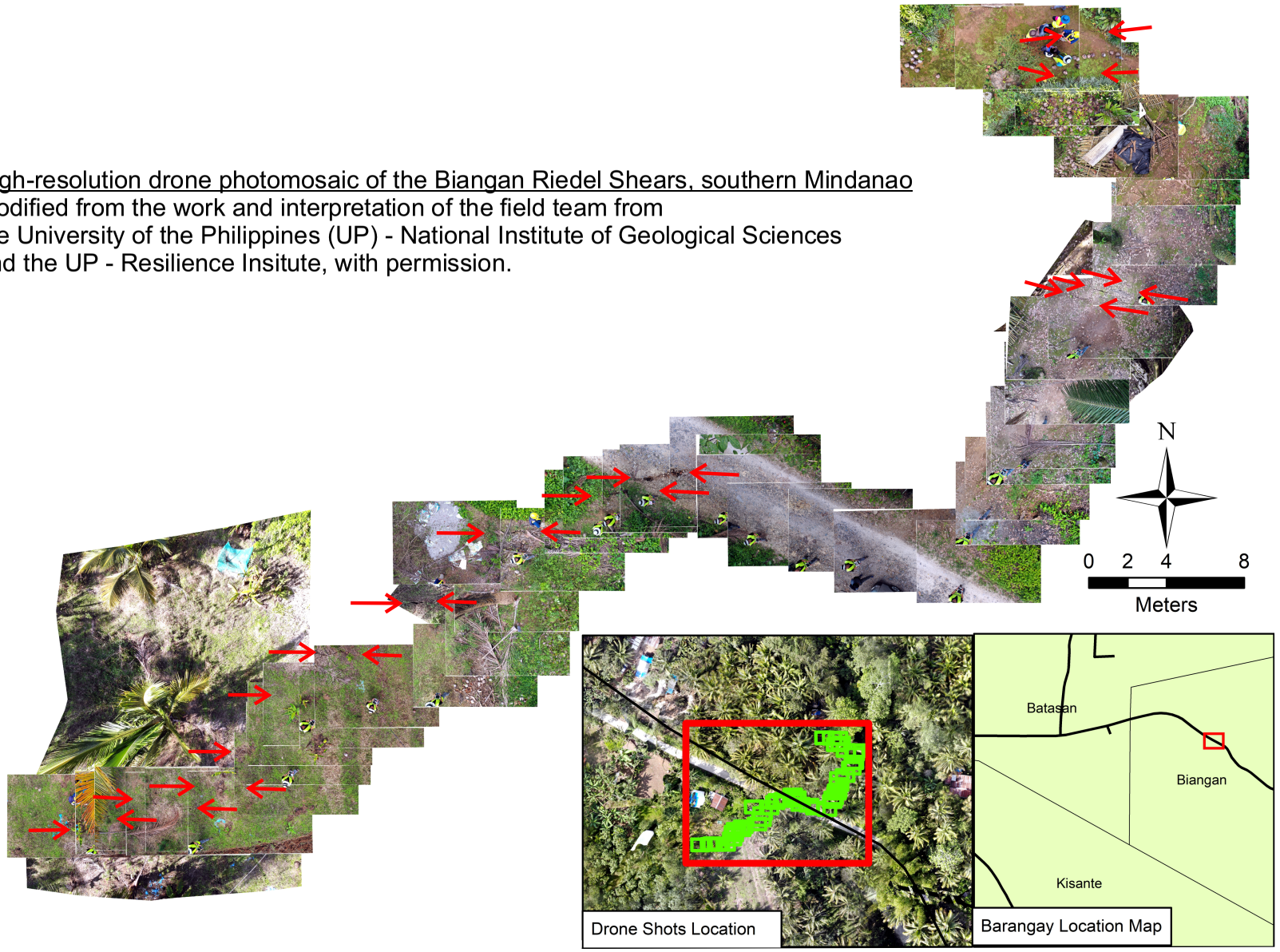


Figure G.1: Photomosaic of fissuring associated with shallow surface rupture of the 2019/10/31 Mindanao earthquake. Red arrows point to the location of fissures on the ground.

Appendix H

Estimating step-change on profiles

To estimate the magnitude of the step in the line-of-sight profiles, we fit a LOS velocity model, v, with the functional form (modified from *Larson et al.*, 2004; *Pousse Beltran et al.*, 2016):

$$v(x) = v_0 + \frac{u}{2}\left[\tanh\left(\frac{x - x_0}{d}\right) - 1\right], \tag{H.1}$$

to each profile, where x is the distance from the fault, v_0 is the far-field velocity on the profile, u is the step in velocity, x_0 is the horizontal position of the step, and d is the horizontal length scale of the step. We only estimate a step on profiles that have a distinct difference in the surface velocity across the fault.

Appendix I

Resolution analysis

The resolving power of inversions can be described by a resolution matrix, $\mathbf{R}$ (e.g., *Jackson*, 1979; *Sagiya and Thatcher*, 1999; *Funning et al.*, 2005; *Atzori and Antonioli*, 2011, amongst many others), a diagonal matrix with values between 0 and 1 (inclusive). A resolution of 1 indicates fully resolved slip, while the resolution will be 0 if slip is unresolved. In probabilistic inversions, $\mathbf{R}$ can be formulated as

$$\mathbf{R} = \mathbf{C_m}\mathbf{G}^T(\mathbf{G}\mathbf{C_m}\mathbf{G}^T + \mathbf{C_d})^{-1}\mathbf{G}, \tag{I.1}$$

where $\mathbf{C_m}$ is a diagonal matrix that contains the standard deviation of the prior PDF of each slip parameter, and $\mathbf{C_d}$ is the data covariance matrix (*Tarantola*, 2005; *Jolivet et al.*, 2012; *Gombert et al.*, 2018). The resolution matrix essentially gives us an idea of the ability of the data to constrain the slip on the individual patches (e.g., *Sagiya and Thatcher*, 1999; *Loveless and Meade*, 2011).

Appendix J

Supporting Information for "The relationship between seismic and aseismic slip on the creeping segment of the Philippine Fault"

J.1 Introduction

This document contains details of the processing and quality of the interseismic and coseismic data. We also show here additional statistical measures of the posterior distribution of the model parameters, as well as the fit of the mean model prediction with the aforementioned datasets not shown in the main text. Finally, we show the results of an inversion using a slightly more complex fault geometry to help explain the observed localized residuals in Tongonan.

J.2 Interseismic data (2007-2011) interferogram network

The following figures show the perpendicular and temporal baseline of interferogram pairs used to estimate the interseismic line-of-sight velocity from ALOS data (Section 4.3.1 of the main paper). To obtain interseismic surface velcoities, we did an N-SBAS time-series analysis of the ALOS ascending track 443 data (Figure J.1), and stacking of data from ALOS descending tracks 76 (Figure J.2) and 77 (Figure J.3).

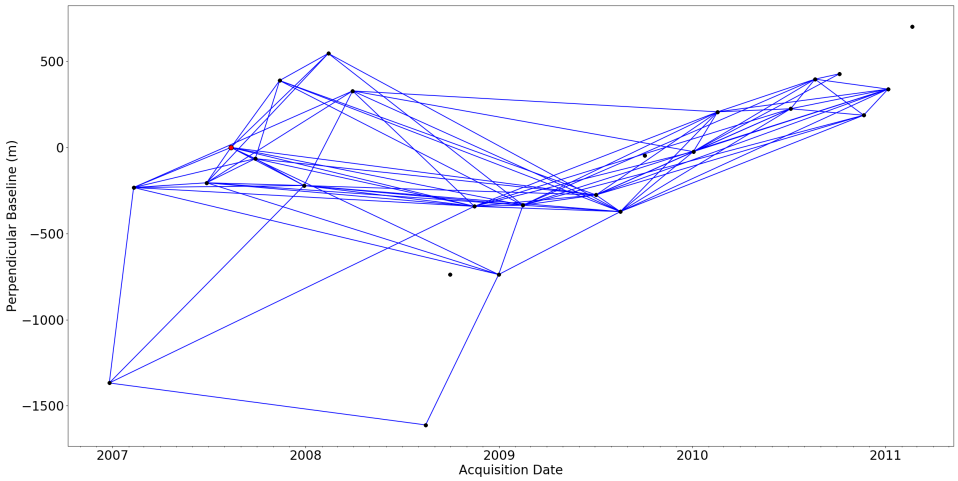


Figure J.1: ALOS ascending track acquisition perpendicular and temporal baseline. Red dot is the reference date used in coregistration, and connections between black dots indicate the interferogram pairs used in the time-series analysis. Black dots that are not on any line segment indicate acquisitions that had interferograms that were manually removed from the time-series analysis (i.e., those with non-linear ramps likely due to ionospheric perturbation).

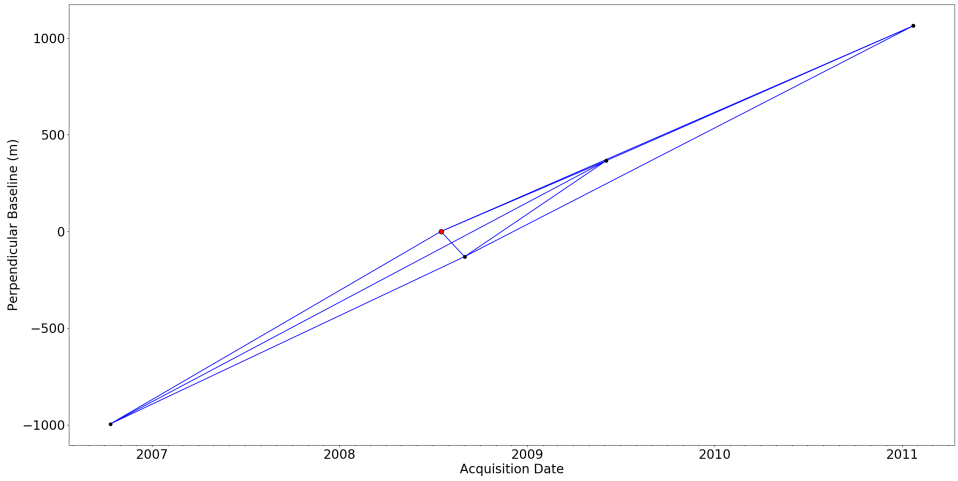


Figure J.2: Similar to J.1, but for ALOS descending track 76 acquisition perpendicular and temporal baseline.

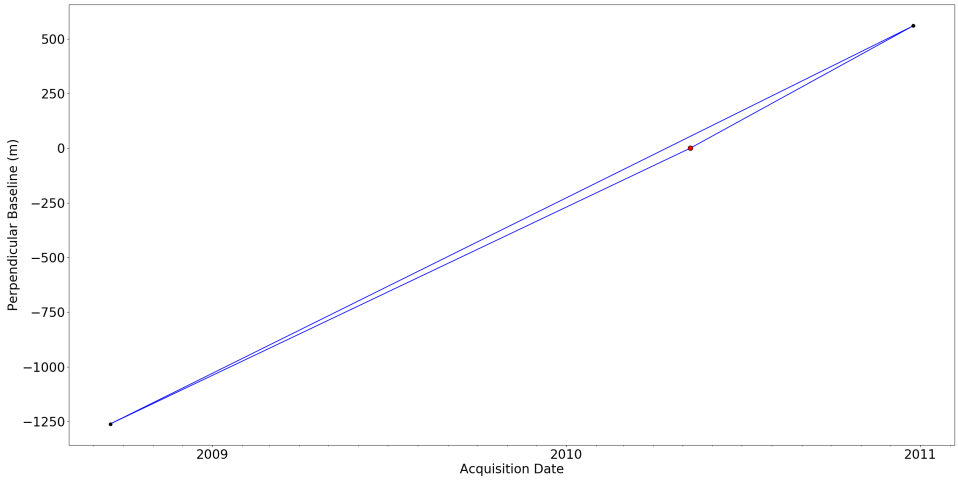


Figure J.3: Similar to J.1, but for ALOS descending track 77 acquisition perpendicular and temporal baseline.

J.3 Uncertainties in interseismic velocity estimates from N-SBAS time-series analysis and stacking

We determined the interseismic velocities between 2007-2011 from N-SBAS time-series analysis and stacking of the data (Section 4.3.1). Here we show the uncertainties of these estimates. For the ALOS ascending track 443 data, we fit a linear function to the displacement time-series of each pixel. We show the root mean square error to that linear fit (Figure J.4a).

For ALOS descending tracks 76 and 77, the stacking algorithm of GAMMA provides the standard deviation (Figure J.4b). Where Equation 1 in the main text gives the average phase displacement rate in descending line-of-sight, $\dot{\phi}_d$, the standard deviation (σ) is:

$$\sigma^2 = \sum_{j=1}^{N} \frac{\left(\phi_j - \dot{\phi}_d \Delta t_j \right)^2}{\Delta t_j^2} \tag{J.1}$$

where ϕ_j is the displacement in interferogram j, Δt_j is the temporal baseline, and $\dot{\phi}_d$ is the estimated velocity.

It will be important to note that the uncertainty in the velocity estimates between the different tracks are not directly comparable due to the different methods used to derive the deformation rate, as well as the significantly more acquisitions used for the ascending track. With more acquisitions, it may be the case that more temporal fluctuations on the surface displacement (whether real or due to noise) are captured, which effectively registers as a misfit to a linear time-series velocity fit.

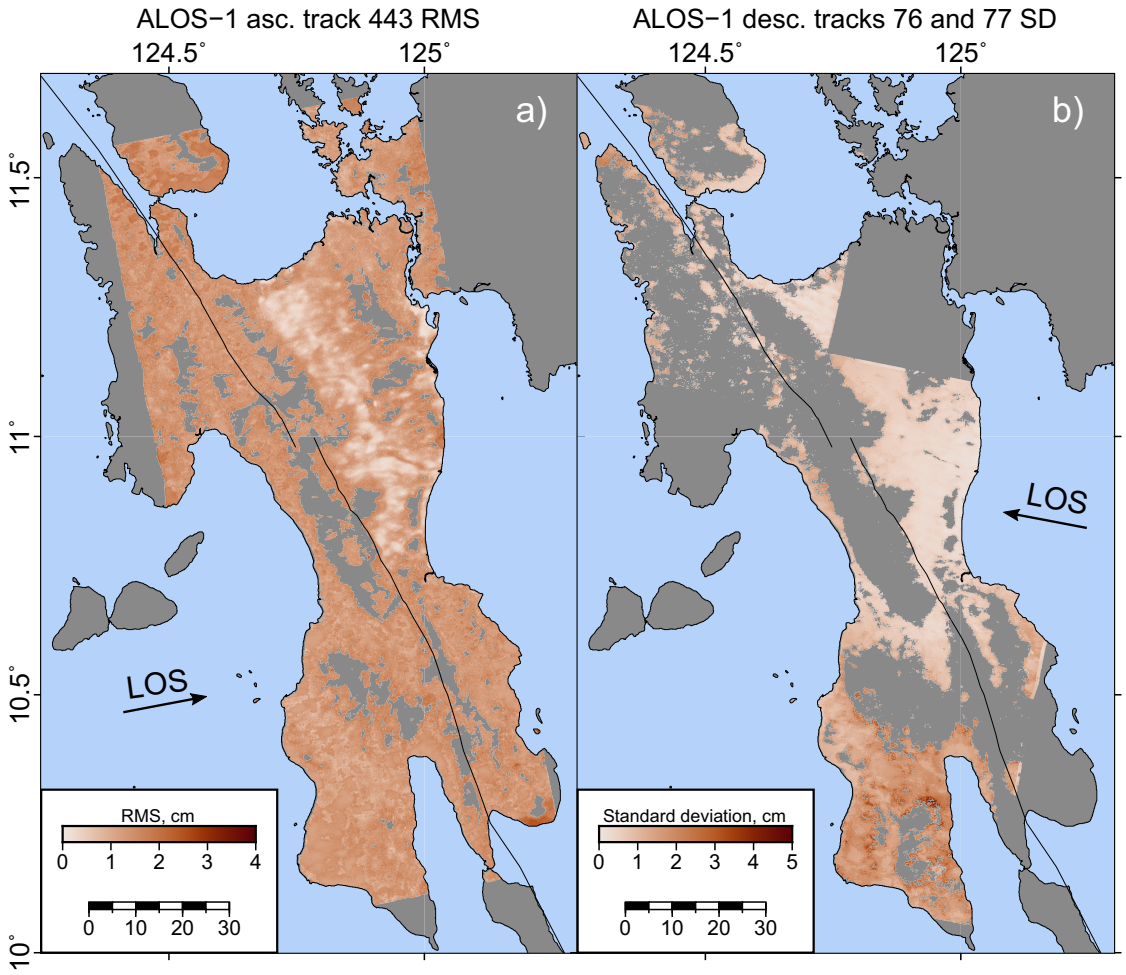


Figure J.4: A) Root-mean-square error of N-SBAS linear velocity, in cm/yr, for ALOS ascending track 443. B) Standard deviation of displacement rate estimated from stacking interferograms of ALOS descending tracks 76 and 77.

J.4 Manifestation of shallow aseismic slip on cultural features in Leyte

Previous unpublished work have identified locations on the ground that show evidence of aseismic slip on the surface along the Philippine Fault *Tsutsumi et al.* (2016). We visited some of these sites to compare with our observations from the InSAR data.

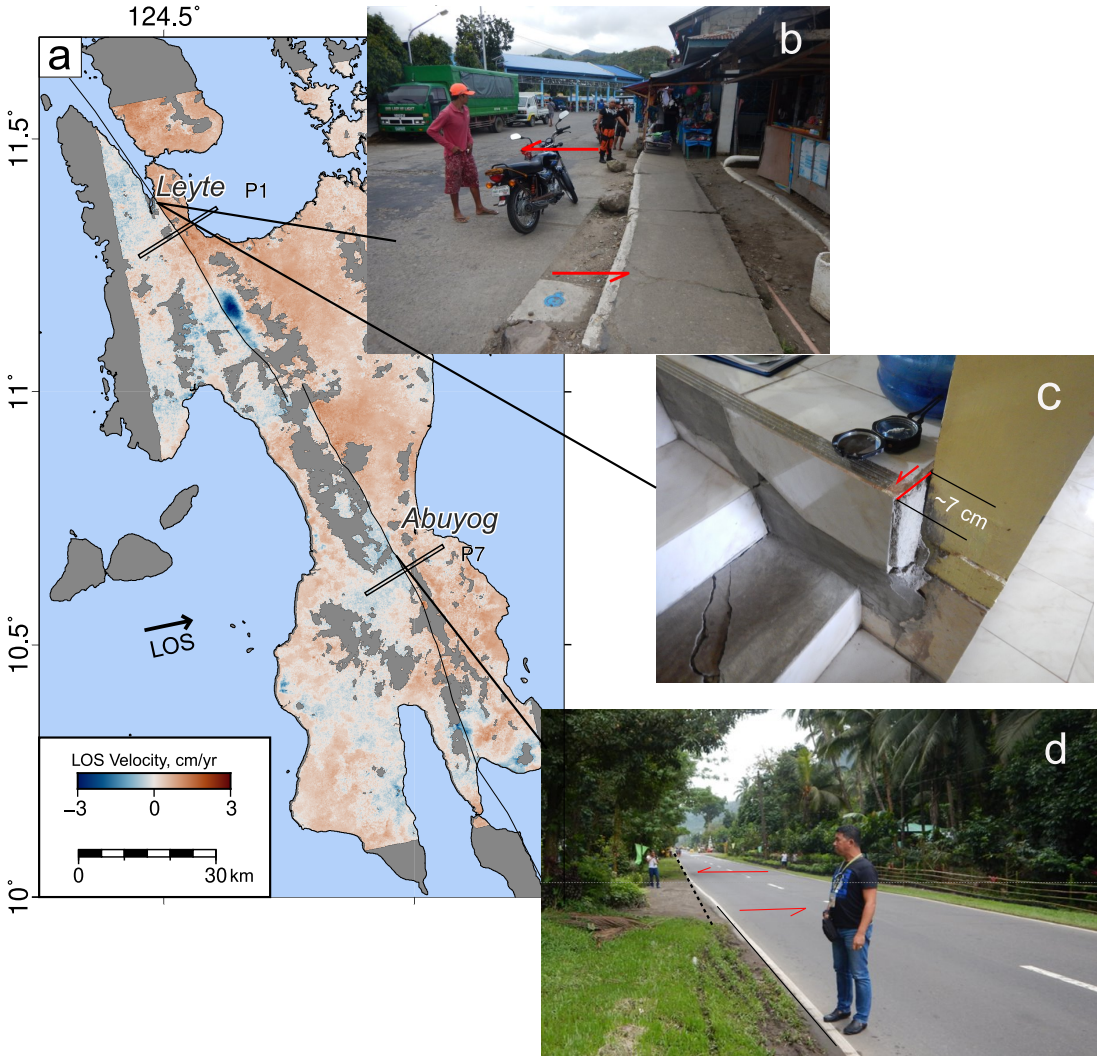


Figure J.5: Indications of aseismic left-lateral displacement from field assessment of displaced cultural features in Leyte. Field assessment was done in early January 2019. A couple of these sites (b and d) have been previously reported by (*Tsutsumi et al.*, 2016). A) Displaced concrete sidewalk in the town of Leyte in northern Leyte. Photo looking northeast. B) Inside a house in Leyte town, the upper level floor is displaced from the stair column by around seven centimeters. Photo looking west-northwest. C) In the town of Abuyog, freshly repaved road on national highway crossing the fault has preserved the original offset concrete road. Photo looking south.

J.5 Geothermal wells in Tongonan in relation to the subsidence source

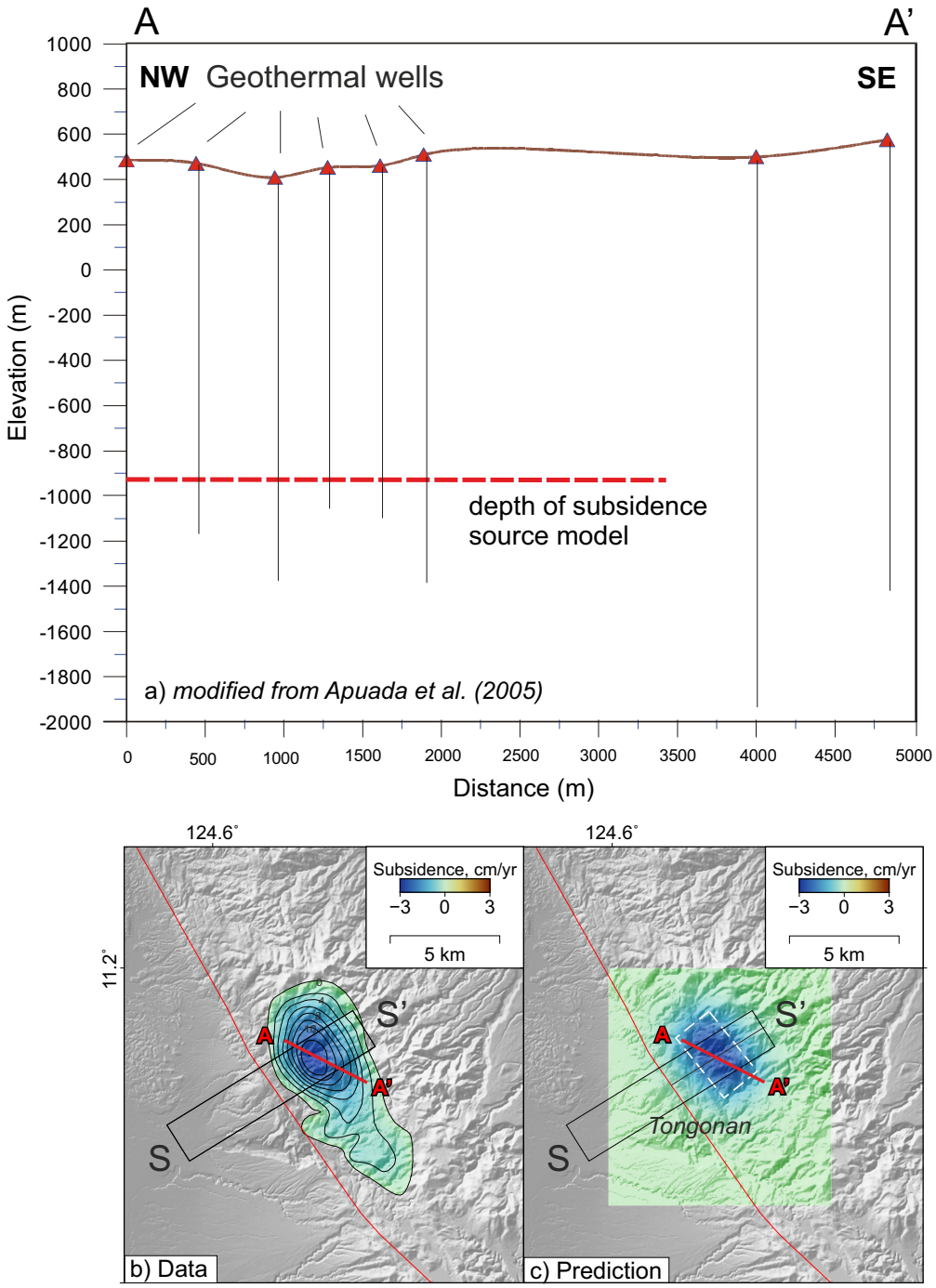


Figure J.6: Schematic location of the subsidence source model. a) Geothermal well cross-section A-A' (modified from *Apuada et al.*, 2005) and the subsidence model (dashed red line), plotted at the optimal depth from the surface (∼1.4 km). (b, c) Same as Figures 4.6a and 4.6b in the main text, showing the data and model predictions from the subsidence source inversion.

J.6 Empirical statistics (covariance functions) of noise in interseismic InSAR velocity maps

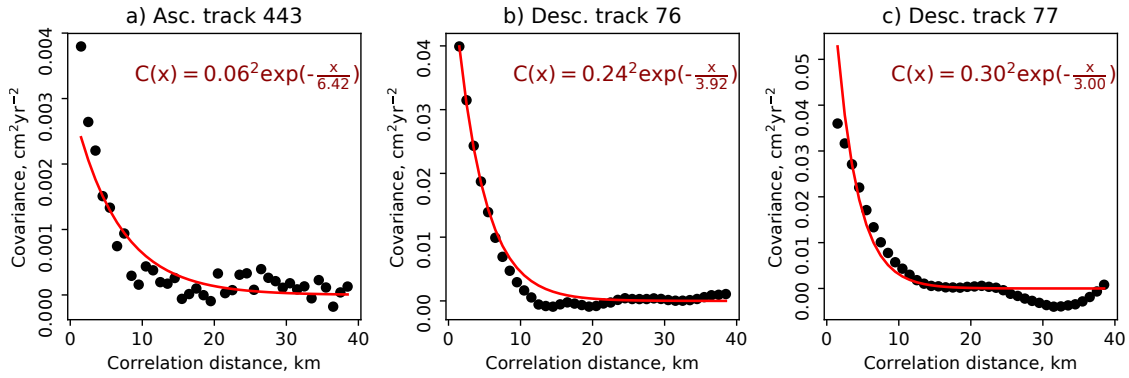


Figure J.7: Covariograms of interseismic InSAR data and empirical exponential fit (as in *Sudhaus and Jónsson*, 2009; *Jolivet et al.*, 2012) for ALOS ascending track 443 (a), descending track 77 (b), and descending track 76 (c). The coefficient of the exponential is the empirical standard deviation, and the denominator in the exponential term is the correlation distance.

J.7 Fit of interseismic mean model prediction in the ALOS descending line-of-sight (LOS)

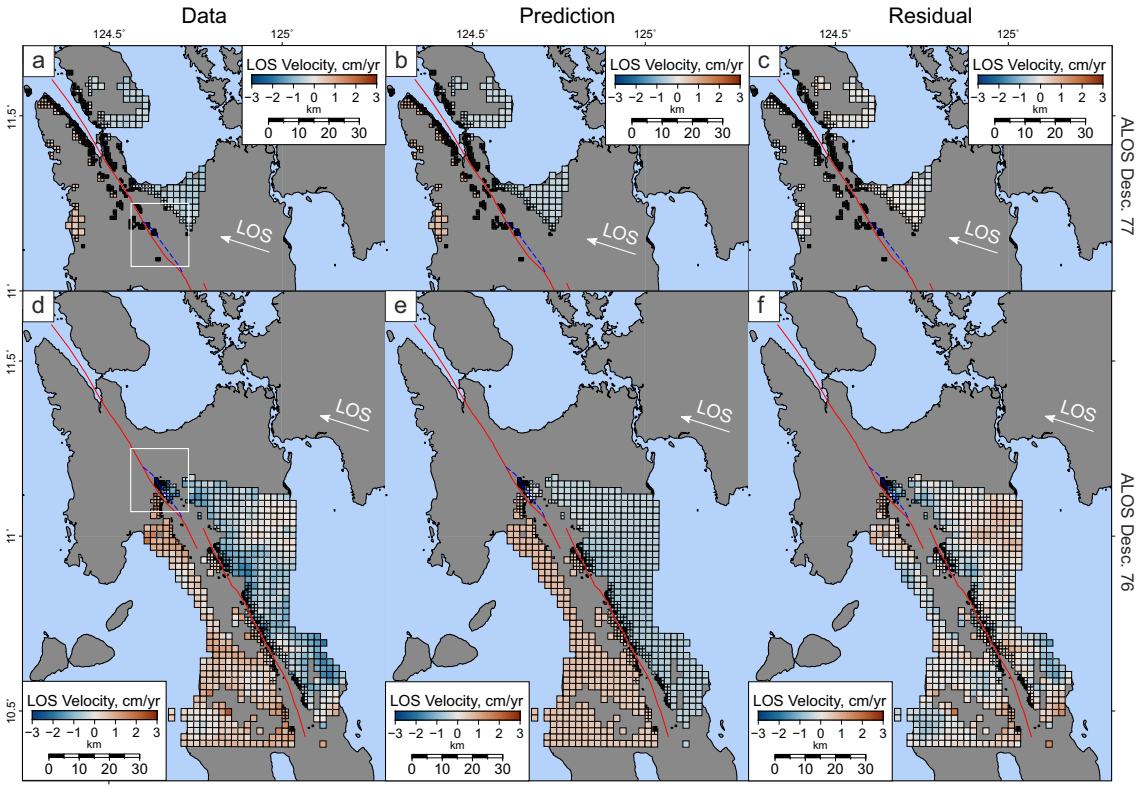


Figure J.8: Fit of mean model of interseismic slip on the Philippine Fault in Leyte in ALOS descending track data. a) Downsampled ALOS descending track 77 data with ramp correction. b) Predicted LOS velocity from mean model. c) Residuals. d-f) Same, but for ALOS descending track 76.

J.8 Correlation analysis between aseismic slip rate and subsidence parameters

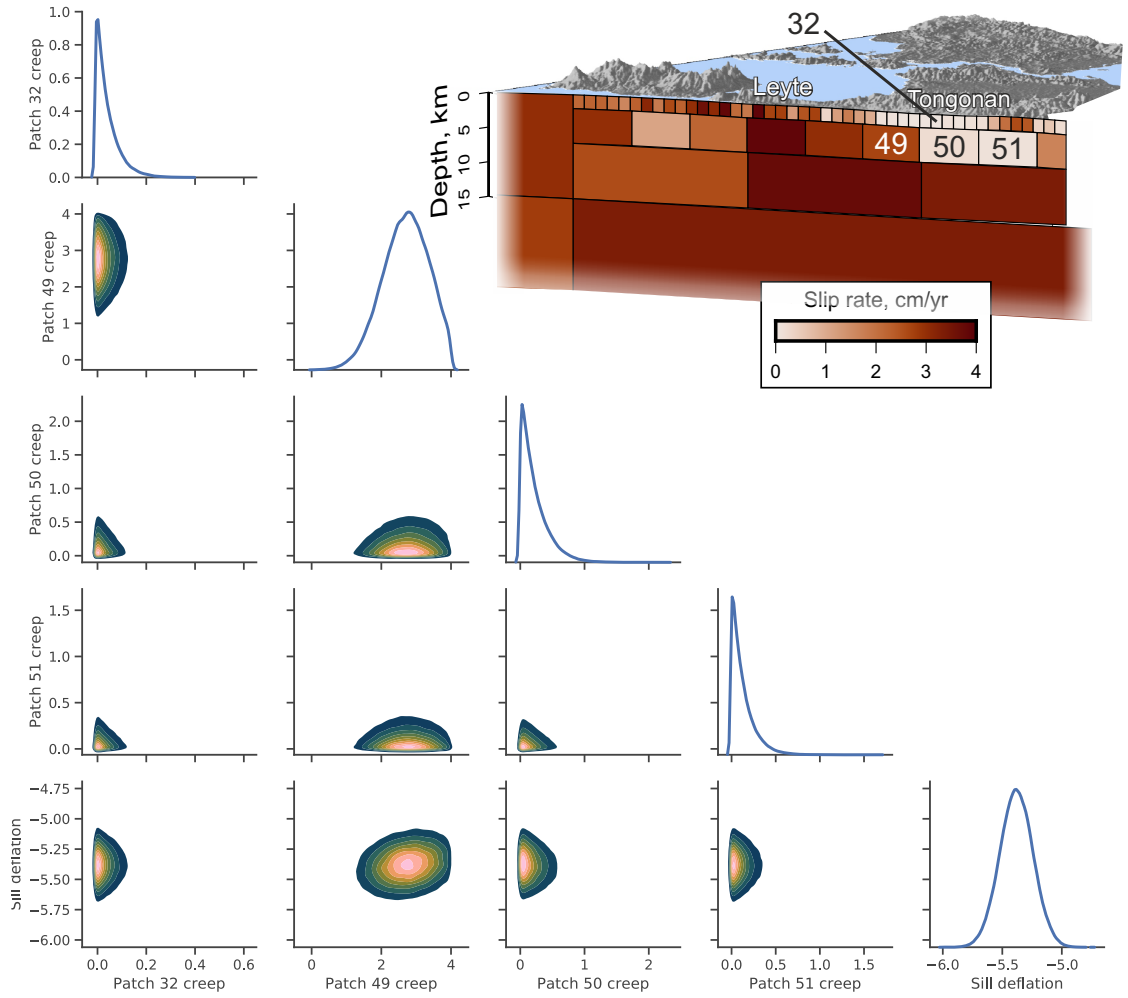


Figure J.9: Joint marginals of aseismic slip rate (i.e., of patches adjacent to subsidence signal) with sill deflation rate. Brighter areas indicate higher joint density, pointing to higher *a posteriori* probability. All axes units are in cm/yr. Location of patches are shown in the inset fault model (top right). No correlation between the parameters is apparent, suggesting that these adjacent deformation sources are independent of each other.

J.9 Empirical statistics (covariance functions) of noise in coseismic InSAR displacement maps

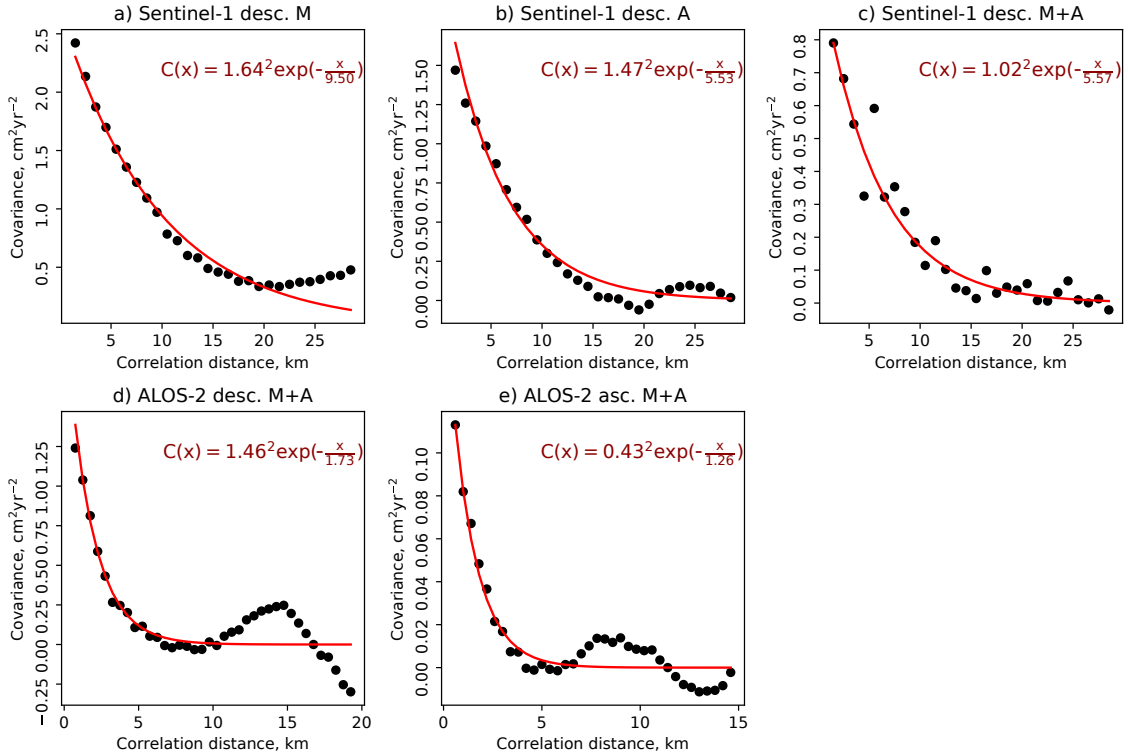


Figure J.10: Covariograms of coseismic InSAR data and empirical exponential fit (as in *Sudhaus and Jónsson*, 2009; *Jolivet et al.*, 2012) for a) Sentinel-1 descending track 61 covering the mainshock, b) the aftershock, and c) both events. d) Same, but for ALOS-2 descending track 136, and e) ascending track 24, both covering the mainshock and aftershock. The coefficient of the exponential is the empirical standard deviation, and the denominator in the exponential term is the correlation distance.

J.10 Mean and mode of posterior distribution of coseismic slip

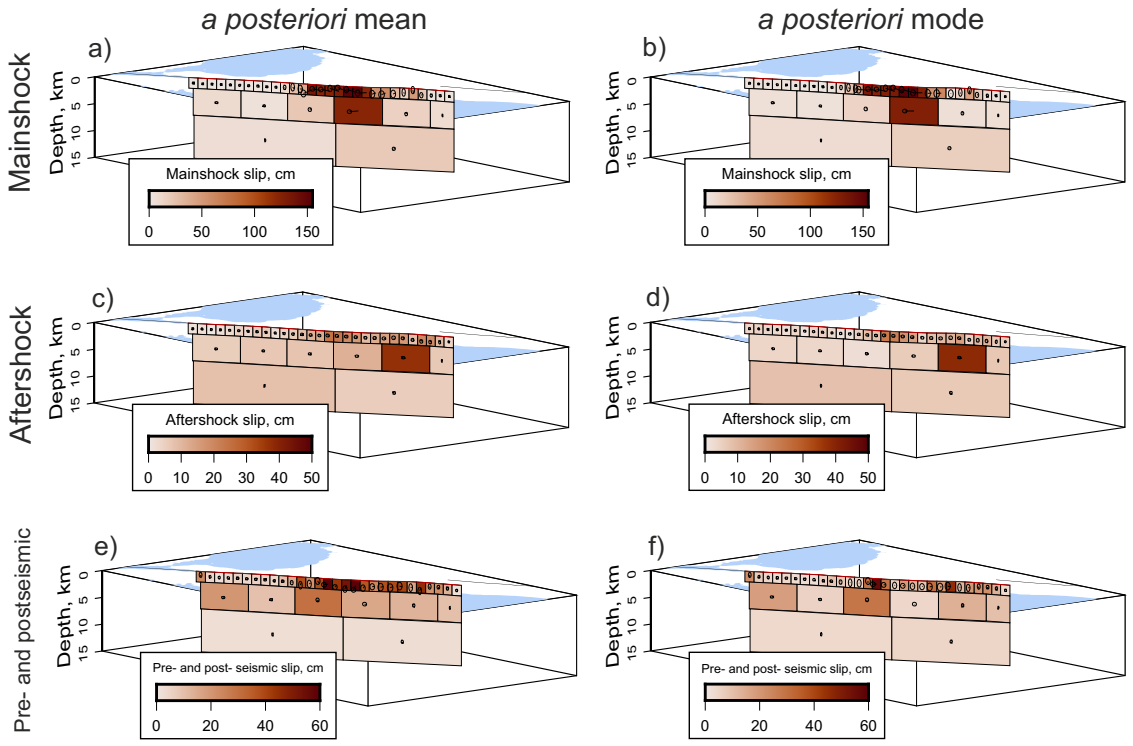


Figure J.11: Comparison of mean and mode of the posterior PDF of coseismic slip. a,b) 6 July 2017 M_w 6.5 mainshock. c,d) 10 July 2017 M_w 5.8 aftershock e,f) Pre- and postseismic slip. Arrows and ellipses indicate direction and 95% confidence interval of slip, respectively.

J.11 Downsampled Sentinel-1 coseismic LOS displacement data and model predictions for the July 2017 earthquakes

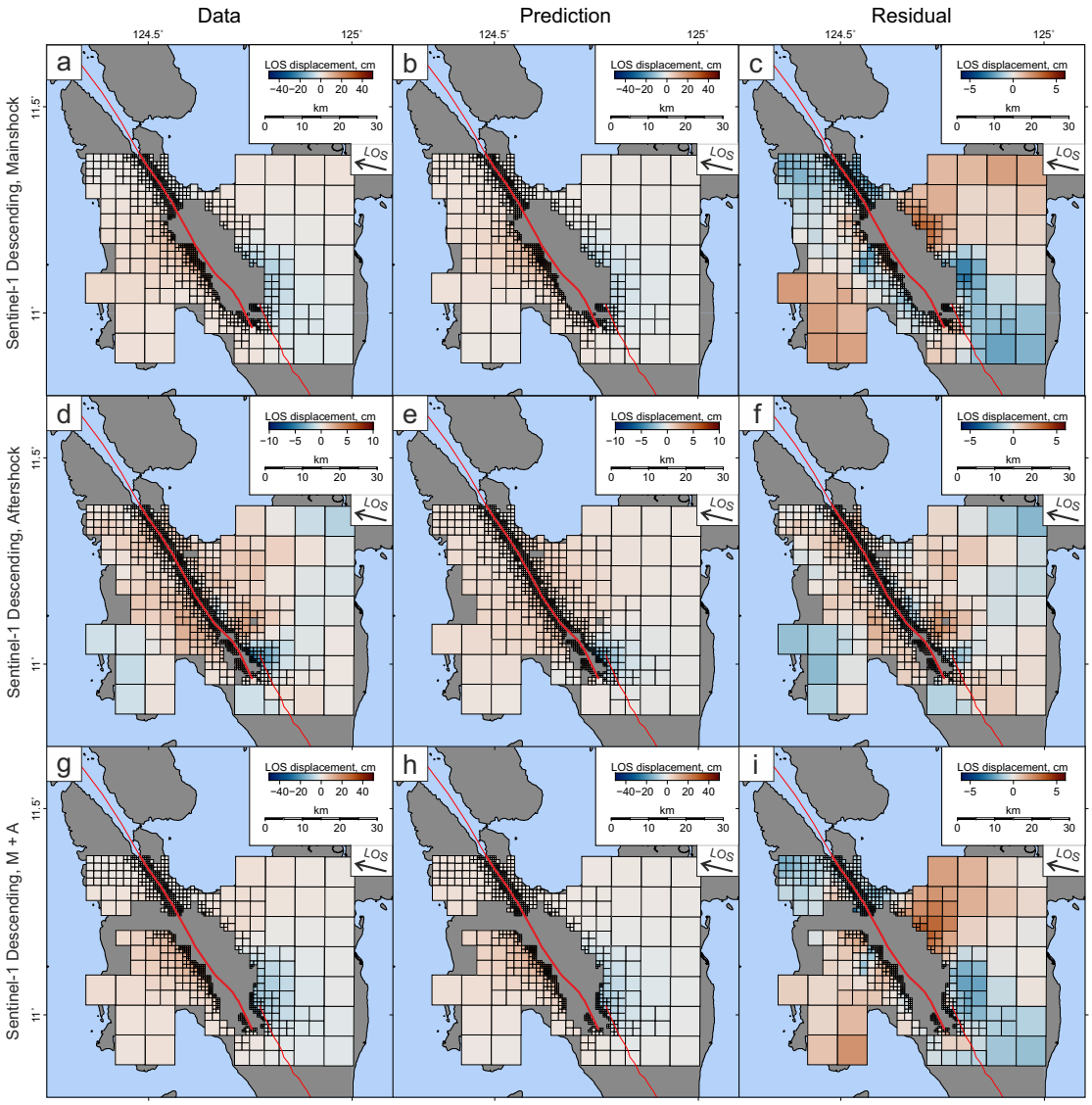


Figure J.12: Sentinel-1 descending LOS displacement data with ramp correction (left column), prediction (middle column), and residuals (right column), from downsampled interferograms including only the 6 July 2017 M_w 6.5 mainshock (a-c), only the 10 July 2017 M_w 5.8 aftershock (d-f), and both events (g-i).

J.12 Downsampled ALOS-2 coseismic LOS displacement data and model predictions for the July 2017 earthquakes

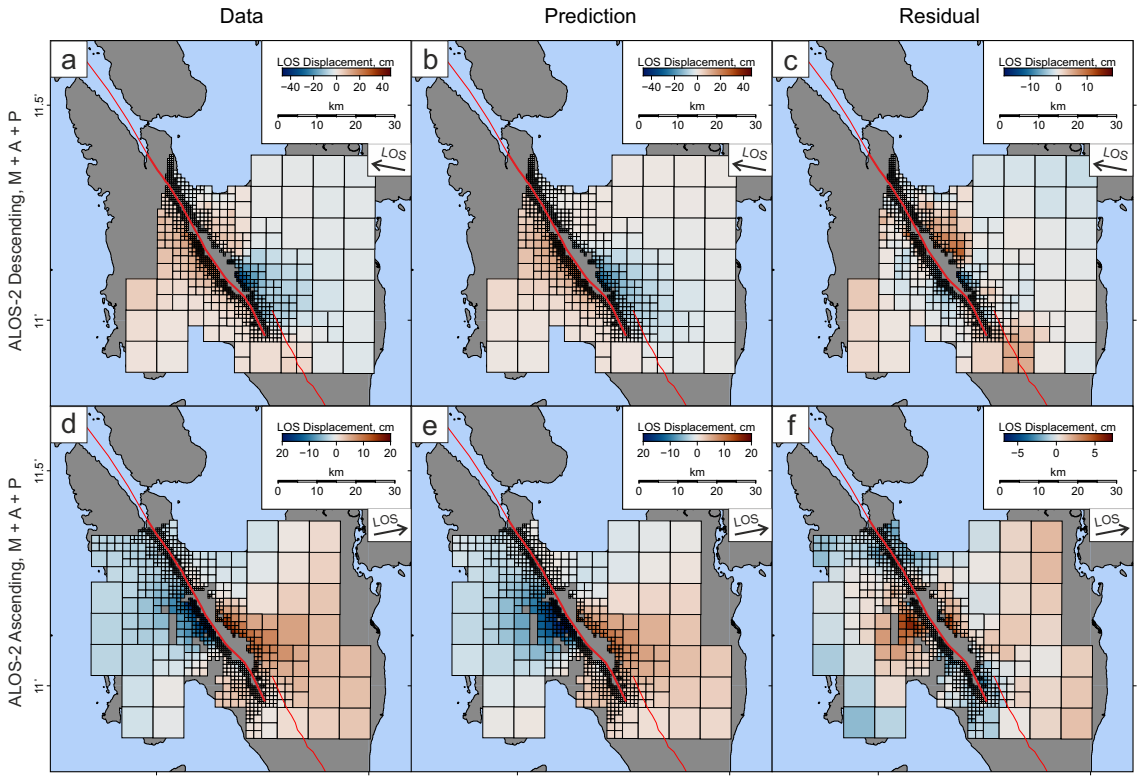


Figure J.13: ALOS-2 LOS displacement data with ramp correction (left column), prediction (middle column), and residuals (right column), from downsampled interferograms including both the 6 July 2017 M_w 6.5 mainshock and the 10 July 2017 M_w 5.8 aftershock, in descending (a-c) and ascending (d-f) LOS. Aside from the mainshock (M) and aftershock (A) deformation, both include the modeled "pre- and post-seismic" (P) deformation signals captured by the interferograms, as discussed in Chapter 4.4.1 of the main text, and shown in Figure J.11.

J.13 Results of test where we include a Central Fault Line in the modeling of interseismic aseismic slip

We tested a model that includes the Central Fault Line, a secondary branch of the Philippine Fault mapped in Tongonan (*Prioul et al.*, 2000; *Aurelio et al.*, 1993). We are interested if this model: 1) provides a better prediction of the observed LOS displacements by resolving aseismic slip on the Central Fault; and/or 2) affects the modeled slip on the primary fault plane (Tongonan Segment). Figure J.14 shows that the only conspicuous residual reduction is in descending track 76 (Figure J.14b). Figure J.15 shows that, in this model, the Central Fault line slips aseismically, while the Tongonan Segment still remains locked. See Section 4.3.5, and Section 4.5.2 (The role of geometry and structural complexity on seismic and aseismic slip distribution) of the main text for the full discussion.

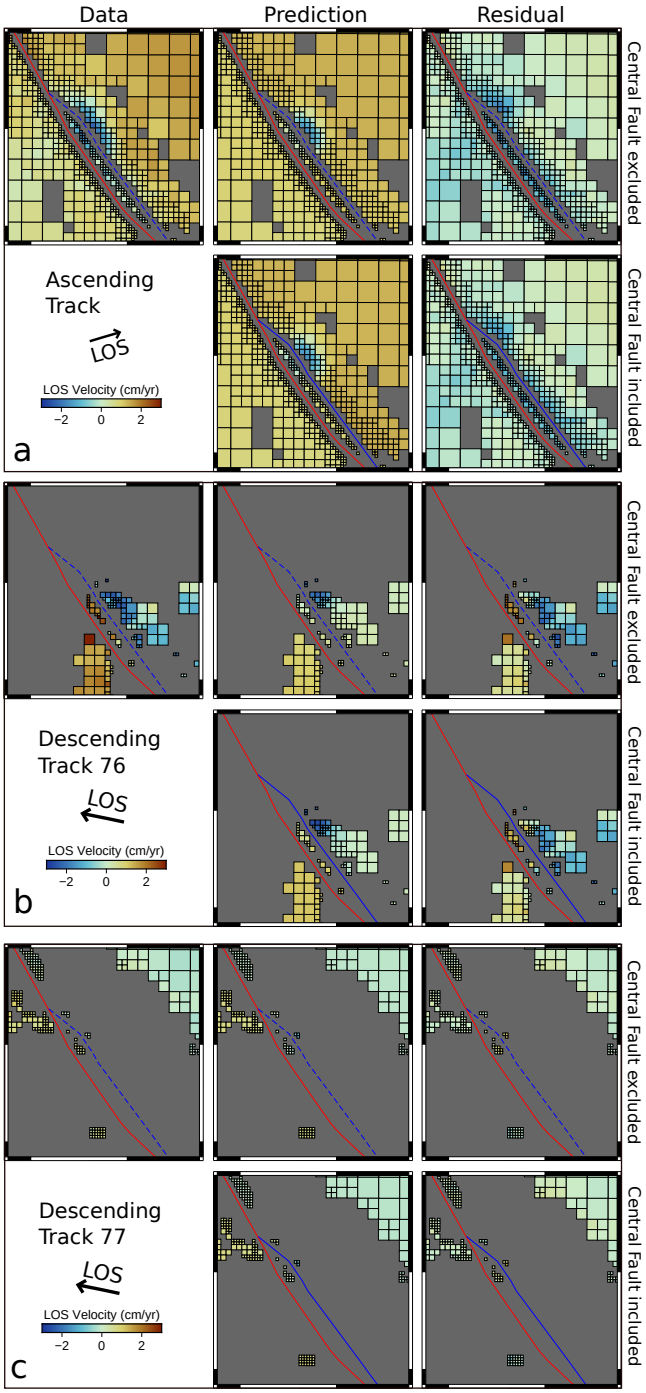


Figure J.14: Downsampled data (left), predictions (middle), and residuals (right) in Tongonan for an inversion with a model including the Central Fault (solid blue line), compared to a model without the Central fault (dashed blue line). a) ALOS ascending track 443 LOS. b) ALOS descending track 76 LOS. c) ALOS descending track 77 LOS. The most appreciable reduction of residuals is in ALOS descending track 76.S See Chapter 4.5.2 of main text for the discussion.

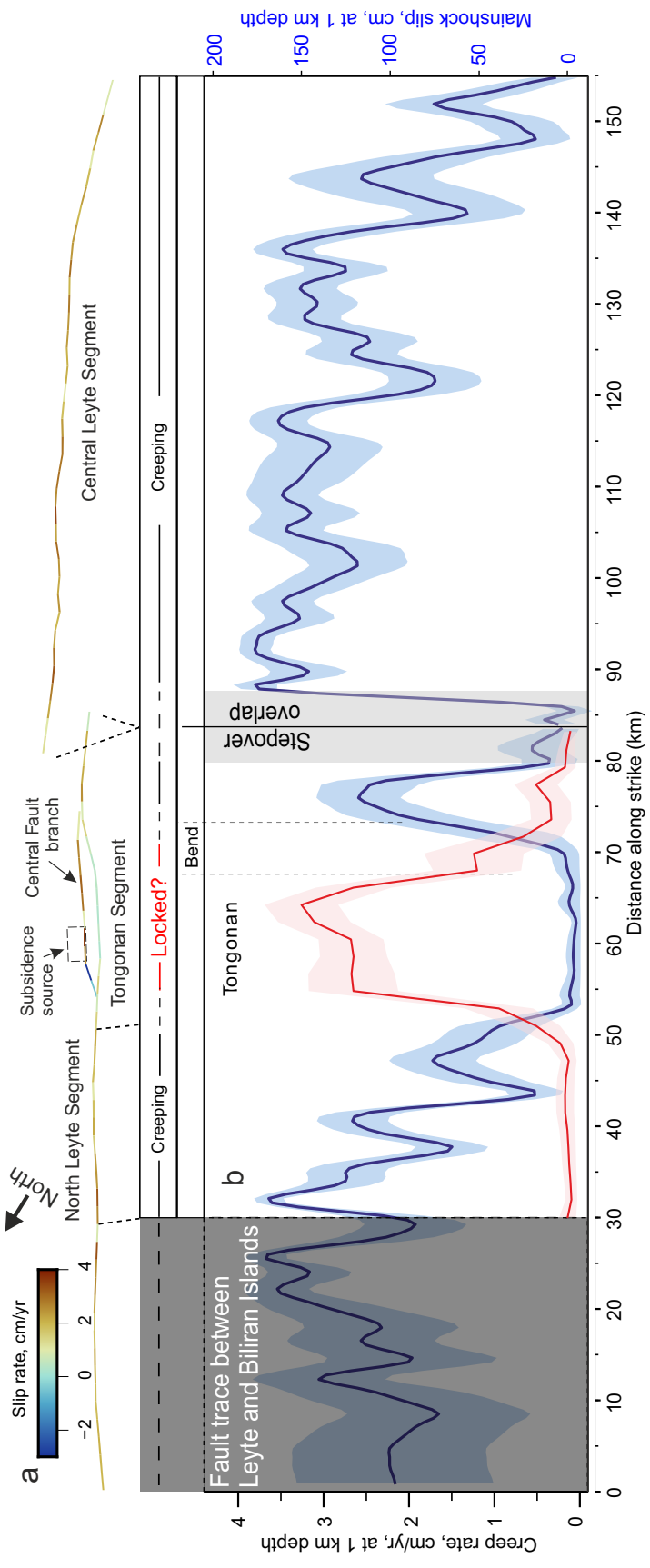


Figure J.15: Modeled shallow aseismic slip rate on the Philippine Fault in Leyte, similar to Figure 15 in the main text, but from a model where we include the Central Fault branch. Shown are the aseismic slip rate (blue) and the strike-slip component of M_w 6.5 mainshock (red) at 1 km depth. Shaded area from 0–30 km distance indicates section of the fault that goes off the coast of Leyte where aseismic slip at 1 km depth may be poorly resolved. Map view of the surface trace of the main Philippine Fault and Central Fault splay, and surface projection of the subsidence source is also shown for reference. Pink and cyan area: uncertainty of seismic and aseismic slip, respectively, based on the 1-σ range of their PDF.